BULGARIAN CHEMICAL COMMUNICATIONS

Journal of the Chemical Institutes
of the Bulgarian Academy of Sciences
and of the Union of Chemists in Bulgaria

Studies on conductivity and dielectric properties of PEO/PVP nanocomposite electrolytes for energy storage device applications

M. T. Iliev[1*], H. K. Koduru[1,2], L. Marino[1], Y. G. Marinov[1], D. Karashanova[3], N. Scaramuzza[2,4]

[1]*Georgi Nadjakov Institute of Solid State Physics, Bulgarian Academy of Sciences, Sofia, Bulgaria*
[2] *Department of Physics, University of Calabria, Rende (CS), Italy*
[3]*Institute of Optical Materials and Technologies, Bulgarian Academy of Sciences, Sofia, Bulgaria*
[4]*CNISM Unit, Molecular Biophysics Laboratory, Department of Physics, University of Calabria, Rende (CS), Italy*

Investigations on sodium-ion conducting polymer blend electrolyte systems based on PEO/ PVP, complexed with NaIO$_4$ salt and TiO$_2$ nanofiller, are presented in this report. The complexed polymer blend electrolytes were prepared in the form of dimensionally stable and free-standing films by conventional solution cast technique. Micro Raman and XRD studies confirmed the miscibility between PEO and PVP and the complexation of the salt with PEO/PVP polymer host. TEM measurements were carried out to evaluate size & distribution of the dispersed TiO$_2$ nanofiller. Complex impedance spectroscopy was performed in the 1 Hz – 1 MHz frequency range within the temperature range from room temperature to 343 K. Ionic conductivity of blend electrolytes increased with the increase of TiO$_2$ nanofiller concentration. Electrical conductivity and dielectric properties of NaIO$_4$ salt-complexed blend PEO/PVP/Na+ electrolytes were analyzed as a function of TiO$_2$ nanofiller concentration.

Keywords: Complexed polymer blend electrolytes, NaIO$_4$ salt, TiO$_2$ nanofiller, Ionic and electrical conductivity, Dielectric properties.

INTRODUCTION

Solid polymer electrolytes (SPEs) based on poly(ethylene oxide) (PEO) and complexed with various alkali metal salts have been recognized as potential systems to employ them in solid state rechargeable batteries [1, 2].Amongst the accessible battery chemistries, sodium (Na)-based rechargeable batteries (SIBs) have recently captured much attention because they are environmentally friendly, non-toxic, low-cost and abundant materials [3, 4]. Substantial research efforts, development, and demonstration are currently in progress to replicate the performance of the well-established Li-ion batteries using sodium ion batteries. Compared to the traditional organic liquid electrolytes, SPEs offer enhanced safety, stability and thin-film manufacturability but their low ionic conductivity especially at room temperature has suppressed their development.

Polyethylene oxide (PEO)-based polymer electrolytes have been employed extensively for battery applications since Armand *et al.* demonstrated the feasibility of using PEO as a potential ion-conductive electrolyte [5]. PEO is one of the widely investigated host polymers used for synthesizing SPEs to employ in alkali metal ion-conducting batteries due to its high electrochemical stability, good solvation, complexation and ion dissociation abilities. Several researchers have reported about various sodium salt complexes of PEO-based polymer electrolytes for sodium ion battery applications [6-8]. However, based on previous reports, the semicrystalline nature of PEO at room temperature, subsequently limits its ionic conductivity. The most straightforward approach to overcome this problem is modifying the PEO matrix in order to decrease its degree of crystallinity. One of the most promising alternate choices of enhancing the amorphous phase in PEO- based electrolyte systems is blending of PEO with a suitable higher-amorphous polymer [9]. Polyvinyl pyrrolidone (PVP) has been identified as a compatible partner to PEO, which exhibits higher order of amorphosity. PVP has high glass transition temperature, mechanical and thermal stability, provided its carbonyl group (C=O) enables forming of different complexes of alkali metal ion salts in a wide range of concentrations. In particular, reinforcement of nano-sized materials with polymer electrolyte systems can modify their microstructural properties and enhance their conductivity properties. In the present report, we made an attempt to prepare NaIO$_4$ salt-complexed and 1 wt% nano-sized TiO$_2$ fillers-doped PEO/PVP blend based electrolyte systems, using solution casting technique. X-ray diffraction (XRD), micro Raman and transmission electron microscopy (TEM) were employed to characterize the microstructural properties of the polymer electrolytes.

Impedance spectroscopy was used to study the ionic conductivity of the 1 wt% TiO_2 nanofiller-doped polymer blend electrolyte as a function of temperature.

EXPERIMENTAL

PEO and PVP of molecular weights of 5×10^6 and 3.6×10^5 respectively, were procured from Aldrich and employed without any further purification to prepare PEO/PVP solid state blend electrolytes. Sodium periodate salt ($NaIO_4$, Sigma Aldrich) and titanium dioxide nanopowder (TiO_2, Sigma Aldrich) were used as additives and methanol (Aldrich) was used as a solvent. Appropriate amounts of PEO and PVP polymers were dissolved in methanol solution, followed by mechanical stirring at room temperature for 15 hours to obtain uniform mixture of blend. In the meanwhile, 10 wt% of $NaIO_4$ salt was dissolved separately in methanol and the solution was added to the prepared viscous PEO/PVP polymer solution to obtain 'PEO/PVP/$NaIO_4$' polymer complex. Nano-sized TiO_2 powder (1 wt%) was dispersed in methanol separately, and the solution was sonicated for 30 min, and added to the 'PEO/PVP/$NaIO_4$(10 wt%)' electrolyte solution to prepare 'PEO/PVP/$NaIO_4$(10 wt%)/TiO_2(1 wt%)' nano composite electrolyte. The as-prepared viscous solutions were poured into polypropylene dishes and the solvent (methanol) was allowed to evaporate slowly at room temperature to harvest free-standing polymer electrolyte films of 150 μm thickness. All electrolyte films were vacuum-dried at 45°C to remove traces of methanol solvent and then kept in desiccators filled with silica gel desiccant for several hours before being characterized to avoid any traces of moisture.

The structural properties of the electrolytes were analysed by recording X-ray diffraction patterns (XRD) in the 2θ range of 10° – 80° with a constant step of 0.02^0, counting time 35s/step on a Bruker D8 Advance diffractometer with Cu Kα radiation and Lynx Eye detector. The Raman spectra were measured on a HORIBA Jobin Yvon LabRAM HR visible spectrometer equipped with a Peltier-cooled CCD detector. The laser beam was focused on a spot of about2 μmusing microscope optics and 633 nm line of He-Ne laser was used for excitation. The spectra were calibrated using the T_{2g} vibrational Raman line of Si at 520.7 cm^{-1}. TEM (HR STEM JEOL JEM 2100 acceleration voltage 80 - 200 kV, maximum resolution – 0.23 nm) measurements were carried out to estimate the size and distribution of doped nano-sized TiO_2 fillers in the matrices of polymer electrolytes. Solid polymer electrolyte films were sandwiched between two copper electrodes and ionic conductivity studies were carried out at room temperature by a.c. impedance measurements using Biologic potentiostat/galvanostat (SP – 200) in the frequency range of 1 Hz - 1 MHz.
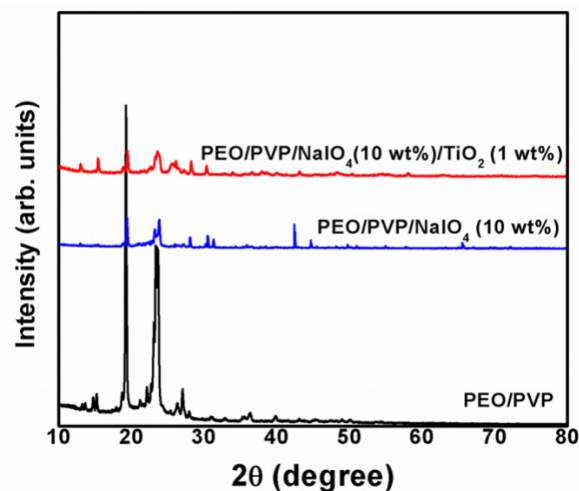
RESULTS AND DISCUSSION

Figure 1. X-ray diffraction patterns for various polymer electrolytes.

Figure 1 presents the X-ray diffractions patterns of pure PEO/PVP, 10 wt% $NaIO_4$ salt-complexed and 1 wt% TiO_2 nanofiller-doped blend electrolyte films. Significantly, the intensity of all crystalline peaks of PEO considerably decreases upon the addition of salt to the polymer blend, suggesting a decrease in the degree of crystallinity of the complexes. This could be due to the disruption of the semicrystalline structure of the film by salt [10]. When salt dissolves in the PEO/PVP polymer host, the interaction between PEO/PVP host matrix and $NaIO_4$ salt leads to an increase of the amorphous region. The relative intensities of sharp peaks of PEO at around 19.2^0 and 23.4^0 in the10 wt% $NaIO_4$ salt-complexed PEO/PVP blend decrease further as a result of doping of 1 wt% of TiO_2 nanofiller, which indicates a decrease of crystallinity in the electrolyte films. It can be attributed to the possible interaction between the polymer chains and TiO_2 nanofiller which leads to a decrease of the intermolecular interaction of polymer chains [11]. This facilitates the possible motion of the polymer chains in the amorphous domain and favors mobility enhancement of the charge carriers in the polymer electrolytes and leads to an increase in ionic conductivity.
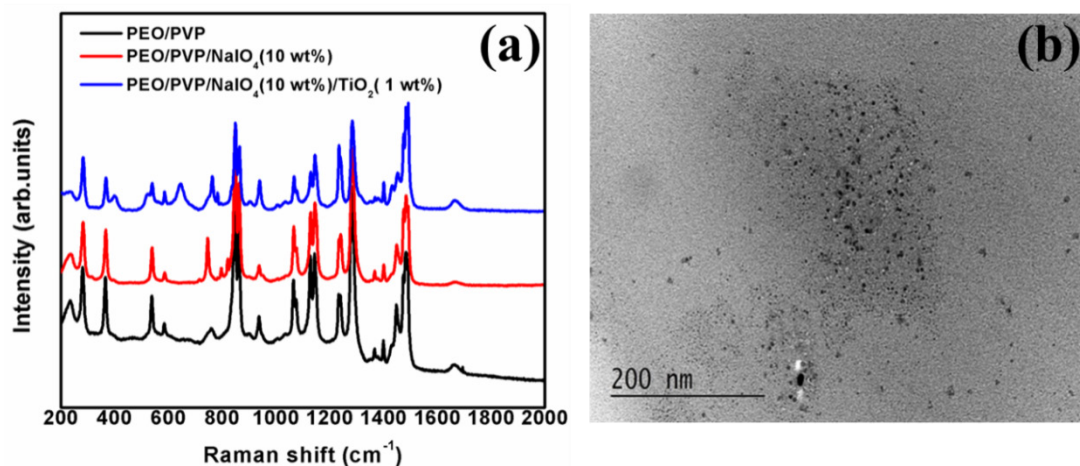
Figure 2. Raman spectra for different polymer electrolytes (a) and TEM image of 'PEO/PVP/NaIO$_4$ (10 wt%)/TiO$_2$ (1 wt%)' electrolyte (b).

Figure 2a shows the Raman spectra of pure, NaIO$_4$ salt-complexed and TiO$_2$ nanofiller-doped PEO+PVP blend electrolytes in the wavenumber region of 200 – 2000 cm^{-1}. Raman spectrum of pure blend displays bands at 759 cm^{-1}, 1229 cm^{-1}, 1231cm^{-1}, 1425 cm^{-1} and1663 cm^{-1}corresponding to C-N vibration, C-N stretching and C-H bending vibrations of pure PVP, respectively. The characteristic principal bands at 354, 843, 857, 932 and 1062 cm^{-1} are observed corresponding to PEO [12]. The band of lower intensity present at 932 cm^{-1} is assigned to CO stretching mixed with CH$_2$ rocking vibration of PEO. The band is observed at 1480 cm^{-1} and can be attributed to in-phase bending of the CH$_2$ group of PEO [13]. This mode is active in the Raman spectrum and not active in the infrared spectrum. The bands observed at around 1275 cm^{-1} and 1235 cm^{-1} are assigned to the out-of-phase twisting for the CH group of PEO [14]. As a result of addition of 10 wt% of NaIO$_4$ salt to the PEO+PVP blended polymer film, the relative intensity of the spectral band at 1063 cm^{-1} due to C-O stretching and /or rocking modes of CH$_2$ vibrations, is dramatically reduced, which suggests the formation of a complex between sodium ions and PEO+PVP matrix. Further decrease in intensity of the spectral band at 1063 cm^{-1} is observed due to doping of 1 wt% of TiO$_2$ nanofiller. This indicates an increase in the strong interaction between the dissociated salt and the blended polymer matrix as a result of the presence of TiO$_2$ nanofiller and this process leads to a decrease of the semi-crystalline nature of polymer blend. From TEM measurements (Figure 2b) the average size of the nanofiller particles is found to be 10 nm and TiO$_2$ nanoparticles are observed to be uniformly distributed in the matrix of salt-complexed blend electrolytes.

Impedance spectroscopy is a promising method for the investigation of ionic conductivity of solid polymer electrolyte films. The 'PEO/PVP/NaIO$_4$ (10 wt%)/TiO$_2$(1 wt%)' electrolyte films were properly dried and impedance measurements were carried out at room temperature by sandwiching the electrolyte films between two copper electrodes. Figure 3a shows the variation of real and imaginary parts of impedance as a function of applied frequency for 'PEO/PVP/NaIO$_4$ (10 wt%)/TiO$_2$ (1 wt%)' electrolyte film. Figure 3b presents the complex impedance plane plot (Z′ *vs* Z″) for the TiO$_2$ nanofiller (1 wt%)-doped 'PEO/PVP/NaIO$_4$ (10 wt%)' electrolyte film at room temperature. The ionic conductivity of the sample is calculated by the equation $\sigma = \left(t / {R_b * A} \right)$, where t and A are thickness and area of the electrodes, respectively. The complex impedance plot demonstrates a well-defined semicircle at intermediate frequencies, which can be explained by parallel combination of bulk resistance and bulk capacitance. This could be a result of the migration of ions and the immobile polymer chains, respectively [15]. The bulk resistance is obtained from the intercept of the semicircle at the high frequency side (1 MHz to 1 Hz) of the plot with the real axis. The estimated room temperature conductivity for 'PEO/PVP/NaIO$_4$ (10 wt%)' electrolyte film is 1.57×10^{-7} S/cm. As a result of the inclusion of 1 wt% of TiO$_2$ nanofiller, the corresponding room temperature conductivity increases to 4.56×10^{-7}S/cm. The enhancement of conductivity as a result of inclusion of TiO$_2$ nanofiller could be due to reduction in crystallinity of the polymer chains in the blend polymer electrolyte.
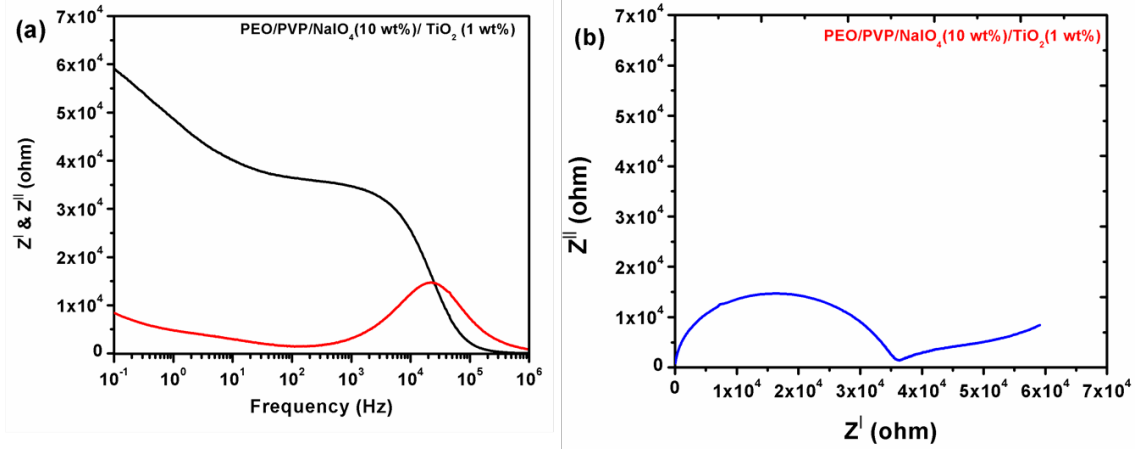
Figure 3. Variation of real and imaginary parts of impedance as a function of frequency. (a) Cole-Cole plot; (b) for 'PEO/PVP/NaIO$_4$ (10 wt%)/TiO$_2$ (1 wt%)' electrolyte film.
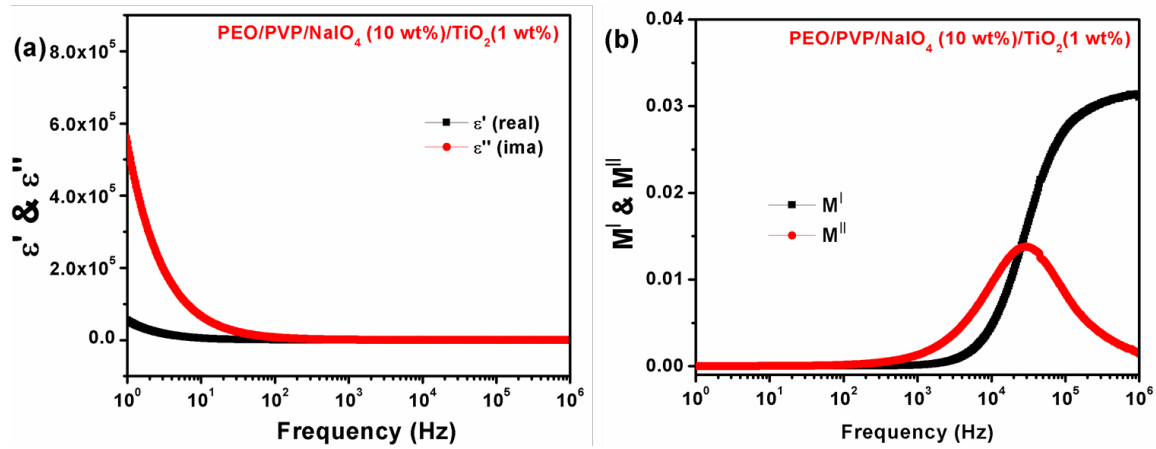

Figure 4. Variation of real and imaginary parts of dielectric permittivity (a) and Variation of real and imaginary parts of dielectric modulus (b) as a function of frequency for 'PEO/PVP/NaIO$_4$ (10 wt%)/TiO$_2$ (1 wt%)' electrolyte film.

This improves the capacity of sodium ion transport in the electrolyte film and hence improves the ionic conductivity of the polymer electrolyte film [16, 17].

Dielectric materials are recognized as media that have an ability to store electrical energy. This property of dielectric materials can be estimated by measuring the permittivity or dielectric constant of the material. In alternating electric fields the relative permittivity exhibits a complex behavior and is defined by $\varepsilon^* = \varepsilon' - j\varepsilon''$. The real ($Z_r$) and imaginary ($Z_i$) parts of complex impedance (Z^*) are also used for the evaluation of real and imaginary parts of dielectric permittivity using the following equations:

$$\varepsilon' = \frac{Z_i}{\omega C_0 (Z_r^2 + Z_i^2)} \qquad (1)$$

$$\varepsilon'' = \frac{Z_r}{\omega C_0 (Z_r^2 + Z_i^2)}, \qquad (2)$$

where C_o is the vacuum capacitance given by $\varepsilon_o A/d$, where ε_o is the permittivity of free space and is equal to 8.85×10^{-12} Fm^{-1}. The angular frequency is given

as $\omega = 2\pi f$, where f is the frequency of applied field. The real part of complex dielectric permittivity ε' has the same significance as that of the ordinary dielectric constant of the material. It measures the energy stored in the material during each cycle, to be returned to the electric field at the end of the cycle.

Figure 4a describes the frequency dependency of real and imaginary parts of dielectric permittivity of nano-composite 'PEO/PVP/NaIO$_4$(10 wt%)/TiO$_2$(1 wt%)' electrolyte. Significantly, nano-composite electrolyte films demonstrate relatively higher dielectric constant values in comparison to the pure and salt-complexed PEO/PVP electrolyte films. This can be explained by the capability of TiO$_2$ nanoparticles that leads to dissociation of undissociated salt/ion aggregates into free ions (anions) in the matrix of PEO/PVP/NaIO$_4$(10 wt%) electrolyte. It also supports the enhancement of dielectric constant values [18, 19]. The dielectric behavior could be easily explained by using the formulation of dielectric moduli. A complex electric modulus was used to investigate the conductivity relaxation phenomena. It suppresses the effects of

electrode polarization to give a clearer picture of electrical property inherited in the polymer electrolyte. Complex electric modulus can be calculated from the impedance data using the following relations:

$$M' = \frac{\varepsilon'}{\varepsilon'^2 + \varepsilon''^2} \qquad (3)$$

$$M'' = \frac{\varepsilon''}{\varepsilon'^2 + \varepsilon''^2}. \qquad (4)$$

In the above expressions M', M'' and $\varepsilon', \varepsilon''$ are the real and imaginary parts of the electric modulus and dielectric constants, respectively. The frequency dependence of M' for 'PEO/PVP/NaIO$_4$ (10 wt%)/TiO$_2$ (1 wt%)' electrolyte film is shown in Figure 4b. It is obvious that M' reaches a maximum saturation at high frequency. This is ascribed to the fact that in the high frequency region the dielectric constant values of both pure and salt-complexed PEO/PVP blend electrolytes decrease to a minimum value and thus M' becomes maximum [20].The imaginary part of modulus (M'') spectra, a distinct relaxation peak is observed which is related to the conductivity processes and it evidences that conduction in polymer electrolytes takes place through charge migration of ions between coordinated sites of the polymer along with the segmental relaxation of polymer [21]. In comparison to salt-complexed electrolytes, TiO$_2$-doped electrolyte films demonstrated better dielectric properties. For the 'PEO/PVP/NaIO$_4$ (10 wt%)/TiO$_2$ (1 wt%)' electrolyte film, relaxation frequency is found to be in a higher frequency region and the corresponding relaxation time is 3.4×10^{-5} sec.

CONCLUSIONS

PEO/PVP blend-based solid polymer blend electrolytes complexed with NaIO$_4$ salt were prepared by solution casting method. The modifications in microstructural properties of pure and salt-complexed PEO/PVP blend electrolytes were studied by XRD and micro Raman techniques. The decrease in intensity of characteristic peaks of PEO reveals the increase in amorphous nature, which supports the increase in ionic conductivity. The presence of well resolved vibrational bands in the micro Raman spectra, corresponding to ether oxygen groups (C – O – C) of PEO and carbonyl group of PVP, evidences for co-existence and miscibility of PEO and PVP polymers. The TiO$_2$ nanocomposite 'PEO/PVP/NaIO$_4$ (10wt%)/TiO$_2$ (1 wt%)' polymer blend electrolyte exhibits higher room temperature ionic conductivity of 4.56×10^{-7} S/cm. The increase in the dielectric constant upon addition of TiO$_2$ nanofiller exposes the increase of dissociated ions in the polymer blend matrix. The

distinctive peak in the M'' vs. frequency spectrum suggests that TiO$_2$-doped salt-complexed polymer electrolytes are potential ionic conductors.

REFERENCES

1. J. M. Tarascon, M. Armand, *Nature,* **414,** 359 (2001).
2. S. K. Kim, D. G. Kim, A. Lee, H. S. John, J. J. Wie, N. A. Nguyen, M. E. Mackay, J. C. Lee, *Macromolecules,* **45,** 9347 (2012).
3. V. Palomares, P. Serras, I. Villaluenga, K. B. Hueso, J. Carretero-Gonzalez, T. Rojo, *Energy & Environ. Sci.*, **5,** 5884 (2012).
4. L. Wang, Y. Lu, J. Liu, M. Xu, J. Cheng, D. Zhang, J. B. Goodenough, *Angew. Chem.*, **52,** 1964 (2013).
5. M. B. Armand, J. M. Chabagno, M. Duclot, in: St. Andrews (ed.), Proceedings of 2nd International Meeting Solid Electrolytes, Scotland, 1978.
6. S. Mohapatra, A. Thakur, R. N. P. Choudhary, *Ionics,* **14,** 255 (2008).
7. A. Manuel Stephan, K. S. Nahm, *Polymer,* **47,** 5952 (2006).
8. M. Patel, K. G. Chandrappa, A. J. Bhattacharyya, *Solid State Ionics,* **181,** 844 (2010).
9. R. Borkowska, J. Laskowski, J. Plocharski, J. Przyluski, W. Wieczorek, *J. Appl. Electrochem.,* **23,** 991 (1993).
10. R. M. Hodge, G. H. Edward, G. P. Simon, *Polymer,* **37,** 1371 (1996).
11. C.W. Lin, C. L. Hung, M. Venkateswarlu, B. J. Hwang, *J. Power Sources,* **146,** 397 (2005).
12. T. Yoshihara, H. Tadokoro, S. Murahashi, *Journal of Chemical Physics,* **41,** 2902 (1964).
13. H. Matsuuta, K. Fukuhara, *Journal of Polymer Science: Part B: Polymer Physics*, **24**, 1383 (1986).
14. J. Maxfield, I. W. Shepherd, *Polymer,* **16,** 505 (1975).
15. B. L. Papke, M. A. Ratner, D. F. Shriver, *J. Electrochem. Soc.,* **129,** 1694 (1982).
16. D. Carlier, J. H. Cheng, R. Berthelot, M. Guignard, M. Yoncheva, R. Stoyanova, B. J. Hwang, C. Delmas, *Dalton Trans.,* **40,** 9306 (2011).
17. Y.-C. Lin, J.-H. Cheng, M. Venkateswarlu, F.-M. Wang, R. Santhanam, B. J. Hwang, J. *Chin. Chem. Soc. ,***59,** 1250 (2012).
18. D. Kumar, S. A. Hashmi, *Solid State Ionics,* **181,** 416 (2010).
19. A. Bhide, K. Hariharan, *Polym. Int.,* **57,** 523 (2008).
20. A. S. A. Khiar, R. Puteh, A. K. Arof, *Physica B Condensed Matter,* **373,** 23 (2006).
21. M. A. L. Nobre, S. J. Langfredi, *Phys. Chem. Solids,* **62,** 1999 (2001).

Synthesis and antimicrobial studies of tetrazol-5-yl-methoxy-8,9-dihydropyrano[2,3-ƒ]chromene-2,10-diones and their coumarin derivatives

B. Srinivas[1, 2*], M. Subramanyam[3], G. K. Srinivasulu[4], K. Prabhakara Rao[1*]

[1]New Generation Materials Lab (NGML), Department of Science and Humanities, Vignan's Foundation for Science Technology and Research (Deemed to be University), Vadlamudi, Guntur-522 213, Andhra Pradesh, India
[2]Department of H&S, Guru Nanak Institutions Technical Campus, Hyderabad, Telangana, India
[3]Department of Chemistry, SR & BGNR Govt. College, Khammam, Telangana, India
[4]Department of H&S, Keshav Memorial Institute of Technology, Hyderabad, Telangana, India

Twelve new coumarin-tetrazole derivatives, tetrazol-5-yl(methoxy)-8,9-dihydropyrano[2,3-ƒ] chromene-2,10-diones, were synthesized by 6-((2H-tetrazol-5-yl)methoxy)-4-methyl-8,9-dihydropyrano[2,3-f]chromene-2,10-dione derivatives treated with alkyl bromides in dry acetone and anhydrous potassium carbonate. The structures of all the newly synthesized molecules were assigned by spectral data and elemental analysis. The synthesized compounds were screened for their antimicrobial activities strains using the diffusion plate method. Most of the compounds showed moderate to good activity against *Staphylococcus aureus, Bacillus subtilis, Escherichia coli* and *Pseudomonas aeruginosa.* Out of two strains of fungi, these compounds showed moderate to good activity against *Aspergillus fumigatus* and *Aspergillus niger*.

Keywords: Tetrazole, coumarin, antibacterial, antifungal, zone of inhibition

INTRODUCTION

Coumarins are an important class of natural and synthetic compounds that possess a wide spectrum of biological and pharmacological activities [1]. The coumarin skeleton is found in many natural products and is used as an important synthetic intermediate for the preparation of numerous heterocyclic compounds which show unique physical properties [2]. Furthermore, a large number of pharmaceutical drug products like novobiocin, warfarin, contain 7-hydroxy-4-methyl-2-coumarin as an important structural element [2, 3]. Coumarins containing heterocyclic moieties have a noteworthy medicinal value due to their high potential pharmacological activities such as antibacterial [3-12], antifungal [13-15], anti-tuberculosis activities [16-19], etc. Tetrazole derivatives are well known for their various potential biological activity [20]. Moreover, they are also observed as biologically comparable to the carboxylic acid group [21]. In fact, it has been also noticed that the toxic properties of a drug can be decreased by incorporation of a tetrazole ring into the molecule [22]. Generally, synthesis of tetrazoles can be achieved most commonly *via* the formal [2 + 3] cycloaddition of azides and nitriles. However, various reports in the literature describe that the mechanism of the reaction is different for diverse azide species. When an organic azide is used as the dipole, only certain highly activated nitriles are competent dipolarophiles [23]. In these cases, the reaction is region- selective, and only the 1-alkylated product is observed [24-32]. In this study we report the synthesis and characterization of twelve new coumarin derivatives by incorporation of tetrazole moiety for better biological and pharmacological activities.

EXPERIMENTAL

All reagents were purchased commercially (SD fine, India) and used without further purification. Melting points were determined by the open capillary method. The IR spectra (in KBr pellets) were recorded on a Perkin-Elmer FTIR spectrophotometer. ^{1}H NMR (300 MHz, DMSO-D6) and ^{13}C NMR (75 MHz, DMSO-D6) spectra were recorded on a Bruker Avance 300 spectrometer, TMS as internal standard (chemical shifts and ppm). Mass spectra were recorded on a VG micromass70-70H instrument.

A mixture of benzene-1,2,4-triol (5 mmol) **(1)** and ethyl 3-oxobutanoate (20 mL) **(2a-b)** in conc. H_2SO_4 (20 mL) was stirred for 10-12 h at room temperature (TLC monitoring) to obtain the desired product 6,7-dihydroxy-4-methyl-2H-chromen-2-one **(3a-b)** (Scheme 1) [3,11, 12, 33]. The product **(3a-b)** reacts with Ac_2O and HCl in presence of pyridine after reflux (TLC monitoring) to obtain the desired product 8-acetyl-6,7-dihydroxy-4-methyl-2H-chromen-2-one **(4a-b).** The latter reacts with HCHO and ethanol in presence of K_2CO_3 and pyridine after reflux (TLC monitoring) to obtain the

desired product 6-hydroxy-4-methyl-8,9-dihydropyrano [2,3-f] chromene-2,10-dione **(5a-b)**. The latter product and chloroacetonitrile **(6)** were dissolved in dry acetone and refluxed over anhydrous potassium carbonate for 3 h on a water bath (TLC monitoring). The excess solvent was evaporated under reduced pressure and the obtained residue was treated with petroleum ether (60–85%). The solid product was filtered off and washed with petroleum ether (60–85%) to obtain the desired product 2-((4-methyl-2,10-dioxo-2,8,9,10-tetrahydropyrano[2,3-f] chromen-6-yl) oxy) acetonitrile **(7a-b).**

General procedure for the synthesis of 6-((2H-tetrazol-5-yl) methoxy)-4-methyl-8,9-dihydropyrano[2,3-f]chromene-2,10-dione, 9(a-b)

A mixture of **7(a-b)** (3 g, 0.013 mol), sodium azide **(8)** (1 g, 0.014 mol) and NH_4Cl (0.85 g, 0.016 mol) in 75 ml of DMF was heated for 8 h at 120 °C (Scheme 2). The reaction mixture was cooled to room temperature and after crushed ice was added, a light cream colour precipitate was obtained. It was collected by filtration and washed with water, dried at 50°C to get the crude compound which was purified by recrystallization in methanol to furnish the pure compound **9(a)** as light cream solid. IR (KBr): v NH at 3222cm^{-1}, C=O at 1722 cm^{-1}, and O=C of coumarin at 1573 cm^{-1}. Anal. calcd. for $C_{15}H_{12}N_4O_5$: C, 54.88; H, 3.68; N, 17.07; O, 24.37. Found: C, 54.87; H, 3.69; N, 17.09; O, 24.35. ^1H NMR (300 MHz, DMSO-D6) δ 2.44 (s, 3H), 2.62 (d, J = 10.2 Hz, 2H), 4.71 (d, J = 10.2 Hz, 2H), 5.10 (s, 1H), 5.60 (s, 2H), 6.43 (s, 1H), 10.13 (s, 1H). ^{13}C NMR (75 MHz, DMSO-D6) δ 191.2, 161.1, 154.7, 154.1, 152.2, 148.5, 142.1, 120.7, 118.7, 111.2, 108.1, 63.6, 61.2, 37.1 and 19.0. Mass (ES): m/z = 328. M.P =146°C, Yield: 76%.

6-((2H-Tetrazol-5-yl) methoxy)-3,4-dimethyl-8,9-dihydropyrano[2,3-f]chromene-2,10-dione, (9b): Similar reaction conditions of **9a**, were employed for **9b**. The spectral data for **9b** are as follows: IR (KBr): u NH at 3213cm^{-1} and C=O at 1715 cm^{-1}, O=C of coumarin at 1566 cm^{-1}. Anal. calcd. for $C_{16}H_{14}N_4O_5$: C, 56.14; H, 4.12; N, 16.37; O, 23.37. Found: C, 56.16; H, 4.10; N, 16.38; O, 23.36. ^1H NMR (300 MHz, DMSO-D6) δ 2.01 (3H, s), 2.42 (3H, s), 2.78 (2H, d, J = 10.2 Hz), 4.46 (2H, d, J = 10.2 Hz), 5.10 (2H, s), 7.16 (1H, s), 10.05 (s, 1H). ^{13}C NMR (75 MHz, DMSO-D6) δ 192.2, 162.4, 157.7, 157.4, 154.0, 149.5, 142.7, 121.8, 119.8, 111.4, 109.2, 64.6, 62.6, 37.6, 35.1 and 21.7.Mass (ES): m/z= 342. Yield: 79%.

General procedure for the synthesis of 4-methyl-6-((2-methyl-2H-tetrazol-5-yl) methoxy)-8,9-dihydropyrano[2,3-f]chromene-2,10-dione, 11(a-l)

6-((2H-Tetrazol-5-yl) methoxy)-4-methyl-8,9-dihydropyrano[2,3-f]chromene-2,10-dione, **9a** (1 g, 0.003 mol) and methyl bromide, **10a** (0.35 ml, 0.003 mol) were dissolved in 50 ml of dry acetone, refluxed at 70 °C over anhydrous potassium carbonate for 3 h on a water bath (Scheme 1). The acetone was removed under reduced pressure and crushed ice was added to the residue. The product **(11a)** was filtered and washed with plenty of water, yield 80%. The spectral data for **11a** are as follows: mp: 131°C, IR (KBr): v C=O at 1723 cm^{-1}, O=C of coumarin at 1567 cm^{-1}. Anal. calcd. for $C_{16}H_{14}N_4O_5$: C, 56.14; H, 4.12; N, 16.37; O, 23.37. Found: C, 56.12; H, 4.13; N, 16.38; O, 23.37. ^1H NMR (300 MHz, DMSO-D6) δ 2.43 (3H, s), 2.68 (2H, d, J = 10.2 Hz), 3.90 (3H, s), 4.77 (2H, d, J = 13.2 Hz), 5.11 (2H, s), 5.89 (1H, s), 7.46 (1H, s). ^{13}C NMR (75 MHz, DMSO-D6) δ 199.2, 159.3, 153.7, 153.3, 152.9, 149.2, 145.2, 116.8, 113.8, 111.4, 105.8, 69.5, 67.0, 38.8, 37.5, 19.1. ESI-HRMS: m/z [M + H]$^+$ = 342.10 (Calcd. M$^+$ = 342.31)

Similar reaction conditions of **11a** were employed for all the other compounds **11(b-l)** and the spectral data are as follows:

6-((2-Ethyl-2H-tetrazol-5-yl) methoxy)-4-methyl-8,9-dihydropyrano[2,3-f]chromene-2,10-dione **(11b):** Yield: 80%. mp: 139°C, IR (KBr): v C=O at 1724 cm^{-1}, O=C of coumarin at 1566 cm^{-1}. Anal. Calcd for $C_{17}H_{16}N_4O_5$: C, 57.30; H, 4.53; N, 15.72; O, 22.45. Found: C, 57.32; H, 4.52; N, 15.72; O, 22.44. ^1H NMR (300 MHz, DMSO-D6) δ 1.15 (3H, t), 2.41 (3H, s), 2.63 (2H, d, J = 2.5 Hz), 4.25 (2H, q), 4.75 (2H, d, J = 10.2 Hz), 5.02 (2H, s), 5.29 (1H, s), 6.76 (1H, s). ^{13}C NMR (75 MHz, DMSO-D6) δ 196.1, 159.2, 153.4, 153.1, 151.9, 148.1, 145.3, 114.8, 113.3, 110.9, 106.5, 69.2, 67.3, 38.6, 37.9, 19.5, 10.2, ESI-HRMS: m/z [M + H]$^+$ = 356.11 (Calcd. M$^+$ = 356.33)

4-Methyl-6-((2-propyl-2H-tetrazol-5-yl) methoxy)-8,9-dihydropyrano[2,3-f]chromene-2,10-dione (11c): Yield: 82%. mp: 151°C, IR (KBr): v C=O at 1738 cm^{-1}, O=C of coumarin at 1569 cm^{-1}. Anal. Calcd for $C_{18}H_{18}N_4O_5$: C, 58.37; H, 4.90; N, 15.13; O, 21.60. Found: C, 58.38; H, 4.90; N, 15.12; O, 21.60. ^1H NMR (300 MHz, DMSO-D6) δ 0.92 (3H, t), 1.80 (2H), 2.43 (3H, s), 2.60 (2H, d, J = 10.5 Hz), 4.42 (2H, t), 4.75 (2H, d, J = 10.2 Hz), 5.02 (2H, s), 5.66 (1H, s), 7.06 (1H, s). ^{13}C NMR (75 MHz, DMSO-D6) δ 197.3, 158.5, 153.7, 152.4, 151.2, 148.7, 145.6, 116.2, 114.2, 108.9, 106.6, 68.8, 67.8, 37.6, 34.9, 20.1, 19.2, 11.1, ESI-HRMS: m/z [M + H]$^+$ = 369. 13 (Calcd. M$^+$ = 370.36).

6-((2-Butyl-2H-tetrazol-5-yl)methoxy)-4-methyl-8,9-dihydropyrano[2,3-f]chromene-2,10-dione **(11d):** Yield: 86%. mp: 158°C, IR (KBr): *v* C=O at 1732 cm^{-1}, O=C of coumarin at 1563 cm^{-1}. Anal. calcd. for $C_{19}H_{20}N_4O_5$: C, 59.37; H, 5.24; N, 14.58; O, 20.81. Found: C, 59.39; H, 5.23; N, 14.59; O, 20.82. ^{1}H NMR (300 MHz, DMSO-D6) δ 0.81 (3H, t), 1.23 (2H), 1.76 (2H, t), 2.41 (3H, s), 2.61 (2H, d, *J* = 3.2 Hz), 4.22 (2H, t), 4.65 (2H, d, *J* = 10.2, Hz), 5.01 (2H, s), 5.80 (1H, s), 7.01 (1H, s). ^{13}C NMR (75 MHz, DMSO-D6) δ 195.3, 156.5, 152.9, 151.1, 150.8, 147.0, 144.1, 116.2, 115.1, 111.5, 106.4, 68.2, 67.3, 41.2, 33.2, 30.1, 20.6, 19.8, 11.4, ESI-HRMS: m/z [M + H]$^+$ = 384.14 (Calcd. M$^+$ = 384.39)

4-Methyl-6-((2-pentyl-2H-tetrazol-5-yl) methoxy)-8,9-dihydropyrano[2,3-f]chromene-2,10-dione **(5e):** Yield: 90%. mp: 166°C, IR (KBr): *v* C=O at 1733 cm^{-1}, O=C of coumarin at 1573 cm^{-1}. Anal. calcd. for $C_{20}H_{22}N_4O_5$: C, 60.29; H, 5.57; N, 14.06; O, 20.08. Found: C, 60.27; H, 5.59; N, 14.07; O, 20.07. ^{1}H NMR (300 MHz, DMSO-D6) δ 0.84 (3H, t), 1.24-1.33 (4H, t), 1.66 (2H, t), 2.43 (3H, s), 2.54 (2H, d, *J* = 10.5 Hz), 4.16 (2H, t), 4.66 (2H, d, *J* = 13.2 Hz), 5.22 (2H, s), 5.55 (1H, s), 6.76 (1H, s). ^{13}C NMR (75 MHz, DMSO-D6) δ 195.1, 153.5, 152.7, 151.4, 150.2, 146.7, 141.6, 112.9, 110.8, 109.1, 104.9, 64.7, 63.6, 44.9, 32.8, 30.1, 22.7, 20.6, 19.3, 11.4, ESI-HRMS: m/z [M + H]$^+$ = 398.16 (Calcd. M$^+$ = 398.41)

6-((2-Isobutyl-2H-tetrazol-5-yl) methoxy)-4-methyl-8,9-dihydropyrano[2,3-f]chromene-2,10-dione **(11f):** Yield: 89%. mp: 160°C, IR (KBr): *v* C=O at 1732 cm^{-1}, O=C of coumarin at 1563 cm^{-1}. Anal. Calcd for $C_{19}H_{20}N_4O_5$: C, 59.37; H, 5.24; N, 14.58; O, 20.81. Found: C, 59.38; H, 5.25; N, 14.59; O, 20.80. ^{1}H NMR (300 MHz, DMSO-D6) δ 0.90 (6H, d, *J* = 6.8 Hz), 2.07 (1H), 2.40 (3H, s), 2.58 (2H, d, *J* = 14.5 Hz), 4.29 (2H, d, *J* = 6.4 Hz), 4.70 (2H, d, *J* = 10.2 Hz), 5.11 (2H, s), 5.69 (1H, s), 6.88 (1H, s). ^{13}C NMR (75 MHz, DMSO-D6) δ 195.6, 156.1, 152.9, 151.1, 150.1, 147.1, 144.2, 115.1, 114.3, 111.1, 106.2, 68.1, 66.2, 40.1, 38.1, 20.2, 19.1,19.0, 11.2, ESI-HRMS: m/z [M + H]$^+$ = 384.14 (Calcd M$^+$ = 384.39)

3,4-Dimethyl-6-((2-methyl-2H-tetrazol-5-yl) methoxy)-8,9-dihydropyrano[2,3-f]chromene-2,10-dione **(11g)***:* Yield: 70%. mp: 141°C, IR (KBr): v C=O at 1733 cm^{-1}, O=C of coumarin at 1567 cm^{-1}. Anal. Calcd for $C_{17}H_{16}N_4O_5$: C, 57.30; H, 4.53; N, 15.72; O, 22.45. Found: C, 57.32; H, 4.51; N, 15.71; O, 22.45. ^{1}H NMR (300 MHz, DMSO-D6) δ 2.13 (3H, t), 2.43 (3H, s), 2.54 (2H, d, *J* = 10.2 Hz), 3.67 (3H, s), 4.44 (2H, d, *J* = 10.2 Hz), 5.22 (2H, s), 6.78 (1H, s), ^{13}C NMR (75 MHz, DMSO-D6) δ 197.6,

159.1, 152.7, 151.3, 150.9, 147.2, 145.2, 116.2, 113.3, 111.2, 105.7, 69.6, 67.3, 38.5, 37.3, 19.2, 13.4, ESI-HRMS: m/z [M + H]$^+$ = 356.11 (Calcd M$^+$ = 356.33)

6-((2-Ethyl-2H-tetrazol-5-yl)methoxy)-3,4-dimethyl-8,9-dihydropyrano[2,3-f]chromene-2,10-dione **(11h):** Yield: 80%. mp: 148°C, IR (KBr): *v* C=O at 1723 cm^{-1}, O=C of coumarin at 1575 cm^{-1}. Anal. calcd. for $C_{18}H_{18}N_4O_5$: C, 58.37; H, 4.90; N, 15.13; O, 21.60. Found: C, 58.39; H, 4.91; N, 15.13; O, 21.61. ^{1}H NMR (300 MHz, DMSO-D6) δ 1.09 (3H, t), 2.01 (3H, s), 2.34 (3H, s), 2.56 (2H, d, *J* = 10.5 Hz), 4.24 (2H, q), 4.73 (2H, d, *J* = 10.2 Hz), 5.10 (2H, s), 6.66 (1H, s). ^{13}C NMR (75 MHz, DMSO-D6) δ 197.6, 158.1, 152.7, 151.9, 151.2, 148.2, 144.2, 115.2, 112.3, 110.2, 104.7, 68.6, 65.3, 48.5, 37.2, 19.3, 13.1, 10.1, ESI-HRMS: m/z [M + H]$^+$ = 370.13 (Calcd. M$^+$ = 370.36)**.**

3,4-Dimethyl-6-((2-propyl-2H-tetrazol-5-yl) methoxy)-8,9-dihydropyrano[2,3-f]chromene-2,10-dione **(11i):** Yield: 86%. mp: 157°C, IR (KBr): *v* C=O at 1724 cm^{-1}, O=C of coumarin at 1573 cm^{-1}. Anal. calcd. for $C_{19}H_{20}N_4O_5$: C, 59.37; H, 5.24; N, 14.58; O, 20.81. Found: C, 59.39; H, 5.25; N, 14.58; O, 20.82. ^{1}H NMR (300 MHz, DMSO-D6) δ 0.94 (3H, t), 1.93 (2H, t), 2.11 (3H, s), 2.43 (3H, s), 2.74 (2H, d, *J* = 14.5 Hz), 4.22 (2H, t), 4.46 (2H, d, *J* = 13.2 Hz), 5.02 (2H, s), 7.02 (1H, s). ^{13}C NMR (75 MHz, DMSO-D6) δ 195.6, 159.7, 154.2, 152.1, 150.1, 148.5, 145.1, 116.1, 114.5, 109.6, 103.1, 65.1, 63.1, 51.6, 41.1, 20.5, 19.1, 13.1, 10.1 , ESI-HRMS: m/z [M + H]$^+$ = 384.14 (Calcd. M$^+$ = 384.39)

6-((2-Butyl-2H-tetrazol-5-yl) methoxy)-3,4-dimethyl-8,9-dihydropyrano[2,3-f]chromene-2,10-dione **(11j):** Yield: 88%. mp: 167°C, IR (KBr): *v* C=O at 1728 cm^{-1}, O=C of coumarin at 1563 cm^{-1}. Anal. calcd. for $C_{20}H_{22}N_4O_5$: C, 60.29; H, 5.57; N, 14.06; O, 20.08. Found: C, 60.28; H, 5.58; N, 14.07; O, 20.07. ^{1}H NMR (300 MHz, DMSO-D6) δ 0.82 (3H, t), 1.43 (2H, t), 1.58 (2H, t), 2.34 (3H, s), 2.64 (3H, s), 2.88 (2H, d, *J* = 14.5 Hz), 4.58 (2H, t), 4.96 (2H, d, *J* = 10.2 Hz), 5.40 (2H, s), 7.01 (1H, s). ^{13}C NMR (75 MHz, DMSO-D6) δ 194.9, 156.7, 153.2, 152.3, 150.1, 146.2, 142.1, 113.1, 110.1, 107.2, 101.1, 66.4, 62.1, 50.1, 40.2, 30.2, 20.1, 19.2, 13.2, 10.1 , ESI-HRMS: m/z [M + H]$^+$ = 398.16 (Calcd. M$^+$ = 398.41)

3,4-Dimethyl-6-((2-pentyl-2H-tetrazol-5-yl) methoxy)-8,9-dihydropyrano[2,3-f]chromene-2,10-dione **(11k):** Yield: 91%. mp: 171°C, IR (KBr): *v* C=O at 1725 cm^{-1}, O=C of coumarin at 1573 cm^{-1}. Anal. calcd. for $C_{21}H_{24}N_4O_5$: C, 61.15; H, 5.87; N, 13.58; O, 19.40. Found: C, 61.17; H, 5.88; N, 13.57; O, 19.41. ^{1}H NMR (300 MHz, DMSO-D6) δ 0.81 (3H, t), 1.22-1.35 (4H, t), 1.79 (2H, t), 2.01 (3H, s),

2.41 (3H, s), 2.69 (2H, d, $J = 14.5$ Hz), 4.36 (2H, t), 4.70 (2H, d, $J = 10.2$ Hz), 5.22 (2H, s), 7.11 (1H, s). ^{13}C NMR (75 MHz, DMSO-D6) δ 195.9, 158.2, 156.1, 152.1, 151.1, 147.2, 140.5, 112.1, 110.1, 107.2, 100.1, 67.2, 61.1, 55.2, 41.1, 32.2, 23.1, 21.1, 18.4, 11.5, 10.3, ESI-HRMS: m/z [M + H]$^+$ = 412.17 (Calcd. M$^+$ = 412.44)

6-((2-Isobutyl-2H-tetrazol-5-yl) methoxy)-3,4-dimethyl-8,9-dihydropyrano[2,3-f]chromene-2,10-dione **(11l):** Yield: 88%. mp: 170°C, IR (KBr): v C=O at 1728 cm^{-1}, C=C of coumarin at 1567 cm^{-1}. Anal. calcd. for $C_{20}H_{22}N_4O_5$: C, 60.29; H, 5.57; N, 14.06; O, 20.08. Found: C, 60.28; H, 5.58; N, 14.07; O, 20.07. ^{1}H NMR (300 MHz, DMSO-D6) δ 0.89 (6H, d, $J = 6.8$ Hz), 2.04 - 2.13 (4H, m), 2.43 (3H, s), 2.62 (2H, d, $J = 14.5$ Hz), 4.04 (2H, d, $J = 6.4$ Hz), 4.65 (2H, d, $J = 10.2$ Hz), 5.19 (2H, s), 6.99 (1H, s). ^{13}C NMR (75 MHz, DMSO-D6) δ 196.9, 158.1, 155.7, 154.1, 152.1, 147.1, 142.5, 112.3, 110.4, 108.7, 104.2, 66.2, 63.8, 48.6, 40.1, 30.7, 20.9, 20.1, 19.1, 10.2, ESI-HRMS: m/z [M + H]$^+$ = 398.16 (Calcd. M$^+$ = 398.41).

All synthesized compounds were screened for their antimicrobial and anti-fungal activities by using the diffusion plate method [23-30]. A filter paper sterilized disk saturated with the measured quantity (25 μL) of the sample (1 mg/mL) was placed on a plate (9 cm diameter) containing a solid bacterial medium (nutrient agar) or a fungal medium (potato dextrose agar) that was seeded with the spore suspension of the test organism. After incubation at 37°C for 24 h for bacteria (in case of fungi, at 25°C for 72 h), the diameter of the clear zone of inhibition surrounding the sample was taken as a measure of the inhibitory power of the sample against the particular test organism (% inhibition = sample inhibition zone (cm)/plate diameter × 100). All measurements were done in methanol as a solvent that has zero inhibition activity. The antimicrobial activity of the new compounds was examined against two Gram-positive bacteria (*Staphylococcus aureus,* MTCC 096 and *Bacillus subtilis,* MTCC 441) and two Gram-negative bacteria (*Escherichia coli,* MTCC 443 and *Pseudomonas aeruginosa,* MTCC 424), whereas, for antifungal studies two fungi (*Aspergillus niger*, MTCC 282 and *Aspergillus fumigates,* MTCC 343) were taken. The obtained results are compared with the reference antibiotics purchased from Hyderabad chemicals center. Table 2 contains data of the antibacterial and antifungal testing.

RESULTS AND DISCUSSION

Chemistry

Benzene-1,2,4-triol **(1)** with ethyl 3-oxobutanoate **(2a-b)** undergo conventional cyclocondensation reaction in presence of conc. H$_2$SO$_4$, and by stirring for 10-12 h at room temperature 6,7-dihydroxy-4-methyl-2H-chromen-2-one **(3a-b)** was prepared in 80% yield. The compound **(3a-b)** was treated with Ac$_2$O and HCl in presence of pyridine after reflux to obtain the product (78% yield) 8-acetyl-6,7-dihydroxy-4-methyl-2H-chromen-2-one **(4a-b).** The latter reacted with HCHO and ethanol in presence of K$_2$CO$_3$ and pyridine after reflux to obtain 6-hydroxy-4-methyl-8,9-dihydropyrano[2,3-f] chromene-2,10-dione **(5a-b)** (65% yield). Compound **(5a-b)** was treated with chloroacetonitrile **(6)** dissolved in dry acetone and was refluxed over anhydrous potassium carbonate for 3 h on a water bath. After purification the desired product 2-((4-methyl-2,10-dioxo-2,8,9,10-tetrahydropyrano [2,3-f] chromen-6-yl) oxy) acetonitrile **(7a-b)** (68% yield) was obtained.

Finally, a mixture of **7(a)**, sodium azide **(8)** and NH$_4$Cl in DMF was heated for 8 h at 120 °C (Scheme 2). The crude compound, purified by recrystallization, furnished the pure compound **9(a)** as light cream solid with 76% yield. In the IR spectrum, amine at 3222 cm^{-1}, carbonyl at 1722 cm^{-1}, and O=C of coumarin at 1573 cm^{-1} are seen. Compound **9a** was treated with methyl bromide, **10a** was dissolved in dry acetone, and was refluxed at 70 °C over anhydrous potassium carbonate for 3 h on a water bath (Scheme 2). The acetone was removed under reduced pressure and crushed ice was added to the residue. The product **(11a)** was filtered and washed with plenty of water. The yield was 80%, observed mp: 181°C, IR (KBr): v C=O at 1723 cm^{-1}, O=C of coumarin at 1567 cm^{-1}. The ^{1}H NMR spectrum showed a typical singlet signal attributable to 2.43, 3.90, 5.11, 5.89 7.46. Compound **11a** was also confirmed from its mass spectrum which revealed the parent ion peak at m/z [M + H]$^+$ = 342.10 that coincided well with the suggested calcd. M$^+$ = 342.31. A methyl group-containing **7(b)**, sodium azide **(8)** and NH$_4$Cl in DMF were heated for 8 h at 120 °C (Scheme 2), the purified compound **9(b)** yielded 79%. In the IR spectrum amine at 3213 cm^{-1}, carbonyl at 1715 cm^{-1}, and O=C of coumarin at 1566 cm^{-1} are seen. The ^{1}H NMR spectrum showed a typical singlet signal attributable to 2.01, 2.42, 5.10, 7.16 and 10.05.

Compound **9b** was also confirmed from its mass spectrum which revealed the parent ion peak at m/z = 342. After compound **9b** was treated with methyl bromide, **10a** was dissolved in dry acetone, refluxed at 70 °C over anhydrous potassium carbonate for 3 h on a water bath (Scheme 2). The acetone was removed under reduced pressure and crushed ice was added to the residue. The product (**11b**) was filtered and washed with plenty of water. The yield was 70%, observed mp: 141°C, IR (KBr): *v* C=O at 1733 cm⁻¹, O=C of coumarin at 1567 cm⁻¹. The ¹H NMR spectrum showed a typical singlet signal attributable to 2.13, 2.43, 3.67, 5.22, 6.78. Compound **11a** was

also confirmed from its mass spectrum which revealed the parent ion peak at m/z [M + H]⁺ = 356.11 that coincided well with the suggested calcd. M⁺ = 356.33. Also, in our present research work we observed that if methyl groups are present in the title compounds, their yield is low, for example, **11a** compound contains R=H, R₁= CH₃, its yield is 80% and **11g** compound contains R= CH₃, R₁= CH₃, its yield is only 70%. Increasing carbon chain on the title compounds increases yield, e.g., **11e** compound contains R=H, R₁= n-C₅H₁₁, its yield is 90% and **11g** compound contains R= CH₃, R₁= n-C₅H₁₁, its yield is 91%.
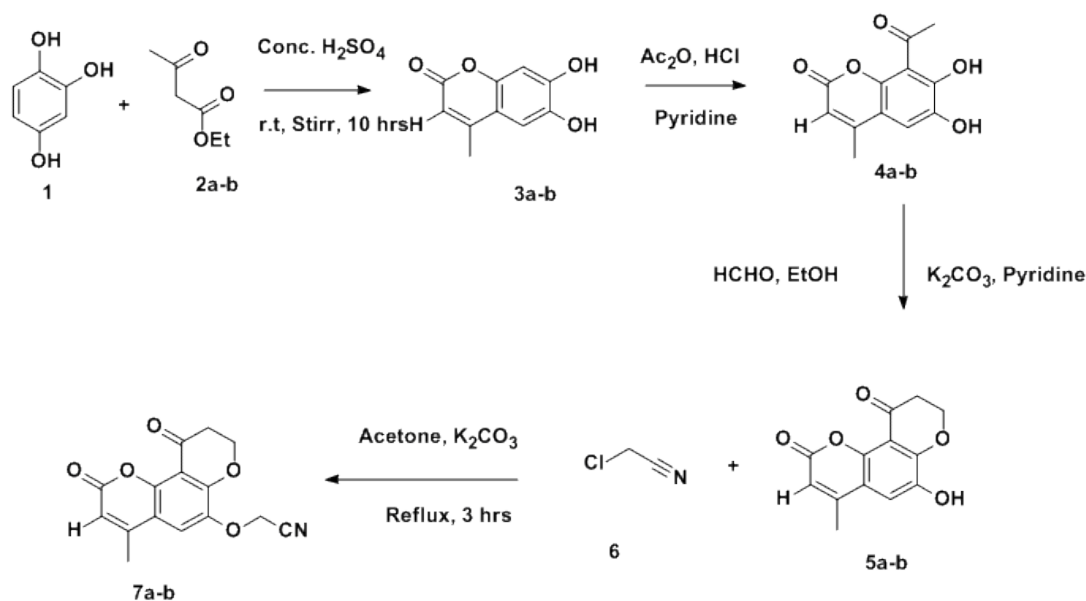
Scheme 1. Reagents and conditions for synthesis of 2-((4-methyl-2,10-dioxo-2,8,9,10-tetrahydropyrano[2,3-f]chromen-6-yl)oxy)acetonitrile (7a-b)
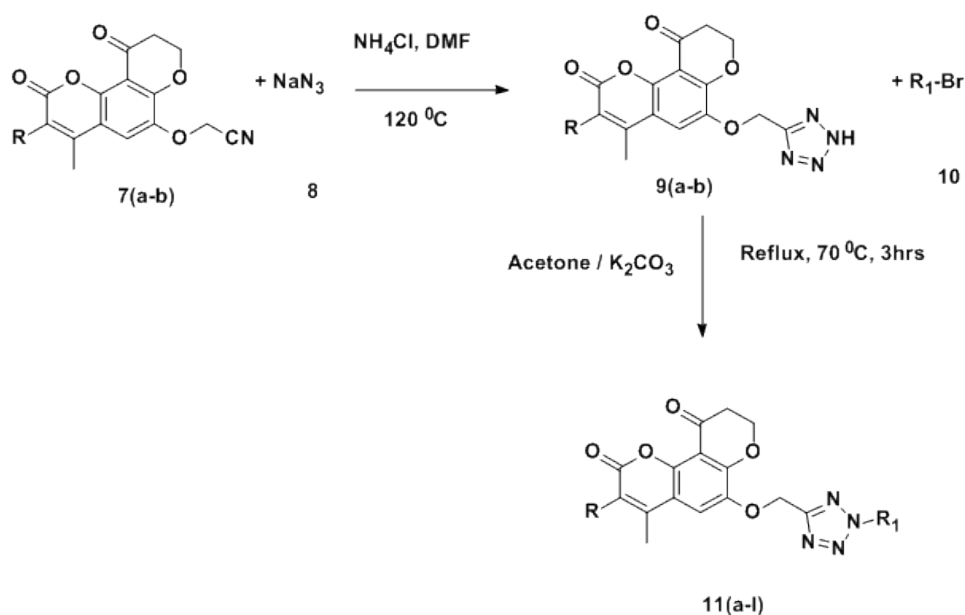
Scheme 2. Reagents and conditions for synthesis of the title compounds (11a-l)

Table. 1. R, R_1 substituents and yield of title compounds, 11(a-l).

Product	R	R_1	Yield (%)
11a	H	CH_3	80
11b	H	C_2H_5	80
11c	H	$n-C_3H_7$	82
11d	H	$n-C_4H_9$	86
11e	H	$n-C_5H_{11}$	90
11f	H	$iso-C_4H_9$	89
11g	CH_3	CH_3	70
11h	CH_3	C_2H_5	80
11i	CH_3	$n-C_3H_7$	86
11j	CH_3	$n-C_4H_9$	88
11k	CH_3	$n-C_5H_{11}$	91
11l	CH_3	$iso-C_4H_9$	88

Bioactivity

Go through the biological assay of the novel coumarin-tetrazole derivatives shows that most of the compounds were highly to moderately potent against the specific strains (Table 3). In general, most of the tested derivatives displayed better activity against Gram-positive bacterial strains as compared to Gram-negative bacterial strains. The new compounds were screened to determine their antimicrobial activity *in vitro* against two pathogenic Gram-positive bacteria, *viz. Staphylococcus aureus* MTCC 096, and *Bacillus subtilis,* MTCC 441, two pathogenic Gram-negative bacteria, *viz. Escherichia coli,* MTCC 443 and *Pseudomonas aeruginosa,* MTCC 424, and fungal cultures of *Aspergillus niger*, MTCC 282 and *Aspergillus fumigates,* MTCC 343. The reference drugs were ciprofloxacin for antibacterial and miconazole for antifungal tests, respectively.

Based on the values of the inhibition zone diameter shown in Table 2, it could be concluded that most of the evaluated tetrazole coumarin derivatives displayed moderate to significant broad-spectrum antimicrobial activity comparing to the used reference drugs. The parent tetrazole-coumarin compound exhibited moderate antibacterial and fungal activity, while its conversion to the compounds **11a–l** affected the potency.

Table. 2. Antimicrobial activity studies of the title compounds, **11(a-l)**, using Gram-positive bacteria, Gram-negative bacteria and two fungi in inhibition zone diameter mm/mg.

Compound	Gram-positive bacteria		Gram-negative bacteria		Fungi	
	Staphylococcus aureus	*Bacillus subtilis*	*Escherichia coli*	*Pseudomonas aeruginosa*	*Aspergillus niger*	*Aspergillus fumigatus*
9a	10	12	12	15	10	20
9b	15	20	15	20	15	20
11a	20	15	10	10	15	15
11b	10	20	20	0	15	15
11c	25	30	15	10	25	20
11d	15	10	10	20	15	10
11e	10	10	25	15	10	20
11f	0	10	15	15	30	30
11g	10	15	10	20	35	25
11h	20	15	10	25	30	30
11i	15	10	20	25	35	30
11j	20	25	15	10	10	15
11k	15	30	10	15	15	20
11l	10	15	10	20	30	25
Ciprofloxacin	25	35	30	25		
Miconazole	–	–	–	–	40	35

Inhibition zone diameter units in mm/mg

It was found that the tetrazole-coumarin derivative **11c** exhibited potent antibacterial activity against the Gram-positive *S. aureus* and *B. subtilis* and the Gram-negative *E. coli,* and *P. aeruginosa* of inhibition zones 15, 20 mm/mg, respectively, *vs* 30, 25 mm/mg of the reference drug ciprofloxacin, while its antifungal potency was moderate, producing inhibition zone 25, 20 mm/mg when compared to that of the reference antifungal drug 40, 35 mm/mg. It was found that the tetrazole-coumarin derivative **11g** exhibited low potent antibacterial activity against the two Gram-positive *S. aureus* and *B. subtilis* and the Gram-negative *E. coli,* and *P. aeruginosa* of inhibition zones 10, 15, 10, 20 mm/mg, respectively, *vs* 25, 30, 30, 25 mm/mg of the reference drug ciprofloxacin, while its antifungal potency was high, producing inhibition zone 35, 25 mm/mg when compared to that of the reference antifungal drug 40, 35 mm/mg. The antifungal potency of **11h** was high, producing inhibition zone 30, 30 mm/mg when compared to that of the reference antifungal drug 40, 35 mm/mg. The antifungal potency of **11f** was high, producing inhibition zone 30, 30 mm/mg when compared to that of the reference antifungal drug 40, 35 mm/mg but its antibacterial activity was very low. The antifungal potency of **11i** was high, producing inhibition zone 35, 30 mm/mg when compared to that of the reference antifungal drug 40, 35 mm/mg. Iso butyl group-containing 11f and 11l compounds showed high antifungal potency, producing inhibition zone 25, 30 mm/mg when compared to that of the reference antifungal drug 40, 35 mm/mg but the least anti-bacterial activity.

In antibacterial studies, all the compounds tested were found with moderate to good activity towards Gram-positive and Gram-negative strains. Most of the compounds showed moderate to good activity against Gram-positive *Staphylococcus aureus* bacteria. Compounds **11a, 11c, 11h** and **11j** showed good antibacterial activity against *Staphylococcus aureus.* Some of the compounds showed moderate to good activity against Gram-positive *Bacillus subtilis* bacteria. Compounds **11c, 11j** and **11k** showed good antibacterial activity against *Bacillus subtilis.* **11b, 11e** and **11i** showed good antibacterial activity against *Escherichia coli.* **11h** and **11i** showed good antibacterial activity against *Pseudomonas aeruginosa.* Out of two strains of fungi, all these compounds showed moderate to good activity against *Aspergillus niger and Aspergillus fumigatus.* Compounds **11g, 11h, 11i** and **11l** possessed high antifungal activity against *Aspergillus niger;* **11f, 11h** and **11i** possessed high antifungal activity against *Aspergillus fumigatus,* which was almost

similar to that of the standard drug. Further modification and optimization are needed to get more significant antimicrobial activity against various types of bacteria and fungi.

CONCLUSION

We have successfully synthesized tetrazol-5-yl)methoxy)-8,9-dihydropyrano[2,3-*f*]chromene-2,10-diones by 6-((2H-tetrazol-5-yl)methoxy)-4-methyl-8,9-dihydropyrano[2,3-f]chromene-2,10-dione derivatives treated with alkyl bromide in good yields. The structures of all compounds were assigned by their spectral data and CHN analysis. All newly synthesized compounds were screened for their zone of inhibition against two strains of bacteria. Most of the compounds showed moderate to good antimicrobial activities, whereas some compounds showed promising antifungal properties. These were further used to determine the minimum bacterial concentration (MBC) and minimum fungal concentration (MFC) against some selected strains of bacteria and fungi. This study will provide a road map to design new coumarin derivatives which can be used as antibacterial and antifungal drugs.

Supplementary material: *supportive/supplementary material containing ^{1}h-nmr, and ^{13}c-nmr for all 8,9-dihydropyrano 6- [(2-alkyl-2h-tetrazol-5-yl) methoxy]-4-methyl-2h-cromen-2-ones (11a-l) is provided.*

REFERENCES

1. H. H. Licht, H. Ritter, *J. Energ. Mater.,* **12**, 223 (1994).
2. H. Singh, A. S. Chawla, V. K. Kapoor, D. Paul, R. K. Malhotra, *Prog. Med. Chem.,* **17**, 151 (1980).
3. B. Srinivas, J. Suryachandram, Y. K. Devi, K. P. Rao, *J. Heterocyclic Chem.,* **54(6)**, 3730 (2017).
4. B. Srinivas, J. Prashant, M. V. Basaveswara Rao, K. P. Rao, *J. Heterocyclic Chem.,* **56(1)**, 73 (2019).
5. B. Srinivas, N. Saritha Devi, G. K. Sreenivasulu, R. Parameshwar, *Der Pharma Chemica*, **7(5)** 251 (2015).
6. B. Srinivas, N. Saritha Devi, G. K. Sreenivasulu, R. Parameshwar, *Heterocyclic Lett.,* **5(3)***,* 459 (2015).
7. K. P. Rao, T. Kusamoto, F. Toshimitsu, K. Inayoshi, S. Kume, Y. Yamamoto, R. Sakamoto, H. Nishihara, *J. Am. Chem. Soc.,* **132**, 12472 (2010).

8. K. P. Rao, M. Kondo, R. Sakamoto, T. Kusamoto, S. Kume, M. Nihei, H. Oshio, H. Nishihara, *Chem. Eur. J.,* **17**, 14010 (2011).
9. K. P. Rao, M. Kondo, S. Kume, R. Sakamoto, H. Nishihara, *Chem. Lett.,* **40**, 1456 (2011).
10. B. Srinivas, J. Suryachandram, P. Sadanandam, M. V. Basaveswara Rao, K. Prabhakara Rao, J. Pharm. Sci. & Res. **11(5)**, 1918 (2019).
11. B. Srinivas, K. Prabhakara Rao, Mapana Journal of Sciences. **19(2)**, 21 (2020).
12. B. Srinivas, K. Saidulu, N. Saritha Devi, D. Neetha, *Heterocyclic Lett.,* **10(2)**, 251 (2020).
13. B. Schmidt, B. Schieffer. *J. Med. Chem.,* **46(12)**, 2261 (2003).
14. R. J. Herr. *Bioorg. Med. Chem.,* **10(11),** 3379 (2002).
15. R. N. Butler, Tetrazoles. Comprehensive Heterocyclic Chemistry II*, Pergamon, Oxford, vol. 4, 1996, p. 621.
16. H. Quast, L. Bieber, *Tetrahedron Lett.,* **18**, 1485 (1976).
17. W. R. Carpenter, *J. Org. Chem.,* **27**, 2085 (1962).
18. R. Huisgen, *J. Org. Chem.,* **33**, 2291 (1968).
19. O. Dimroth, G. Fester, *Chem. Ber.,* **43**, 2219 (1910).
20. J. V. Dunica, M. E. Pierce, J. B. Santella, *J. Org. Chem.,* **56**, 2395 (1991).
21. W. G. Finnegan, R. A. Henry, R. Lofquist, *J. Am. Chem. Soc.,* **80**, 3908 (1958).
22. T. Travis, Denton, X. Zhang, R. John, Cashman, *J. Med. Chem.,* **48**, 224 (2005).
23. P. M. Reddy, Y. P. Ho, K. Shanker, R. Rohini, V. Ravinder, *Eur. J. Med. Chem.,* **44**, 2621 (2009).
24. A. L. Barry, in: The Antimicrobic Susceptibility Test: Principles and Practices, Lea and Febiger, Philadelphia, 1976, p. 180.
25. M. Imran, S. A. Khan, *Trop. J. Pharm. Res.*, **14(7)**, 1265 (2015).
26. G. F. Brooks, K. C. Carroll, J. S. Butel, S. A. Morse, Melnick & Adelberg's Medical Microbiology, McGraw-Hill, 24th edn., 2007, p. 1954.
27. O. Irobi, M. Moo-Young, W. Anderson, *Int. J. Pharmacol.,* **34**, 87 (1996).
28. D. Muanza, B. Kim, K. Euler, L. Williams, *Int. J. Pharmacol.,* 337 (1994).
29. R. J. Grayer, J. B. Harborne, *Phytochemistry,* **37**, 19 (1994).
30. B. Porwal, B. S. Jayashree, M. Attimarad, *J. Basic Clin. Pharm.,* **1(1)**, (2009).
31. M. Mladenovic, N. Vukovic, N. Niciforovic, S. Sukdolak, S. Solujic, *Molecules*, **14(4)**, 1495 (2009).
32. R. Khajuria, S. Mahajan, A. Kapoor, K. K. Kapoor, *J. Chem. Sci.,* **129**, 1549 (2017).
33. N. Yadav, D. Agarwal, S. Kumar, A. K. Dixit, R. D. Gupta, S. K. Awasthi, *Eur. J. Med. Chem.,* **145**, 735 (2018).

Correlations between optical characteristics and structure of sodium oxide-bismuth oxide-boron oxide glasses

T. R. Tasheva[*], V. V. Dimitrov

Department of Silicate Technology, University of Chemical Technology and Metallurgy, 8, Kl. Ohridski Blvd., Sofia 1756, Bulgaria

Glasses from the Na_2O-Bi_2O_3-B_2O_3 system were prepared using a conventional melt-quenching method. Oxide ion polarizability and optical basicity of the glasses were estimated. Both parameters were changed in a wide range (1.545-2.457 Å^3 for oxide ion polarizability and 0.589-0.990 for optical basicity). The theoretical refractive index was also determined and on its basis, the third-order nonlinear optical susceptibility $\chi^{(3)}$ was established by using generalized Miller's rule. Glasses possess comparatively high values for $\chi^{(3)}$ (0.90-2.42×10^{-13} esu). The structure of glasses was elucidated based on the interaction parameter, single bond strength, and IR spectral analysis. It was found that glasses with high Bi_2O_3 content possess low values for the interaction parameter (0.224-0.051 Å^{-3}) and low values for the single bond strength (377-198 kJ/mol) due to the presence of weak chemical bonds in the glass structure which were confirmed by IR spectral analysis. It was found that glasses with low Bi_2O_3 content were built-up by pyroborate and orthoborate groups, while those with high Bi_2O_3 content were built-up by orthoborate BO_3 groups linked with BiO_6 groups with mixed Bi-O-B bonds.

Keywords: borate glasses, bismuthate glasses, IR spectra, electronic polarizability, chemical bonding, nonlinear optical materials.

INTRODUCTION

In recent years attention of many researchers has been focused on exploring new functional materials with application in nonlinear optics. In this connection bismuth oxide (Bi_2O_3) based glasses are of great interest because of the high potential for application as photonic switches and THG (third-harmonic generation) materials due to high linear refractive index n_o and large third-order nonlinear optical susceptibility $\chi^{(3)}$ [1-3]. They are also promising candidates for broadband optical amplifiers and fiber laser applications [4]. Along with the excellent optical properties, the bismuthate glasses possess low melting temperatures, extensive glass formation range, and physical stability [5]. The Bi_2O_3-B_2O_3 binary system is a good example in this regard. During the years many studies on glass structure and optical properties have been carried out. For instance, data for refractive index and Abbe number, as well as data for density, glass transition temperature, and thermal expansion coefficient, have been reported by Ehrt [6]. The structure through ^{11}B MAS NMR and Raman spectroscopy, as well as the third-order nonlinear optical properties of Bi_2O_3-B_2O_3 glasses, have been examined by Terashima *et al.* [2]. Change of the boron coordination polyhedron from BO_3 to BO_4 has been proved. It has been found that the glasses exhibit large third-order nonlinear optical

susceptibility $\chi^{(3)}$ of the order of 10^{-12} esu. Since the optical nonlinearity is caused by the electronic polarization of the glass upon exposure to intense light beams, polarizability is one of the most important properties which govern the nonlinearity response of the glass. The determination of electronic polarizability is the subject of the so-called polarizability approach which is well known in glass science [7-10]. The correlation between electronic polarizability, optical basicity, and XPS spectra of Bi_2O_3-B_2O_3 glasses has been studied by Honma *et al.* [11]. The glasses possess large electronic oxide ion polarizability and high optical basicity indicating their basic nature. The role of the single bond strength on the optical basicity of bismuth-borate glasses has been estimated by Dimitrov and Komatsu [12] and weak chemical bonds have been confirmed in the glass structure.

It is of scientific and practical interest to check the influence of a third oxide on the structure and optical properties of Bi_2O_3-B_2O_3 glasses. In this connection, the structure of ZnO-Bi_2O_3-B_2O_3 glasses and the role of the electronic oxide ion polarizability on the optical properties have been investigated by Inoue *et al.* [13] and Komatsu *et al.* [14]. Also, the polarizability approach has been applied and high third-order nonlinear optical properties have been predicted for TeO_2-Bi_2O_3-B_2O_3 glasses by Tasheva and Dimitrov [15].

---

* To whom all correspondence should be sent:
E-mail: tina.tasheva@gmail.com

The presence of weak chemical bonds between TeO_3, TeO_4, BiO_6, BO_3, and BO_4 groups has been confirmed by IR spectral analysis. According to Bishay and Maghrabi [16], a large range of glass formation exists in the Na_2O-Bi_2O_3-B_2O_3 system. In a recent review by Maeder [5] on bismuthate glasses, there is no evidence about the application of the polarizability approach for sodium oxide-bismuth oxide- boron oxide glasses. That is why the purpose of the present study was to synthesize Na_2O-Bi_2O_3-B_2O_3 glasses, to apply the polarizability approach to them, and to look for some relationships between the obtained polarizability parameters and the predicted third-order nonlinear optical susceptibility. The structure of the glasses in terms of IR-spectroscopy was also investigated.

EXPERIMENTAL

Four series with different compositions, Series A: $(30-x)Na_2O.xBi_2O_3.70B_2O_3$ (x=15, 20 and 25 mol%), Series B: $(70-x)Na_2O.xBi_2O_3.30B_2O_3$ (x=40, 50 and 60 mol%), Series C: $(50-x)Na_2O.50Bi_2O_3.xB_2O_3$ (x=45, 40, 35 and 30 mol%), Series D: $(40-x)Na_2O.60Bi_2O_3.xB_2O_3$ (x=35, 30, and 25 mol%) and glass with composition $5Na_2O.70Bi_2O_3.25B_2O_3$ were prepared using a conventional melt-quenching method. The compositions of the obtained glasses are visualized in Figure 1.
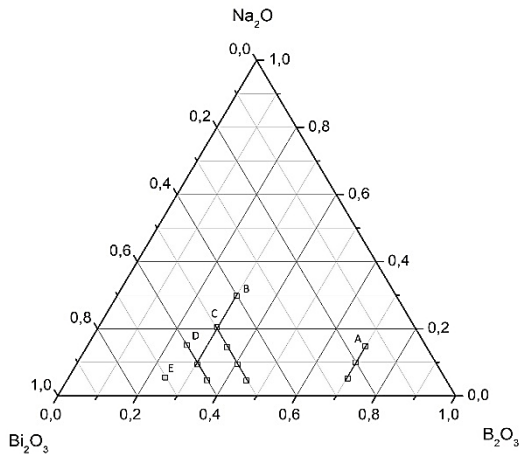

Fig. 1. Glass compositions in the Na_2O-Bi_2O_3-B_2O_3 ternary system.

Reagent-grade commercial powders of Bi_2O_3 (Alfa Aesar, 99%), H_3BO_3 (Alfa Aesar, 99.8%), and Na_2CO_3 (Sigma Aldrich, 99.8%) were mixed. Glasses from Series A were melted in porcelain crucibles at 850 °C for 20 min, and those from Series B, C, and D, as well as $5Na_2O.70Bi_2O_3.25B_2O_3$, were melted in alumina crucibles at 900 °C for 20-30 min, depending on the

composition, in an electric furnace. The melts were poured onto an alumina plate and pressed to a thickness of 1~2 mm by a copper plate. The experimental density was measured by the Archimedes method by using an analytical scale Mettler Toledo New Classic ME 104 equipped with a density kit. XRD analysis was carried out on a Bruker D8 Advance diffractometer (Germany), Cu K_α radiation. The IR spectra were recorded in KBr discs in the 2000 - 400 cm⁻¹ range on the FT-IR spectrometer Varian 600-IR The precision of the absorption maxima was ±3 cm⁻¹.

RESULTS AND DISCUSSION

X-ray diffraction analysis

The XRD patterns of $10Na_2O.20Bi_2O_3.70B_2O_3$ and $10Na_2O.50Bi_2O_3.40B_2O_3$ glasses are presented in Fig. 2. They prove the amorphous nature of the samples because no sharp peaks are observed in the whole range from 10 to 80° 2θ.

Electronic polarizability and optical basicity of glasses

The polarizability approach is based on the Lorentz-Lorenz equation which relates the molar refraction R_m to the refractive index n_0 and the molar volume V_m of the glass by:

$$R_m = \frac{(n_o{}^2 - 1)}{(n_o{}^2 + 2)} V_m = \frac{(n_o{}^2 - 1)}{(n_o{}^2 + 2)} \frac{M}{d} \qquad (1)$$

where M is molar mass, and d is density.

Assuming that the molar refraction of the Na_2O-Bi_2O_3-B_2O_3 glasses is an additive quantity it follows that:

$$R_m = 2.52(x\alpha_{iNa^+} + y\alpha_{iBi^{3+}} + z\alpha_{iB^{3+}} + n\alpha_{O^{2-}}) \quad (2)$$

where α_{iNa^+}, $\alpha_{iBi^{3+}}$, and $\alpha_{iB^{3+}}$ are the polarizabilities of the cations Na^+, Bi^{3+}, and B^{3+}, $\alpha_{O^{2-}}$ is the polarizability of the oxide ion, *x, y,* and *z* are the numbers of the cations Na^+, Bi^{3+}, and B^{3+}, and *n* is the number of the oxide ions in one molecule of glass.

Duffy and Ingram [17, 18] proposed an approach for calculating the theoretical optical basicity and the electronic oxide ion polarizability of the glass based on the following equations:

$$\Lambda_{th} = X_1\Lambda_1 + X_2\Lambda_2 + X_3\Lambda_3 \qquad (3)$$

and

$$a_{O^{2-}} = \frac{1.67}{1.67 - \Lambda_{th}} \qquad (4)$$

where X_1, X_2, X_3 are equivalent fractions based on the amount of oxygen each oxide contributes to the overall material stoichiometry and $\Lambda_1, \Lambda_2, \Lambda_3$ are basicities assigned to the individual oxides.
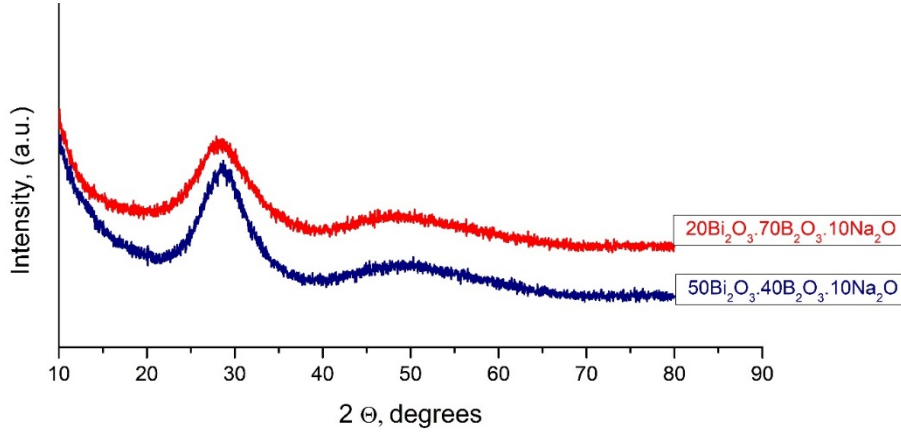
Fig. 2. XRD patterns of 10Na$_2$O.20Bi$_2$O$_3$.70B$_2$O$_3$ and 10Na$_2$O.50Bi$_2$O$_3$.40B$_2$O$_3$ glasses.

We calculated the theoretical optical basicity and oxide ion polarizability of Na$_2$O-Bi$_2$O$_3$-B$_2$O$_3$ glasses by Eqs. 3 and 4 using optical basicity data of Na$_2$O (Λ=1.15), Bi$_2$O$_3$ (Λ=1.19), and B$_2$O$_3$ (Λ=0.42) [8, 9, 17]. The molar refraction was calculated by Eq. 2 taking into account the cation polarizability and oxide ion polarizability. According to [8, 9] the cation polarizabilities are $\alpha_{Bi^{3+}}$= 1.508 Å^3; $\alpha_{B^{3+}}$= 0.002 Å^3, and $\alpha_{Na^{2+}}$= 0.175 Å^3. The molar volume was estimated based on the experimental data of density (Table 1). It should be noticed that our density data are in good agreement with the experimental data of binary Bi$_2$O$_3$-B$_2$O$_3$ glasses measured by Honma *et al.* [11], given in Table 1 in brackets. The obtained results of the optical basicity, oxide ion polarizability, and molar refraction are also presented in Table 1. As can be seen Λ_{th}, and $\alpha_{O^{2-}}$ are changed in a wide range (0.589-0.990 and 1.545-2.457 Å^3, respectively). Glasses with high Bi$_2$O$_3$ content possess the highest values for both parameters which indicates an increase in the basic nature of the glasses (0.911-0.990 and 2.199-2.457 Å^3, respectively).

Optical characteristics

According to the Lorentz-Lorentz equation, the refractive index n$_0$ could be expressed by:

$$n_0 = \sqrt{\frac{V_m + 2R_m}{V_m - R_m}} \qquad (5)$$

The refractive indices of Na$_2$O-Bi$_2$O$_3$-B$_2$O$_3$ glasses were calculated by us using equation 5 and the obtained results are presented in Table 2. It is seen that glasses possess comparatively high values in the 1.8 to 1.95 range. The refractive index increases with increasing Bi$_2$O$_3$ content.

A comparison in Table 2 is given in brackets with experimental data for binary compositions reported by Honma *et al.* [11] which are very close to our results for the ternary system. This means that the prediction of the refractive index using the Lorentz-Lorentz equation is suitable.

The third-order nonlinear optical susceptibility $\chi^{(3)}$ can be predicted by generalizing the so-called Miller's rule:

$$\chi^{(3)} = [\chi^{(1)}]^4 . 10^{-10} \text{, esu} \qquad (6)$$

where $\chi^{(1)}$ is the linear optical susceptibility calculated by:

$$\chi^{(1)} = \frac{(n_o^2 - 1)}{4\pi} \qquad (7)$$

We used the equations above to predict the third-order nonlinear optical properties of our glasses. The results are presented in Table 2. It is seen that glasses possess relatively high values for $\chi^{(3)}$ (1.00-2.45×10^{-13} esu). According to Terashima *et al.* [2, 19], the $\chi^{(3)}$ experimental values of Na$_2$O-B$_2$O$_3$ glasses are in the 0.324 - 0.658×10^{-13} esu range, while the $\chi^{(3)}$ values of binary Bi$_2$O$_3$-B$_2$O$_3$ glasses are in the 3.19 – 11.8×10^{-13} esu range. It is seen that the results in this study are close to those of Bi$_2$O$_3$-B$_2$O$_3$ glasses which means that the role of bismuth and boron oxide in our glasses is significant. Simultaneously, we have plotted the third-order nonlinear optical susceptibility as a function of the optical basicity of the glasses in Fig. 3. It is seen that optical nonlinearity increases with increasing the basic nature of the glasses, as well as glasses with increased Bi$_2$O$_3$ content, which possess the highest values for $\chi^{(3)}$, which means that glasses with increased electron donor ability possess higher values for the third-order nonlinear susceptibility.

Table 1. Series, compositions, molar mass M, density d, molar volume V_m, optical basicity Λ, oxide ion polarizability α_{O2-}, molar refraction R_m.

Series		Compositions			M, g/mol	d, g/cm³	V_m, cm³/mol	Λ	α_{O2-}, Å³	R_m, cm³/mol
		Na₂O	Bi₂O₃	B₂O₃						
Series A	A3	15	15	70	127.93	4.661	27.45	0.589	1.545	11.79
	A4	10	20	70	148.12	5.170	28.65	0.611	1.577	12.74
	A5	5	25	70	168.32	5.702	29.52	0.632	1.608	13.71
		(0)	(30)	(70)		(5.709)				
Series B	B4	30	40	30	225.86	5.800	38.94	0.896	2.158	16.36
	B5	20	50	30	266.26	6.375	41.77	0.920	2.228	18.58
	B6	10	60	30	306.66	7.105	43.16	0.941	2.291	20.82
Series C		(0)	(50)	(50)		(6.941)				
	C1	5	50	45	267.41	6.537	40.91	0.831	1.990	18.39
	C2	10	50	40	267.03	6.520	40.95	0.859	2.058	18.41
	C3	15	50	35	266.64	6.506	40.98	0.888	2.136	18.47
	C4/B5	20	50	30	266.26	6.375	41.77	0.920	2.228	18.58
Series D		(0)	(60)	(40)		(7.479)				
	D1	5	60	35	307.04	7.013	43.78	0.911	2.199	20.68
	D2/B6	10	60	30	306.66	7.105	43.16	0.941	2.291	20.82
	D3	15	60	25	306.28	6.700	45.71	0.974	2.399	21.02
	E1	5	70	25	346.68	7.159	48.43	0.990	2.457	23.32

Note: in brackets are given data according to Ref. 11.

Table 2. Series, compositions, refractive index n_0, third-order nonlinear optical susceptibility $\chi^{(3)}$, interaction parameter A, average single bond strength B_{M-O}

Series		Compositions			n_0	$\chi^{(3)}$. 10⁻¹³ esu	A, Å⁻³	B_{M-O}, kJ/mol
		Na₂O	Bi₂O₃	B₂O₃				
Series A	A3	15	15	70	1.805	1.05	0.224	376.6
	A4	10	20	70	1.845	1.34	0.194	377.5
	A5	5	25	70	1.897	1.84	0.167	378.4
		(0)	(30)	(70)	(1.836)			
Series B	B4	30	40	30	1.781	0.90	0.132	215.6
	B5	20	50	30	1.845	1.34	0.098	217.5
	B6	10	60	30	1.948	2.45	0.072	219.3
		(0)	(50)	(50)	(2.074)			
Series C	C1	5	50	45	1.858	1.45	0.095	279.6
	C2	10	50	40	1.858	1.45	0.098	258.9
	C3	15	50	35	1.861	1.48	0.099	238.2
	C4/B5	20	50	30	1.845	1.34	0.098	217.5
Series D		(0)	(60)	(40)	(2.097)			
	D1	5	60	35	1.920	2.09	0.072	240.0
	D2/B6	10	60	30	1.948	2.45	0.072	219.3
	D3	15	60	25	1.855	1.71	0.071	198.6
	E1	5	70	25	1.946	2.42	0.051	200.5

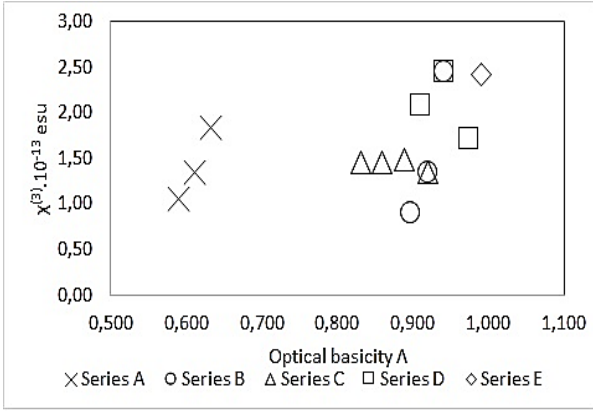Note: in brackets are given data according to Ref. 11.

Fig. 3. Third-order nonlinear optical susceptibility as a function of optical basicity.

Chemical bonding of glasses

In the present communication, we applied two approaches proposed for estimation of the chemical bonding in simple oxides and ionic crystals, namely the thermodynamical approach by Sun [20] and the quantum-mechanical approach by Yamashita and Kurosawa [21]. Dimitrov and Komatsu [10, 22] adapted both approaches for the calculation of average single bond strength B_{M-O} and interaction parameter A of oxide glasses. On this basis, in the case of our ternary oxide glasses we used the following equation for B_{M-O}:

$$B_{M-O} = x B_{Na-O}^{(6)} + y B_{Bi-O}^{(6)} + (1-x-y) B_{B-O}^{(3)}$$

$$(8)$$

where x, y, and (1-x-y) are molar parts of each oxide in the glass composition, and B_{Na-O}, B_{Bi-O}, and B_{B-O} are 59 kJ/mol, 102.5 kJ/mol, and 498 kJ/mol, respectively, according to Refs. [12, 20].

The interaction parameter A of our ternary oxide glasses could be calculated by using the following equation:

$$A = X_{Na_2O} \frac{(3.921 - \alpha_{O^{2-}})}{2(\alpha_{iNa^+} + 3.921)(\alpha_{O^{2-}} + \alpha_{iNa^+})} + X_{Bi_2O_3} \frac{(3.921 - \alpha_{O^{2-}})}{2(\alpha_{iBi^{3+}} + 3.921)(\alpha_{O^{2-}} + \alpha_{iBi^{3+}})} + X_{B_2O_3} \frac{(3.921 - \alpha_{O^{2-}})}{2(\alpha_{iB^{3+}} + 3.921)(\alpha_{O^{2-}} + \alpha_{iB^{3+}})} \quad (9)$$

where X_{Na_2O}, $X_{Bi_2O_3}$, and $X_{B_2O_3}$ are equivalent fractions based on the amount of oxygen each oxide contributes to the overall glass stoichiometry, $\alpha_{O^{2-}}$ is oxide ion polarizability of the glass and α_{iNa^+}, $\alpha_{iBi^{3+}}$, and $\alpha_{iB^{3+}}$ are cation polarizabilities of Na^+, Bi^{3+}, B^{3+}. Pauling's value of 3.921 $Å^3$ for the electronic polarizability of the free oxide ion is used.

We applied the equations above to our glasses and the results are presented in Table 2. The values for both parameters vary in a wide range (377 to 200 kJ/mol for B_{M-O} and 0.224 to 0.051 $Å^{-3}$ for interaction parameter). It is seen that glasses with the highest values for A and B_{M-O} are those with high boron content. On this basis, it should be noticed that glasses with the highest B_2O_3 content are built-up by strong predominantly covalent bonds, such as B-O-B. Such bonds were confirmed by Matsumoto *et al.* [23] based on the O1s XPS spectra of alkali borate and alkaline earth borate glasses. On the other hand, low values for A and B_{M-O} suggest a small overlap between metal and oxide ions valence orbitals which leads to the presence of weak predominantly ionic bonds such as Bi-O-B and Bi-O-Bi which were proved by Honma *et al.* [11] using O1s XPS spectra of Bi_2O_3-B_2O_3 glasses. The third-order nonlinear optical susceptibility as a function of the interaction parameter is shown in Fig. 4. It is seen that the optical nonlinearity increases with decreasing interaction parameter of the glasses.

IR spectral analysis

To confirm the presence of such bonds the structure of the glasses in the present study was investigated in terms of IR spectroscopy. The IR spectra of Na_2O-Bi_2O_3-B_2O_3 glasses are shown in Figs. 5 and 6. All spectra are characterized by four groups of well-defined bands in the following spectral ranges: at about 1400-1000 cm^{-1}, at around 900 cm^{-1}, 700 cm^{-1}, and 480 cm^{-1}.
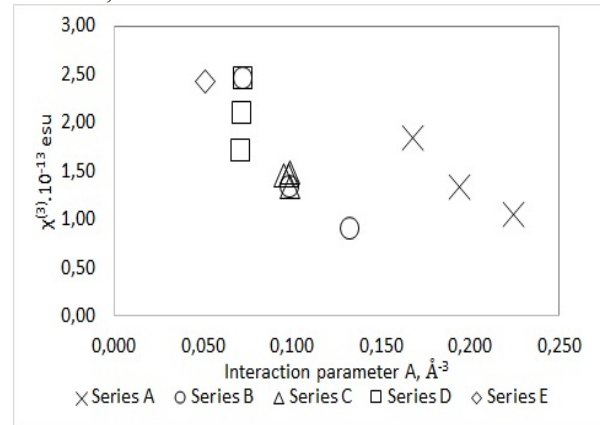

Fig. 4. Third-order nonlinear optical susceptibility as a function of the interaction parameter.

At the same time, it is seen that there is a strong increase in the intensity of the second (about 900 cm^{-1}) and fourth groups in the spectra (about 480 cm^{-1}) with increasing Bi_2O_3 content.

It is well known that the addition of a second oxide to B_2O_3 in oxide glasses leads to the transformation of BO_3 units to BO_4 units. This

change of coordination number of boron in Bi_2O_3 – B_2O_3 glasses has been studied by Terashima *et al.* [2] using ^{11}B MAS NMR spectroscopy. According to this study, the maximal concentration of BO_4 fractions (N_4) was found at about 30 mol% Bi_2O_3 and after that composition, a rapid decrease of N_4 fraction was observed.

The characteristic bands of boron-containing crystal and glasses are in the high-frequency range of the spectra in which are located the stretching vibrations of BO_3 and BO_4 structural units participating in different superstructural groups, namely pentaborate, diborate, pyroborate, and orthoborate groups. According to Plusnina [24], BO_3 group belongs to D_{3h} point group of symmetry and its vibrations in the spectra of borates are: double degenerate antisymmetric stretching vibration v_d^s located at 1310-1000 cm^{-1}, symmetrical stretching vibration v^s at 940-925 cm^{-1}, bending vibration δ at 725-765 cm^{-1} and doubly degenerate bending vibration δ_d at 680-590 cm^{-1}. According to the review study by Gautam *et al.* [25] on IR spectra of borate glasses, the antisymmetric stretching vibrations of B-O bonds of trigonal BO_3 units could be observed in the 1480-1200 cm^{-1} range. The band at about 1345-1235 cm^{-1} is connected with the presence of pyroborate and orthoborate groups, while the band at about 1235 cm^{-1} only to antisymmetric stretching vibrations of B-O bonds from orthoborate groups.

The bands at about 1046-1020 cm^{-1} are assigned to the B-O stretching vibrations of BO_4 units. Thakur *et al.* [26] have reported that the peak at about 914 cm^{-1} can be described as the fundamental peak due to the B-O stretching vibrations accruing in the BO_4 units from diborate groups in the structure of Bi_2O_3-B_2O_3 glasses. Also, the peak at 1185 cm^{-1} can be attributed to antisymmetric stretching vibrations of B-O bonds of the BO_3 units from pyroborate and orthoborate groups.

On the other hand, according to IR spectral data of a large number of bismuthate crystals and glasses collected by Iordanova *et al.* [27] the stretching vibrations of BiO_6 units are in the 480-420 cm^{-1} range.

Based on the above discussion, the assignment of the bands in the spectra presented in Figs. 5 and 6 could be made. The bands at 1400-1100 cm^{-1} in the Series A and Series B glasses are connected with antisymmetric stretching vibrations of B-O bonds in BO_3 groups participating in pyroborate and orthoborate groups while the single band at about 1240 cm^{-1} in the spectra of the glasses of Series C and Series D is attributed to the same vibrations of BO_3 groups in orthoborate groups only. The shoulder at 1046 cm^{-1} in the spectra of Series A is assigned to stretching vibrations of BO_4 units, which probably participate in diborate structural groups.
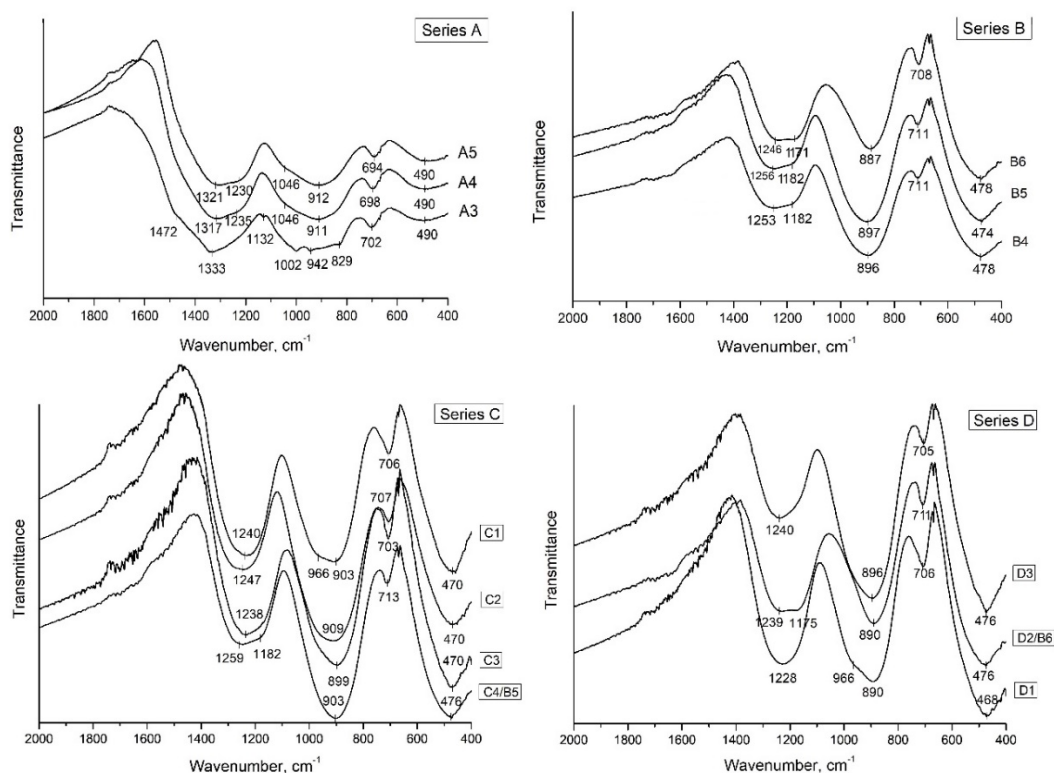

Fig. 5. IR spectra of Na₂O-Bi₂O₃-B₂O₃ glasses of Series A, Series B, Series C, Series D.
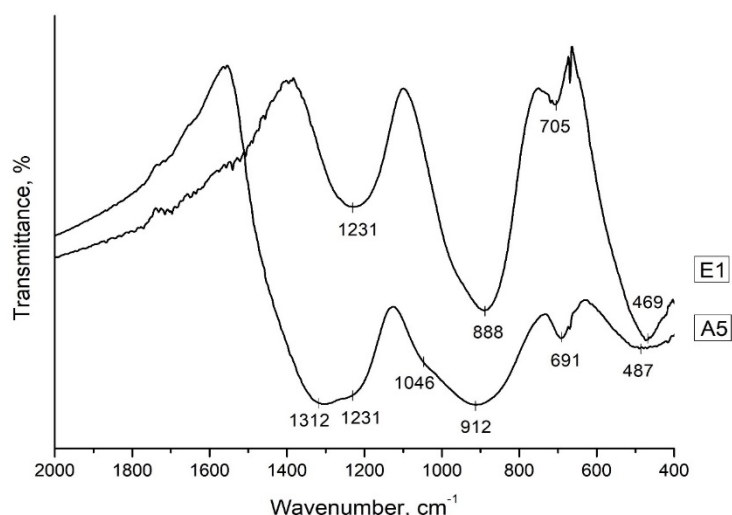
Fig. 6. IR spectra of Na$_2$O-Bi$_2$O$_3$-B$_2$O$_3$ glasses of 5Na$_2$O-25Bi$_2$O$_3$-70B$_2$O$_3$ (A5) glasses and 5Na$_2$O-70Bi$_2$O$_3$-25B$_2$O$_3$ glasses (E1).

The strong band at 470 - 490 cm^{-1} is attributed to the stretching vibrations of BiO$_6$ structural groups. The evidence of that is its intensity which increases with increasing Bi$_2$O$_3$ content.

The crystal structures of 2Bi$_2$O$_3$.B$_2$O$_3$ compounds and orthoborate BiBO$_3$ have been investigated by Hyman and Perloff [28], and Becker and Fröhlich [29]. The structure of the first compound contains discrete planar BO$_3$ groups held together by coordination to BiO$_6$ groups. The structure of the second compound consists of [Bi$_2$O$_{10}$] groups that are formed by two edge-sharing distorted [BiO$_6$] octahedra. These groups are further sharing corners with planar BO$_3$ groups giving a three-dimensional framework. In both crystal structures, Bi-O-Bi and Bi-O-B bonds are formed. In this connection, the strong band at about 900 cm^{-1} in the spectra with high Bi$_2$O$_3$ content is probably due to similar BO$_3$ groups linked with BiO$_6$ octahedra with mixed Bi-O-B bonds. The increase in Bi$_2$O$_3$ content leads to increasing the number of such bonds in the structure which is responsible for the rapid increase of this band. A good example of such orthoborate glass compared with the IR spectrum of glass with a low Bi$_2$O$_3$ content is given in Fig. 6. The IR spectrum of 5Na$_2$O.70Bi$_2$O$_3$.30B$_2$O$_3$ (E1) represents the spectrum of pure orthoborate glass built-up by isolated BO$_3$ groups connected with BiO$_6$ units.

Finally, the band at about 700 cm^{-1} could be assigned to the bending vibrations of borate groups.

Based on the structural analysis in this study presented above, the obtained low values of the average single bond strength B$_{M-O}$ and the interaction parameter A of glasses with high Bi$_2$O$_3$ content, as well as the increase of the third-order

nonlinear optical susceptibility χ$^{(3)}$ (See Table 2 and Fig. 4) should be connected with the formation of Bi-O-Bi and Bi-O-B bonds with increased ionicity instead of strong covalent B-O-B bonds.

CONCLUSION

It was established that Na$_2$O-B$_2$O$_3$-B$_2$O$_3$ glasses with high Bi$_2$O$_3$ content possess high values of electronic oxide ion polarizability, refractive index, and third-order nonlinear optical susceptibility. The chemical bonding of the glasses was investigated by the interaction parameter, single bond strength, and IR spectroscopy. We found that glasses with low Bi$_2$O$_3$ content are built-up by pyroborate and orthoborate groups, while those with high Bi$_2$O$_3$ content are built-up by orthoborate BO$_3$ groups connected with BiO$_6$ groups with mixed Bi-O-B bonds between them.

REFERENCES

1. M. Yamane, Y. Asahara, Glasses for photonics, Cambridge University Press, 2000, p. 159.
2. K. Terashima, T. H. Shimoto, T. Yoko, *Phys. Chem. Glasses,* **38(4),** 211 (1997).
3. T. Hasegawa, T. Nagashima, N. Sugimoto, *Opt. Commun.,* **250**, 411 (2005).
4. S. N. Raju, C. A. Reddy, S. Sailaja, H. J. Seo, B. S. Reddy, *Luminescence,* **27**, 334 (2012).
5. T. Maeder, *Int. Mater. Rev.,* **58**, 3 (2013).
6. D. Ehrt, *Glass Technol.* **41**, 182 (2000).

24

7. W. A. Weyl, E. G. Marboe, The Constitution of Glasses, Wiley, New York, 1962.
8. V. Dimitrov, S. Sakka, *J. Appl. Phys.,* **79**, 1736 (1996).
9. V. Dimitrov, T. Komatsu, *Solid State Chem.,* **163**, 100 (2002).
10. V. Dimitrov, T. Komatsu, *J. Solid State Chem.,* **178**, 831 (2005).
11. T. Honma, Y. Benino, T. Komatsu, R. Sato, V. Dimitrov, *Phys. Chem. Glasses,* **43(1)**, 32 (2002).
12. V. Dimitrov, T. Komatsu, *J. Non-Cryst. Solids,* **382**, 18 (2013).
13. T. Inoue, T. Honma, V. Dimitrov, T. Komatsu, *J. Solid State Chem.,* **183**, 3078 (2010).
14. T. Komatsu, T. Inoue, T. Tasheva, T. Honma, V. Dimitrov, *J. Ceram. Soc. Japan,* **126(1)**, 8 (2018).
15. T. Tasheva, V. Dimitrov, *Bulg. Chem. Commun.,* **49(G)**, 43 (2017).
16. A. Bishay, C. Maghrabi, *Phys. Chem. Glasses,* **10(1)**, 1 (1969).
17. J. A. Duffy, M. D. Ingram, in: Optical Properties of Glass, D. Uhlman N. Kreidl (eds.), Am. Ceram. Soc., Westervill, 1991.
18. J. A. Duffy, *Phys. Chem. Glasses,* **30**, 1 (1989).
19. K. Terashima, S. H. Kim, T. Yoko, *J. Am. Ceram. Soc.,* **78(6)**, 1601 (1995).
20. K. H. Sun, *J. Am. Ceram. Soc.,* **30**, 277 (1947).
21. J. Yamashita, T. Kurosawa, *J. Phys. Soc. Japan,* **10**, 610 (1955).
22. V. Dimitrov, T. Komatsu, *Phys. Chem. Glasses: Eur. J. Glass Sci. Technol.* B, **46**, 521 (2005).
23. S. Matsumoto, Y. Miura, C. Murakami, T. Namba, *Proc. Second Int. Conf. on Borate Glasses, Crystals and Melts* 1997, A. C. Wright, S. A. Feller, A. C. Hannon (eds.), Society of Glass Technology, Sheffield, p. 112.
24. I. I. Plusnina, IR spectra of minerals, Moskwa, 1977 (in Russian).
25. C. Gautam, A. Kunar Yadav, A. Kunar Singh, *Int. Scholarly Res. Network* ISRN Ceramics, Article ID 428497 (2012).
26. S. Thakur, V. Thakur, A. Kaur, L. Singh, *J. Non-Cryst. Solids,* **512**, 60 (2019).
27. R. Iordanova, Y. Dimitriev, V. Dimitrov, S. Kassabov, D. Klissurski, *J. Non-Cryst. Solids,* **204**, 141 (1996).
28. A. Hyman, A. Perloff, *Acta Cryst.,* **B28**, 2007 (1972).
29. P. Becker, R. Fröhlich, *Z. Naturforsch.,* **59b,** 256 (2004).

Study of the impact of radiation treatment upon biochemical properties of lyophilized dairy products

D. Miteva, S. Dyankova*, S. Ivanova, M. Doneva, I. Nacheva, A. Solak, P. Metodieva

Institute of Cryobiology and Food Technologies, Cherni vrah Blvd. 53, 1407 Sofia, Bulgaria

The effect of freeze-drying and radiation treatment on the protein profile and fatty acid composition of lyophilized cow's milk and curd was studied. The results of SDS-PAGE showed that lyophilization did not alter the qualitative composition of the main proteins in milk and curd. A significant decrease in casein and whey proteins was observed after irradiation with 10 kGy. These changes in protein components are associated with a decrease in allergenicity after radiation treatment. Changes in fatty acid composition are reflected by an increase in saturated fatty acid content and a decrease in monounsaturated and polyunsaturated fatty acids. In connection with the reported experimental data it is recommended that milk and curd should be totally skimmed before radiation treatment for potential decrease of the allergenicity.

Keywords: dairy products, fatty acids profile, irradiation, lyophilization, protein profile.

INTRODUCTION

The irradiation of food is a perspective technology for prevention of food spoilage by reducing the number of microorganisms, increasing the safety and extending the shelf life with minimal impact over the functional, nutritional and sensorial properties [1-3].

In addition, some results indicate that treating with ionizing radiation could cause decrease of the allergenicity by destruction of IgE-binding epitopes in nutritional allergens [4-6].

The appearances of allergic diseases, especially in children, are becoming more frequent during the last several decades. Food allergy is a serious health problem that is affecting 4-6% of the children and 1-3% of the adults [7]. Cow milk allergy is probably the most common food allergy in infancy and it is a clinical manifestation of an abnormal immunological response to one or more milk proteins [8]. The main allergens in cow milk are caseins, β-lactoglobulin, α-lactalbumin, bovine serum albumin and bovine serum IgG [9]. The β-lactoglobulin is considered as the most important allergen of them, because it is not present in the human milk and gives the highest percentage of positive reactions in oral administration (66%), although the casein shows the highest reactivity degree in skin test (68%) [10, 11].

Different technological approaches are tested to solve the problem with allergenicity of cow's milk. The decrease of the allergenicity of cow's milk by enzyme hydrolysis with proteolytic enzymes is the most common method [12, 13].

These hypoallergenic formulas have unsatisfactory taste, due to the presence of bitter peptides and amino acids [8]. Also it is reported about cases of allergy to some milk hydrolysates [14].

Other strategies for elimination or modification of allergens in milk are heat treatment, glycation reactions, high pressure processing and lactic acid bacteria fermentation. A lot of research for the structural modification of food allergens by gamma irradiation is done over the last few years.

The ionizing radiation could decrease allergenicity of the milk proteins by eliminating of the IgE-binding epitopes [4, 15]. Lee *et al.* investigated the changes in the allergenicity and antigenicity of irradiated milk proteins by competitive indirect enzyme-linked immunosorbent assay. The authors reported that epitopes in milk allergens are structurally changed by the gamma-irradiation and concluded that allergenicity of the milk proteins could be decreased by this method [16]. For better understanding of the possible decrease of the allergenicity by irradiation technology, it is important that the effect upon the specific milk proteins is clarified. Besides this, the information for the changes in fatty acids compounds of milk fat after irradiation of milk or dairy products is limited.

The purpose of the present study is to perform a comparative analysis of the protein profile and fatty acids content of the lyophilized milk and curd, and to evaluate the impact of radiation treatment for potential decrease of the allergenicity to these indicators.

---

* To whom all correspondence should be sent:
E-mail: svetla.diankova@ikht.bg

EXPERIMENTAL

Material: Skimmed cow milk (3.1% protein, 0.5% fat) and whey curd from cow milk (13.2 % protein, 0.5 % fat) were bought from a local supermarket in Sofia, Bulgaria. The curd was prepared by coagulation of the proteins in the whey after producing of the white brine cheese. All the chemicals used were of analytical grade.

The samples from homogenized curd and milk were distributed in metal trays (Food-Grade Stainless Steel) and frozen under (-25°C).

Lyophilization: The freeze drying was carried out in a freeze dryer TG 16.50 (Hochvacuum–Germany), at the following parameters: primary drying temperature – $(-40)^0$C, temperature of the desublimator – (-65°C), maximal working vacuum – 2.10^1 Pa; secondary drying temperature + 30°C. Duration of the process – 24 ± 1 h.

The lyophilizates were crushed and distributed in vacuum-sealed packages of triple aluminium foil. All samples were kept at 10 ± 2°C until the analyses were done.

Radiation treatment: Part of the lyophilized samples were irradiated in the National Centre of Radiobiology and Radiation Protection (NCRRP), Sofia, Bulgaria, on a gamma-irradiating installation - "NIGU-7", with cobalt-60 as a source of gamma-rays and dose rate - 2 kGy.h^{-1}. The applied dose was 10 kGy. The measurements of the dose were done by alanine dosimetry system with film alanine dosimeters (BioMax Kodak) and ESR spectrometer E-scan Bruker.

Physicochemical analysis

Determination of residual moisture after lyophilization - the moisture content of the lyophilized samples was measured with a Sartorius Thermo Control YTC 01L balance; total protein content – by the Kjeldahl method [17]; total fats - by extraction with hexane in a "Soxtec 2005" apparatus; total ash – by sample mineralization in a muffle oven [18].

SDS – Polyacrylamide gel electrophoresis

SDS–PAGE was performed by the method of Laemmli [19] at concentrations of stacking gel – 6% and running gel – 12%, using an OmniPAGE WAVE Electrophoresis System (Cleaver Scientifics). Samples were rehydrated with distilled water and diluted with sample buffer (0.2 M Tris-HCl, pH 6.80, containing 2% SDS, 16% glycerol and 10 mM DDT). Protein Test Mixture for SDS PAGE (SERVA Electrophoresis), α–lactalbumin, β-lactoglobulin, α-casein and β-casein (Sigma-Aldrich) were used as standard proteins. Gel was stained using 0.1% Coomassie Brilliant Blue (30-40 min).

Fatty acids analysis

The extraction of total lipids was done by the method of Roese-Gottlieb [20] using diethyl and petroleum ether. The transesterification of milk fat was done using sodium methylate (Merck) followed by drying with $NaHSO_4.H_2O$.

The fatty acids methyl esters (FAME) were analyzed using a gas chromatograph Shimadzu-2010 (Kyoto, Japan) with a flame ionization detector and an automated injection system (AOC-2010i). The analysis was done on a capillary column CP7420 (100 m × 0.25 mm i.d., 0.2 μm film, Varian Inc., Palo Alto, CA). Hydrogen was used as a carrier gas, and nitrogen as a make-up gas.

Statistical analysis

All experimental measurements were carried out in triplicate. Differences in mean values for fatty acids before and after irradiation were calculated by t-test. The statistical processing of data was performed by using Microsoft Excel 2013. The molecular weights of the main protein fractions in cow's milk and curd samples were calculated using the protein standards. The applied software was GelAnalyzer 19.0.

RESULTS AND DISCUSSION

Physicochemical analysis of lyophilized milk and curd

The obtained lyophilized products are with significant differences in quantity of the total protein – from 33.58% in milk to 43.58% in curd (Table 1). The lipid content in both types of samples is about 5 %. All samples are with low residual moisture: 3.14% and 2.96%, respectively. The low water content guarantees the long-term storage at room temperature without any changes in the main components.

Table 1. Composition of samples of lyophilized cow's milk and curd. Data represent means ± SD (n = 3)

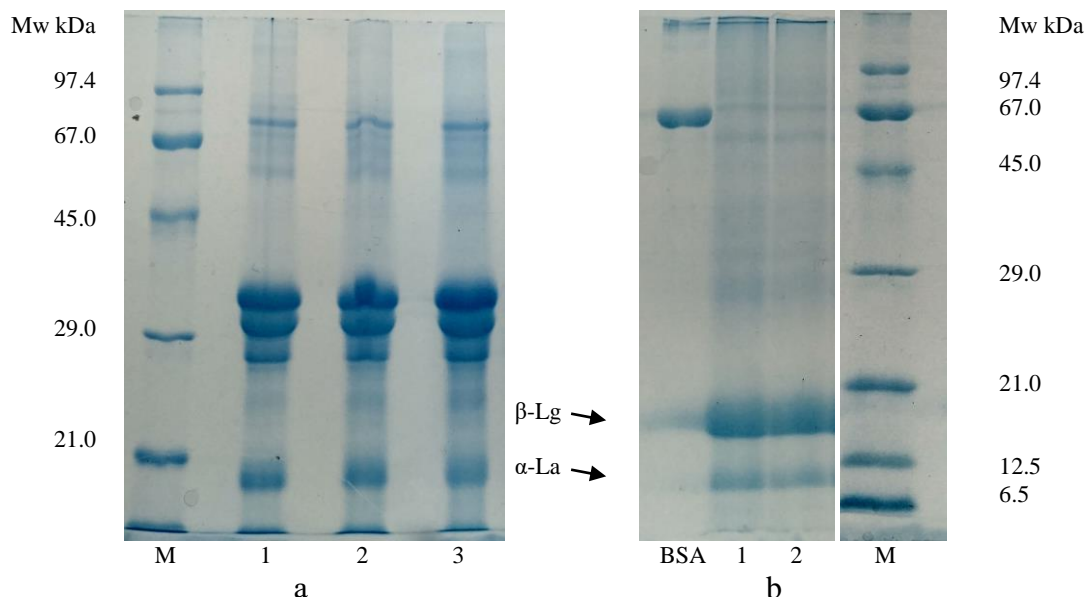| Parameter	Lyophilized milk	Lyophilized curd
Residual moisture (%)	3.14±0.32	2.96±0.24
Fat (%)	4.80 ± 0.15	5.20±0.56
Protein (%)	33.58± 0.78	43.58±0.89
Ash (%)	1.95±0.38	2.82±0.21

Fig. 1. SDS – PAGE of raw and lyophilized dairy products. a) milk: 1 and 2 – raw milk; 3- lyophilized milk; M- protein marker; b) BSA–bovine serum albumin,1-raw curd; 2-lyophilized curd; M-protein marker

SDS – PAGE of the lyophilized and irradiated cow's milk and curd

The results from electrophoretic analysis of milk samples show a similar picture of casein and whey fractions before and after lyophilization (Fig. 1a). In all samples the presence of intensive casein fractions (α-casein, β-casein and to a lesser extent κ-casein), β-lactoglobulin (β-Lg) and α–lactalbumin (α-La) is detected. A fraction with a molecular mass of 67 kDa, corresponding to serum albumin and a fraction with a molecular mass about 82-84 kDa, which respond to lactoferrin, are also observed.

The whey curd contains mainly β-lactoglobulin and α-lactalbumin while the casein fractions are minimal (Fig. 1b). In both curd samples (raw and lyophilized) an intensive band with Mw of 18 kDa (β-lactoglobulin) and a band with Mw – 12.4 kDa, (α-lactalbumin) are estimated. In the upper section of the gel, faint bands with molecular weight of 83 kDa (lactoferrin), 67 kDa (BSA) and 59 kDa are detected. Therefore, the lyophilization does not change the protein profile and the composition of the main protein components in milk and curd.

Figure 2 presents SDS – PAGE of lyophilized milk and curd, irradiated with a dose of 10.0 kGy.

Distinguishable changes in the protein profile are observed in both types of irradiated samples, compared to unirradiated. In milk samples, irradiated with 10 kGy (2A), the fractions with higher molecular mass - 83 kDa, 67 kDa (BSA) and 59 kDa are missing. The intensity of the α-casein band is reduced by 20.0% and those of the β-casein - by 13.0%. For the whey proteins, β-lactoglobulin and α-lactalbumin, the decrease is with 11.0 and 19.8%, respectively. The main protein components of the curd are also changed after gamma-irradiation (2B). The decrease in the intensity of β-lactoglobulin and α-lactalbumin is by 15.5% and 32.1%, respectively.

A similar reduction in the content of the α-casein and β-casein in milk and Queso Blanco cheese after irradiation with 10 kGy was reported by Ham *et al.* [21]. Their results suppose that from the casein fractions, α_{S1}-casein and β_{A1}-casein are more susceptible to gamma-irradiation and could be connected with the decrease of the allergenicity after radiation treatment. Significant changes in electrophoretic profile after gamma-irradiation of isolated β-lactoglobulin and α-casein in solution, are estimated, while the dose is increased [16].

These and other similar results from different authors refer mainly to the irradiation of milk and

milk proteins in aqueous solutions. There is little data in the available literature about the changes in the proteins in lyophilized dairy products, after radiation treatment. According to Audette-Stuart *et al.* [22], the radiolysis induces mainly fragmentation and/or aggregation of the protein, and it matters whether it is in solution, or in solid form (frozen or lyophilisate). There is a significant reduction of structural damage in the lyophilized proteins and it is mainly represented by partial fragmentation.

Fatty acids composition of the milk fat in lyophilized milk and curd

Milk fat is a mixture of short-, medium- and long-chain fatty acids, in different quantitative ratios depending on the nutrition, lactation and species specificity of the organism and technological treatment of producing dairy products. More detailed study of the fatty-acids profile of the samples of cow's milk and curd is presented in Tables 2 and 3. The lyophilized milk contains 70.91 g/100 g fat saturated fatty acids (SFA), while in the lyophilized curd the quantity of SFA is 61.38 g/100 g fat. The total amount of lauric (C12:0), myristic (C14:0) and palmitic (C16:0) acids in milk is 51.70 g/100 g fat, and in curd – 45.65 g/100 g fat. The content of stearic acid (C 18:0) in milk and curd is 12.31 g and 13.24 g/100 g fat, respectively. The data for the branched chain fatty acids (BFA) show that depending on the product, their content is different and varies from 3.10 g/100 g fat in lyophilized milk to 1.35 g/100 g fat in curd (Table 2).

Monounsaturated fatty acids (MUFA) are in concentrations of 24.37 g/100 g fat in lyophilized milk and 31.17 g/100 g fat in lyophilized curd (Table 3). The main representatives of MUFA in the investigated dairy products are palmitoleic (C-16:1n7), vaccenic (C18:1trans11) and oleic (C18:1 cis9) acid. The total amount of trans fatty acids in lyophilized milk is 1.61 g/100 g fat, and in curd – 2.44 g/100 g fat.

								Mw kDa
								97.4
								67.0
								45.0
								29.0
								21.0
								12.5

1A 2A   1B   2B   β-Lg α-CN β-CN M   BSA
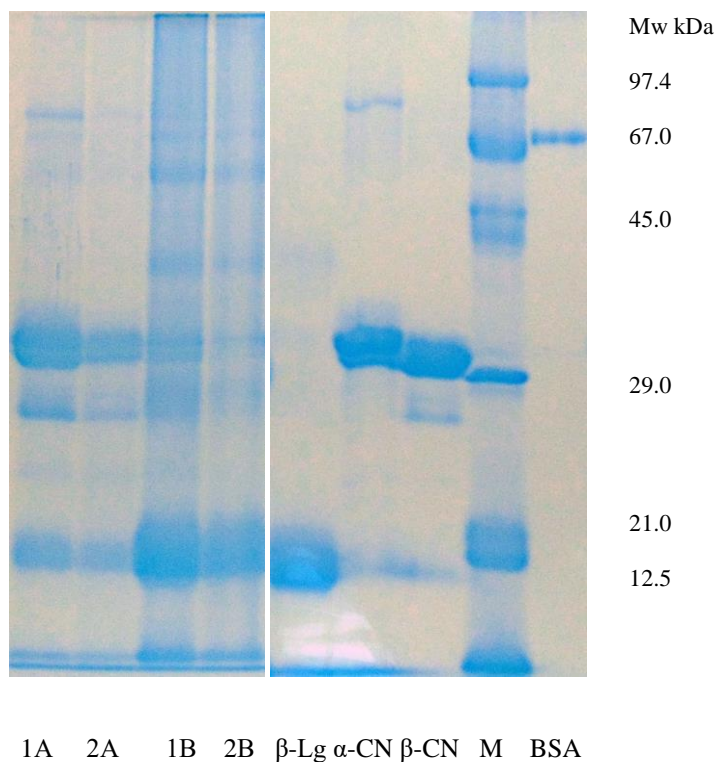
Fig. 2. SDS – PAGE of irradiated samples of lyophilized dairy products. 1A–lyophilized milk (0 kGy); 2A-lyophilized milk (10 kGy); 1B–lyophilized curd (0kGy); 2A- lyophilized curd (10 kGy); β-Lg – β-lactoglobulin; α-CN – α-casein; β-CN- β-casein; M – protein marker; BSA – bovine serum albumin.

Table 2. Saturated fatty acids and branched fatty acids (g /100 g fat) of lyophilized cow's milk and curd

Saturated fatty acids					
SFA	Milk	Curd	SFA	Milk	Curd
C-4:0	2.37	0.48	C-13:0	0.00	0.03
C-6:0	1.11	0.23	C-14:0	11.58	8.71
C-7:0	0.06	0.02	C-15:0	0.65	0.07
C-8:0	0.56	0.16	C-16:0	37.87	35.09
C-9:0	0.03	0.02	C-17:0	0.72	0.25
C-10:0	1.27	1.03	C-18:0	12.31	13.24
C-11:0	0.02	0.01	C-20:0	0.01	0.07
C-12:0	2.25	1.85	C-23:0	0.10	0.08
Branched fatty acids					
BFA	Milk	Curd	BFA	Milk	Curd
C-13iso	0.25	0.02	C:16iso	0.29	0.02
C-13aiso	0.03	0.04	C-17iso	0.42	0.24
C-14iso	0.09	0.00	C-17aiso	0.41	0.54
C-15iso	0.24	0.35	C-18iso	0.05	0.01
C-15aiso	1.33	0.14			

Table 3. Monounsaturated and polyunsaturated fatty acids (g/100 g fat) of lyophilized cow's milk and curd

Monounsaturated fatty acids					
MUFA	Milk	Curd	MUFA	Milk	Curd
C-10:1	1,10	0.02	C-18:1c9/C-18:1t12/13/	18.07	26.02
C-12:1n1	0.02	0.02	C-18:1t15	0.17	0.25
C-14:1n5	0.08	0.13	C-18:1c11	0.04	0.03
C-15:1n5	0.05	0.00	C-18:1c12	0.03	0.03
C-16:19tr	0.49	0.03	C-18:1c13	0.00	0.04
C-16:1n7	2.33	1.77	C-18:1t16	0.23	0.01
C-17:1n7	0.05	0.02	C-18:1c14	0.07	0.11
C-16:3n4	0.02	0.00	C-18:1c15	0.23	0.08
C-18:1t4	0.03	0.21	C-20:1n9	0.00	0.06
C-18:1t5/6/7	0.13	0.38	C-22:1n11	0.03	0.01
C-18:1t9	0.24	0.65	C-22:1n9	0.01	0.11
C-18:1t10	0.37	0.53	C-24:1n9	0.00	0.02
C-18:1t11	0.58	0.63			
Polyunsaturated fatty acids					
PUFA	Milk	Curd	PUFA	Milk	Curd
C-18:2t9,12	0.06	0.01	CLA9t,11t	0.01	0.04
C-18:2c9,12/19:0	2.01	5.49	C-20:2n6	0.08	0.08
gC-18:3n6	0.29	0.26	C-20:3n6	0.06	0.05
aC-18:3n3	0.06	0.22	C-20:4n6	0.40	0.04
CLA9c,11t	0.21	0.03	C-20:3n3	0.16	0.01
CLA10t,12c	0.02	0.06	C-20:5n3	0.03	0.20
C-18:4n3	0.07	0.01	C-22:2n6	0.06	0.05
CLA9c,11c	0.02	0.09			

MUFA, as a part of the human diet, do not cause cholesterol accumulation like the saturated acids, and do not oxidize easily like polyunsaturated ones. Also, the consumption of oils rich in monounsaturated fatty acids has a positive effect upon high-density lipoproteins (HDL) transporting the cholesterol from the walls of the blood vessels to the liver, where it is degraded. Meanwhile, monounsaturated fats lead to a decrease in the concentration of low-density lipoproteins (LDL) [23].

The content of the polyunsaturated fatty acids (PUFA) in lyophilized milk is 3.56 g/100 g, and in curd – 6.64 g/100g. The quantity of α- and γ-linolenic acid in milk and curd is 2.01 g/100 g and 5.49 g/100 g, and the total content of conjugated linoleic acids (CLA) is 0.26 g/100 g and 0.21 g/100 g, respectively.

The differences in the fatty-acids profile of the two lyophilized products are most significant in terms of the content of unsaturated fatty acids. The curd contains 27.90% more monounsaturated fatty acids and 86.50% more polyunsaturated fatty acids as compared to milk.

The application of gamma-irradiation with 10 kGy in cow's milk and curd leads to a significant ($P \leq 0.05$ and $P \leq 0.01$) increase of saturated fatty acids. The content of SFA in lyophilized milk rises by 19.22%, and in curd - by 28.57%. The amount of short-chain fatty acids (C4:0, C6:0, C8:0 and C10:0) also rises during the irradiation, and so does the content of stearic acid (C 18:0) while the content of myristic (C14:0) and lauric (C12:0) acid remains almost constant in milk but grows in curd.

Table 4. Groups of fatty acids (g/100 g fat) of lyophilized cow's milk and curd, before and after treatment with 10 kGy. Data are expressed as means ± SD (n = 3)

Group FA	Milk		Curd	
	0 kGy	10 kGy	0 kGy	10 kGy
Σ CLA	0.26±0.02***	0.04±0.01	0.21±0.03**	0.27±0.05
ΣC-18:1Trans-FA	1.61±0.54*	0.34±0.10	2.44±0.48**	0.85±0.23
Σ C-18:1Cis-FA	18.40±0.60**	12.88±1.12	26.28±1.81**	17.51±1.43
SFA	70.91±4.83*	84.54±6.07	61.38±2.40**	78.62±3.87
MUFA	24.37±4.68*	14.98±2.74	31.17±2.95**	19.30±3.48
PUFA	3.56±1.17*	0.23±0.05	6.64±1.99*	1.85±0.38
Σ n-3	0.33±0.01***	0.08±0.02	0.44±0.06	0.34±0.10
Σ n-6	3.00±0.27***	0.10±0.02	6.02±0.78**	1.31±0.17
Σ n-6/Σ n-3	9.19±0.71***	1.28±0.09	13.60±2.46	3.84±0.37
Branched FA	3.10±0.32*	2.59±0.31	1.35±0.15*	0.85±0.20
CLA	0.21±0.02***	0.01±0.00	0.03±0.01**	0.08±0.01

*$P \leq 0.05$, **$P \leq 0.01$, ***$P \leq 0.001$

The monounsaturated fatty acids in lyophilized milk are in a concentration of 24.37 g/100 g fat and decrease significantly ($P \leq 0.05$) to 14.98 g/100 g fat after irradiation with 10 kGy. The results of the studied curd are analogous – significant decrease from 31.17 g/100 g fat to 19.30 g/100 g fat ($P \leq 0.01$). The content of the polyunsaturated fatty acids significantly decreases ($P \leq 0.05$) in both milk and curd samples after gamma-irradiation. The same trend is observed in biologically active fatty acids from the group of omega-3, omega-6 and CLA.

The assumed data for the fatty-acids content of the lyophilized milk and curd samples, treated with 10 kGy are shown in Table 4.

CONCLUSION

The results from the study show significant differences in the protein profile and fatty-acids content of the two investigated types of lyophilized products – skimmed cow's milk and curd produced by coagulation of the proteins of whey after the production of white brine cheese. The amount of total protein in the lyophilisates is much higher in curd, while the fat content in both products is about 5%. The results from SDS-PAGE show that the lyophilization does not change the content of the main protein component in cow's milk and curd. In the lyophilized milk, the main casein fractions, β-Lg, α-La, serum albumin and lactoferrin are established. The lyophilized whey curd contains mainly β-Lg and α-La and minimal amounts of casein fractions. As far as the fatty-acids content in the curd is concerned, a lower content of saturated fatty acids and higher content of mono- and polyunsaturated fatty acids was estimated in comparison to milk.

A change was observed in the electrophoretic image of casein fractions (mainly α-casein) and whey proteins, after irradiation of lyophilized milk

with 10 kGy. There was also a significant decrease in the intensity of β-lactoglobulin and α-lactalbumin bands in irradiated curd. These changes in the protein components could be connected with the decrease in the allergenicity after radiation treatment. Changes in fatty acids profile after gamma irradiation in both types of lyophilized products were expressed in an increase in saturated fatty acids content and a decrease of monounsaturated and polyunsaturated fatty acids. In connection with the reported experimental data it is recommended that milk and curd should be totally skimmed before radiation treatment for potential decrease of the allergenicity.

REFERENCES

1. WHO, High dose irradiation, in: Wholesomeness of food irradiated with doses above 10 kGy, WHO Technical Report Series 890, Geneva, 1999, p. 9.
2. H. Gharaghani, M. Zaghari, G. Shahhosseini, H. Moravej, *Asian-Australas. J. Anim. Sci.,* **21**(10), 1479 (2008).
3. K. A. Da Silva Aquino, in: Gamma Radiation, F. Adrovic (ed.), InTech, Rijeka, 2012, p. 171.
4. M. W. Byun, J. W. Lee, H. S. Yook, C. Jo, H.Y. Kim, *Radiat. Phys. Chem*., **63**, 369 (2002).
5. J. W. Lee, J. H. Seo, J. H. Kim, S. Lee, K. S. Kim, M. W. Byun, *Radiat. Phys. Chem*, **72,** 645 (2005).
6. J. H. Seo, J. W. Lee, J. H. Kim, E. B. Byun, S. Y. Lee, I. J. Kang, M. W. Byun, *Radiat. Phys. Chem*., **76**, 1855 (2007).
7. T. Rahaman, T. Vasiljevic, L. Ramchandran, *Trends Food Sci. Tech.,* **49,** 24 (2016).
8. E. I. El-Agamy, *Small Ruminant Res.,* **68**, 64 (2007).
9. G. H. Docena, R. Fernendez, F. G. Chirdo, C. A. Fossati, *Allergy*, **51**(6), 412 (1996).
10. E. Savilahti, M. Kuitunen, *J. Pediatr.* **121** (5), 12 (1992).
11. D. Bogahawaththa, J. Chandrapala, T. Vasiljevic, *Int. Dairy J.,* **69**, 239 (2017).
12. L.Terracciano, P. Isoardi, S. Arrigoni, A. Zoja, A. Martelli, *Ann. Allergy Asthma Immunol*., **89** (6), 86 (2002).
13. Y. Vandenplas, *Nutrients*, **9**(7), 731 (2017).
14. A. Martorell-Aragonés, L. Echeverría-Zudaire, E. Alonso-Lebrero, J. Boné-Calvo, M. F. Martín-Muñoz, S. Nevot-Falcó, M. Piquer-Gibert, L. Valdesoiro-Navarrete, *Allergol. Immunopathol*., **43** (5), 507(2015).
15. S. Y. Lee, G. R. Jeon, J. W. Lee, S. J. Oh, H. S.Yook, K. H. Cho, M. W. Byun, *J. Allergy Clin. Immunol*, **109**, S307, (2002).
16. J. W. Lee, J. H. Kim, H. S. Yook, K. O. Kang, W. Y. Lee, H. J. Hwang, M. W. Byun, *J. Food Prot*., **64**, 272 (2001).
17. ISO 8968-1:2014, Milk and milk products — Determination of nitrogen content, 2014.
18. AOAC Official Method 930.30: Ash of dried milk, 17th edn, 2000.
19. U. K. Laemmli, *Nature,* **227,** 680 (1970)
20. AOAC. Official method 905.02, Fat in milk, 17th edn., 2000.
21. J. S. Ham, S. G. Jeong, S. G. Lee, G. S. Han, H. S. Chae, Y. M. Yoo, D. H. Kim, W. K. Lee, C. Jo, *Radiat. Phys. Chem*., **78,** 158 (2009).
22. M. Audette-Stuart, C. Houée-Levin, M. Potier, *Radiat. Phys. Chem*., **72**, 301 (2005).
23. M. Markiewicz-Kęszycka, G. Czyżak-Runowska, P. Lipińska, J. Wójtowski, *Bull. Vet. Inst. Pulawy*, **57,** 135 (2013).

The effect of silica nanoparticles and crumb rubber additives on chemical and physical properties of bitumen

S. M. Kandomal[*], *M.* Ashjari

Chemical Engineering Department, Faculty of Engineering,
University of Kashan, P.O. Box 87317-51167 Kashan, Islamic Republic of Iran

Bitumen modified by suitable additives enjoys many benefits such as increase in strength against rutting and fatigue, as well as against cryogenic cracks, reducing damage and thermal sensitivity. In this work, we investigated the effect of silica nanoparticles and crumb rubber additives to improve the quality of bitumen. The chemical and physical properties of bitumen were investigated after modification with silica nanoparticles and crumb rubber additives. The effects of silica nanoparticles in the range of 2-8% (w/w) and crumb rubber at ratios of 5-20% (w/w) on softening point, rheological properties, penetration, tensile strength, and weight loss of bitumen were investigated. The results exhibit an improvement in the quality of bitumen in the presence of silica nanoparticles and crumb rubber additives. According to the experimental data, the tensile strength of bitumen increased from 1000 mm to 1160 mm, and 113 mm after addition of 15% of crumb rubber and 6% of silica nanoparticles, respectively. In addition, the results showed an improvement in all properties of the bitumen in the presence of silica nanoparticles and crumb rubber additives.

Keywords: Silica nanoparticles, Crumb rubber, Bitumen, Modification process

INTRODUCTION

The use of industrial waste materials for engineering applications is considered as a useful tool for environmental protection. The high value of industrial waste materials is a major problem in environmental health. Therefore, various designs have been proposed for the use of industrial wastes. In between, using industrial wastes in bitumen is a useful and economic strategy for environmental protection and engineering applications. Due to its good properties and low cost, the crumb rubber was suggested as a modifier for bitumen since the 1930s and application of crumb rubber increased in the recent years with an increase in rubber waste in human and industrial societies. The swelling process of rubber particles helps to improve properties of bitumen. The swell up of crumb rubber in a bitumen matrix can be related to absorption of maltenes component [2, 3]. The scientific reports showed that crumb rubber could be used for modification of bitumen by dry or wet process as two different strategies. The scientific researchers showed that wet process could be useful for improving bitumen properties such as fatigue cracking, resistance of asphaltic, and resilience modulus compared to dye process [4].

Nano-materials with unique properties such as high thermal stability, high resistance, and good electrical conductivity were suggested as a new approach in engineering applications [5-10]. They improve the pavement durability, enhance the decrease in moisture susceptibility, and in aging, storage stability, and decreases maintenance costs which are the main advantages of bitumen modified with nano-materials [11]. The silica nanoparticles are a good choice for modification of bitumen due to their chemical purity, good dispersing ability, excellent stability, low cost, and strong adsorption [12-18]. Due to these properties, many researchers focused on the application of silica nanoparticles in modification of bitumen. As an example, Shafabakhsh and Ani used nano TiO_2/SiO_2 particles to improve properties of bitumen. They showed that the presence of nano TiO_2/SiO_2 particles could improve some properties of bitumen such as viscosity, adhesive bonding, and softening point [19]. Shi *et al.* investigated the role of nano-silica and rock asphalt as a high-quality additive on the rheological properties of bitumen. Results showed an improvement in G^* factor of bitumen [20]. In this research, the effects of silica nanoparticles and crumb rubber additives on the chemical and physical properties of bitumen were investigated.

EXPERIMENTAL

Materials

Bitumen 60/70 penetration grade was chosen as an unmodified bitumen for all of the investigations. Tetraethyl orthosilicate (TEOS), ammonium hydroxide, and ethanol were purchased from

---

Sigma-Aldrich Company for synthesis of SiO_2 nanoparticles. SiO_2 nanoparticles were synthesized according to the following procedure: 100 mL of ethanol (4.0 M) was sonicated for 10 min. In continuation, 4 mL of TEOS (0.04 M) was added to the ethanol under sonication. After 20 min, ammonium hydroxide (14.0 M) was added to the solution under sonication, as a catalyst to promote the condensation reaction and sonication process was continued for 50 min. The obtained gel dried at 100 °C for 6 h.

Methods

Process of addition of silica nanoparticles. 200 g of bitumen 60/70 was placed in a metal container and heated at 190 ^{0}C for 30 min. After melting the bitumen, the obtained sample was homogenized by a stirrer for 10 min. In continuation, we added silica nanoparticles at different ratios (2%; 4%; 6 and 8% w/w) at a stirring speed of 900 rpm for 15 min.

Process of addition of crumb rubber. 200 g of bitumen 60/70 was placed in a metal container and heated at 190 ^{0}C for 30 min. After melting the bitumen, the obtained sample was homogenized by a stirrer for 10 min. In continuation, we added the crumb rubber at different ratios (5.0%; 10%; 15.0% and 20% w/w) at a stirring speed of 900 rpm for 15 min.

Softening point determination. For the determination of softening point, we used the standard test ASTM D36 for unmodified and modified bitumen. The proposed test method covers the determination of the softening point of bitumen in the range from 30 to 157°C [86 to 315°F] using a ring-and-ball apparatus immersed in distilled water [30 to 80°C] or USP glycerin (above 80 to 157°C).

Bitumen weight loss test. We used the standard test ASTM D6 to investigate bitumen weight loss; the results of this test were reported according to weight ratio for total samples according to the following equation:

Loss of weight = $(W_a – W_b/W_a) \times 100$ (eq. 1)

where W_a is the weight of the sample before placing it in air furnace, and W_b is the weight of the sample after removing it from the furnace.

Tensile test. For studying the tensile factor, we used standard test ASTM D113 for the unmodified and modified bitumen. The present test method describes the procedure for determining the ductility of an asphalt material measured by the distance to which it will elongate before breaking when the two ends of a briquet specimen of the material, described in Experimental, are pulled apart at a specified speed and temperature. Unless otherwise specified, the test shall be carried out at a temperature of 25-60.5 °C [77-60.9 °F] and at a speed of 5 cm/min 65.0 %. The speed for other temperatures should be specified.

DSR Test. Viscoelastic behavior of bitumen-modified samples was investigated by a dynamic shear rheometer (DSR) test by employing standard test ASTM D-7175. The present test determines the dynamic shear modulus and phase angle of asphalt binders when tested in dynamic (oscillatory) shear using parallel-plate geometry. It is applicable to asphalt binders having dynamic shear modulus values in the range of 100 Pa to 10 MPa.

RESULTS AND DISCUSSION

Characterization of SiO_2 nanoparticles and bitumen morphology

The synthesized silica nanoparticles were characterized by SEM method. As can be seen in Figure 1a, silica nanoparticles with spherical shape were synthesized by the procedure recommended above. The SEM image of the unmodified bitumen (Figure 1b) and bitumen modified with silica nanoparticles (Figure 1c) and crumb rubber (Figure 1d) are presented. As can be seen, the silica nanoparticles and crumb rubber additives were successfully dispersed in the bitumen matrix. Due to the high adhesion strength of the additives, as well as their placement in the porous space of the bitumen, the cracks of the bitumen after their increase were significantly reduced.

Effect of silica nanoparticles and crumb rubber additives on softening point

The softening point of bitumen was investigated as an important factor in the preparation of asphalt. The results showed a softening point of ~51 ^{0}C for unmodified bitumen. After modification of bitumen with silica nanoparticles and crumb rubber, the softening point of asphalt changed. We detected an increase in the softening point of the modified bitumen in the range of 2.0-6.0 % of silica nanoparticles (Figure 2A).
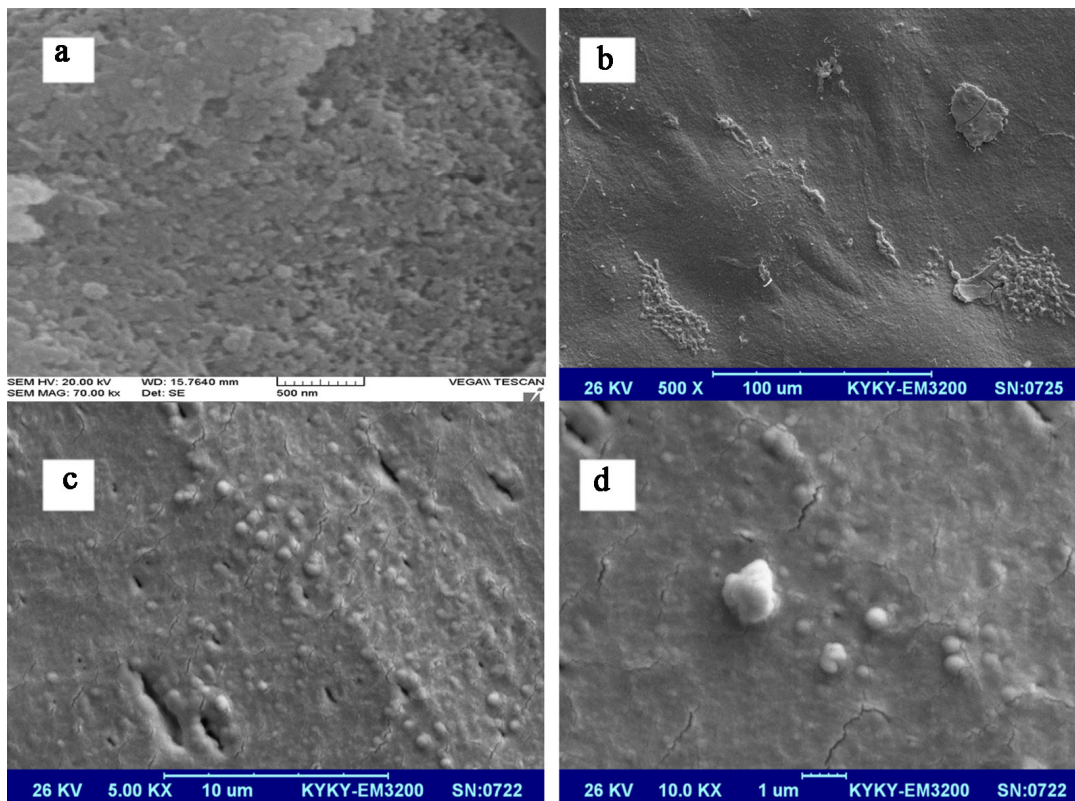
Figure 1. SEM image of a) SiO₂ nanoparticles; b) bitumen; c) bitumen after addition of silica nanoparticles; and d) bitumen after addition of crumb rubber
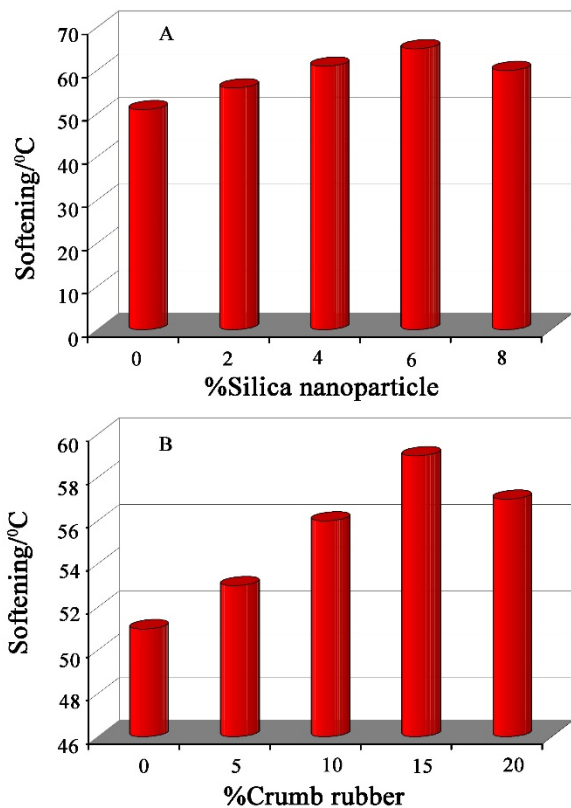

Figure 2. Softening point diagram of bitumen after addition of silica nanoparticles (A) and crumb rubber (B).

After this value, the softening point of the modified bitumen decreased due to a decrease in the homogeneity of nanoparticles, which might decrease the softening point of the whole composite. The softening point of bitumen increased in the presence of 5%-15% of crumb rubber and after that value it decreased (Figure 2B). With an increase in the amounts of the additives, their aggregation created a major problem, decreasing the softening point of the modified bitumen.

Effect of silica nanoparticles and crumb rubber on weight loss

The effect of silica nanoparticles and crumb rubber on the weight loss of bitumen was investigated. To this goal, we compared the weight of bitumen before and aftr its placement in a furnace. As can be seen, the value of bitumen weight before placing in a furnace is very similar to its weight after its removal from the furnace, which exhibits good stability of silica nanoparticles and crumb rubber as additives in bitumen modification (see Tables 1 and 2). According to the data in the Tables, the silica nanoparticles and crumb rubber are stable in the bitumen matrix.

Table 1. Data obtained for the effect of the addition of silica nanoparticles on bitumen weight loss

Percentage of silica particles (w/w)	Weight (g) of bitumen before furnace	Weight (g) of bitumen after furnace
2	70	69.6
4	70	69.3
6	70	69.1
8	70	68.7

Table 2. Data obtained for the effect of the addition of crumb rubber on bitumen weight loss

Percentage of crumb rubber (w/w)	Weight (g) of bitumen before furnace	Weight (g) of bitumen after furnace
5	70	64.4
10	70	62.1
15	70	62.0
20	70	61.8

Penetration investigation

The penetration properties of bitumen in the presence of silica nanoparticles and crumb rubber were investigated and the obtained data are presented in Figures 3A and 3B, respectively. The results showed a decrease in penetration after the addition of silica nanoparticles and crumb rubber, which means an increase in the binder hardness.
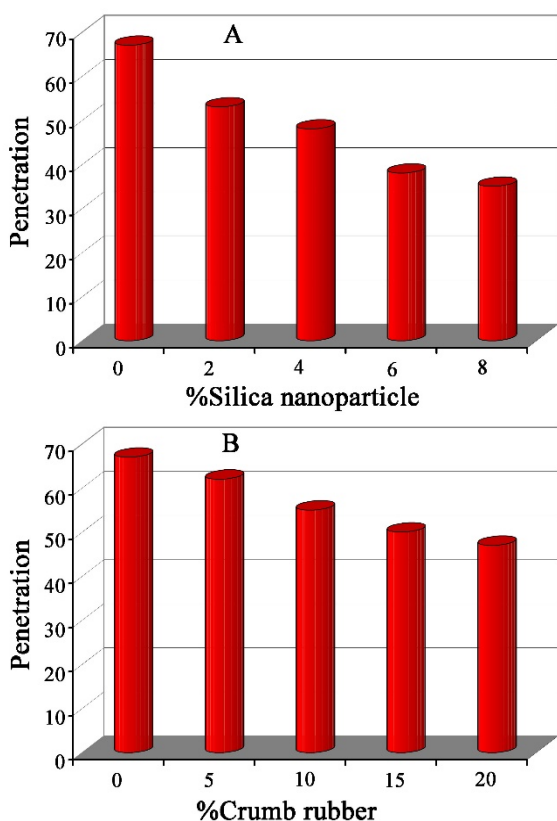
Figure 3. Penetration diagram of bitumen after the addition of silica nanoparticles (A) and crumb rubber (B).

Tensile strength investigation

The tensile factors of bitumen after the addition of silica nanoparticles and crumb rubber are presented in Figures 4A and 4B. As can be seen, the values of tensile strength in the presence of 6% of silica nanoparticles and 15% of crumb rubber showed good stability and after these values the tensile factor was stable.
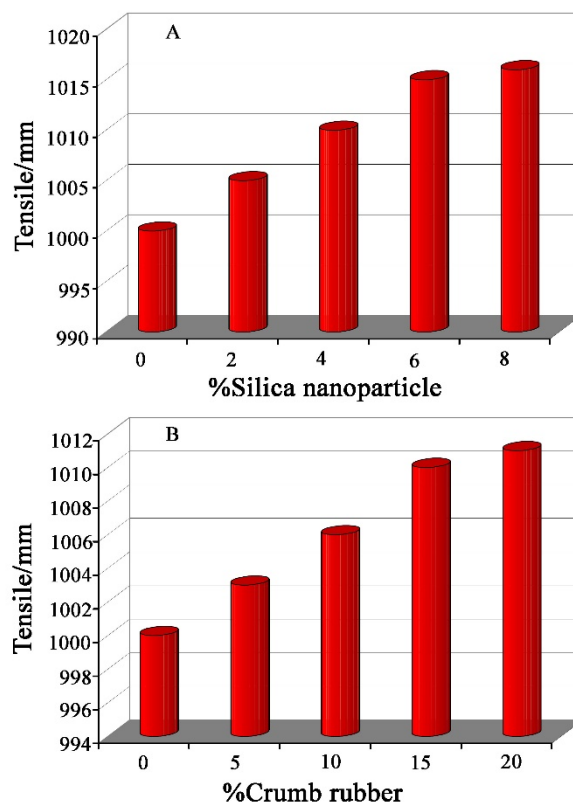
Figure 4. Tensile diagram of bitumen after the addition of silica nanoparticles (A) and crumb rubber (B).

DSR test results

The G* values of unmodified bitumen and bitumen modified with silica nanoparticles and crumb rubber at 40 °C are shown in Figure 5. As can be seen, the value of G* increased with an increase in the percentages of silica nanoparticles and crumb rubber that can be related to improved bitumen elasticity and viscoelasticity for the high amounts of modifiers. The good bond between bitumen and silica nanoparticles and crumb rubber with high surface area is the main cause of improving G* of bitumen after modification with modifiers. Due to good compatibility of bitumen and silica nanoparticles, we detected an increase in G* for all of the percentages of nanoparticles. The little decrease in G* after addition of 15% of crumb rubber can be related to low compatibility of bitumen and crumb rubber that changes the nature and rheological behavior of bitumen.
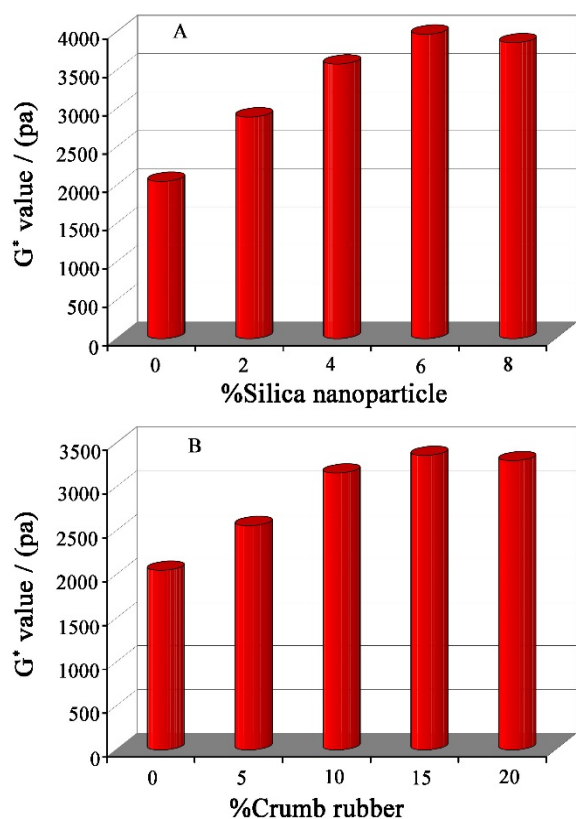
Figure 5. G* diagram of bitumen after the addition of silica nanoparticles (A) and crumb rubber (B).

CONCLUSION

The present work revealed the significance of the chemical composition of base bitumen for its modification. The present study suggested new types of modifiers for improving the bitumen quality. The silica nanoparticles and crumb rubber showed very interesting properties for the modification of bitumen. The effect of silica nanoparticles in the range of 2-8% (w/w) and crumb rubber at ratios of 5-20% (w/w) on softening point, rheological properties, penetration, tensile strength, and weight loss of bitumen was investigated. The softening point, rheological properties, penetration and tensile properties of bitumen were improved in the presence of 6% of silica nanoparticles and 15% of crumb rubber.

REFERENCES

1. J. L. McQuillen, H. B. Takallou, R. Gary Hicks, D. Esch, *J. Transp. Eng,.* **114,** 259 (1988).
2. J. Peralta, H. M. R. D. Silva, A. V. Machado, J. Pais, P. A. A. Pereira, J. B. Sousa, *Road Mater. Pavement,* **11,** 1009 (2010).
3. W .C. Vonk, A .L. Bull, in: Proceedings of the 7th International Roofing Congress, Munich, Germany, *1989.
4. M. R. Ibrahim, H. Y. Katman, M. R. Karim, S. Koting, N. S. Mashaan, *Adv. Mater. Sci. Eng.,* Article ID 415246, 8 pages, http://dx.doi.org/ 10.1155/2013/415246, (2013).
5. H. K. Maleh, F. Karimi, Y. Orooji, G. Mansouri, A. Razmjou, A. Aygun, F. Sen, *Sci. Rep.,* **10**, 11699 (2020).
6. H. Karimi-Maleh, B. G. Kumar, S. Rajendran, J. Qin, S. Vadivel, D. Durgalakshmi, F. Gracia, M. Soto-Moscoso, Y. Orooji, F. Karimi, *J. Mol. Liq.,* **314**, 113588 (2020).
7. X. Chen, C. Burda, *J. Am. Chem. Soc.,* **130,** 5018 (2008).
8. H. K. Maleh, M. Shafieizadeh, M. A. Taher, F. Opoku, E. M. Kiarii, P. P. Govender, S. Ranjbari, M. Rezapour, Y. Orooji, *J. Mol. Liq.,* **298,** 112040 (2020).
9. H. Karimi-Maleh, F. Karimi, S. Malekmohammadi, N. Zakariae, R. Esmaeili, S. Rostamnia, M. L. Yola, N. Atar, S. Movagharnezhad, S. Rajendran, A. Razmjou, Y. Orooji, S. Agarwal, V. K. Gupta, *J. Mol. Liq.,* **310**, 113185 (2020).
10. S. Cuenot, C. Fre´tigny, S. Demoustier-Champagne, B. Nysten, *Phys. Rev. B,* **69,** 165410 (2014).
11. H. Ezzat, S. El-Badawy, A. Gabr, E. Ibrahim Zaki, T. Breakah, *Procedia Eng.,* **143,** 1260 (2016).
12. Z. A. Zhou, Z. Xu, J. H. Masliyah, J. Czarnecki, *Coll. Surf. A,* **148,** 199 (1999).
13. Y. H. Hu, C. Y. Chen, C. C. Wang, *Polym. Degrad. Stab.,* **84,** 545 (2004).
14. C. F. Cheng, H. H. Cheng, P. W. Cheng, Y. J. Lee, *Macromolecules,* **39,** 7583 (2006).
15. C. H. Liu, C. Y. Pan, *Polymer,* **48,** 3679 (2007).
16. L. Senff, J. A. Labrincha, V. M. Ferreira, D. Hotza, W. L. Repette, *Constr. Build. Mater.,* **23,** 2487 (2009).
17. D. Kong, X. Du, S. Wei, H. Zhang, Y. Yang, S. P. Shah, *Constr. Build. Mater.,* **37,** 707 (2012).
18. L. P. Singh, S. R. Karade, S. K. Bhattacharyya, M. M. Yousuf, S. Ahalawat, *Constr. Build. Mater,.* **47,** 1069 (2013).
19. G. H. Shafabakhsh, J. Ani, *Constr. Build. Mater.,* **98**, 692 (2015).
20. X. Shi, L. Cai, W. Xu, J Fan, X. Wang, *Constr. Build. Mater.,* **161**, 705 (2018).

Effect of different feed strategies on integrated toluene-aniline production reactor

A. Javaid*, R. Ajaz

*Department of Chemical Engineering, Pakistan Institute of Engineering & Applied Sciences,
Nilore, 45650, Islamabad, Pakistan*

Hydrogen is an important energy transporter and is widely used in hydrogenation reactions for the synthesis of various valuable chemicals. It can be obtained through dehydrogenation reactions and the acquired hydrogen can directly be utilized in hydrogenation reactions. As a result, external hydrogen supply is minimized which makes it an economical process. Technique of coupling exothermic and endothermic reactions in a single reactor is among the methods of process intensification. Simultaneous production of toluene and aniline in an integrated reactor has been found feasible, economical and controllable in our previous study. The scope of this research is to study the effect of different feed strategies for simultaneous production of aniline and toluene. Both reactions are carried out in an adiabatic reactor curtailing the requirement of heating or cooling and eliminating a large amount of hydrogen recycle needed to avoid reaction run-away. Using Aspen plus, alternative feed strategies for both the reactants are employed to find out the best possible strategy in terms of reactant conversion. Preeminent option found is to feed both reactants completely at the reactor inlet. The conversion of methyl-cyclohexane and nitrobenzene is 74% and 98%, respectively. The results achieved in this study can be correlated with relevant chemical processes.

Keywords: Design, Feed Strategy, Process Integration, Reaction Coupling, Aspen

INTRODUCTION

The idea of combining several processes in a single unit is not new. The process integration concept has started back in 1970's [1]. Coupling of exothermic and endothermic reactions is among the methods of process intensification for material and energy utilization. The heat produced by exothermic reactions is used to drive the endothermic reactions, improving thermal efficiency and increasing equilibrium conversion & reaction rate for reversible reactions [2]. Coupling could be hydrogenation with dehydrogenation, oxidation with reduction, or hydration with dehydration. Many researchers have studied the possibility of coupling of more than one reaction in a single unit. It resulted in a small-sized reactor with reduced complexity and energy savings as an additional benefit [3]. These energy savings combined with reduced reactor investment must overshadow the cost of required additional separation units [4].

Studying coupling of exothermic and endothermic reactions has been a field of interest for researchers for a while but the real intensity in this field is seen since 1994 [5, 6]. The study of simultaneous dehydrogenation and hydrogenation reactions are important as they have several advantages over individual reactions. Coupling reactions offer various advantages as: mild reaction environment, simpler operation, optimum hydrogen

usage, thermodynamic limitations shift, eco-friendliness and good quantitative yields [7]. On the other side, individual reactions have limitations and these limitations can be eliminated by combination of these categories of reactions. Owing to aspects listed above, coupling reactions have gained momentum and lot of research methodologies are in process of continuous development. Extensive reviews of different catalytic reactors used for coupling exothermic and endothermic reactions, particularly hydrogenation and dehydrogenation are provided elsewhere [8, 9].

Over the period, many researchers tried to carry out simultaneous reactions in a single reactor and found this intensification technique useful but their studies are limited to reactor only, more specifically for catalyst selection. In our previous studies [10-12] an integrated toluene-aniline plant is found feasible in terms of economy and controllability. The goal of this research is to find out the best feed strategy in terms of reactants (MCH and AN) conversion. Although in some studies coupled behavior is analyzed in a stand-alone integrated plant [13-16], there is no research regarding using alternative feed strategies either for maximizing product yield or to focus uniform temperature profile in the reactor. Hence, this study is an attempt to fill that gap.

Types of thermal reactors

The reactors used for coupling processes can be divided into three types: direct, regenerative and

---

recuperative.

Direct coupling reactor. In this mode of coupling two or more reactions occur simultaneously in an identical reaction zone, where the material and energy are interchanged directly in the reaction mixture. However, there are some limitations to carry out direct coupling, e.g. the catalysts for both the reactions shall be in a similar temperature and pressure condition because both reactions are occurring simultaneously in the same catalyst bed. Direct coupled reactor is further classified into simultaneous direct coupling adiabatic reactor (SIMDCAR) which is made of uniformly mixed exothermic and endothermic catalysts favoring both the exothermic and the endothermic reaction, and sequential direct coupling adiabatic reactor (SEQDCAR) in which alternating exothermic and endothermic catalytic bed is used.

Regenerative coupling reactor. In a regenerative reactor, reactions are conducted in a single reaction zone but only one reaction is occurring at one time, so by storing and discharging cycles, energy and material are interchanged. It is generally suitable for the integration of several process steps with the main advantages: direct heat supply and efficient heat recovery. They are well suited for weak exothermic reactions. Main drawbacks are the development of hot spots which can damage the catalyst and the reactor walls.

Recuperative coupling reactor. In this type of coupling the reactions are occurring simultaneously but are separated physically either by separation wall or membrane. The energy interchange is anticipated through the wall or membrane but material interchange is only possible by permeation through the membrane. These types of reactors can be operated co-currently or counter-currently.

The detailed comparison among different schemes of coupling and guidelines regarding effective coupling for better results and linear temperature profiles are provided elsewhere [17]. Types of coupling reactors are shown in Fig. 1.

This study and outcomes are only based on coupling of hydrogenation and dehydrogenation reactions occurring simultaneously in a directly coupled single-tube adiabatic reactor.
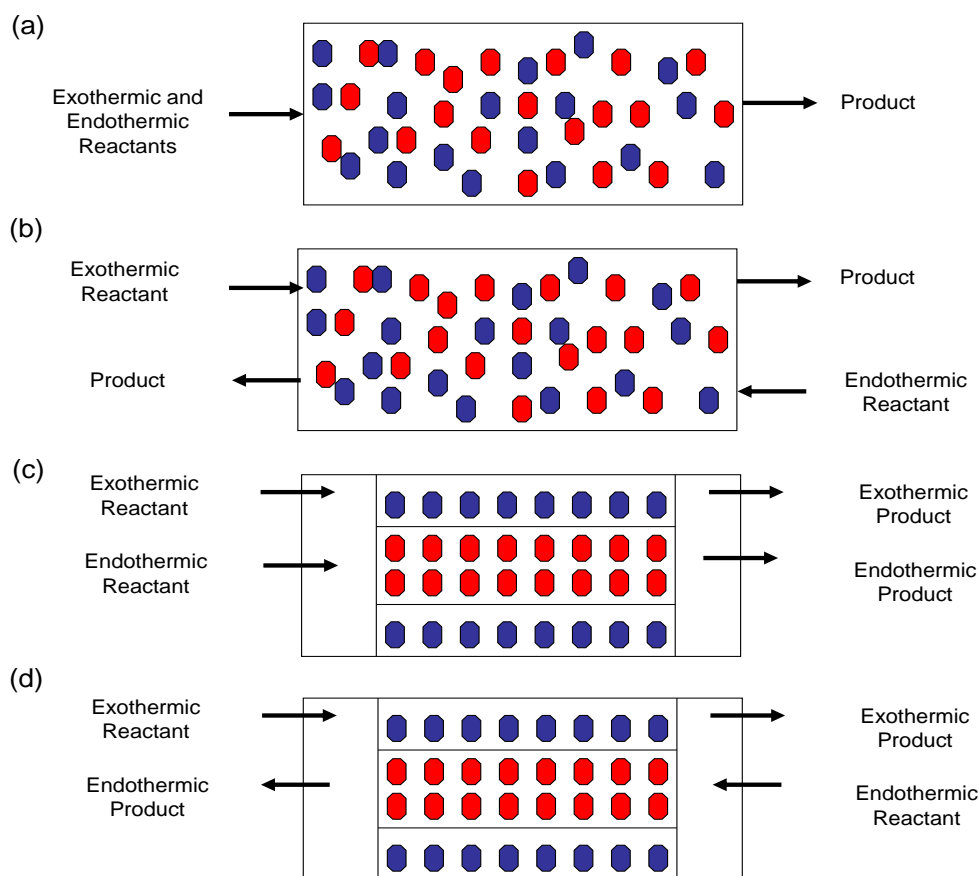
Figure 1. **Reactors for** coupling of reactions**: (a)** direct (b) regenerative (c & d) recuperative co- and counter-current

EXPERIMENTAL

Integrated toluene-aniline system

Aniline (AN) is produced industrially by hydrogenation of nitrobenzene (NB). The reaction is highly exothermic so a multi-tubular reactor is used. In spite of the large heat transfer area, still excess hydrogen is required up to 100:1 to keep temperature under control. Moreover, the recycling of hydrogen adds additional costs. Endothermic dehydrogenation of methyl-cyclohexane (MCH) to toluene (TOL) is a process which requires a large amount of heat and results in increased total annual cost of the plant. Both reactions are given in Eqns. 1 and 2.

$$C_6H_5\text{-}NO_2 + 3H_2 \rightarrow C_6H_5\text{-}NH_2 + 2H_2O$$
ΔH = - 443.0 KJ/mole   (1)

$$C_6H_{11}\text{-}CH_3 \rightarrow C_6H_5\text{-}CH_3 + 3H_2$$
ΔH = + 205.3 KJ/mole   (2)
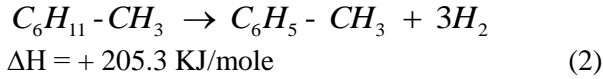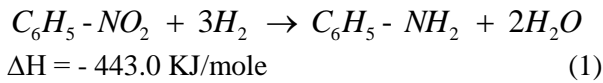
Design procedure

Reactor performance is specified as reactant conversion in Aspen Plus [18]. It allows preliminary mass balance which gives the reactor-inlet stream and consequently reactor diameter can be calculated. Using knowledge of reaction kinetics, the reactor length can be found. The following kinetic expressions are used in the simulation:

Nitrobenzene hydrogenation (copper-nickel catalyst) [19]:

$$r_1 = k \cdot p_{NB}^{0.5} \cdot p_{H_2}^{0.5} \qquad (3)$$

$$k = 0.114 \exp\left(-\frac{8323}{T}\right) \text{kmol} \times \text{m}^{-3} \times \text{s}^{-1} \times \text{Pa}^{-1} \qquad (4)$$

MCH dehydrogenation (platinum on alumina catalyst) [20]:

$$r_1 = k_1 \cdot p_{MCH} \qquad (5)$$

$$k_1 = 3.07 \times 10^{13} \exp\left(\frac{-26539}{T}\right) \text{kmol} \times \text{m}^{-3} \times \text{s}^{-1} \times \text{Pa}^{-1} \qquad (6)$$

Integrated reactor

To assess the feasibility of simultaneously performing MCH dehydrogenation and NB hydrogenation, an adiabatic reactor having 4 m length and 1.5 m diameter was considered. Catalysts were mixed and used in equal proportions. Ratio between the catalysts can be changed to tune the reaction rates. Peng-Robinson thermodynamic model was used for simulation. Reactants were mixed and fed to reactor; MCH 60 kmol/h, NB 20 kmol/h, and H₂ 100 kmol/h at 1.5 bars and 300 ºC. The ratio between reactants was chosen to approximately match the theoretical value for which heats of reactions balance each other. The conversion of MCH to toluene and of nitrobenzene to aniline was 74% and 98%, respectively. Temperatures and molar profiles along the reactor length are given in Fig. 2. The uniform temperature distribution resists the catalyst deactivation.

Due to limitation of simulation software the feed cannot be introduced at different length intervals or sections of the reactor, so the reactor of 4-m length was disintegrated into 4 reactors each having length of 1 m. By disintegrating, the effect of different feed strategies on the temperature and molar profiles will be more prominent. In this research, two case studies were considered where behavior of both the reactants was studied by using alternate feed strategies for nitrobenzene and methyl-cyclohexane.

Case 1. Alternative feed strategies for NB in the coupled system

In the first scenario the total feed of NB (20 kmol/h) was divided equally (50%) in the first two reactors at 10 kmol/h in each reactor. In the second scenario, the feed was divided equally (33%) in the first three reactors at 6.67 kmol/h. In the third scenario, the feed was divided equally (25%) in all four reactors at 5 kmol/h. Schematic diagram of the latter scenario is given in Fig. 3.
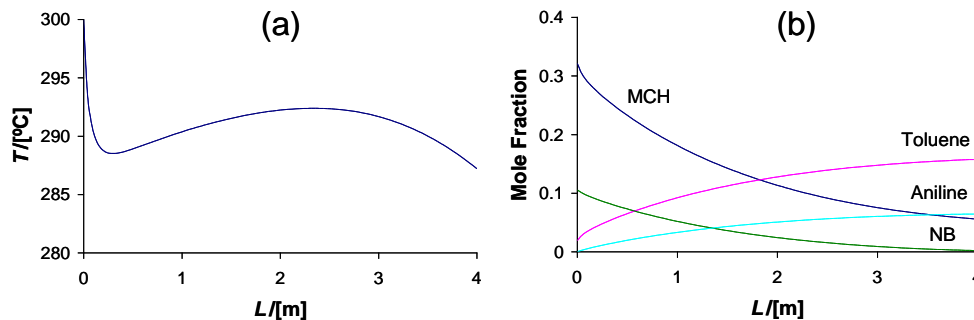

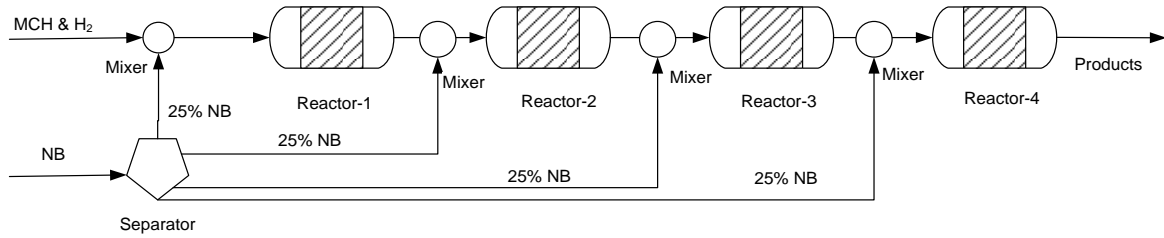**Figure 2.** Reactor profiles: (a) Temperature (b) Molar

Figure 3. Alternative feed strategies for NB (25%)

The stream coming out of reactor-4 consisted of products (toluene, aniline, water, hydrogen) and un-reacted reactants (methyl-cyclohexane and nitrobenzene), the components in the mixture were analyzed with the help of modern analytical (quantitative and qualitative) methods prior to its separation. The basis of separation was the miscibility and difference in boiling points. Hydrogen and water were separated from the mixture in a vapor-liq-liq separator and two distillation columns were required to separate the two organic phases. Toluene and aniline were taken out as products (required production rate & purity) while un-reacted MCH and hydrogen were recycled into the system. Details of the separation section in an integrated plant are provided in previous studies [10-12].

Case 2. Alternative feed strategies for MCH in the coupled system

On the similar lines as in NB feed, the effect of different feed strategies for MCH was also studied. In the first scenario the total feed of MCH (60 kmol/h) was divided equally (50%) in the first two reactors at 30 kmol/h in each reactor. In the second scenario, the feed was divided equally (33%) in the first three reactors at 20 kmol/h. In the third scenario, the feed was divided equally (25%) in all four reactors at 15 kmol/h. Schematic diagram for the latter scenario is provided in Fig. 4.
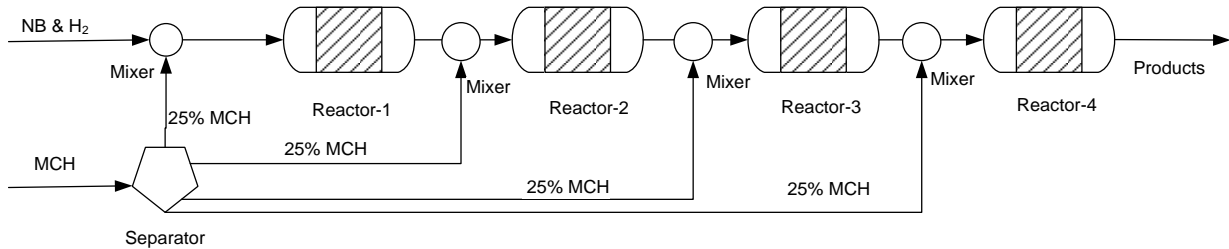
Figure 4. Alternative feed strategies for MCH (25%)

Table I. Comparison b/w NB feed flow strategies

Description/NB Feed Strategy	1	2	3	4
	100%	50%	33%	25%
Temperature R_{out} (°C)	286.4	289.8	292	292.8
Pressure (bar)	1.5	1.5	1.5	1.5
Feed (kmol/h)				
MCH	60	60	60	60
H_2	100	100	100	100
NB	20	20	20	20
Product (kmol/h)				
MCH	15.53	17.51	20.63	25.39
TOL	44.46	42.48	39.37	34.60
H_2	174.52	170.71	165.31	157.42
NB	0.37	1.08	2.40	4.53
AN	19.63	18.91	17.60	15.46
H_2O	39.25	37.82	35.20	30.93
Conversion (%)				
MCH	74	70.80	65.61	57.67
NB	98	94.57	88	77.32

RESULTS AND DISCUSSION

Case 1

In the first scenario, when feed is divided in first two reactors, the temperature sharply decreased from 300 ºC to 278 ºC in the first quarter of the reactor due to the 6:1 (MCH: NB) reactants ratio at the inlet. At the start of the second quarter a sudden increase in temperature is due to injection of nitrobenzene (10 kmol/h) leading to exothermic reaction. Once heats of both reactions started balancing each other the temperature profile was almost linear in the second half of the reactor. Similar effect can be observed in molar profiles. In the second scenario, when feed was divided in the first three reactors, again the temperature sharply decreased from 300 ºC to 270 ºC in the first quarter of the reactor due to the high reactants ratio 9:1 (endo: exo) at the reactor inlet. Sharp increase in

the second and third quarter was observed when nitrobenzene entered in the reactor. Linear temperature profile was observed in the last quarter of the reactor. In the third scenario, the feed was divided between all reactors. As the reactants ratio at the reactor inlet was 12:1 so due to the endothermic reaction the temperature sharply decreased from 300 ºC to 265 ºC in the first quarter of the reactor. As noted in previous scenarios a sharp increase in temperature was observed due to hydrogenation reaction when nitrobenzene was periodically introduced into the reactor.

Comparison between different feed strategies based on NB flow in the reactor is given in Table 1. The temperature and molar profiles of scenarios 1, 2 and 3 are shown in Fig. 5 (top), (center) and (bottom), respectively.
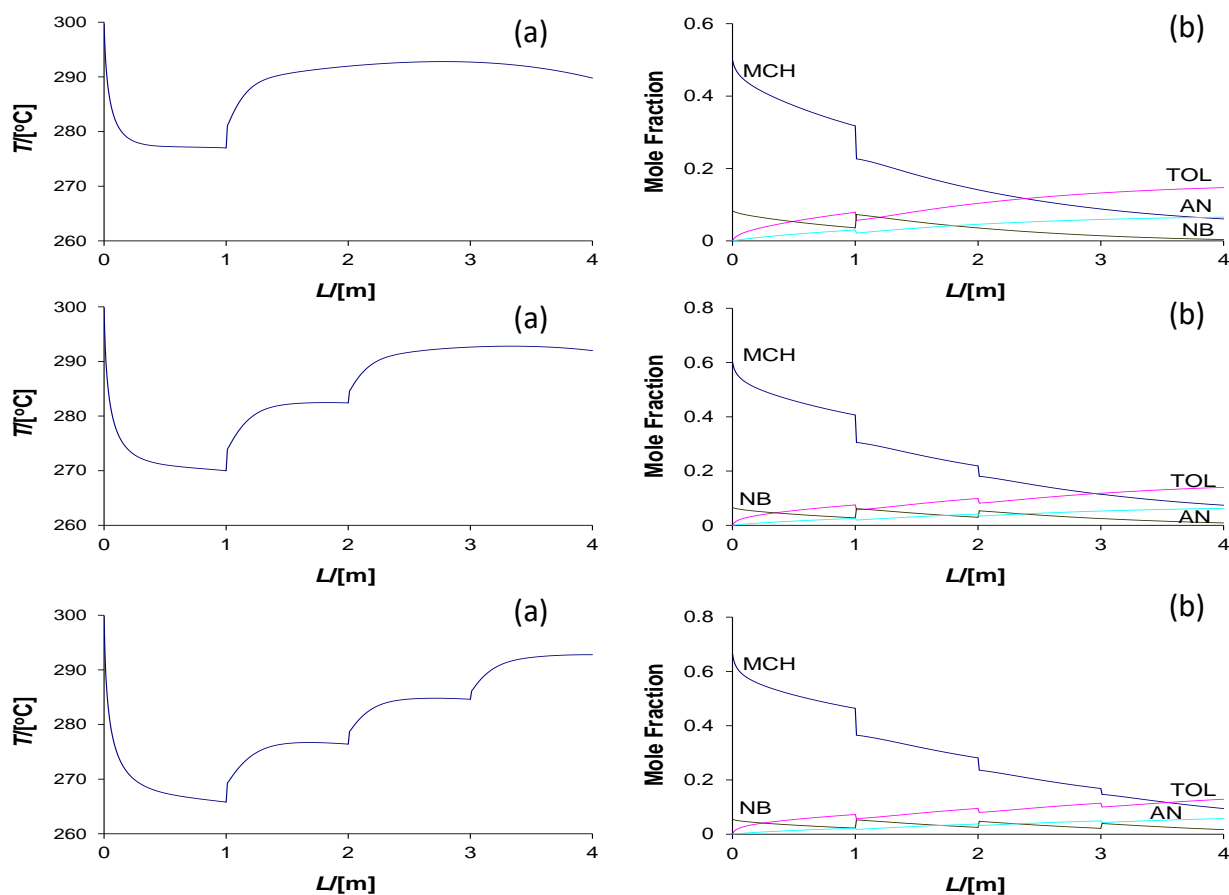
Figure 5. (a) Temperature, (b) Molar profiles (Top) 50% of NB is fed in first two reactors, (Center) 33% of NB in three reactors, (Bottom) 25% of NB in four reactors
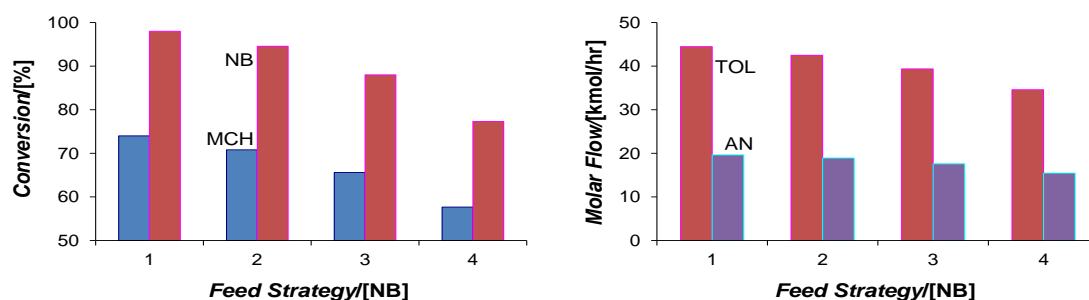
Figure 6. Comparison b/w NB feed flow strategies

It is evident from the results given in Fig. 6 that the conversion of MCH and NB decreases from 74% to 57% and from 98% to 77%, respectively, as NB feed flow is disintegrated.

Case 2

In the first scenario, when feed was divided in the first two reactors, the temperature increased up to 350 ºC by the end of the first quarter of the reactor. As more MCH entered in the system the temperature profile started becoming linear when the heats of reaction started balancing each other. Maximum production of toluene was achieved in the first quarter and then conversion of both reactants was smooth along the reactor length. In the second scenario, MCH to NB ratio was (1:1) so due to the highly exothermic hydrogenation reaction a step-wise increase in temperature was observed and the temperature shot up to 690 ºC. Similar behavior was observed in the third scenario where the highly exothermic reaction increased the temperature up to 780 ºC and then the temperature decreased along the reactor length. In the second and third scenarios maximum conversion of reactants occurred in the first part of the reactor due to improper reactants ratio. In addition to the difficulty to control the reactor conditions sudden high temperature rise will cause damage to the catalyst. The temperature and molar profiles of all scenarios are shown in Fig. 7 (top), (center) and (bottom), respectively. Comparison between different feed strategies based on conversion is given in Table 2. From the results presented in Fig. 8, conversion of MCH to TOL and NB to AN slightly increased from 74% to 78% and 98% to 100% respectively, as MCH feed flow was disintegrated. On the other hand, as the total

reactants conversion was completed in the first quarter of the reactor (1 m), so a sharp increase in temperature led to hot spotting and catalyst deactivation.

It is evident from the results given in Fig. 8 that the conversion of MCH and NB decreases from 74% to 57% and from 98% to 77%, respectively, as the NB feed flow is disintegrated. In this work, four different possible feed strategies were compared to figure out the best strategy in terms of product yield. From all presented data it is clear that to maximize reactants conversion, both reactants should be fed completely together at the first reactor inlet. Linear and controlled temperature profiles were also achieved as an additional benefit which reduces hot spots and resists catalyst deactivation. The results achieved in this study may replicate in chemical processes of practical relevance.

CONCLUSION

Coupling exothermic nitrobenzene hydrogenation with endothermic MCH dehydrogenation is feasible with benefits of simpler chemical reactor, minimum heating/cooling requirement and direct hydrogen utilization which reduce hydrogen recycling cost. After analyzing four different possible feed strategies for each case (nitrobenzene and methyl-cyclohexane), the best strategy found in terms of product yield is to feed both the reactants completely together at the first reactor inlet. The conversion was 74% for MCH dehydrogenation and 98% for NB hydrogenation. Linear temperature profile which reduces hot spots and resists catalyst deactivation was also achieved as an additional benefit.
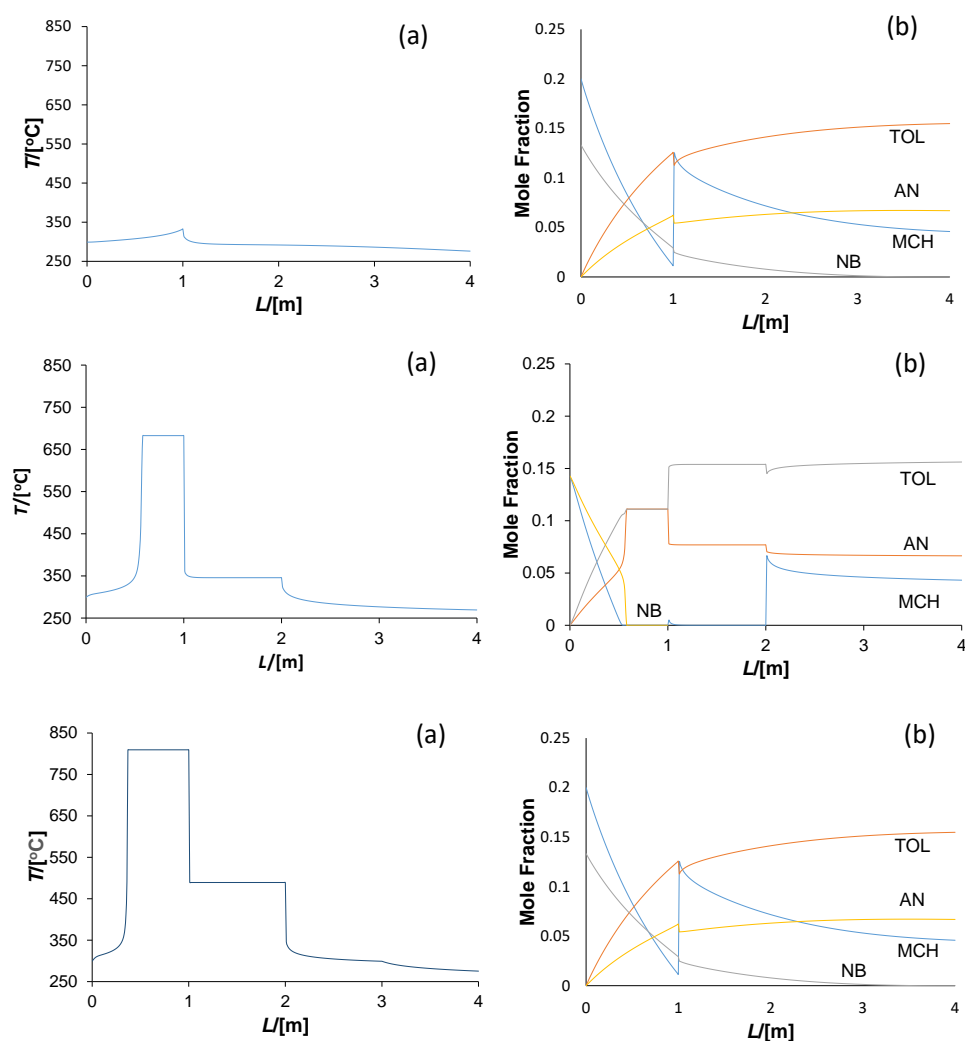
Figure 7. (a) Temperature, (b) Molar profiles (Top) 50% of MCH is fed in first two reactors, (Center) 33% of MCH in three reactors, (Bottom) 25% of MCH in four reactors

Table 2. Comparison b/w MCH feed flow strategies

Description/MCH Feed Strategy	1	2	3	4
	100%	50%	33%	25%
Temperature R_{out} (°C)	286.4	276.2	269.4	275.3
Pressure (bar)	1.5	1.5	1.5	1.5
Feed (kmol/h)				
MCH	60	60	60	60
H_2	100	100	100	100
NB	20	20	20	20
Product (kmol/h)				
MCH	15.533	13.709	13.006	13.622
TOL	44.467	46.209	46.995	46.378
H_2	174.519	178.865	180.977	179.129
NB	0.373	--	--	--
AN	19.627	20	20	20
H_2O	39.255	40	40	40
Conversion (%)				
MCH	74	77	78.32	77.30
NB	98	100	100	100
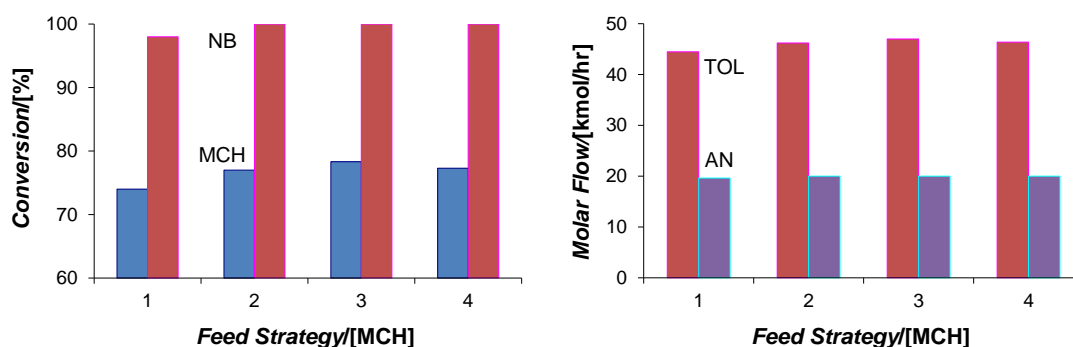
Figure 8. Comparison b/w MCH feed flow strategies

REFERENCES

1. F. Friedler, *Appl. Therm. Eng*., **30**, 2270 (2010).
2. G. Towler, S. Lynn, *Chem. Eng. Sci*., **49(16)**, 2585 (1994).
3. R. Smith, *Appl. Therm. Eng*., **20(15-16)**, 1337 (2000).
4. P. Altimari, C. S. Bildea, *Ind. Eng. Chem. Res*., **47(17)**, 6685 (2008).
5. R. Grasselli, D. Stern, J. Tsikoyiannis, *Appl. Catal. A: Gen*., **189(1)**, 1 (1999).
6. D. Henning, L. Schimdt, *Chem. Eng. Sci*., **57(14)**, 2615 (2002).
7. K. H. P. Reddy, R. Rahul, S. S. V. Reddy, B. D. Raju, K. S. R. Rao, *Catal. Commun*., **10**, 879 (2009),
8. M. R. Rahimpour, M. R. Dehnavi, F. Allahgholipour, D. Iranshahi, S. M. Jokar, *App. Energy*, **99**, 496 (2012).
9. C. V. Pramod, C. Raghavendra, K. H. P. Reddy, G. V. R. Babu, K. S. R. Rao, B. D. Raju, *J. Chem. Sci.*, **126(2)**, 311 (2014).
10. A. Javaid, C. S. Bildea, *Int. J. Chem. Eng. Appl.*, **8(4)**, 267 (2017).
11. A. Javaid, C. S. Bildea, *Asia-Pac. J. Chem. Eng*, **13(4)**, 1 (2018).
12. A. Javaid, C. S. Bildea, *Studia UBB Chemia*, **LXV, 1,** 205 (2020).
13. A. Javaid, C. S. Bildea, *Chem. Eng. Technol*., **37(9)**, 1515 (2014).
14. A. Javaid, C. S. Bildea, *Period. Polyteh. Chem. Eng.*, **58(2)**, 165 (2014).
15. A. Javaid, C. S. Bildea, *U.P.B. Sci. Bull., Series B*, **76(3)**, 33 (2014).
16. P. Octavian, V. van der Last, C. S. Bildea, P. Altimari, *Chem. Prod. Process Model.*, **4(5)**, Article 19, 1 (2009).
17. R. C. Ramaswamy, PhD Thesis, Sever Institute of Washington University, Saint Louis, USA, 2006.
18. ASPENTECH, Aspen Plus Getting Started Building and Running a Process Model, ASPEN Technology, Burlington, 2010.
19. D. N. Rihani, T. K. Naraynan, L. K. Doraiswamy, *Ind. Eng. Chem. Proc. Des. Dev*., **4(4)**, 403, (1965).
20. G. Maria, A. Marin, C. Wyss, S. Muller, E. Newson, *Chem. Eng. Sci*., **51(11)**, 2891 (1996).

Comparison study of the properties of kerosene-naphthalene blends with turpentine

A. Mushtaq[1*], R. Muhammad Khan[1], Z. Uddin Ali[2], A. R. Ali Khan[1], M. Mazhar-ul-Haque[1], T. Ali[1], M. Sharyar Khan[1]

[1]Polymer and Petrochemical Engineering Department, NED University of Engineering & Technology, Karachi, Sindh, Pakistan

[2]Chemical Engineering Department, NED University of Engineering & Technology, Karachi, Sindh, Pakistan

Blending of kerosene with naphthalene to improve the properties of turpentine is the chief objective of this research. Through blending the cost of turpentine will be reduced by around 20 to 30% of its actual price. Kerosene and naphthalene are only used for blending whereas turpentine is used for comparison. The blending process was carried out using a hot plate magnetic stirrer. Distinct wt. % of naphthalene was measured and inserted into the calculated wt. % of kerosene. Different tests were performed for comparing the properties of blend and pure turpentine. Flash point of the blend exactly corresponds to that of turpentine whereas the boiling point is deflecting from the boiling point of turpentine. This blend cannot exactly replace turpentine but further research and delving can make it more comparable with turpentine.

Keywords: Blending; kerosene; naphthalene; turpentine; flashpoint; boiling point; fluorescent indication.

INTRODUCTION

Kerosene, turpentine and naphthalene are the materials required for preparing blends of kerosene and naphthalene. The properties of the blends were compared with the properties of turpentine. This research is a step towards synthetic turpentine, which will yield a cost-effective solution.

Paint is a viscous form of material that needs thinning for easy coating on the wall. Turpentine is one of the few means of thinning paint [1, 2].

Turpentine oil is made of the resin of certain pine trees, having 75-90 wt. % of resin and 10-25 wt. % of oil. Turpentine is a mixture of Turpen and essential oil which vary in wt. % based on geographical location, tree species and distillation process. It is also used in soap, cosmetics, and medicine (but it is unsafe when taken by mouth or used over a large area of skin). Recently, fragrant chemical compounds are synthesized, in which turpentine is used as a raw material. The expense of distilled turpentine is much higher than that of its alternates. Mineral spirits solvent or acetone is an inexpensive, petroleum-based replacement for turpentine [3, 4].

In this research, the blend between kerosene and naphthalene (mock ball) is to get the properties of turpentine most cheaply. As like dissolves like an expression used to show how solvents work on polarity.

Kerosene, like naphthalene, is non-polar. This means that naphthalene is dissolved in kerosene and their blend is possible. A magnetic stirrer was used to prepare the blend at room temperature. To measure the properties different testing equipment

were used (flash point, boiling point, fire point and others) of blends of different composition. However, this method of fabricating turpentine is time-consuming. In industry, a different mixing system is used which is brisk and efficient. For example, a turn-key liquid mixing system consists of tanks, control, and top- or bottom-mounted mixers. These mixing modules are designed to blend, dissolve, hydrate, emulsify, and homogenize powders into liquids.

Turpentine

Turpentine is obtained by distillation of gum resin from pine trees, called oleoresin. The word turpentine derives from the Greek word terebinthine meaning 'feminine of resin'. Turpentine oil is used in medications, paints, perfumes, food additives, household cleaning agents and insecticides. It is also a cure of skin aging. Hippocrates used turpentine against lung diseases and other [5, 6]. Pine is having five species that make Turkey a dominating conifer area. Figure 1 shows tapping of exudates from pine trees.

Fig. 1. Tapping of exudates from pine trees

* To whom all correspondence should be sent:
E-mail: engrasimmushtaq@yahoo.com

Pine oleoresin is gained by bark tapping (chips obtained from pine trees) and the collection of exudates of forestry products. The structure of alpha-pinene is given in Figure 2. Acidic and neutral di-turpentine together give a complicated mixture having volatile compounds. Turpentine collected from different forests was having different percentage of constituents [7, 8].
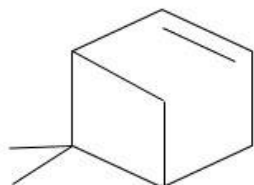

Fig. 2. Structure of alpha-pinene, a major component of turpentine.

Turpentine unit of active resins-dissolved semi-fluid substances associated with very volatile oil is separable by various distillation techniques into a volatile portion referred to as turpentine oil and a non-volatile portion called rosin. It is originally stated that complete oleo resin exudates change in a very extreme way the turpentine fraction (that has different uses in business and assortment of the ensuing exudates, and is a crucial biology product). Acidic and neutral di-turpentine in a mixture having volatile compounds (mono- and sesquiterpenes) compose the oleoresins [9, 10].

Steam distillation is employed to convert the mixture into gum turpentine (volatile compounds) and gum rosin (di-terpenes). Steam distillation is a special style of distillation (a separation process) for temperature-sensitive materials like natural aromatic compounds. It was a well-liked laboratory methodology for purification of organic compounds, which, although of diminished use, thanks to the proliferation of vacuum distillation and steam distillation, remains important in certain industrial sectors.

Many organic compounds tend to decompose at high sustained temperatures. Separation by distillation at the traditional (1 atmosphere) boiling points isn't a possibility. The little amounts of the volatile compounds are conveyed by vapor to the condensation flask, wherever the condensed-liquid part separates and permits fluent collection. This method effectively allows distillation at lower temperatures, reducing the deterioration of the specified product. If the substances to be distilled are sensitive to heat, steam distillation is also applied under reduced pressure, thereby reducing the operative temperature.

After the distillation the vapors are condensed. Normally, the instant product is also a two-phase system of water and organic liquid, permitting discriminating of the parts by decantation, portioning or appropriate alternative ways. The bottom-most is cheaper. But the maximum use of turpentine oil is at present in the chemical industry, as a raw material in the manufacturing of resins, insecticides, oil additives, synthetic pine oil and camphor. Turpentine oil is also used as a rubber solvent in the synthesis of plastic products [11, 12].

Turpentine is also being used by experimentation for the handling of MS and sexual dysfunctions. It is also being studied for its actions to prevent drug activity and inhibition of bone cell activity. Turpentine is used in scientifically experimented models of inflammation to induce general inflammation that is not capable of being affected in animals.

Naphthalene

Naphthalene ($C_{10}H_8$) is made from coal tar or crude oil. Naphthalene is a white solid polycyclic hydrocarbon. It is produced by burning of cigarettes, car smoke and also during forest fires. It is used as an insecticide pest repellant, first registered as a pest repellent in the USA in 1948. Naphthalene is obtained by distillation from either coal tar or petroleum. It is used to manufacture phthalic anhydride and is also used in moth repellents as shown in Figure 3. It is a white crystalline volatile solid which sublimes at room temperature. Naphthalene is water-insoluble and is soluble in C_6H_6, hydro-naphthalene, absolute EtOH, CCl_4, CS_2 and in fixed volatile oils. It is a component of naturally produced crude oil and is also produced by natural uncontrolled combustion. It is non-polar [3, 13].

Fig. 3. Commercial grade of naphthalene (mothballs)

The molecular structure shows a fused pair of benzene structures, as shown in Figure 4. By and large, naphthalene is used as a controller of the clothes moth. In this usage, the naphthalene vapor fills the airtight container and kills the insects. Naphthalene is metabolically actuated by the body. Different tissues produce different metabolites, which is ultimately leading to specific site toxicity. Naphthalene is a non-polar solute. Hence, it dissolves in kerosene which is a non-polar solvent.

47

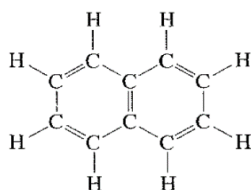Naphthalene doesn't dissolve in water which is a polar solvent.

Fig. 4. Structure of naphthalene.

Kerosene

Kerosene is a flammable liquid used in industries for light and fuel heat/ power. Kerosene is used for making wax and other viscous and non-viscous substances. It is also called paraffin or kerosene derived from the Greek word Keros meaning 'wax'. It was first discovered by the Persian scholar Raazi. Kerosene is obtained by fractional distillation from the crude oil giving a thin oil which is roughly 0.81 g/cm^3. It is extracted at a temperature between 150-275 °C. It has a non-polar nature. Consumption of crude around the world is 12 million barrels per day; 1 barrel is 45 gallons or 205 liters [14, 15].

Kerosene is obtained by crude oil distillation and it is heavier than naphtha. It may also be obtained by catalytic cracking or hydrocracking but is usually less stable than that obtained by the atmospheric distillation process because of the presence of olefinic constituents. It is a colorless liquid that does not stop flowing until temperature drops below -30ºC, due to this reason kerosene is blended with diesel to increase the efficiency of vehicle mobility in cold regions. In old days it was used as a lamp fuel but now it is used as a jet fuel after adjusting its freezing point and burning quality and is classified as JP1, JP2, JP3 and JP4. It is also used as a cleaning agent and is used in many industries for removing lubricants before re-lubrication [16, 17].

Blends

Blending is a unit operation in which two or more components in an unmixed or partially mixed form are treated in such a way that the components lie as nearly as possible in contact with each other. Blending may aim a change in the physical state of components and properties of the materials are shown in Table 1. Jet fuels are made by blending of naphtha, gasoline, or kerosene to meet specific military or commercial specifications. JP-4 is a blend of kerosene with lower boiling distillates. JP-7 is a blend of kerosene distillates with a maximum of 5% aromatics by volume and a maximum total weight of 0.1% sulfur. In case of dissolving a solid in a solvent the process is too slow and for fastening a process agitator is used. In this research, as turpentine is an expensive material and not easily available but used on a large scale in paint and many industries, a blend of naphthalene and kerosene was studied to achieve properties of turpentine which will reduce the cost of the raw material. It was calculated to make a blend of different compositions of 5wt. %, 10wt. %, 15wt. %, 20wt. %, 25wt. %, and 30wt. % of naphthalene in kerosene. By comparing the properties of different refined products, naphthalene and kerosene were found to be closer to turpentine. Both kerosene and naphthalene are non-polar and miscible with turpentine [3, 18-20]. Turpentine is used as a paint thinner for reducing the viscosity of the paint. However, turpentine is very expensive and not easily available while this blend will be of low cost owing to the ease in availability of raw material and ease in the process. Therefore, it will be highly effective for the paint industry and it will reduce around 2/3 of the cost of turpentine [21, 22].

Table 1. Properties of the materials

Properties	Kerosene	Naphthalene	Turpentine
Molecular weight (g/mol)	185	128.16	136
Boiling point, ºC	175 to 325	217.9	150 to 180
Melting point, °C	-48 to -26	80	-55
Flash point, ºC	40-65	88	38
Density, g/cm^3	0.77 to 0.81	1.16	0.86 to 0.9
Autoignition temperature, ºC	220	540	300-330
Molecular formula	C$_9$ to C$_{16}$ hydrocarbons	C$_{10}$H$_8$	C$_{10}$H$_{16}$

METHODOLOGY

Chemical blending is a process in which different chemicals may be liquid or powder, inorganic, or organic blended. Blended substances have various chemical and physical properties to achieve blends of combined or mixed constituents so the constituents are indistinguishable. By blending a product is changed to meet a specification, dilute contamination to insignificance and make a new product. There are two main classes of components in a blend – blend stocks and additives.

Blend stocks

Major components are referred to as blend stocks. They make up a significant part of the blend, generally measured in percentage terms – e.g. 1 wt. %, 10 wt. %, 20 wt. %, 50 wt. %. In this research kerosene and naphthalene were used as the blend stock. The percentage of naphthalene was 5 wt. %, 10 wt. %, 15 wt. %, 17.5 wt. %, 20 wt. %, 25 wt. %, and 30 wt. %. This percentage assigns the main characteristics to the blend. Naphthalene may be introduced as a blend stock into kerosene to affect the properties of turpentine. Blend stocks must produce the required specification in the mixture across a variety of parameters of quality. They must be an economical choice for the production of the required product. So in this project the achieved property of turpentine is the cost of 200 Pkr/L whereas, turpentine can be bought at the rate of 1000 Pkr/L. They must be compatible, so that the mixture is stable, in this research 10 wt. % of naphthalene can be dissolved in kerosene so it must be stable at 10% solubility.

Additives

Additives are substances that can be added to a blend to modify its performance. They are generally used in very small amounts, often measured in parts per million. In this research there are no additives, only a blend stock is used. In experience there are four main classes of problems that arise in making petroleum blends as compatibility and stability issues. Blend design does not perform as mathematically predicted blends not being properly mixed and there is lack of quality reserve.

Blending processes

The research to improve the properties of kerosene by naphthalene or synthesis of turpentine by making a blend between kerosene and naphthalene powder involved four separate tasks. The apparatus used for the blending procedure included beaker, conical flask, hand chopper, Duran bottle, funnel and magnetic stirrer. This blend is consisting of kerosene and naphthalene powder. Make powder of mock ball by a hand chopper for perfect mixing. Weigh naphthalene powder (mock ball powder) according to the calculation. According to requirement there is 5 wt.%, 10 wt.%, 15 wt.%, 17.5 wt.%, 20 wt.%, 25 wt.%, 30 wt.% of naphthalene in 100 ml of solution. The 17.5 wt.% in 100 ml solution is the volume of solute 17.5 ml, the density of solute 1.14 g/ml, the mass of solute 19.95 g, the volume of solvent 82.5 ml and 19.95 g of naphthalene added into 82.5 ml of solution for making this blend. Put naphthalene powder into the Duran bottle using a spatula. Convert the volume of kerosene into mass by density. Weigh mass of kerosene according to the calculation and mix with naphthalene powder into the Duran bottle using a magnetic stirrer. Provide electricity and activate the apparatus for the test. Without any heat mix the kerosene and naphthalene up to six hours at room temperature. Remove the blend from the magnetic stirrer. Detach the magnetic beat from the bottle with the help of a forceps. Filter through filter paper in order to remove undissolved naphthalene from the liquid. Figure 5 shows the blend ready for further testing.

Fig. 5. Blend of kerosene and naphthalene.

Characterization testing

After filtration the sample is ready for testing the properties of the blend. The following results show many comparable properties of the blend with turpentine.

Flash point test. Flash point is the lowest temperature at which the material emits sufficient to form a combustible mixture with air. There are two approaches to doing the flash point test. An open cup flash point test is conducted in an open environment with complete access to air to interact with the sample. It is the most practical phenomenon because most of the substances are being stored in an open environment where the air has clear access to contact with the substance stored. A closed cup flash point test is conducted in a closed vessel which is not open to the environment. In the present research the sample was tested in the Pensky-Martens flash point

test apparatus with ASTM D-56 in a closed cup flash point test apparatus.

Boiling point test. The boiling point is the most basal physical property of an organic compound. There are several methods for estimating the boiling point of a chemical compound, such as distillation method, reflux method, Thiele tube method. In this research, all the samples were tested by the Thiele tube method.

Pour point test. Pour point is the temperature below which the liquid loses its flow characteristics. In this study, all pour tests were performed by inserting the sample into a cooling bath according to ASTM D-97. No results were found even at -40ºC which is clear evidence that the pour point must be beyond -40ºC.

Density. Density is the ratio between the mass of the sample and the volume. In this study, density was measured using an RD-bottle which has a constant volume of 100 ml. Insert the sample of 100 ml blend and measure the weight of the sample. By dividing both of them density can be determined.

Aniline test. Aniline point is the temperature at which aniline ($C_6H_5NH_2$) and the sample are miscible and form a single phase. This value tells the number of aromatic compounds present in the sample because aniline itself is an aromatic compound. The higher the aniline point, the lower is the amount of aromatics present in the sample. In this study, the sample was tested according to ASTM D-611. For aromatic oil with 75% aromatic content, the aniline point would be around 50. In this research, the aniline point of the blend was 51.5 which means 75% aromatic content present in the sample.

Fluorescence indicator test. This test was performed to check the amount of paraffin, olefin and aromatic compounds present in the sample. Different colors were observed at different levels of the tube by which the amounts of paraffins, olefins and aromatics can be calculated through a formula.

pH Test. pH is the measure of hydrogen ions present in the solution. It is a figure indicating the nature of the sample either acidic or alkaline. Low values are acidic and high values are alkaline. Pure water has a pH of exact 7.

RESULTS AND DISCUSSION

Flash point, boiling point, pour point, density, aniline, fluorescence indicator and pH testing results show the comparable properties of the blends with turpentine.

Flash point

The flash points of kerosene and turpentine (52 and 44 ºC, respectively) are shown in Figure 6. All samples made were then tested for flash point at 5, 10, 15, 20, 25, 30 wt.% and showed that the required results were obtained at 17.5 and 15 wt. %. Samples in wt. % were compared with the properties of turpentine as shown in Figure 7.
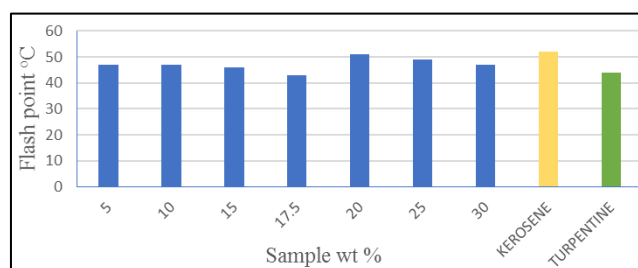

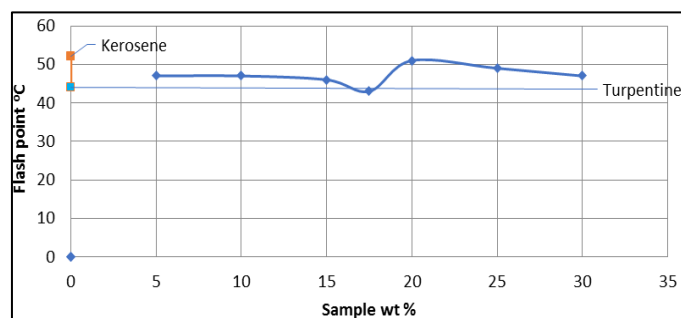**Fig. 6.** Comparison of flash points of pure kerosene, turpentine and blends

Fig. 7. Graphical representation of flash points of kerosene, turpentine and blends
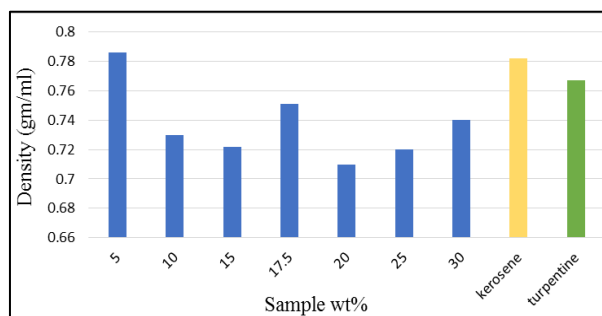
Fig. 8. Comparison of densities of kerosene, turpentine and blends.

From the above results it was concluded that the flash point of a sample changes as the amount of naphthalene changes in the blend because there is a change in blend composition. After all, flash point depends on the molecule structure. As naphthalene is added in kerosene the molecular mass of the blend decreases and this causes an increase in vapor pressure. Vapor pressure indicates the substance volatility and it shows the strength of interaction forces between the molecules. So, when the temperature increases there is an increase in vapor pressure and this causes a decrease in the flash point [13, 18].

Density

Figure 8 shows the density test of the samples. The density of kerosene is 0.782 g/ml and that of turpentine is 0.767 g/ml. Densities of the samples were determined at 5, 10, 15, 20, 25, 30 wt. % of naphthalene and showed that the required results were obtained at 17.5 and 15 wt. %. The trend of the densities was plotted against different wt. % of naphthalene blended.

From the above results it was concluded that as naphthalene quantity in kerosene increases, the density increases. As the density of the material is affected by one factor, namely, how atoms are arranged in a certain volume or the concentration of atoms in a volume, this indicates the molecule structure of a material. As the density of naphthalene is high as compared to kerosene because naphthalene is a solid, the molecules are tightly packed to each other and there is no space between the molecules in a given volume while the density of kerosene is lower because it is a liquid, which means that there is a space between molecules which are not tightly packed and have less intermolecular forces. It shows that the molecular structure also affects density [8, 21].

pH

Initially, the pH of the pure samples of kerosene and turpentine was calculated, which showed kerosene as a basic product and turpentine with acidic nature. Figure 9 shows the 17.5 and 15 wt. %

naphthalene samples tested along with the pure samples of kerosene and turpentine. The sample with 17.5 wt. % was found neutral and that with 15 wt. % acidic. As an aromatic hydrocarbon, naphthalene's structure consists of a combined pair of benzene rings. In that way, naphthalene is named a benzenoid polycyclic aromatic hydrocarbon. The eight carbons that are not shared by the two rings convey one hydrogen atom each. The particle is planar, similar to benzene. In contrast to benzene, the carbon-carbon bonds in naphthalene are not of a similar length. In electrophilic aromatic substitution responses, naphthalene responds more promptly than benzene. The selectivity for alpha over beta substitution can be explained as far as the resonance structures of the moderate: for the alpha substitution intermediate, seven resonance structures can be drawn, of which four protect an aromatic ring. For beta substitution, the moderate has six resonance structures, and just two of these are aromatic. Protonated cations of naphthalene ($C_{10}H_{+9}$) are a part of the range of the Unidentified Infrared Emissions (UIRs). Protonated naphthalene differs from impartial naphthalene in that it has an extra hydrogen atom [16, 18].

Boiling point

Figure 10 shows that the boiling point of the sample is increasing concerning the increment of wt. % of naphthalene in the blend. The boiling point of a substance gives the strength of intermolecular forces and to break these strong intermolecular forces it is required to increase the kinetic energy which can only be done by the increase of its temperature. The boiling point is affected by molecule size, presence of a functional group, number of carbon atoms and degree of branching and types of intermolecular bonding. As the amount of naphthalene in kerosene increases, the boiling point increases because the molecule size increases as there are more nuclei and electrons in the large molecule that create intermolecular force and this causes an increase in density and an increase in boiling point [5, 8].
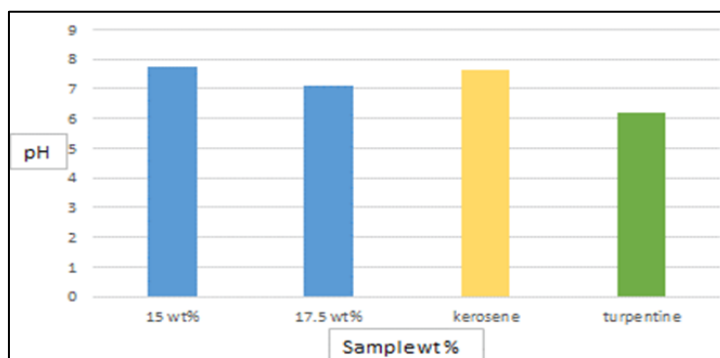
51

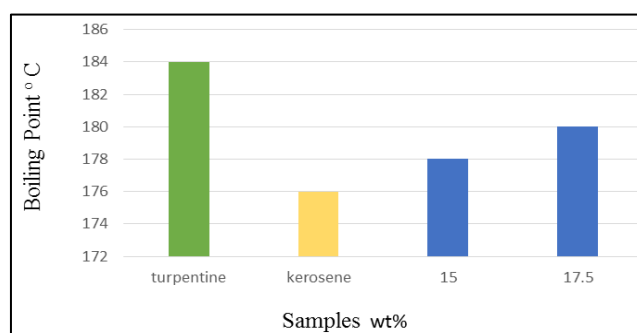**Fig. 9.** Comparison of pH values of kerosene, turpentine and blends

Fig. 10. Comparison of boiling points of kerosene, turpentine and blends

Table 2. Results of fluorescent indicators for turpentine and blends

Property	Minimum length, mm	Maximum length, mm	Length, mm	Total length, mm	Length/Total length, %
For turpentine					
1st reading					
Olefins (blue) %	365	415	50	65	76.92
Saturated (yellow) %	415	430	15		23.07
2nd reading					
Olefins (blue) %	470	520	50	69	72.46
Saturated (yellow) %	525	544	19		27.53
For 15 wt.% blend					
1st reading					
Aromatic (red) %	651	664	13		15.4
Olefins (blue) %	664	714	50	84	59.5
Saturated (yellow) %	714	735	21		25
2nd reading					
Aromatic (red) %	730	745	15		17.6
Olefins (blue) %	745	797	52	85	61.2
Saturated (yellow) %	797	815	18		21.2
For 17.5 wt.% blend					
Aromatic (red) %	642	660	18		20.93
Olefins (blue) %	660	715	55	86	63.95
Saturated (yellow) %	715	728	13		15.11
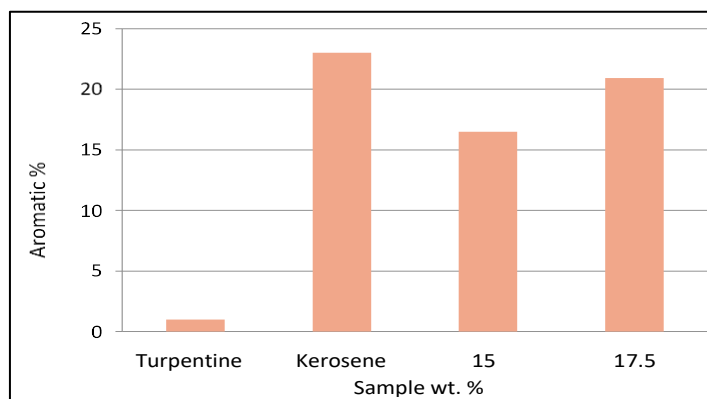
Fig. 11. Percentage of aromatics in turpentine, kerosene and blend
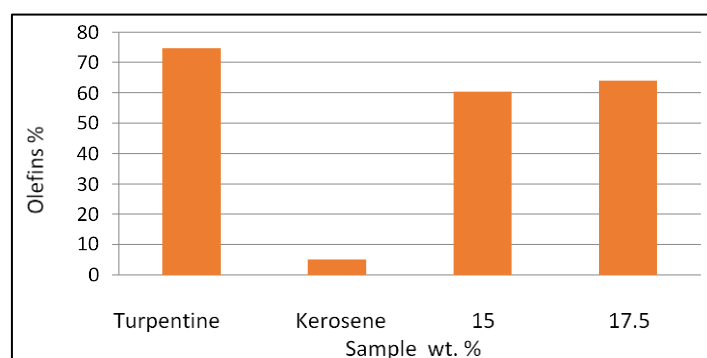
Fig. 12. Percentage of olefins in turpentine, kerosene and blend
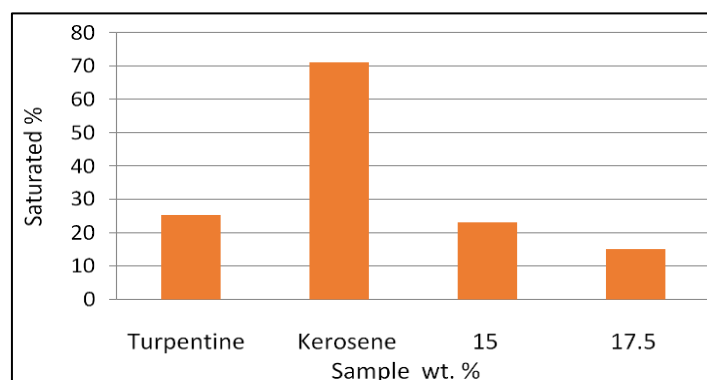
Fig. 13. Percentage of saturated hydrocarbons in turpentine, kerosene and blend

Fluorescent indicator

Cyclic terpenes are another significant wellspring of inexhaustible phenols. Even though not as rich as lignin, normally happening terpenoids, including p-cymene, α-and β-pinene, are promptly accessible as turpentine. Naphthalene was inspected as a fuel-added substance to liquor during a whirl combustor to get conservative consuming and ultra-low outflow exploitation entirely unexpected warming value powers. Naphthalene is a poly-fragrant compound frequently viewed as a waste fuel that outcomes in large amounts of contamination outflow. The viability of a hydrocarbon as a fuel-added substance to liquor on NO and CO discharges and soundness was harmless [3, 5, 8, 13, 18].

The above experiment shows the amounts of aromatic hydrocarbons, olefins and saturated hydrocarbons present in the blends. It shows that naphthalene is a polycyclic hydrocarbon (having double benzene rings) and it contains more aromatic hydrocarbons and olefins as compared to kerosene in which saturated hydrocarbons are present in high quantity followed by olefins. As naphthalene amount in kerosene increases to form the required blend the naphthalene rings break and on one ring of naphthalene the kerosene group is attached as a side group and thus it contains less aromatics and more olefins [6, 12, 15, 17].

It was concluded that the blend of kerosene with 17.5 wt.% of naphthalene was showing properties near to those of turpentine and could be used as an

alternative for it. The study also included flash point, boiling point, fluorescent indicating, density and pH tests of kerosene and our blends.

CONCLUSION

In this research, blends of naphthalene and kerosene were made to achieve the properties of turpentine used in the paint industry for reducing the viscosity of paint for better coating and fabrication. The results showed that on increasing the amount of naphthalene the flash point of the blend is decreasing. It was observed that at 17.5 wt. % the flash point of the blend was exact 43 ℃, the same as turpentine. The boiling point temperature of the 17.5 wt. % blend was 180 ℃ and that of turpentine was 184 ℃. The fluorescent indicator test revealed the quantity of olefins, aromatics and saturates present in the blends, turpentine and kerosene. The results showed that turpentine had 2 % of aromatics 74% of olefins and 26 % of saturated hydrocarbons. Blend of 17.5 wt. % had 20.93 % of aromatics, 63.95% of olefins and 15.11% of saturates. The density of turpentine was 0.767 g/ml and that of the sample with 17.5 wt. % was 0.751 g/ml, just close to the required. The pH of turpentine was 7.66 and that of the 17.5wt.% blend was 7.16. The future recommendation for this study is to perform a liquid FTIR study to get a know-how of the mechanism going inside it. Few additives could also enhance its properties.

REFERENCES

1. J. Calder, M. M. Roy, W. Wang, *Energy*, **149**, 204 (2018).
2. R. Toche, S. Borade, M. Malve, B. More, *Chem. Sci. Trans.*, **4**, 975 (2015).
3. S. M. A. Uddin, A. K. Azad, M. M. Alam, J. U. Ahamed, *Procedia Eng.*, **105**, 698 (2015).
4. J.S. Feser, G. Bassioni, A.K. Gupta, *Appl. Energy*, **216**, 1 (2018).
5. U. Rajak, P. Nashine, T. S. Singh, T. N. Verma, *Energy Convers. Manage.*, **156**, 235 (2018).
6. P. Dubey, R. Gupta, *Renewable Energy*, **115**, 1294 (2018).
7. H. L. Birks, A. R. Cochran, T. J. Williams, G. P. Jackson, *Forensic Chem.*, **4**, 32 (2017).
8. K. Loganathan, C. Manoharan, *Therm. Sci.*, **21**, 615 (2017).
9. H. Zhou, Q. Luo, Q.-T. Gong, Z.-Y. Liu, M. Liu, L. Zhang, L. Zhang, S. Zhao, *Colloids Surf. A Physicochem. Eng. Asp.*, **520**, 561 (2017).
10. C. İlkılıç, E. Çılğın, H. Aydın, *J. Energy Inst.*, **88**, 292 (2015).
11. P. Verma, M.P. Sharma, G. Dwivedi, *Energy Rep.*, **2**, 8 (2016).
12. H. T. Alkasasbeh, M. Z. Swalmeh, A. Hussanan, M. Mamat, *CFD Lett.*, **11**, 70 (2019).
13. A. F. Santos, J. A. Oliveira, M. D. Ribeiro da Silva, M. J. Monte, *Chemosphere*, **146**, 173 (2016).
14. M. Anand, S. A. Farooqui, R. Kumar, R. Joshi, R. Kumar, M. G. Sibi, H. Singh, A. K. Sinha, *Fuel Process. Technol.*, **151**, 50 (2016).
15. H. Bayındır, M. Z. Işık, Z. Argunhan, H. L. Yücel, H. Aydın, *Energy*, **123**, 241 (2017).
16. S. R. M. Ibrahim, G. A. Mohamed, *Phytochem. Rev.*, **15**, 279 (2015).
17. J. K. Kumar, C. S. Raj, P. Gopal, P. S. Kumar, *Int. J. Chem. Sci.*, **14**, 1307 (2016).
18. Y. Choi, J. Lee, J. Shin, S. Lee, D. Kim, J.K. Lee, *Appl. Catal. A-G.l*, **492**, 140 (2015).
19. D. García, F. Bustamante, A. L. Villa, M. Lapuerta, E. Alarcón, *Energy Fuels*, **34**, 579 (2019).
20. L. Handojo, I. A. Putra, M. M. Azis, T. Prakoso, T. H. Soerawidjaja, A. Indarto, *AIP Conf. Proc.*, **2085**, 1 (2019).
21. K. F. Sheberstov, V. A. Chertkov, *Russ. Chem. Bull.*, **64**, 794 (2015).
22. F. L. Wang, H. M. Ji, J. Y. Zhu, G. J. Xu, Y. Z. Guan, Y. J. Chen, *Trop. J. Pharm. Res.*, **14**, 1341 (2015).

Determination of imidacloprid, cypermethrin and chlorpyrifos ethyl in water samples using high-performance liquid chromatography

V. V. Mihaylova[1,2*], B. R. Todorov[1,2], V. V. Lyubomirova[1,2], R. G. Djingova[1,2]

[1]Trace analysis laboratory, Faculty of Chemistry and Pharmacy, University of Sofia, 1, J. Bourchier blvd, 1164-Sofia, Bulgaria
[2]Center of Competence "Clean technologies for sustainable environment – water, waste, energy for circular economy", Sofia, Bulgaria

A high-performance liquid chromatography method is developed and validated for determination of imidacloprid, cypermethrin and chlorpyrifos ethyl in water samples. Separation is performed with a chromatographic column C18 (Microsorb-MV, 100-5, C18, 150 × 4.6 mm) using a mobile phase consisting of methanol/water (70:30, v/v) at a flow rate of 0.5 mL min^{-1} and UV detection at 205 nm. The method exhibits good linearity in the range of 1-1000 μg L^{-1} for the analyzed pesticides. The percentage recovery of the method at three concentration levels (10, 100, and 1000 μg L^{-1}) is within 98.6 to 101.6% for the three pesticides. The limit of quantification is low (0.51, 1.20 and 1.50 μg L^{-1} for imidacloprid, cypermethrin and chlorpyrifos ethyl, respectively) which enables their determination in water samples at low concentration levels. A stability test of imidacloprid, cypermethrin and chlorpyrifos ethyl was also performed to predict their stability in surface water under variation of ambient temperature.

Keywords: Pesticides, Water samples, Stability test, HPLC-DAD.

INTRODUCTION

Pesticides are useful in agricultural practice and their application increases the agricultural outputs since they protect crops from pests' infestations. In spite of their importance in agriculture, the use of some pesticides poses a significant risk to non-target populations especially wildlife and aquatic organisms [1]. The health of aquatic organisms and humans may be impaired by pesticides residues in surface water above certain limits [2]. Pesticide residues reach the water body through direct runoff, leaching, equipment washing, etc. Several factors such as soil characteristics, topography, weather, agricultural practices, chemical and environmental properties can affect the transportation of pesticides from agricultural fields to surface waters [3, 4].

Imidacloprid belongs to the neonicotinoid insecticide class. It acts as an antagonist by binding to nicotinic acetylcholine receptors and provides excellent control of a wide range of chewing and sucking pests, such as aphids, jassids and termites [5]. It has very high toxicity and stability in the soil for several months and can easily reach ground water [6].

Cypermethrin is an insecticide used for control of insects in and around residential areas. It belongs to the group of pyrethroids and is a non-systemic insecticide with contact and stomach action. Cypermethrin acts on the nervous system of the insect [7] and consist of eight optical isomers [8]. Among the eight isomers, only two pairs of diastereomers of cypermethrin (cisB and transB) possess biological activity against pests and insects [9-13].

Chlorpyrifos ethyl is one of the organophosphate class pesticides commonly used in small and large agricultural areas. High acute toxicity of chlorpyrifos ethyl poses a potential risk to human and aquatic organisms. Several studies have reported that chlorpyrifos ethyl residues pose a significant risk to children, pregnant women and infants, and this demands continuous monitoring in aquatic ecosystems [14, 15].

Normally these pesticides are present in water in low concentrations, therefore a method with low limit of detection (LOD) and limit of quantification (LOQ) is required to detect the compounds. Several methods have been reported for the separate determination of imidacloprid, cypermethrin and chlorpyrifos ethyl in different environmental matrices by high-performance liquid chromatography (HPLC) with UV-detection [5, 16-23], but in many cases, due to their widespread use, it is necessary to determine the three pesticides in one run. No method has been developed to analyze them simultaneously in the same sample.

The aim of the present paper is to develop a rapid and simple reversed-phase (RP) HPLC method with UV detection for the determination of imidacloprid, cypermethrin and chlorpyrifos ethyl

* To whom all correspondence should be sent:
E-mail: ahvm@chem.uni-sofia.bg

after liquid-liquid extraction (LLE) of the pesticides from the water samples. The potential application of the method is in the assessment of the environmental behavior of the pesticides in surface waters.

EXPERIMENTAL

Chemicals

HPLC-grade solvents and reagents and double deionized water (MilliQ) were used throughout the analysis. Methanol, acetonitrile, dichloromethane (99.5%) were from Merck (Darmstadt, Germany). Imidacloprid (1-(6-chloro-3-pyridinylmethyl)-N-nitroimidazolidin-2-ylideneamine) – 99.9%, cypermethrin ((RS)-α-cyano-3-phenoxybenzyl (1RS,3RS;1RS,3SR)-3-(2,2-dichlorovinyl) 2,2 dimethylcyclopropane- carboxylate) – 99.9%, and chlorpyrifos ethyl (O,O-diethyl O-3,5,6-trichloro-2-pyridyl phosphate) – 99.9% were purchased from Sigma-Aldrich.

Instrumentation

The chromatographic analysis was performed using a HPLC Varian Pro Star (Mulgrave, Australia) system equipped with a quaternary gradient pump and a ternary solvent delivery system, an injection valve with a 20 µL sample loop and a diode-array detector (DAD) detector. The separation was performed with a chromatographic column C18 (Microsorb-MV, 100-5, C18, 150 × 4.6 mm) purchased from Varian (Netherland, Europe). Ultrapure water, purified by a Milli-Q water purification system (Millipore purification system Synergy, France), was used throughout the experiments.

The temperature variation during the stability test of the analyzed pesticides was achieved in a climate chamber Model HPP 108 (Memmert GmbH, Germany).

Preparation of standard solutions

The stock standard solution of each pesticide (10 mg L^{-1}) was prepared in HPLC-grade methanol in amber reagent bottles and kept in the refrigerator at +4°C. Calibration standard solutions in the following concentrations: 10.0, 100.0, 300.0, 500.0, 700.0, and 1000.0 µg L^{-1} of each pesticide were then prepared from the stock solution by appropriate dilution with the mobile phase and were used for instrument calibration.

Extraction procedure

Three parallel water samples of 100 mL volume containing spiked 100 µg L^{-1} of imidacloprid, cypermethrin and chlorpyrifos ethyl each were

extracted three times with dichloromethane. The volumes of organic solvent were 3 × 60 mL. The organic extracts were then collected and concentrated by rotary vacuum evaporation until few drops of the solution were left. Then, 1.0 mL of methanol was added and the final sample was analyzed by HPLC-DAD.

Accuracy and precision of the method

The percent recovery of the studied pesticides was estimated by spiking deionized water with three concentrations (10.0, 100.0 and 1000.0 µg L^{-1}) of each pesticide. The spiked samples were extracted according to the extraction procedure described in the section above and analyzed by HPLC-DAD.

The precision of the method was evaluated by the relative standard deviation (RSD, %) of the areas of six replicate injections of each pesticide at the three concentrations (10.0, 100.0 and 1000.0 µg L^{-1}).

Limit of detection (LOD) and limit of quantification (LOQ)

LOD of the three pesticides was calculated by preparing spiked solutions of imidacloprid, cypermethrin and chlorpyrifos ethyl at low concentrations that were expected to produce a response 3-10 times baseline noise. LOQ was determined in the same manner and selected as the concentration of the pesticide that gives an S/N ratio of 10-20 [16].

Stability test

Two series of three parallel river water samples each free from detectable amounts of imidacloprid, cypermethrin and chlorpyrifos ethyl were spiked with 0.5 mg L^{-1} imidacloprid, 0.5 mg L^{-1} cypermethrin and 0.5 mg L^{-1} chlorpyrifos ethyl.

The first series was stored at room temperature (22±1°C) for six months. The second series was placed in a climate chamber with temperature variation (every 12 hours the temperature was changed, so that it approached the average daily 22±1°C and nightly temperatures 4±0.5°C) for six months.

RESULTS AND DISCUSSION

Determination of λ max of the pesticides

The correct choice of the wavelength is an important step to ensure the highest possible sensitivity of the analysis. The absorption maxima of imidacloprid are reported to be 270 nm [17] and 220 nm (±2 nm) [16], of cypermethrin are 235 nm [21] and 220 nm [20] and chlorpyrifos ethyl at 230

nm (±1 nm) [23]. In this work, the absorption spectra of the three pesticides in the entire UV range from 190 nm to 360 nm range were investigated. The obtained spectra showed that the most intensive absorption peaks were at 202 nm, followed by 205 nm and 212 nm for cypermethrin, 205 nm for chlorphyrifos ethyl, followed by 202 nm and 230 nm, and 270 nm for imidacloprid, followed by 212 nm and 205 nm. In order to analyze the three pesticides in one run, the selected working wavelength was 205 nm as a reasonable compromise. To avoid potential interferences at 205 nm LLE was applied to isolate the pesticides, as described in the experimental part.

Method development
(Optimization of peak separation)

The commonly used mobile phases for the separate elution of imidacloprid, cypermethrin and chlorpyrifos ethyl with a C18 chromatographic column are acetonitrile, methanol and water. A mobile phase of acetonitrile/water (80:20 v/v) was used to elute imidacloprid by Al-Rimawi *et al.* [16] who determined a mixture of pesticides in surface water. Kumar *et al.* [22] used the same acetonitrile/water ratio of the eluent for the determination of cypermethrin. Successful elution of chlorpyrifos ethyl was achieved using ratios 90:10 v/v and 75:25 v/v acetonitrile/1mM PO_4 [24].

The initial experiments in the current study were performed using several mobile phase compositions. As a first step isocratic elution with a mobile phase of acetonitrile/water (80:20 v/v) at a flow rate of 0.5 mL min^{-1} was performed. The results demonstrated that the peak's retention times were very close to each other, thus although the mobile phase consisting of acetonitrile/water (80:20

v/v respectively) is suitable to determine the pesticides separately, it was not suitable for separation of the mixture.

In order to reduce the time for analysis, gradient elution for the separation of the analyzed compounds was used with methanol as an organic eluent. Many authors applied it as a third component in the already used mobile phase [20, 21]. A successful separation of the analyzed pesticides was achieved with a mobile phase containing methanol:water (70% methanol and 30% water, v/v) with isocratic elution at a flow rate of 0.5 mL min^{-1}. The resulting chromatogram of imidacloprid, cypermethrin and chlorpyrifos ethyl separation is presented in Figure. 1. Cypermethrin had two peaks due to cis- and trans- forms.

The obtained retention times t_r (min) of the analyzed pesticides were as follows: for imidacloprid - t_r=3.95 min, for cypermethrin - t_{r1}= 11.87 min; t_{r2}= 14.20 min and for chlorpyrifos ethyl - t_r= 17.80 min.

Method validation

Linearity and range. To evaluate the linearity of the method, different calibration standards of the pesticides were analyzed by HPLC-DAD and the responses were recorded. The dependence concentration *versus* peak response and the respective correlation coefficient are presented in Figure 3. A plot of the peak areas of the pesticides *versus* concentration (in µg L^{-1}) was found to be linear in the range of 10-1000 µg L^{-1} for all analyzed pesticides with a correlation coefficient (R^2) greater than 0.999. This result indicates that the studied pesticides can be determined in surface water samples in a wide concentration range.
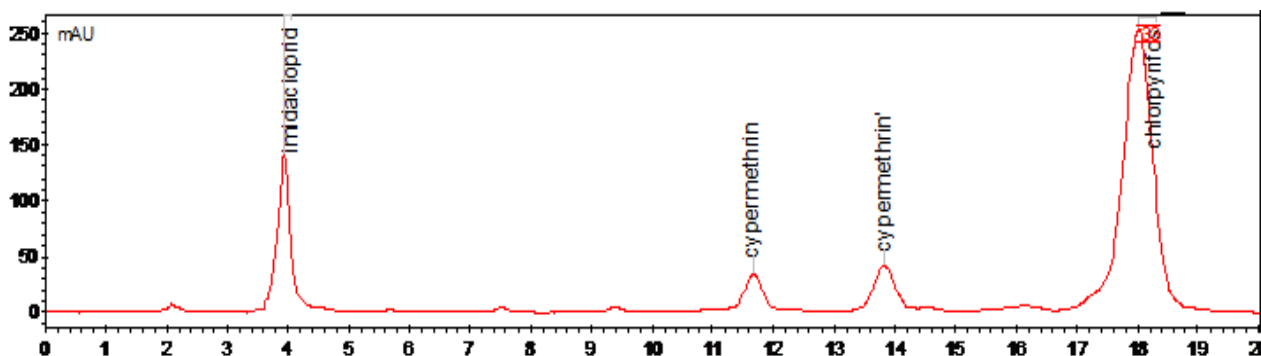

Fig. 1. Chromatogram of the separation of imidacloprid, cypermethrin and chlorpyrifos ethyl with mobile phase methanol/water (70:30 v/v).
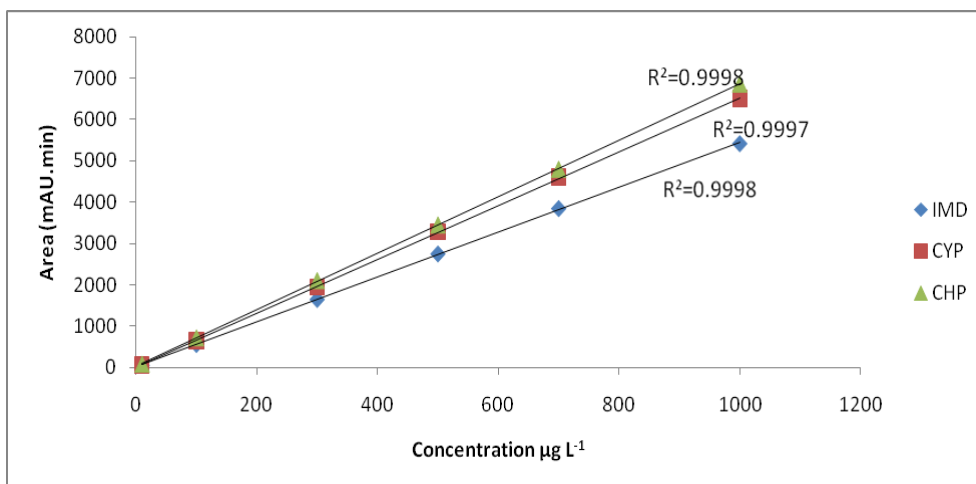
Fig. 2. Calibration curves of imadacloprid (IMD), cypermethrin (CYP) and chlorpyrifos ethyl (CHP).

Table 1. Recovery of imidacloprid, cypermethrin and chlorpyrifos ethyl at three concentration levels (10, 100, and 1000 µg L^{-1}).

	µg L^{-1}	Recovery (%)			Mean	SD*	RSD**
Imidacloprid	10.0	101.2	100.5	101.6	101.1	0.56	0.55
	100.0	98.9	99.5	100.4	99.6	0.75	0.76
	1000.0	99.3	99.5	98.6	99.1	0.47	0.48
Cypermethrin	10.0	100.5	101.0	101.3	100.9	0.40	0.40
	100.0	99.8	98.9	101.4	100.3	1.26	1.26
	1000.0	98.6	99.7	99.8	99.4	0.66	0.67
Chlorpyrifos ethyl	10.0	101.0	101.5	100.6	101.0	0.45	0.44
	100.0	100.2	99.8	99.0	99.7	0.61	0.61
	1000.0	99.4	100.4	99.6	99.8	0.52	0.53

*SD: standard deviation. **RSD (%): relative standard deviation.

Recovery. For the determination of the recovery of the investigated pesticides, the spiked samples were subjected to LLE, and analyzed by HPLC-DAD. The average recovery for each concentration was calculated by the ratio of the peak area of the pesticide in the spiked solution to the peak area of the standard solution with the same concentration. The results showed that the current method had good recovery (from 98.6% to 101.6%) for the three pesticides at the studied concentrations (10.0, 100.0, and 1000.0 µg L^{-1}) with a RSD better than 1.3% (see Table 1).

Precision. The precision of the current method for determination of the three pesticides was evaluated by calculating the RSD of the peak areas of six replicate injections of standard solutions with three concentrations (10.0, 100.0, and 1000.0 µg L^{-1}), and was found to be less than 5.0%.

Efficiency of the extraction procedures

The LOD of the three pesticides were found not low enough (180 µg L^{-1} for imidacloprid, 450 µg L^{-1} for cypermethrin and 800 µg L^{-1} for chlorpyrifos ethyl) to allow the detection and quantification of the pesticides in surface and ground water at low concentrations. This demanded a preliminary step for extraction and pre-concentration. LLE was performed with organic solvent - dichloromethane as described in the experimental part. The extraction efficiency was found to be 98.5%, 99.6% and 99.8% for imidacloprid, cypermethrin and chlorpyrifos ethyl, respectively.

Limit of detection (LOD) and limit of quantification (LOQ)

The LOD and LOQ of each compound were determined before and after LLE. After applying the extraction procedure, the samples were concentrated to the final volume of 1 mL and then HPLC analysis was performed. Table 2 presents the LOD and LOQ of the analyzed pesticides before and after LLE.

Table 2. LOD ($\mu g\ L^{-1}$) and LOQ ($\mu g\ L^{-1}$) of imidacloprid, cypermethrin and chlorpyrifos ethyl before and after the application of liquid-liquid extraction.

Pesticide	Before LLE		After LLE	
	LOD	LOQ	LOD	LOQ
Imidacloprid	180	560	0.17	0.51
Cypermethrin	450	1350	0.30	1.20
Chlorpyrifos ethyl	800	2800	0.40	1.50
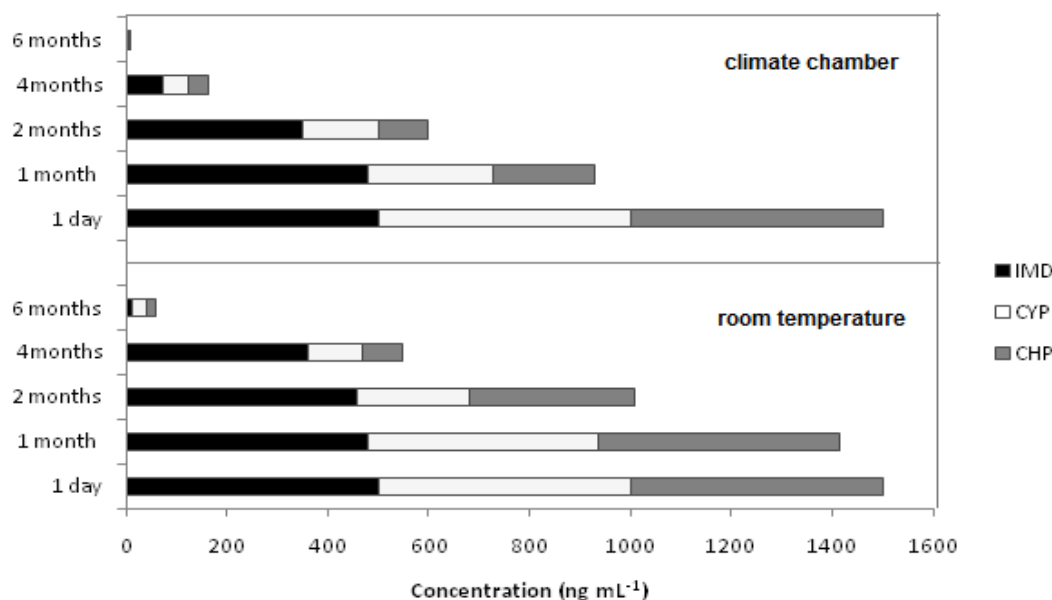
Fig. 3. Stability test of imidacloprid (IMD), cypermethrin (CYP) and chlorpyrifos ethyl (CHP), stored at room temperature (22±1 °C) and in a climate chamber simulating the average daily 22±1°C and nightly temperatures 4±0.5 °C).

The results showed that the imidacloprid had the lowest LOD and LOQ of the analyzed pesticides in water samples. The LODs of all three pesticides decrease between 1000-2000 times after applying the extraction and pre-concentration step which enables the detection and quantification of the pesticides in surface water at low ($\mu g\ L^{-1}$) concentration levels.

Stability test of the analyzed pesticides in a real water sample

The stability of the analyzed pesticides varies in the soil. Imidacloprid is stable for several months [6], cypermethrin more than 50 days [25], and the reported half-life for chlorpyrifos ethyl is in the range of 120-450 days [26]. The high stability of the pesticides enables their entry into surface and groundwater. However, their degradation to hydrolysis products in water depends on many factors - pH, temperature, dissolved oxygen, etc.

To investigate the stability of the analyzed pesticides a river water sample with pH = 6.58 was prepared in triplicate as described in the experimental part. The spiked samples were analyzed immediately after preparation and after periods of 1 month, 2 months, 4 months and 6 months. The results are shown on figure 3.

Imidacloprid was characterized by the highest pesticide stability. After the second month the amount of cypermethrin and chlorpyrifos ethyl detected at room temperature was about 50% of the introduced concentrations and below 30% in the sample with temperature variation. Significantly faster degradation of the analyzed pesticides was observed in the sample stored in the climate chamber with temperature variation. After the sixth month all analyzed pesticides were transformed to degradation products.

Application of the method to real water sample

The applicability of the proposed method was verified with river water samples collected from the basin of Struma river (South West Bulgaria) and analyzed for the three pesticides by the developed method. For comparison tap water samples from the town of Pernik (West Bulgaria) were analyzed. Results showed that only cypermethrin was detected in the river water samples at a concentration of 0.42 ± 0.06 $\mu g\ L^{-1}$. Imidacloprid and chlorpyrifos ethyl were below 0.17 $\mu g\ L^{-1}$ and

0.40 µg L^{-1}, respectively. As expected, no signal of the studied pesticides was detected in the tap water samples.

CONCLUSION

This work shows the potential of HPLC-DAD for the determination of pesticides in surface water samples as a good alternative to gas chromatographic methods.

A simple, accurate, precise, and selective HPLC method has been developed and validated for determination of imidacloprid, cypermethrin and chlorpyrifos ethyl with minimal use of toxic organic solvents. The method is accurate within a wide dynamic range with a recovery from 98.6 to 101.6%. The mobile phase consisting of methanol and water provides short run time with good separation of the analytes. The chromatographic separation was achieved at ambient room temperature.

Low LOD and LOQ of the pesticides analyzed in this study enable their detection and quantification in river water at low concentrations.

The method can be applied for the determination of imidacloprid, cypermethrin and chlorpyrifos ethyl in real water samples, including groundwater and surface water. The results indicate that the proposed method is not time-consuming and does not need extensive clean-up sequence. The method can be recommended for routine analysis of imidacloprid, cypermethrin and chlorpyrifos ethyl in water sample analysis.

REFERENCES

1. S. Bollmohr, J. A. Day, R. Schulz, *Chemosphere,* **68(3)**, 479 (2007).
2. K. E. Banks, S. Hernandez, *Talanta* **61(3)**, 257 (2003).
3. R. J. Wagenet, in: Effect of conservation tillage on groundwater quality: nitrates and pesticides, T. J. Logan, J. M. Davinson, J. L. Baker, M. R. Overcash (eds.) Lewis, Chelsea, 1987, p. 189.
4. R. A. Leonard, in: Pesticides in the soil environment: processes, impacts and modeling, H. H. Cheng (ed.), Soil Science Society of America, Madison, 1990, p. 135.
5. G. G. Yin, R. S. Kookana, *J. Environ. Sci. Health Part B*, **39(5-6)**, 737 (2004).
6. W. Zheng, W. Liu, *Pesticides Science,* **55(4)**, 482 (1999).
7. C. D. S. Tomlin, The Pesticide Manual, 15th edn., British Crop Protection Council, United Kingdom, 2009.
8. W. Liu, J. J. Gan, *J. Agric. Food Chem.,* **52(4)**, 755 (2004).
9. K. Naumann, Synthetic pyrethroid insecticides, structures and properties, Springer-Verlag, Berlin-Heidelberg, 1990.
10. J. E. Casida, *Environ. Health Persp.*, **34**, 189 (1980).
11. W. Liu, J. J. Gan, S. Lee, I. Werner, *J. Agric. Food Chem.,* **52**, 6233 (2004).
12. J. You, M. J. Lydy, *J. Chromatogr. A*, **1166**, 181 (2007).
13. M. G. Nillos, S. Qin, C. Larive, D. Schlenk, J. Gan, *J. Agric. Food Chem.,* **57**, 6938 (2009).
14. R. L. Ellis, in: Immunoassays for Residue Analysis, Food Safety, R. C. Beier, L. H. Stanker (eds.), American Chemical Society, Washington, DC, 1996.
15. D. Pimentel, in: Integrated Pest Management: Innovation-Development Process, R. Peshin, A. K. Dhawan (eds.), Springer Business Media, Houten, Netherlands, 2009, p. 83.
16. F. Al-Rimawi, *Int. J. Adv. Chem.*, **2(2)**, (2014).
17. S. Baskaran, R. Kookana, R, Naidu, *J. Chromatogr. A*, **787 (1-2)**, 271 (1997).
18. P. Samnani, K. Vishwakarma, S.Y. Pandey, *Bull. Environ. Contam. Toxicol.*, **86(5)**, 554 (2011).
19. H. Obana, M. Okihashi, K. Akutsu, Y. Kitagawa, *J. Agric. Food Chem.*, **50(16)**, 4464 (2002).
20. S. Albaseer, *Res. J. Chem. Sci.*, **2(10),** 26 (2012).
21. W. Hu, W. Xie, S. Chen, N. Zhang, Y. Zou, X. Dong, M. Rashid, Y. Xiao, M. Hu, G. Zhong, *J. Chromatogr. Sci.,* **53(4)**, 612 (2014).
22. B. Kumar, S. Kumar, D. Prakash, S.K. Singh, M. Mishra, P. Kumar, R. Gaur, G. Goyal, C. S. Sharma, J. S. Kamyotra, S.P. Gautam, *Proc. Indian National Sci. Acad.*, **77(1)**, 51 (2011).
23. P. O. Otieno, P. O. Owuor, J. O. Lalah, K. W. Pfister, *Talanta*, **117**, 250 (2013).
24. R. E. Mauldin, T. M. Primus, T. A. Buettgenbach, J. J. Johnston, G. M. Linz, *J. Liq. Chromatogr. Relat. Technol.* **29(3)**, 339 (2006).
25. Environmental Protection Agency, Cypermethrin Pesticide Fact Sheet, Washington, DC, United States, 1989.
26. L. K. Chai, M. H. Wong, H. C. Bruun Hansen, *J. Environ. Manage.*, **125**, 28 (2013).

Structural analysis of lead-borate composites containing PbMoO$_4$ nanocrystals

V. D. Lilova*, E. I. Lilov, Y. N. Trifonova

Department of Physics, University of Chemical Technology and Metallurgy,
8 Kl. Ohridski Blvd., 1756 Sofia, Bulgaria

Glass-crystalline composite materials based on a lead-borate glassy matrix and PbMoO$_4$ nanocrystals were obtained by the incorporation technique. The samples were prepared by conventional melting. The content of the PbMoO$_4$ was varied in the range from 5 to 40 wt.%. The appearance of the crystalline phase was identified by powder X-ray diffraction (XRD) analysis. The change in the network structure of the obtained materials was investigated by infrared spectroscopy (IR). The existence of BO$_3$, BO$_4$, PbO$_n$ (where n=3 and/or 4), as well as of MoO$_4$ units was proven. The dependence of the density as a function of the composition was also clarified.

Keywords: composites, density, structural investigations

INTRODUCTION

The methods for fabrication of various glass-ceramic nanostructured materials and nanodevices determine the special properties of the obtained products. The investigations are directed towards the selection of appropriate precursors and a combination of non-traditional methods for the synthesis of nanopowders, nanoparticle suspensions and coatings, bulk nanocomposite materials, nanophase alloys, ultrathin wires, etc. [1]. The structural investigations of the materials are performed concerning the possibility to control and to guide their specific properties.

The obtaining of new nanostructured glass-ceramic composites imposes several requirements towards the matrix: it should be a kinetically stable amorphous compound with a slightly pronounced tendency towards crystallization in the case of an appropriate heat treatment, as well with low melting temperature and limited reaction ability. Thus, lead-borate glasses are suitable materials for this purpose due to their unique properties such as low melting temperatures, wide glass formation regions, as well as good radiation shielding properties [2, 3].

Lead molybdate crystals have recently received even greater attention as possible acousto-optic materials, modulators, ion conductors, scintillators in nuclear instruments, etc. [4, 5].

The present work aims to analyze the influence of the composition on the microstructural transformation and density of the obtained composite materials. In particular, the aim of the structural investigation (using XRD analysis and IR spectroscopy) is to explain the relationship between the structure and properties of these materials.

EXPERIMENTAL

Synthesis of samples

Composite materials based on previously obtained lead-borate glass with composition 2PbO.B$_2$O$_3$ and PbMoO$_4$ nanocrystals were prepared by the incorporation method [6]. The choice of the matrix composition was made according to the phase diagram of the system PbO-B$_2$O$_3$ [7]. The preparation of composite materials consisted of:

i) synthesis of melted glass (g-PbB) using chemically pure materials (B$_2$O$_3$ and Pb$_3$O$_4$ as the main source of PbO [8]) in a platinum crucible at 900°C for 30 min;

ii) synthesis of powdered polycrystalline PbMoO$_4$ by solid-state sintering of a stoichiometric mixture of 50 mol% PbO and 50 mol% MoO$_3$ (Alfa Aesar) or 1:1.55 weight ratios. PbO was heated for 2 hours at 450° C and MoO$_3$ – for 3 hours at 650 °C. The homogenized mixture was sintered in a porcelain crucible at 800 °C for 2.5 hours;

iii) preparation of thoroughly mixed batches of both components in the compositional range from 95 to 60 wt.% g-PbB and, respectively, from 5 to 40 wt.% PbMoO$_4$, melting of the batches under normal atmospheric condition at 850 °C for 2 hours and fast cooling by pouring the melts between two copper plates (Table 1).

---

* To whom all correspondence should be sent:
E-mail: vanya.di@uctm.edu

Table 1. Composition of the investigated samples

Sample abbreviation	Composition	
	g-PbB, (wt.%)	PbMoO₄, (wt.%)
P1	95	5
P2	90	10
P3	80	20
P4	70	30
P5	60	40

Methods of characterization

The phase composition of the obtained materials was determined by powder X-ray diffraction analysis using diffractometer Philips with Bragg-Brentano geometry and graphite monochromated CuK$_\alpha$ radiation (λ=1.54 Å, 40 kV, 50 mA). The performed reflectance angle was in the range 10°-70° (0.5° of each step). All investigations were performed at ambient temperature.

The infrared absorption spectra were measured with a Varian 680-IR spectrometer in transmission mode in the MIR 400-4000 cm^{-1} spectral range with a 2 cm^{-1} spectral resolution. The samples were prepared as standard KBr pellets.

The density of the samples (ρ) was measured by the pycnometric method at a constant temperature. The immersion liquid used as a medium for density measurement was toluene with density at 25 °C - 0.8623 g/cm³. The measurement accuracy was about ±2%.

RESULTS AND DISCUSSION

XRD characterization

The XRD pattern of the polycrystalline PbMoO₄ powder is shown in Fig. 1. The observed diffraction peaks are very sharp and distinct, indicating good crystallinity of the prepared material. The formation of PbMoO₄ (JCPDS 74-1075) was proven. It is well-known that lead molybdate has a scheelite-type tetragonal structure and space group symmetry of I4₁/a [9]. In the crystal lattice, lead (Pb) atoms are connected by eight oxygen (O) atoms to form [PbO₈] clusters whereas molybdenum (Mo) atom is coordinated by four O atoms which result in [MoO₄] tetrahedral units [10]. The previous results of TEM analysis [11] showed that the PbMoO₄ particles exhibited sizes up to 50 nm.

Fig. 2 presents the X-ray diffraction patterns of the composites. The results show that the samples containing 5 wt.%, 10 wt.% and 20 wt.% PbMoO₄ are X-ray amorphous. Only a broad amorphous halo is observed in the diffractograms at an angle of 2θ between 20 and 35°. In the samples with 30 wt.% and 40 wt.% PbMoO₄, distinct diffraction maxima on the halo are observed, i.e. the samples

are glass-crystalline. Crystalline phase identification of PbMoO₄ is made by PDF 77-0431. The diffractograms also show that the intensity of the peaks increases with increasing PbMoO₄, which is an indication of the increase in the crystalline phase content.
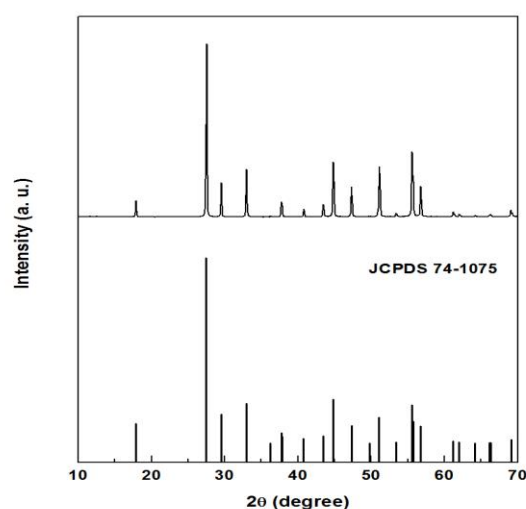

Fig. 1. XRD pattern of polycrystalline PbMoO₄ powder**.** The theoretical pattern is presented below for comparison.
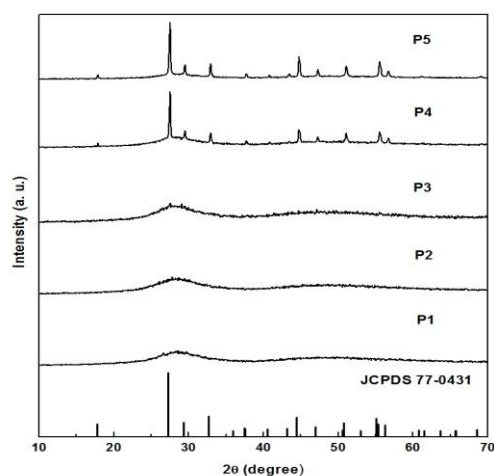

Fig. 2. X-ray diffraction patterns of the composite materials.

IR analysis

The vibrational assignments of the bands for the composite materials spectra were done by comparing the experimental data with those of the related crystalline compounds [12]. To interpret the structure of the investigated samples as accurately as possible, the results obtained were compared to the currently known data on the $PbO-B_2O_3$ system IR spectra, some other binary borate systems, as well as various systems with the participation of B_2O_3 and $PbMoO_4$.

Two spectral ranges are typical of the investigated samples: from 400 to 2000 cm⁻¹ and from 2000 to 4000 cm⁻¹. The large absorption region centered at about 3440 cm⁻¹ is assigned to the vibrations of OH-groups and water molecules. In the second spectral region, there are bands related to the vibrations of the different structural units (Fig. 3). The obtained absorption bands and their assignments are summarized in Table 2.

For easier interpretation of the obtained spectra, they were compared to the spectrum of the matrix of $2PbO.B_2O_3$. The spectra in the range of 1500-1700 cm⁻¹ are similar. The bands are due to the

inevitable moisture in the applied KBr-pellet method [13].
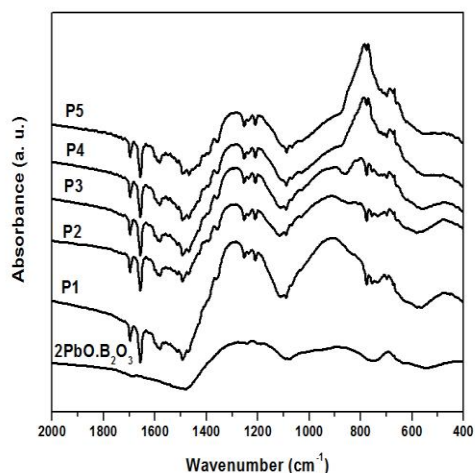
Fig. 3. Infrared absorption spectra of the samples

Table 2. Infrared absorption bands and their assignment

Peak position (cm⁻¹)	Assignment	References
690, 706	Bending vibrations of B-O-B linkage in BO_3 triangles	14, 15
1150-1450	Stretching vibrations in borate triangle units	16, 17
1198 1220	Asymmetric stretching vibrations of B-Ø and/or B-O⁻ bonds in borate triangular units from pyro- and ortho-borate groups	18 19
1240	Stretching vibrations of B-O bonds of borate triangles non bridging oxygens (NBO's)	19
1296	Vibrations of B-O rings, which are formed by the connection of the bridge oxygen ions between $[BO_3]$ triangles and $[BO_4]$ tetrahedra	17
910, 1040	Stretching vibration of B-O bonds in BO_4 units	16, 20, 21
480, 650	Bending vibration of Pb-O-B	23, 24
670	Vibration of Pb-O bonds from PbO_4 pyramidal units	22
1100	Asymmetric stretching vibrations of Pb-O in $[PbO_n]$ units	25
800-830	Characteristic vibrations of distorted isolated MoO_4 tetrahedra	21, 26
770, 790	Mo-O antisymmetric stretching vibration of $[MoO_4]^{2-}$ tetrahedra from $PbMoO_4$	28
418	Symmetric vibration of the Mo-O-Mo linkage	21, 27
1500-1700	Due to the inevitable moisture in the KBr-pellet method	13

The absorption bands may be divided into three regions: 1450-1150 cm⁻¹, 1100-800 cm⁻¹ and 750-600 cm⁻¹. The bands at 690 cm⁻¹ and 706 cm⁻¹ are ascribed to the B-O-B bridges bending vibration of BO_3 triangles [14, 15].

The absorption bands in the region 1450-1150 cm⁻¹ originate from the B-O stretching of various BO_3 units (both bridging and non-bridging types) [16, 17]. The band at 1198 cm⁻¹ [18] is obtained by the asymmetric stretching vibrations of B-Ø and/or BO⁻ bonds in borate triangular units ($BØ_3$ и $BØ_2O^-$) from pyro- and ortho-borate groups (Ø: oxygen atom bridging two boron atoms; O⁻: non-bridging oxygen atom). The band at 1220 cm⁻¹ [19] is also due to asymmetric stretching vibrations of BO⁻ bonds in BO_3 units from pyro- and ortho-borate groups and those at 1240 cm⁻¹ - of borate triangles non-bridging oxygens (NBOs). The broad band about 1296 cm⁻¹ is attributed to the vibrations of B-O rings, which are formed by the connection of the bridge oxygen ions between $[BO_3]$ triangles and $[BO_4]$ tetrahedra [17]. There are also several slightly intensive peaks at 1369 cm⁻¹, 1396 cm⁻¹, 1410 cm⁻¹ and 1433 cm⁻¹ due to B-O bonds stretching vibrations of BO_3 units from various borate groups [12]. The shoulder at about 910 cm⁻¹, due to the asymmetric stretching vibrations of boron in tetrahedral oxygen coordination B_4^- [16, 20], reduces its intensity with the increase of $PbMoO_4$ content. This is related to the decrease in the number of superstructure units (BO_3+BO_4), respectively of the BO_4 groups. This may be due to an increase in the PbO/B_2O_3 ratio due to the partial dissolution of $PbMoO_4$. The same trend is observed for the band at 1040 cm⁻¹ associated to the B-O stretching vibration in BO_4 units from tri-, tetra- and pentaborate groups [16, 21].

The high content of lead oxide in lead-borate glasses plays a dual role - a network former and a network modifier in the glass matrix, having essentially B_2O_3 as a glassy former. At sufficiently large amounts of PbO (60 % or higher), its effect as a glass-forming agent for the structural network of the glass is obvious. The lead oxide is incorporated into the structure as $[PbO_4]$ structural units. This is confirmed by an increase in the intensity of the band located at about 670 cm⁻¹. This band can be attributed to Pb-O bonds vibrations from $[PbO_4]$ pyramidal units [22]. The occurrence of a band around a 650 cm⁻¹ and a shoulder around a 480 cm⁻¹ are attributed to a Pb-O-B bending [23, 24]. Therefore, in this case, PbO can be considered as a network participant as Pb^{2+} modified boron-oxygen rings and chains. The absorption band at a higher frequency, located at about 1100 cm⁻¹, is attributed to Pb-O asymmetric stretching vibrations in $[PbO_n]$ structural units with n = 3 and/or 4 [25]. The dissolution of the lead molybdate is also indicated by the presence of a shoulder in the range 830-800 cm⁻¹ in composites P1-P3. The molybdenum ions, in this case, act as a glass-forming agent and are incorporated in the glass matrix as distorted, isolated MoO_4 tetrahedra [21, 26].

The increase in the $PbMoO_4$ content leads to an increase in the band intensity at 418 cm⁻¹ assigned to the symmetric vibration of the Mo-O-Mo linkage [21, 27]. Additionally, the spectra of composites P4 and P5 exhibit two well-resolved bands at 790 cm⁻¹ and 770 cm⁻¹, which can be specified as Mo–O antisymmetric stretching vibration of the MoO_4^{2-} tetrahedra [28] from $PbMoO_4$.

Density

The density responds to variations in composition sensitively in technological practice. Density, in general, is explained in terms of a competition between the masses and sizes of the various structural groups present in the glasses. Accordingly, density is related to how tightly the ions and ionic groups are packed together in the structure. The density values of all composite materials are listed in Table 3.

The density of the composite materials shows a non-linear dependence with the increase of $PbMoO_4$ content as shown in Fig. 4.

Table 3. Density values of the composite materials

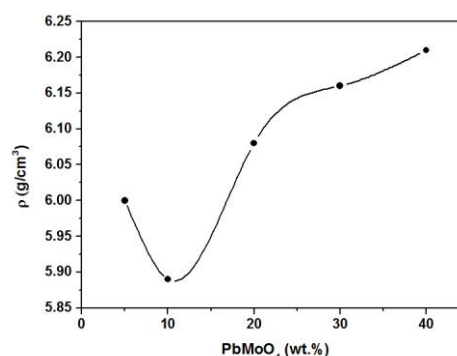| Sample	P1	P2	P3	P4	P5
ρ, (g/cm³)	6.00	5.89	6.08	6.16	6.21

Fig. 4. Density dependence on composition

In fact, there is a sudden drop in density at 10 wt.% $PbMoO_4$. This is attributed to the conversion of BO_4 tetrahedral units into BO_3 triangular units. Then, with the increase in $PbMoO_4$ content, density values gradually increase. This result is consistent with the IR spectroscopy results which show that at

the sample P2 a change in matrix structure takes place - the shoulder at about 910 cm^{-1} reduces its intensity, which is associated with decreasing the amount of the BO_4-groups. This may be due to an increase in the PbO/B_2O_3 ratio due to the partial dissolution of $PbMoO_4$. Moreover, the intensity of the absorption band at 670 cm^{-1} which is the characteristic frequency of Pb–O vibrations from PbO_4 units increases. The presence of a shoulder in the range 830-800 cm^{-1}, which is indicative of the participation of molybdenum in the composite glass matrix as distorted, isolated MoO_4 tetrahedra also indicates dissolution of the lead molybdate.

CONCLUSIONS

IR spectroscopic and XRD analyses were employed to study the structural changes in composite materials based on an amorphous lead-borate matrix and $PbMoO_4$ nanocrystals. IR spectra indicated that the main structural units building the amorphous network are BO_3 triangles and BO_4 tetrahedra in superstructures, in addition to the PbO_n (where n = 3 and/or 4) structural units. It was established that $PbMoO_4$ was dissolved partially. Molybdenum ions acted as network formers as MoO_4 tetrahedra. It was proved that molybdenum favored the $BO_4 \rightarrow BO_3$ transformation.

Typical diffraction patterns of glass-crystalline samples were obtained for the composite materials containing more than 20 wt.% $PbMoO_4$.

The compositional variation of density was discussed. The measurements showed that the densest packing of coordination polyhedra in these materials was obtained for a sample containing 10 wt % $PbMoO_4$.

REFERENCES

1. P. Moriarty, *Rep. Prog. Phys.*, **64**(3), 297 (2001).
2. Y. B. Saddeek, *J. Alloys Compd.*, **467**(1-2), 14 (2009).
3. N. A. Ghoneim, H. A. ElBatal, A. M. Abdelghany, I. S. Ali, *J. Alloys Compd.*, **509**(24), 6913 (2011).
4. F. A. Danevich, B. V. Grinyov, S. Henry, M. B. Kosmyna, H. Kraus, N. Krutyak, V. M. Kudovbenko, V. B. Mikhailik, L. L. Nagornaya, B. P. Nazarenko, A. S. Nikolaiko, O. G. Polischuk, V. M. Puzikov, A. N. Shekhovtsov, V. I. Tretyak, Yu. Ya. Vostretsov, *Nucl. Instrum. Methods Phys. Res. Sect. A*, **622**(3), 608 (2010).
5. M. Minova, K. Itakura, S. Moriyama, W. Ootani, Nucl. Instrum. *Methods Phys. Res. Sect. A*, **320**(3), 500 (1992).
6. T. Komatsu, K. Shioya, K. Matusita, *J. Am. Ceram. Soc.*, **76**(11), 2923 (1993).
7. R. F. Geller, E. N. Bunting, *J. Res. Natl. Bur. Stand.*, **18**(5), 585 (1937).
8. S. Jana, B. Karmakar, P. Kundu, *Materials Science-Poland*, **25**(4), 1127 (2007).
9. T. Hahn (ed.), International Tables for Crystallography Vol. A, Reidel, Boston 1987.
10. M. R. D. Bomio, L. S. Cavalcante, M. A. P. Almeida, R. L. Tranquilin, N. C. Batista, P. S. Pizani, M. Siu Li, J. Andres, E. Longo, *Polyhedron*, **50**(1), 532 (2013).
11. V. Ivanova, E. Kashchieva, Y. Dimitriev, in Functional Properties of Nanostructured Materials, R. Kassing, P. Petkov, W. Kulisch, C. Popov (eds.), Springer, Netherlands, 2006, p. 173.
12. E. I. Kamitsos, A. P. Patsis, M. A. Karakassides, G. D. Chryssikos, *J. Non-Cryst. Solids*, **126**(1-2), 52 (1990).
13. N. Kishore, K. Aggralwal, R. Kamal, R.G. Mediratta, *Phys. Chem. Glasses*, **23**, 202 (1982).
14. C. P. Varsamis, E. I. Kamitsos, G. D. Chryssikos, *Solid State Ionics*, **136-137**, 1031 (2000).
15. Y. Cheng, H. Xiao, W. Guo, W. Guo, *Ceram. Int.*, **33**(7), 1341 (2007).
16. E. I. Kamitsos, M. A. Karakassides, G. D. Cryssikos, *J. Phys. Chem.*, **91**(5), 1073 (1987).
17. J. Lorösch, M. Couzi, J. Pelous, R. Vacher, A. Levasseur, *J. Non-Cryst. Solids*, **69**(1), 1 (1984).
18. Y. D. Yiannopoulos, G. D. Chryssikos, E. I. Kamitsos, *Phys. Chem. Glasses*, **42**(3), 164 (2001).
19. P. Pascuta, L. Pop, S. Rada, M. Bosca, E. Culea, *J. Mater. Sci.: Mater. Electron.*, **19**(5), 424 (2008).
20. S. G. Motke, S. P. Yawale, S. S. Yawale, *Bull. Mater. Sci.*, **25**(1), 75 (2002).
21. S. M. Abo-Naf, *J. Non-Cryst. Solids*, **358**(2), 406 (2012).
22. S. Rada, T. Ristoiu, M. Rada, I. Coroiu, V. Maties, E. Culea, *Mater. Res. Bull.*, **45**(1), 69 (2010).
23. W. A. Pisarski, T. Goryczka, B. Wodecka-Duś, M. Płońska, J. Pisarska, *Mater. Sci. Eng. B*, **122**(2), 94 (2005).
24. M. Ganguli, K. J. Rao, *J. Solid State Chem.*, **145**(1), 65 (1999)
25. M. Rada, V. Maties, M. Culea, S. Rada, E. Culea, *Spectrochim. Acta, Part A*, **75**(2), 507 (2010).
26. R. Iordanova, L. Aleksandrov, A. Bachvarova-Nedelcheva, M. AtaaLa, Y. Dimitriev, *J. Non-Cryst. Solids*, **357**(14), 2663 (2011).
27. M. Rada, S. Rada, P. Pascuta, E. Culea, *Spectrochim. Acta, Part A*, **77**(4), 832 (2010).
28. R. P. Jia, Y. Q. Zhang, *Chin. Opt. Lett.*, **8**(12), 1152 (2010)

Evaluation of antioxidant, anti-inflammatory and anti-arthritic activity of new ibuprofen derivatives

S. P. Manolov[1], I. I. Ivanov[1*], D. G. Bojilov[1], Y. T. Voynikov[2]

[1]Department of Organic Chemistry, University of Plovdiv, 24 Tzar Assen Str., 4000 Plovdiv, Bulgaria
[2]Faculty of Pharmacy, Medical University of Sofia, 2 Dunav Str., Sofia 1000, Bulgaria

Herein, we present the synthesis and *in-vitro* anti-inflammatory, antioxidant, and anti-arthritic activities of new ibuprofen derivatives. All structures were confirmed by spectral analysis (^{1}H NMR, ^{13}C NMR, UV, IR and HRMS). The lipophilicity was established using reversed-phase thin layer chromatography and *in silico* calculations. The anti-inflammatory and anti-arthritic activities correlated with the lipophilicity of the compounds.

Keywords: Ibuprofen derivatives, anti-inflammatory, H_2O_2 scavenging activity, anti-arthritic, lipophilicity, *in-vitro*.

INTRODUCTION

2-Arylpropanoic acids are an important class of non-steroidal anti-inflammatory drugs (NSAIDs) used for the treatment of pain and inflammation in various diseases [1]. One of the most widely used NSAIDs is ibuprofen or 2- (4-isobutylphenyl) propionic acid, well known for its analgesic, antipyretic and anti-inflammatory properties [2]. However, prolonged use of NSAIDs is known to cause gastrointestinal ulceration and bleeding, as well as nephrotoxicity [3].

Numerous ibuprofen amides and other derivatives have been examined for different biological activities [4]. There are data in the literature on isoquinoline derivatives containing electron-donating substituents such as methoxy groups exhibiting diverse biological activity. It is the presence of methoxy groups that enhances the activity of the commented compounds [5]. That is why we have selected these examples, varying the substituents and all with Ibuprofen residue so that we could assess their impact.

In recent years, many newly synthesized organic compounds show significant anti-inflammatory activity [6, 7]. The last few years, despite the hard research efforts in searching of efficient anti-inflammatory drugs, a set of greatly important fundamental questions remains unresolved [8]. Much research has been focused on studying compounds which are capable of decreasing the inflammation while conserving structural silhouettes [9]. In this regard, attempts to create new non-harmful molecules with anti-inflammatory properties continue.

NSAIDs are the most important therapeutic agents used for the treatment of inflammation. Among them, ibuprofen has been widely used, due to its inhibitory activity against cyclooxygenase (COX) enzymes that catalyze the formation of prostaglandin precursors from arachidonic acid. Inflammatory processes increase the concentration of ROS (reactive oxygen species) in the human body. H_2O_2 is transformed into $^{.}OH$ radicals that damage the cell membrane. Thus, one of the aims of the present study was to evaluate the scavenging activity for H_2O_2 of the newly obtained ibuprofen derivatives [10, 11].

MATERIALS AND METHODS

General

All the reagents and chemicals for the synthesis and analysis were purchased from commercial sources (Sigma-Aldrich, S.A., Germany) and used as received. Melting points were determined on a Boetius hot stage apparatus and are non-corrected. The spectral data were recorded on a Bruker Avance II + 600 spectrometer (BAS-IOCCP—Sofia, Sofia, Bulgaria). The ^{1}H-NMR and ^{13}C-NMR spectra were taken in CDCl₃ or DMSO at 600 MHz and 150.9 MHz, respectively. Chemical shifts are given in ppm relative and were referenced to TMS ($\delta = 0.00$ ppm) as an internal standard with the coupling constants indicated in Hz. The NMR spectra were taken at room temperature (ac. 295 K). Mass analyses were carried out on a Q Exactive Plus mass spectrometer (ThermoFisher Scientific) equipped with a heated electrospray ionization (HESI-II) probe (ThermoScientific) (Medical University of Sofia). TLC was carried out on precoated 0.2 mm Fluka silica gel 60 plates and Kieselgel 60 F₂₅₄.

---

* To whom all correspondence should be sent:
E-mail: ivanov@uni-plovdiv.bg

Synthesis

Synthesis of amides 3. To the solution of ibuprofen (1 mmol) in 25 ml of CH_2Cl_2, DCC (1 mmol) was added. The reaction mixture was stirred at room temperature for 10 min. After the addition of the corresponding amine 1 (1 mmol) the reaction mixture was stirred for 50 min and formation of white crystals was observed. The side product dicyclohexylurea (white crystals) was separated *via* sintered glass filter. The filtrate was washed with diluted hydrochloric acid, saturated solution of Na_2CO_3 and brine. The combined organic layers were dried over anhydrous Na_2SO_4, and the solvent was removed under reduced pressure.

2-(4-isobutylphenyl)-N-phenethylpropanamide (3a). Yield = 97%, MP = 100-104ºC, ^{1}H NMR (600 MHz, CDCl₃) δ 7.16 – 7.09 (m, 3H), 7.06 – 7.00 (m, 4H), 6.94 – 6.91 (m, 2H), 5.29 (s, 1H), 3.46 – 3.37 (m, 1H), 3.31 (dt, J = 20.1, 6.9 Hz, 1H), 2.67 – 2.58 (m, 1H), 2.39 (d, J = 7.2 Hz, 2H), 1.86 (dd, J = 12.7, 3.4 Hz, 1H), 1.78 (td, J = 13.6, 6.8 Hz, 1H), 1.65 – 1.61 (m, 1H), 1.41 (d, J = 7.2 Hz, 3H), 0.84 (s, 3H), 0.83 (s, 3H). ^{13}C NMR (151 MHz, CDCl³) δ 174.41, 140.72, 138.84, 138.38, 129.62, 128.75, 128.53, 127.39, 126.37, 46.79, 45.04, 40.69, 35.56, 30.22, 25.58, 22.42, 18.34. UV (Methanol for HPLC), λ_{max} = 232 (ε 1173); λ_{max} = 264 (ε 350). IR(KBr): 701, 748, 760, 779, 856 $\gamma(C_{sp}^2$-H); 1382 (δ_sCH₃); 1467, 1549, 1633, 1654 (νC=C); 1672, 1700 ν(C=O); 2854 ν_s(CH₂); 2932 ν_{as}(CH₂); 2954, 2968 ν_{as}(CH₃); 3026, 3069 ν(C_{sp}^2-H); 3258, 3292 ν(N-H). HRMS found for $C_{21}H_{27}NO$: m/z 310.2157 [M+H]⁺ calcd. m/z 310.2165.

N-(3,4-dimethoxyphenethyl)-2-(4-isobutylphenyl)propanamide (3b). Yield = 98%, MP = 62-64ºC, ^{1}H NMR (600 MHz, CDCl₃) δ 7.06 – 7.01 (m, 4H), 6.64 (dd, J = 8.1, 3.9 Hz, 1H), 6.55 (t, J = 3.6 Hz, 1H), 6.46 (dd, J = 8.1, 2.0 Hz, 1H), 5.32 (t, J = 5.3 Hz, 1H), 3.78 (s, 3H), 3.74 (s, 3H), 3.43 – 3.36 (m, 2H), 3.31 (qd, J = 7.0, 5.9 Hz, 1H), 2.59 (td, J = 6.9, 3.6 Hz, 2H), 1.81 – 1.73 (m, 2H), 1.41 (d, J = 7.2 Hz, 3H), 1.37 (d, J = 6.8 Hz, 1H), 0.83 (s, 3H), 0.82 (s, 3H). ^{13}C NMR (151 MHz, CDCl₃) δ 174.44, 148.94, 147.55, 140.69, 138.40, 131.32, 129.58, 127.37, 120.60, 111.73, 111.15, 55.88, 55.79, 46.78, 45.01, 40.80, 35.16, 30.21, 22.40, 18.48. UV (Methanol for HPLC), λ_{max} = 234 (ε 3707); λ_{max} = 280 (ε 1807). IR(KBr): 698, 724, 766, 785, 805, 851 $\gamma(C_{sp}^2$-H); 1381 (δ_sCH₃); 1465, 1559, 1633, 1654 (νC=C); 1672, 1701 ν(C=O); 2859 ν(OCH₂-H); 2931 ν_{as}(CH₂); 2952, ν_{as}(CH₃); 2999, 3064 ν(C_{sp}^2-H); 3239, 3294 ν(N-H). HRMS found for $C_{23}H_{31}NO_3$: m/z 370.2370 [M+H]⁺ calcd. m/z 370.2377.

N-(2,2-diphenylethyl)-2-(4-isobutylphenyl) propanamide (3c). Yield = 99%, MP = 74-76ºC, ^{1}H NMR (600 MHz, CDCl₃) δ 7.19 – 7.15 (m, 4H), 7.11-7.09 (m, 2H), 7.07 – 7.05 (m, 2H), 7.02 – 7.01 (m, 2H), 6.93 – 6.87 (m, 4H), 5.20 (s, 1H), 4.00 (t, J = 8.0 Hz, 1H), 3.84 – 3.78 (m, 1H), 3.65 (ddd, J = 10.4, 8.2, 5.5 Hz, 1H), 3.33 (q, J = 7.2 Hz, 1H), 2.36 (d, J = 7.2 Hz, 2H), 1.80 – 1.72 (m, 1H), 1.36 (d, J = 7.2 Hz, 3H), 0.83 (s, 3H), 0.82 (s, 3H). ^{13}C NMR (151 MHz, CDCl₃) δ 174.42, 141.72, 140.60, 138.06, 129.55, 128.64, 128.03, 127.30, 126.72, 50.37, 46.71, 45.03, 43.83, 30.21, 22.44, 18.20. UV (Methanol for HPLC), λ_{max} = 229 (ε 3834); λ_{max} = 262 (ε 533). IR(KBr): 699, 750, 764, 850, 885 $\gamma(C_{sp}^2$-H); 1364, 1384 ν_s(CH₃); 1457 ν_{as}(CH₃); 1497, 1559 ν(C=C); 1653 ν(C=O); 2867 ν_s(CH₂); 2930 ν_{as}(CH₂); 3087 ν(C_{sp}^2-H); 3337, 3447 ν_{as} (N-H). HRMS found for $C_{27}H_{31}NO$: m/z 386.2468 [M+H]⁺ calcd. m/z 386.2478.

N-(2,2-bis(4-methoxyphenyl)ethyl)-2-(4-isobutylphenyl)propanamide (3d). Yield = 94%, Oil, ^{1}H NMR (600 MHz, CDCl₃) δ 6.94 (t, J = 2.0 Hz, 1H), 6.93 – 6.92 (m, 1H), 6.91 (d, J = 3.0 Hz, 1H), 6.90 (d, J = 2.7 Hz, 1H), 6.70 (ddd, J = 6.5, 4.8, 3.3 Hz, 1H), 5.20 (t, J = 5.5 Hz, 1H), 3.88 (t, J = 8.0 Hz, 1H), 3.76 – 3.71 (m, 1H), 3.69 (s, 1H), 3.69 (s, 1H), 3.61 – 3.56 (m, 1H), 3.34 (q, J = 7.3 Hz, 1H), 2.36 (d, J = 7.2 Hz, 1H), 1.79 – 1.73 (m, 1H), 1.36 (d, J = 7.4 Hz, 1H), 0.83 (s, 1H), 0.82 (s, 1H). ^{13}C NMR (151 MHz, CDCl₃) δ 174.42, 158.22, 140.58, 138.12, 134.12, 129.50, 128.84, 127.32, 113.96, 113.74, 55.22, 46.71, 45.01, 44.09, 30.21, 22.41, 18.22. UV (Methanol for HPLC), λ_{max} = 234 (ε 4126); λ_{max} = 276 (ε 1800). IR(KBr): 639, 750, 771, 807, 826, 891 $\gamma(C_{sp}^2$-H); 1367, 1383 ν_s(CH₃); 1465 ν_{as}(CH₃); 1510, 1559 ν(C=C); 1636 ν(C=O); 2851 ν_s(CH₂); 2929, 2953 ν_{as}(CH₂); 3318, 3436 ν_{as}(N-H). HRMS found for $C_{29}H_{35}NO_3$: m/z 446.2681 [M+H]⁺ calcd. m/z 446.2690.

N-(2,2-bis(3,4-dimethoxyphenyl)ethyl)-2-(4-isobutylphenyl)propanamide (3e). Yield = 96%, MP = 86-88ºC, ^{1}H NMR (600 MHz, CDCl₃) δ 6.91 (dd, J = 19.6, 8.1 Hz, 4H), 6.68 (dd, J = 9.5, 8.0 Hz, 2H), 6.61 – 6.55 (m, 4H), 5.26 (t, J = 5.6 Hz, 1H), 3.92 (t, J = 8.0 Hz, 1H), 3.78 (s, 6H), 3.76 – 3.73 (m, 1H), 3.72 (s, 3H), 3.71 (s, 3H), 3.66 – 3.59 (m, 1H), 3.34 (q, J = 7.2 Hz, 1H), 2.35 (d, J = 7.2 Hz, 2H), 1.79 – 1.70 (m, 1H), 1.36 (d, J = 7.2 Hz, 2H), 0.82 (s, 3H), 0.81 (s, 3H). ^{13}C NMR (151 MHz, CDCl₃) δ 174.47, 148.98, 148.96, 147.73, 140.62, 138.06, 134.36, 129.47, 127.26, 119.73, 119.64, 111.07, 118.18, 111.22, 55.84, 55.81, 49.54, 46.70, 44.97, 44.05, 30.20, 25.53, 24.88, 22.38, 18.29. UV (Methanol for HPLC), λ_{max} = 234 (ε 7000); λ_{max} = 264 (ε 4158). IR(KBr): 647, 765, 806, 852 γ(Csp2-

H); 1365 $\nu_s(CH_3)$; 1464, 1541, 1606 $\nu(C=C)$; 1649, 1654 $\nu(C=O)$; 2835 $\nu(OCH_2\text{-}H)$; 2869 $\nu_s(CH_2)$; 2932 $\nu_{as}(CH_2)$; 2964 $\nu_{as}(CH_3)$; 3323, 3370 $\nu(N\text{-}H)$. HRMS found for $C_{31}H_{39}NO_5$: m/z 506.2891 $[M+H]^+$ calcd. m/z 506.2901.

Biological experiments

Hydrogen peroxide scavenging activity (HPSA). The ability of ibuprofen derivatives to scavenge hydrogen peroxide was assessed according to the method reported by Ruch *et al.* [12] with minor modification. The solution of hydrogen peroxide (43 mM) was prepared in potassium phosphate buffer solution (0.2 M, pH 7.4). Sample analysis was performed as follows: in test tubes were mixed 0.6 ml of hydrogen peroxide (43 mM), 0.1 ml of sample/standard with different concentration (15-1000 µg/ml) and 2.4 ml of potassium phosphate buffer solution. The mixture was stirred and incubated in dark for 10 min at 37 °C. Absorbance was measured at 230 nm with a spectrophotometer (Camspec M508, England) against a blank solution containing phosphate buffer and hydrogen peroxide without the sample. Ascorbic acid (AA) was used as a standard.

$$I, \% \text{ (HPSA)} = [(A_{blank} - A_{sample}) / A_{blank}] * 100$$

In-vitro anti-inflammatory activity. In-vitro analysis of anti-inflammatory activity was carried out by inhibition of albumin denaturation. The analysis was performed according to Sakat's method [13] with minor modification. The solution of 1 % albumin (egg and human) was prepared in distilled water. The tested compounds were dissolved firstly in 1.2 ml of DMF and PBS up to 25 ml, so the final concentration of the stock solution was 1000 µg/ml. Then, a series of working solutions with different concentrations in PBS (20-500 µg/ml) was prepared. The reaction mixture contained 2 ml of test sample/standard of different concentrations and 1 ml of albumin (1%). The mixture was incubated at 37ºC for 15 min and then heated at 70ºC for 15 min in a water bath. After cooling the turbidity was measured at 660 nm with a spectrophotometer (Camspec M508, England). Ibuprofen was used as a standard. Percentage inhibition of albumin denaturation (IAD) was calculated against control. The control sample was albumin with the same concentration dissolved in distilled water.

$$\% \text{ IAD} = [(A_{control} - A_{sample}) / A_{control}] * 100$$

In-vitro anti-arthritic activity. The analysis was performed according to the method of Sakat [13]

with minor modification. The reaction mixture contained 2 ml of 0.06 mg/ml trypsin, 1 ml of Tris–HCl buffer (20 mM, pH 7.4) and 1 ml of test sample/standard (in methanol) of different concentrations (20-500 µg/ml). The mixture was incubated at 37ºC for 5 min. Then, 1 ml of human albumin (4% v/v) was added. The mixture was incubated for an additional 20 min. To the mixture, 2 ml of 70% perchloric acid was added for termination of the reaction. The cloudy suspension was cooled and centrifuged at 5000 rpm for 20 min. The absorbance of the supernatant was measured at 280 nm with a spectrophotometer (Camspec M508, England) against a control solution.

$$\% \text{ PIA} = [(A_{control} - A_{sample}) / A_{control}] * 100$$

Prediction of anti-inflammatory and anti-arthritic activity. A computerized prediction of biological activity (anti-inflammatory and anti-arthritic) for the obtained compounds was performed using PASS Online program [14].

Physicochemical characterisation

Determination of lipophilicity as R_M values. Determination of lipophilicity of ibuprofen derivatives was performed according to the method reported by Pontiki and Hadjipavlou-Litina [16].

Determination of lipophilicity as clogP. The lipophilicity was evaluated by calculating LogP of the obtained compounds *via* ACD/ChemSketch/ LogP Predictor v.14.08.

Statistical analysis

The presented experimental data were generated in triplicate. Data were expressed as mean ± SD. The level of significance was set at $p < 0.05$. The correlation between HPSA, IAD, PIA and lipophilicity was analysed using Pearson's test.

RESULTS AND DISCUSSION

Chemistry

The amides synthesis is very important in the pharmaceutical industry. Different amides are present in around 25% of the top-selling pharmaceutical products and in many other medicinally important compounds [17]. The desired amides can be obtained from wide variety of different precursors by a range of reaction pathways. Three of the most effective methods for synthesis of amides are nucleophilic acyl substitution, partial hydrolysis of nitriles and combination of amines with carboxylic acids in the presence of DCC, EDC or other "dehydrating" reagents. Using *N,N'*-dicyclohexylcarbodiimide

different amides can be formed under very mild conditions (Scheme 1). A convenient method for the preparation of the amides of amines and carboxylic acids is the method described in the literature using *N,N*-dicyclohexylcarbodiimide. DCC reacts with the carboxyl group of ibuprofen to produce an activated acylation agent that reacts with the amino group of the other molecule to form an amide bond (Scheme 1). All compounds are characterized for their melting points (MP), ^1H and ^{13}C NMR, UV, IR and HRMS spectra.

Biological evaluation

All synthesized ibuprofen derivatives were tested for their *in-vitro* antioxidant, anti-inflammatory and anti-arthritic activity, assessed by HPSA, IAD and PIA. The data from these analyses were compared with the *in-silico* obtained data (Table 1).

H₂O₂ scavenging activity

It has been demonstrated that free radicals play an important role in the pathogenesis of specific diseases [16]. Comparing with ascorbic acid (87.60 μg/ml), the newly obtained ibuprofen derivatives demonstrated lower *in-vitro* antioxidant activity. Despite their lipophilic nature, the synthetic

analogue **3c** (195.24 μg/ml) showed the highest antioxidant activity compared to ibuprofen, while the rest of the compounds exhibited weaker antioxidant activity (Table 1, Figure 1). We assume that the high activity of **3c** is due to the obtained reactive OH radicals bound to the benzene nuclei at the free *para*-positions. From the literature is known that OH radicals hydroxylate the most electron-rich phenolic moiety over the benzoic ring, generating mainly ortho and para phenols [15]. Although hydrogen peroxide is not very reactive, it can cause cytotoxicity by generating hydroxyl radicals in the cell. Hydroxyl radicals are the most reactive and are thought to be responsible for some tissue damage caused by inflammation. In living organisms, the superoxide anion radical ($O_2^{-\cdot}$) and H_2O_2 are transformed into $\cdot OH$ radicals and $\cdot O_2$, which are responsible for cell damage. The inflammatory process causes the generation of a superoxide anionic radical at the inflammation site and this is associated with the formation of other oxidizing species such as $\cdot OH$. Scavengers of hydroxyl radicals can increase the synthesis of prostaglandins [16]. Therefore, the removal of H_2O_2 is very important in the prevention of the generation of $\cdot OH$.

3a R=R₁=R₂=H;
  b R=R₁=OCH₃, R₂=H;
  c R=R₁=H, R₂=C₆H₅;
  d R=OCH₃, R₁=H, R₂=4-OCH₃(C₆H₄);
  e R=R₁=OCH₃, R₂= 3, 4-(OCH₃)₂(C₆H₃).
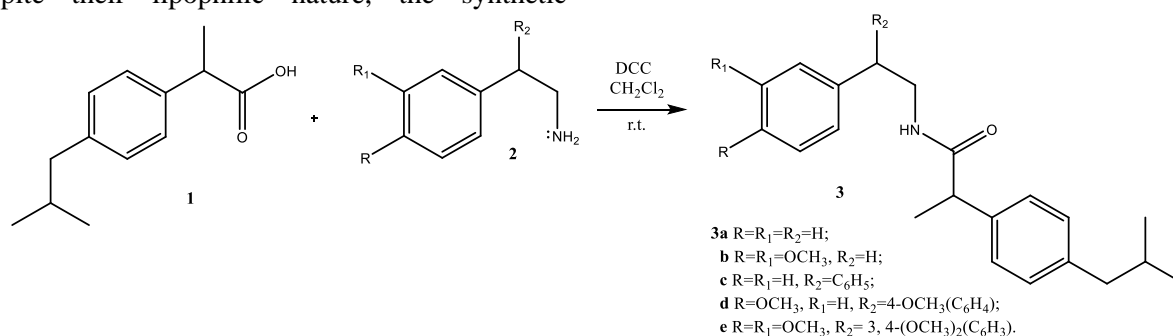
Scheme 1. Synthesis of ibuprofen amide derivatives.

Table 1. *In-vitro* and *in-silico* results. The *in-vitro* results are expressed as IC₅₀.

Compound	HPSA μg/ml	IAD$_{Egg Alb}$ μg/ml	IAD$_{Human Alb}$ μg/ml	PIA μg/ml	R$_M$	*clogP*	*cAnti-I*	*cAnti-A*
AA	87.60 ± 7.48	–	–	–	–	–	–	–
Ibuprofen	382.62 ± 12.40	69.34 ± 5.59	81.50 ± 4.95	259.82 ± 9.14	1.02 ± 0.024	3.72	0.903	0.573
3a	930.41 ± 79.74	243.52 ± 17.15	200.33 ± 5.59	79.51 ± 3.98	1.46 ± 0.029	4.93	0.402	0.311
3b	542.26 ± 52.03	133.98 ± 0.59	137.61 ± 3.54	85.45 ± 4.68	1.37 ± 0.041	4.67	0.408	0.34
3c	195.24 ± 15.89	133.97 ± 0.69	130.34 ± 0.65	22.85 ± 3.04	1.30 ± 0.040	6.52	0.330	0.264
3d	263.22 ± 17.15	152.47 ± 0.56	157.52 ± 3.77	61.04 ± 4.52	1.44 ± 0.045	6.35	0.342	0.282
3e	603.88 ± 63.48	178.83 ± 13.43	146.41 ± 6.11	49.15 ± 4.14	1.35 ± 0.043	6.00	0.350	0.298

R$_M$ – lipophilicity; cAnti-I – calculated anti-inflammatory activity; cAnti-A – calculated anti-arthritic activity.
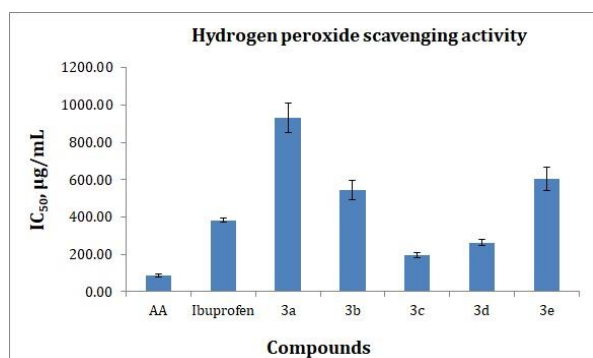
Figure 1. HPSA of ibuprofen derivatives. Ascorbic acid (AA) used as a standard.

Anti-inflammatory activity

Denaturation of proteins is a well-documented cause of inflammation in rheumatoid arthritis. Several anti-inflammatory drugs have shown dose-dependent ability to inhibit thermally induced protein denaturation [13]. The newly obtained ibuprofen amides were screened for anti-inflammatory activity *via* inhibition of albumin denaturation method. For this purpose, we used egg and human albumin.

Anti-arthritic activity

Proteinases have been implicated in arthritic reactions. Neutrophils are known to be a rich source of proteinase which carries in their lysosomal granules many serine proteinases. It was previously reported that leukocytes' proteinase plays an important role in the development of tissue damage during inflammatory reactions and significant level of protection was provided by proteinase inhibitors [13].

Anti-arthritic activity was assessed by PIA. The obtained results present that ibuprofen derivatives show higher anti-arthritic activity compared to ibuprofen (Table 1, Figure 2B). The highest activity was demonstrated by compound **3c** (22.85 µg/ml), which correlated well with the results of the HPSA

and IAD tests. Despite the low anti-arthritic activity shown by compound **3c** in the *in-silico* analysis, the experimental data showed the opposite results. The percentages of inhibition of synthesized ibuprofen derivatives are presented in Figure 2A. The IC_{50} values of ibuprofen, estimated as IAD against egg and human albumin, are 69.34 µg/ml and 81.50 µg/ml, respectively (Table 1, Figure 2A). It is therefore used as a standard to compare the anti-inflammatory activity of synthetic ibuprofen analogues. Compounds **3b** and **3c** showed the highest anti-inflammatory activity, followed by **3d** and **3e**. In vitro analysis of ibuprofen derivatives by IAD is essential for the study of new potential anti-inflammatory agents. Obtaining these data may allow creating a model that can reliably predict the anti-inflammatory efficacy of new synthetic analogues of ibuprofen. The studied synthetic analogues showed high lipophilicity, which to some extent affects the anti-inflammatory activity.

Lipophilicity

Lipophilicity is the most regularly appliedparameter used in SAR drug discovery studies. It can be experimentally determined or calculated. Lipophilicity has been correlated to permeability, solubility, increases in target potency and toxicity. We determined the lipophilicity by reverse-phase thin layer chromatography (RPTLC) method as R_M values and compared them with the corresponding theoretically calculated c*LogP* values in *n*-octanol-buffer using ACD/ChemSketch/ LogP Predictor v.14.08. This is considered to be a reliable, fast, and convenient method for expressing lipophilicity. Aside from the essential role of lipophilicity for the kinetics of biologically active compounds, antioxidants of hydrophilic or lipophilic character are both needed to act as radical scavengers in the aqueous phase or as chain-breaking antioxidants in biological membranes [16].
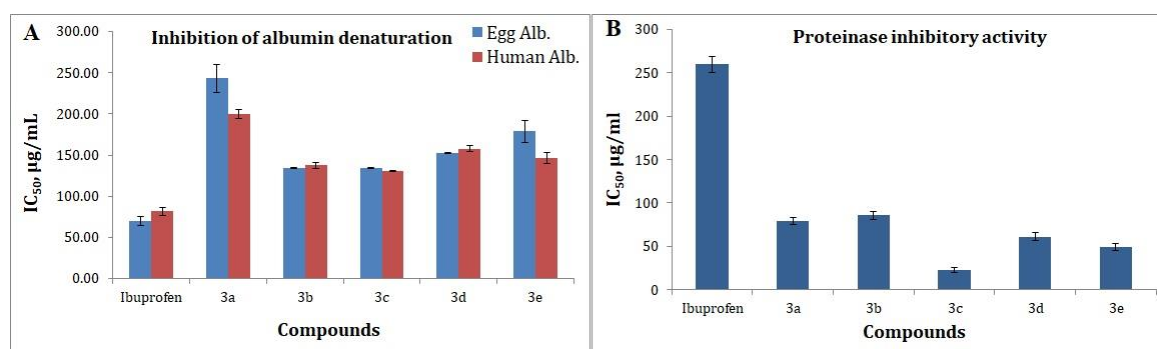

Figure 2. (**A**) *In-vitro* anti-inflammatory activity of ibuprofen derivatives. (**B**) *In-vitro* anti-arthritic activity of ibuprofen derivatives. Ibuprofen is used as a standard.

Table 2. Correlation between antioxidant, anti-inflammatory and antiarthritic activities with lipophilicity, expressed as r.

	HPSA	*IAD$_{Egg\ Alb}$*	*IAD$_{Human\ Alb}$*	*PIA*	*R$_M$*
HPSA	1	0.8579	0.7643	0.6568	0.5030
IAD$_{Egg\ Alb}$		1	0.9355	0.3781	0.6326
IAD$_{Human\ Alb}$			1	0.5238	0.8360
PIA				1	0.6928
R$_M$					1

The obtained results allowed us to establish a correlation between *in-vitro* biological activity and lipophilicity, expressed as r (Table 2). Good correlation dependence of HPSA with IAD and PIA (r > 0.6) shows that the synthetic analogues of ibuprofen possess complex activity, i.e. antioxidant, anti-inflammatory and anti-arthritic. In addition, we can assume that the results of anti-inflammatory and anti-arthritic activities show that they are influenced by lipophilicity (Table 2).

CONCLUSION

In conclusion, we have successfully synthesized a sequence of amides containing ibuprofen fragment in their scaffold. The compounds were biologically evaluated *in-vitro* and *in-silico* for their anti-inflammatory, anti-arthritic and antioxidant activities. Lipophilicity as R$_M$ values and Log*P* as a fundamental property were also evaluated. Good correlation dependence of HPSA with IAD and PIA (r > 0.6) was observed. The newly synthesized compounds showed low antioxidant and anti-inflammatory and high anti-arthritic activity.

REFERENCES

1. I. Melnikova, *Nat. Rev. Drug Discov,.* **4**, 453 (2005).
2. K. Manjunatha, B. Poojary, P. L. Lobo, J. Fernandes, N. S. Kumari, *Eur. J. Med. Chem.,* **45**, 5225 (2010).
3. M. Amir, S. Kumar, *Acta Pharm.,* **57**, 31 (2007).
4. M. T. Cocco, C. Congiu, V. Onnis, M. Morelli, O. Cauli, *Eur. J. Med. Chem.,* **38**, 513 (2003).
5. A. R. Hajipour, L. W. Guo, A. Pal, T. Mavlyutov, A. E. Ruoho, *Bioorganic Med. Chem.,* **19**, 7435 (2011).
6. B. B. Kashid, P. H. Salunkhe, B. B. Dongare, K. R. More, V. M. Khedkar, A. A. Ghanwat, *Bioorg. Med. Chem. Lett.,* **30**, 127136 (2020).
7. S. Sharma, D. Kumar, G. Singh, V. Monga, B. Kumar, *Eur. J. Med. Chem.,* **200**, 112438 (2020).
8. P. N. Praveen Rao, E. E. Knaus, *J. Pharm. Pharm. Sci.,* **11**, 81s (2008).
9. H. M. Suranji Wijekoon, S. Kim, E. C. Bwalya, J. Fang, K. Aoshima, K. Hosoya, M. Okumura, *Res. Vet. Sci.,* **122**, 179 (2019).
10. D. Costa, A. Gomes, S. Reis, J. L. F. C. Lima, E. Fernandes, *Life Sci.,* **76**, 2841 (2005).
11. B. M. Ali, M. Boothapandi, A. Sultan Nasar, *Data Br.,* **28**, 104972 (2020).
12. R. J. Ruch, S.-J. Cheng, J. E. Klaunig, *Carcinogenesis,* **10**, 1003 (1989).
13. S. S. Sakat, A. R. Juvekar, M. N. Gambhire, *Int. J. Pharm. Pharm. Sci.,* **2**, 146 (2010)
14. D. A. Filimonov, A. A. Lagunin, T. A. Gloriozova, A. V. Rudik, D. S. Druzhilovskii, P. V. Pogodin, V. V. Poroikov, *Chem. Heterocycl. Compd.,* **50**, 444 (2014).
15. G. Capocasa, G. Olivo, A. Barbieri, O. Lanzalunga, S. Di Stefano, *Catal. Sci. Technol.,* **7**, 5677 (2017).
16. E. Pontiki, D. Hadjipavlou-Litina, *Bioorg. Med. Chem.,* **15**, 5819 (2007).
17. M. Zhang, S. Imm, S. Bähn, L. Neubert, H. Neumann, M. Beller, *Angew. Chemie - Int. Ed.,* **51**, 3905 (2012).

Synthesis of efficient iron phosphide catalyst for electrocatalytic hydrogen generation

T. Chouki[1], D. Lazarević[2], B. V. Donkova[3], S. Emin[1*]

[1]*Materials Research Laboratory, University of Nova Gorica, Vipavska 11c, 5270, Ajdovščina, Slovenia*
[2]*Faculty of Sciences, Department of Chemistry, University of Novi Sad, 21000, Novi Sad, Serbia*
[3]*Faculty of Chemistry and Pharmacy, University of Sofia, 1 James Bourchier Blvd., 1164, Sofia, Bulgaria*

A solvothermal synthesis of iron phosphide electrocatalysts using triphenylphosphine (TPP) as phosphorus precursor is presented. The synthetic protocol generates Fe_2P/FeP phase at 350°C. After deposition of the catalyst onto graphite substrate heat-treatment at higher temperature was carried out. Annealing at 500°C under reductive atmosphere induced structural changes in the Fe_2P/FeP samples which yielded a pure Fe_2P phase. The electrocatalytic activity of the Fe_2P catalyst was studied for hydrogen evolution reaction (HER) in 0.5 M H_2SO_4. The recorded overpotential for HER was about 130 mV *vs.* a reversible hydrogen electrode (RHE) at 10 mA cm^{-2}.

INTRODUCTION

It has been demonstrated that transition metal phosphides (TMPs) such as iron phosphides [1, 2], cobalt phosphides [3], nickel phosphides [4], molybdenum phosphides [5], and tungsten phosphides [6], among others, are efficient electrocatalysts for hydrogen evolution reaction (HER). TMPs are considered as alternative catalysts to platinum group metals because of their abundance, low cost, and high catalytic activity [7]. Usually, traditional methods, such as chemical vapor deposition (CVD), temperature-programmed reduction (TRP), or solvothermal synthesis, are used to synthesize TMPs [8, 9]. In CVD, volatile precursors decompose on a heated substrate and give the corresponding class of materials like TMPs. The TRP approach is based on the reduction of metal phosphates using hydrogen gas. However, both CVD and TRP have limitations because these require expensive equipment [10] and high temperatures (~600 – 900°C) during the reaction process. The solvothermal technique is a preferred way for preparation of TMPs at low temperatures based on the reaction of a metal precursor with phosphorus (P)-containing reagents [9] such as trioctylphosphine (TOP), red phosphorus [11], tributyl phosphine (TBP) [12], tri-*n*-octylphosphine oxide (TOPO) [13], and tris(diethylamino) phosphine (TEAP) [12]. Among these P-precursors, TOP was the most studied for the synthesis of iron phosphides (Fe_2P and FeP) [14, 15], cobalt phosphide (CoP) [3], nickel phosphide (Ni_2P) [16], molybdenum phosphide (MoP) [17], tungsten phosphide (WP) [6], etc.

However, TOP and most of the cited above precursors are expensive, toxic, and unstable in air. To overcome these limitations, triphenylphosphine (TPP) and triphenyl phosphite (TPOP) were introduced in the synthesis of TMPs [18]. TPP possesses moderate stability against oxidation in air and has been used for synthesis of TMPs in Ullmann-type reactions with ferrocene in vacuum-sealed tubes [19] or open-tube furnaces in an inert atmosphere at 350 to 400°C [20]. The application of TPP in solvothermal synthesis of TMPs was demonstrated for cobalt phosphide (Co_2P) NPs [21], nickel phosphide (Ni_xP_y) NPs [22] and for Fe_2P and FeP NPs in our previous study [23]. However, little is known about the preparation of mixed Fe_2P/FeP phases using TPP precursor and their use in HER studies.

Herein, we report the solvothermal synthesis of iron phosphide microspheres (MS) using a TPP precursor. At the conditions applied the synthesis procedure generated Fe_2P/FeP MS. With the goal to test the obtained Fe_2P/FeP MS in HER studies these were spin-coated onto graphite substrate and heat-treated under reductive ($Ar:H_2$) atmosphere. However, the heat treatment caused structural transformations of mixed Fe_2P/FeP to Fe_2P phase. The electrocatalytic tests showed that the obtained Fe_2P phase is an efficient catalyst for HER.

EXPERIMENTAL

Materials

Iron pentacarbonyl (>99.99%, Fe (CO)$_5$), OLA (70%), ethanol (98%, EtOH), acetone (95%), and sulfuric acid (97%, H_2SO_4) were purchased from Sigma-Aldrich. TPP (99%), SQ (98%), and chloroform (99.5%, $CHCl_3$) were purchased from

Alpha Aesar (United Kingdom). A graphite block (99.9%) used as a substrate was obtained from Beijing Great Wall Co., Ltd. (China).

Synthesis of Fe₂P/FeP MS and preparation of Fe₂P catalyst

The synthesis of Fe₂P/FeP NPs was achieved under the following conditions: 0.6 g of Fe(CO)₅, 3.14 g of TPP, 3 ml of OLA, and 8 ml of SQ were mixed in a 100 ml three-neck flask (Ar atmosphere) and heated at 150°C (ramp rate: 10°C/min) until the TPP was dissolved. Later, the reaction temperature was increased and kept at 350°C for 15 min. After cooling the suspension, the product was isolated by adding a mixture of solvents (10 ml, ethanol/acetone –v/v, 1:1). Following centrifugation at 8000 rpm for 5 min and decantation of the solution, the Fe₂P/FeP product was isolated as a solid material. After this the solid mass was dried at 50°C for 30 min, roughly 0.27 g of powder was obtained. The obtained iron phosphide powder (e.g., 0.27 g) was dispersed in 2 ml of CHCl₃ and spin-coated on graphite at 600 rpm for 20 s. To remove the organics from the surface heat treatment of the Fe₂P/FeP thin film was conducted at 500°C for 30 min (heating ramp: 10°C min⁻¹) in a muffle furnace under a mixture of Ar:H₂ gasses (65:35 % v/v, Inoxline H35, Messer) where the gas flow rate was adjusted to 3 L min⁻¹. In our earlier studies we found that it is essential to use a mixture of gases and the cited above ratio to produce active catalyst for HER [23]. The amount of catalyst loaded onto the graphite was in the range of 20 mg cm⁻².

Characterization

The morphology of the catalyst was studied using a scanning electron microscope (JEOL JSM 7100 F). Transmission electron microscopy (TEM) study of Fe₂P/FeP particles was carried out using a JEOL 2100F microscope at an accelerating voltage of 200 kV. X-ray diffraction (XRD) studies were performed using the MiniFlex 600 (Rigaku) and the diffractograms were analyzed using the PDXL software package, Ver. 1.4. Rietveld analysis of the mixed Fe₂P/FeP phase was carried out using the MAUD software [24]. All electrochemical measurements were performed using a potentiostat (EDAQ SP1) in a typical three-electrode system, in a 0.5 M H₂SO₄ aqueous solution (pH ≈ 0). Linear sweep voltammetry (LSV) tests were performed using Ag/AgCl (Sigma-Aldrich) as the reference electrode, iron phosphide-coated graphite substrates as the working electrodes, and graphite as the counter electrode with a scan rate of 5 mV s⁻¹. Experimentally measured potentials were converted

to a reversible hydrogen electrode (E_{RHE}) scale using the following equation:

$$E_{RHE} = E_{Ag/AgCl} + E^0_{Ag/AgCl} + (0.059 \times pH),$$

where $E_{Ag/AgCl}$ is the measured potential *vs.* Ag/AgCl and $E^0_{Ag/AgCl} = 0.197$ V is the standard potential of the Ag/AgCl reference electrode vs. RHE (at 25°C). Charge-transfer resistance was accessed using EIS measurements in 0.5 M H₂SO₄, at various applied potentials from −0.35 to −0.6 V *vs.* Ag/AgCl and frequencies from 100 to 1 MHz (10 mV AC dither).

RESULTS AND DISCUSSION

The XRD pattern (Fig. 1) of the not well crystallized mixed Fe₂P/FeP sample shows characteristic diffraction peaks at 41.05°, 44.33°, and 48°, which matched (111), (201) and (210) plane peaks of hexagonal Fe₂P ($P\bar{6}2m$, PDF# 1008826).
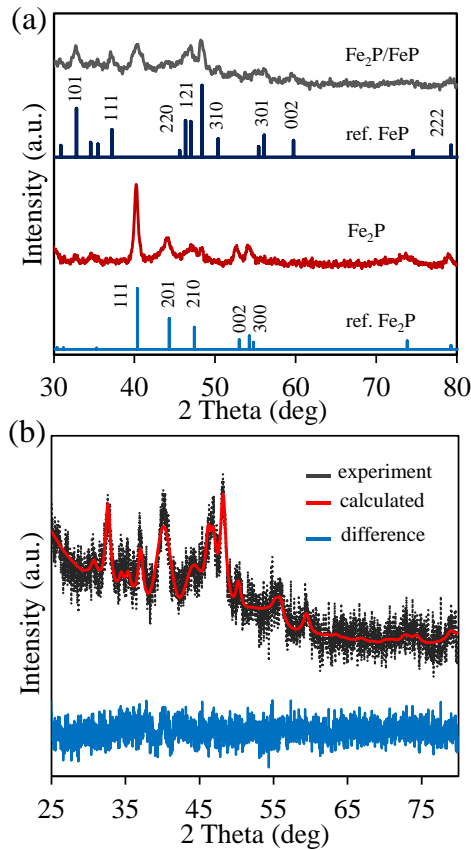

Fig. 1. (a) XRD patterns of Fe₂P/FeP synthesized at 350°C and Fe₂P obtained after the heat-treatment at 500°C. The XRD patterns of reference phases are given with labels. (b) Rietveld refinement of the mixed Fe₂P/FeP sample.

The calculated crystal lattice parameters $a = b = 5.8220 \pm 0.0070$ Å and $c = 3.5204 \pm 0.0061$ Å show a good agreement with existing literature values for hexagonal Fe₂P. The XRD diffraction peaks at 32.8°, 46.3°, and 48.38° are typical for the (101), (211), and

(121) planes of the orthorhombic FeP phase (*Pbnm*, PDF# 9008932). The determined crystal lattice parameters are equal to $a = 5.8097 \pm 0.0041$ Å, $b = 5.2042 \pm 0.0031$ Å, and $c = 3.1091 \pm 0.0018$ Å. The crystallite size calculated using the Williamson-Hall (W-H) method yielded an average size of 9.2 ± 0.4 nm for Fe_2P and 13.6 ± 0.3 nm for FeP samples. The calculated microstrain ($\times 10^{-5}$) was found as 1.63 ± 0.03 a.u. (FeP) and 2.2 ± 0.02 a.u. (Fe_2P). The mean crystallite size of Fe_2P and FeP estimated by W-H method and Scherrer's equation [25] is highly intercorrelated in the frame of standard deviation. The Rietveld quantification gives a weight ratio of different phases in the as-synthesized Fe_2P/FeP sample equal to 45.1 ± 2.4 % (Fe_2P) and 54.9 ± 2.4 % (FeP). The heat-treatment process under reductive atmosphere converted the mixed Fe_2P/FeP to pure hexagonal Fe_2P ($P\bar{6}2m$, PDF# 1008826) where the calculated crystallite size of Fe_2P is 14.7 nm.

TEM images of iron Fe_2P/FeP particles are shown in Fig. 2.
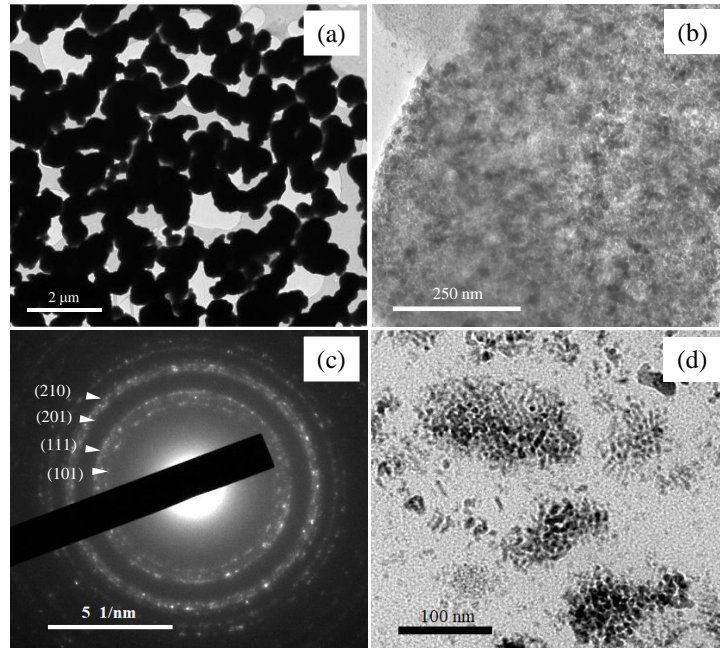
Fig. 2. (a,b,d) TEM images of Fe_2P/FeP particles at different magnifications. (c) The SAED is taken from the image in (b).
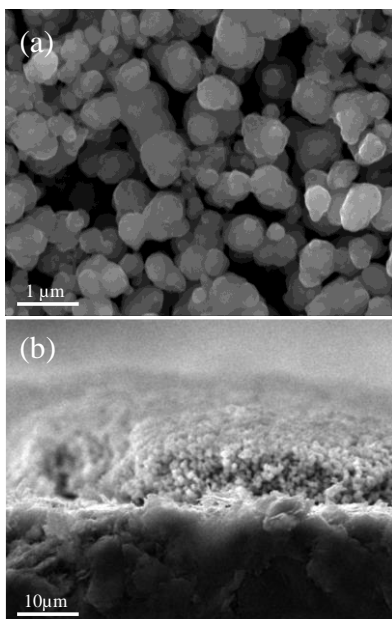
Fig. 3. SEM images of Fe_2P thin film in (a) top- and (b) cross-section views.

Detailed analysis of the obtained Fe_2P/FeP sample confirmed the presence of microspheres (MS) (Fig. 2a). The agglomerates in the TEM image do not reveal the real morphology since these are composed of individual Fe_2P/FeP MS. Closer look of the agglomerates show that these MS are made of small Fe_2P/FeP nanoparticles (NPs) with sizes in the range of 10 to 30 nm (Figs. 2b, d). The selected area electron diffraction (SAED) pattern confirms that the Fe_2P/FeP NPs are polycrystalline (Fig. 2). The lattice fringes in SAED image are equal to 2.835, 2.415 and 2.083 Å and correspond to (101), (111) and (201) planes for the Fe_2P and FeP. Figure 3 shows SEM images of Fe_2P MPs obtained after spin-coating of Fe_2P/FeP chloroform suspension onto graphite substrate and heat-treatment stage. The typical size range of Fe_2P microspheres is between 200 - 1000 nm (e.g. 1 µm). The average film thickness determined from the cross-section profile is close to ~10 µm (Fig. 3b).
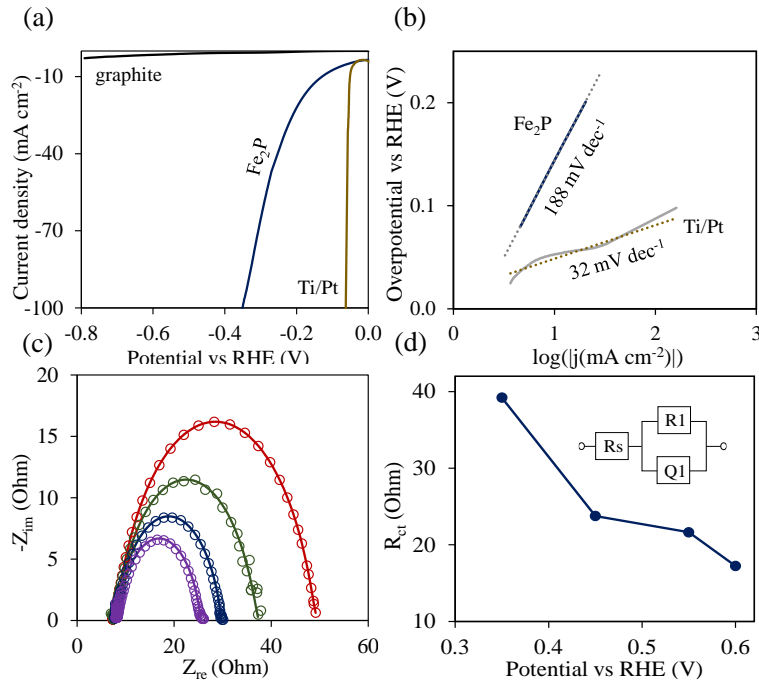
Fig. 4. (a) LSV characteristics (*iR*-corrected) of Fe_2P catalyst recorded at 5 mV s^{-1} in 0.5 M H_2SO_4. For comparison, the pure graphite and a reference Ti/Pt electrode are also given. In (b) the Tafel plots of Fe_2P and Ti/Pt are given. In (c), EIS characteristics of Fe_2P. (d) Plot of R_{ct} *vs*. potential (negative values) for Fe_2P. The inset in (d) is a circuit element used to fit the EIS data.

Table 1. Selected summary of the HER performance of some iron phosphide particles in 0.5 M H_2SO_4. The overpotential of the electrocatalyst at a current density of 10 mA cm^{-2} (η_{10}).

Material	P source	Tafel slope (mV dec^{-1})	η_{10} (mA cm^{-2})	Ref.
FeP NPs/Ti	TOP	37	50	[15]
FeP NAs/CC	NaH_2PO_2	45	58	[26]
FeP@GPC	NaH_2PO_2	68	72	[27]
FeP NAs/Ti	NaH_2PO_2	60	85	[28]
FeP NWs array	(PH_3) gas	39	96	[29]
FeP$_x$-300	NaH_2PO_2	64	100	[30]
FeP NR	($NaH_2PO_2 \cdot H2O$)	54	107	[31]
Fe_2P/FeP	TPP	119	110	[23]
HMFeP@C	PB	56	115	[32]
FeP NRs	NaH_2PO_2	55	120	[1]
Fe_2P NPs	**TPP**	**188**	**130**	**This study**
FeP NPs	TOP	64	135	[14]
FeP NPs	NaH_2PO_2	65	154	[33]
FeP NWs - free	(PH_3) gas	66	193	[29]
Fe_2P@APC	NaH_2PO_2	90	196	[27]
FeP NSs	TOP	67	235	[34]
FeP$_x$-Ca	NaH_2PO_2	105	263	[30]
Bulk FeP	NaH_2PO_2	82	285	[1]

Legend: PC – porous carbons; NAs – nanorod arrays; Ca – calcination; CC – nanorod arrays on carbon cloth; GPC – graphitic carbon; NWs – nanowires; NRs – nanorods; NS – nanosheets; APC – amorphous carbon; and NPC – nitrogen & phosphorus co-doped carbon.

The HER performance of the iron phosphide catalyst is presented in Fig. 4. LSV characteristics of Fe$_2$P recorded in 0.5 M H$_2$SO$_4$ revealed 130 mV at 10 mA cm^{-2}. The recorded overpotential of 130 mV for Fe$_2$P was found to be smaller than that of many iron phosphide electrocatalysts reported in the literature (Table 1). Another useful metric for interpreting polarization curves is the Tafel plot which indicates potential *vs.* log|j/ (current in logarithm)| [35]. In terms of the Volmer limiting step, the Tafel slope provides illustrative information for the comparison of the kinetic rate for the proton discharge reaction: H$^+$ + e$^-$ + M → H$_{ad}$−M. The Tafel slopes of Ti/Pt (reference) and Fe$_2$P were 32 and 188 mV dec^{-1}, respectively (Fig. 4b). As a rule, the lower the Tafel slope, the better is the catalytic performance of the material. The higher Tafel slope observed in this study can be attributed to the rate-limiting steps associated with H$^+$ (adsorption)/H$_2$ (desorption) to different parameters such as exposed crystallographic facets, anionic/cationic vacancies, etc. [36]. EIS was used to determine the contribution of the Fe$_2$P catalyst toward HER at different applied potentials [21]. Figs. 4c, d show Nyquist plots for Fe$_2$P in 0.5 M H$_2$SO$_4$, recorded with a bias from −150 to − 400 mV *vs.* RHE. The electrical circuit used to fit the data was assumed to be made of sheet resistance (R_s), contact phase ($Q1$) and resistance ($R1$) elements (Fig. 4d). At the surface of the electrode, the kinetics of electrochemical reaction was governed by charge-transfer resistance (R_{ct}) [21]. Fig. 4d shows the R_{ct} values obtained from the fitted semi-circles as a function of applied bias. At high overpotentials, the observed drop of R_{ct} was the result of the faster charge-transfer kinetics for HER [21]. EIS measurements of the Fe$_2$P film showed a low R_{ct} of 11 Ohms cm^2 which indicated efficient catalytic activity toward HER.

CONCLUSIONS

Fe$_2$P/FeP catalyst was successfully synthesized using a low-cost TPP precursor. The obtained iron phosphide particles were spin-coated on a graphite substrate and heat-treated at 500°C. Heating of the Fe$_2$P/FeP sample under reductive atmosphere yielded Fe$_2$P phase. The overpotential for HER recorded with Fe$_2$P catalyst in this study was comparable with or lower than most state-of-the-art iron phosphide catalysts. EIS measurements revealed that iron phosphide samples showed low charge-transfer resistance (R_{ct}) of 11 Ohms cm^2 which was ascribed to efficient HER.

REFERENCES

1. H. Du, S. Gu, R. Liu, C. M. Li, *Int J Hydrogen Energy*, **40**, 14272 (2015).
2. X. Peng, A. M. Qasim, W. Jin, L.Wang, L. Hu, Y. Miao,W. Li, Y. Li, Z. Liu, K. Huo, K. Y. Wong, P. K. Chu, *Nano Energy*, **53**, 66 (2018).
3. E. J. Popczun, C. G. Read, C. W. Roske, N. S. Lewis, R. E. Schaak, *Angew. Chemie – Int. Edn.*, **53**, 5427 (2014).
4. Z. Zhou, L.Wei, Y. Wang, H. E. Karahan, Z. Chen, Y. Lei, X. Chen, S. Zhai, X. Liao, Y. Chen, *J. Mater. Chem. A*, **5**, 20390 (2017).
5. A. Adam, M. H. Suliman, H. Dafalla, A. R. Al-Arfaj, M. N. Siddiqui, M. Qamar, *ACS Sustain. Chem. Eng.*, **6**, 11414 (2018).
6. J. M. McEnaney, J. Chance Crompton, J. F. Callejas, E. J. Popczun, C. G. Read, N. S. Lewis, R. E. Schaak, *Chem. Commun.*, **50**, 11026 (2014).
7. Z. Gao, Q. Gao, Z. Liu, C. Zhang, X. Zhang, X. Liu, R. Wang, N. Li, *RSC Adv.*, **6**, 114430 (2016).
8. Q. Yang, R. Zhang, W. Wang, P. Zhou, L. Wang, T. Chen, H. Xu, L. Zheng, *Sustain. Energy Fuels*, **3**, 3078 (2019).
9. Y. Pei, Y. Cheng, J. Chen, W. Smith, P. Dong, P. M. Ajayan, M. Ye, J. Shen, *J. Mater. Chem. A*, **6**, 23220 (2018).
10. V. S. Milusheva, B. R. Tzaneva, M. C. Petrova, B. I. Stefanov, *Bulg. Chem. Commun.*, **5**, 15 (2020).
11. N. Coleman, M. D. Lovander, J. Leddy, E. G. Gillan, *Inorg. Chem.*, **58**, 5013 (2019).
12. Y. Park, H. Kang, Y. Hong, G. Cho, M. Choi, J. Cho, D. Ha, *Int. J. Hydrogen Energy*, (2020) doi.org/10.1016/j.ijhydene.2020.03.051.
13. S. Cao, Y. Chen, C. C. Hou, X. J. Lv, W. F. Fu, *J. Mater. Chem. A*, **3**, 6096 (2015).
14. G. Cho, H. Kim, Y. S. Park, Y. K. Hong, D. H. Ha, *Int. J. Hydrogen Energy*, **43**, 11326 (2018).
15. J. F. Callejas, J. M. McEnaney, C. G. Read, J. C. Crompton, A. J. Biacchi, E. J. Popczun,T. R. Gordon, N. S. Lewis, R. E. Schaak, *ACS Nano*, **8**, 11101 (2014).
16. Y. Shi, Y. Xu, S. Zhuo, J. Zhang, B. Zhang, *ACS Appl. Mater. Interfaces*, **7**, 2376 (2015).
17. J. M. McEnaney, J. C. Crompton, J. F. Callejas, E. J. Popczun, A. J. Biacchi, N. S. Lewis, R. E.Shaak, *Chem. Mater.*, **26**, 4826 (2014).

18. J. Liu, M. Meyns, T. Zhang, J. Arbiol, A. Cabot, A. Shavel, *Chem. Mater.*, **30**, 1799 (2018).

19. J. Wang, Q. Yang, Z. Zude, *J. Phys. Chem. Lett.*, **1**,102 (2010).

20. G. Li, Q. Yang, J. Rao, C. Fu, S. Liou, G. Auffermann,Y. Sun, C. Felser, *Adv. Funct. Mater.*, ****30**, 1907791 (2020).

21. Z. Huang, Z. Chen, Z. Chen, C. Lv, M. G. Humphrey, C. Zhang, *Nano Energy*, **9**, 373 (2014).

22. J. Wang, A. C. Johnston-Peck, J. B. Tracy, *Chem. Mater.*, **21**, 4462 (2009).

23. T. Chouki, M. Machreki, S. Emin, *Int. J. Hydrogen Energy*, **45**, 21473 (2020).

24. L. Lutterotti, *Nucl. Instrum. Methods Phys. Res., B*, **268**, 334 (2010).

25. P. Paunović, O. Popovski, G. Načevski, E. Lefterova, A. Grozdanov, A. T. Dimitrov, *Bulg. Chem. Commun*, **50**, 82 (2018).

26. Y. Liang, Q. Liu, A. M. Asiri, X. Sun,Y. Luo, *ACS Catal.*, **4**, 4065 (2014).

27. Y. Yao, N. Mahmood, L. Pan, G. Shen, R. Zhang, R. Gao, F. Aleem, X. Zhang, J. J. Zou, *Nanoscale*, **10**, 21327 (2018).

28. R. Liu, S. Gu, H. Du, C. M. Li, *J. Mater. Chem. A*, **2**, 17263 (2014).

29. C. Y. Son, I. H. Kwak, Y. R. Lim, J. Park, *Chem. Commun.*, **52**, 2819 (2016).

30. M .Wang, R. Zhao, X. Li, X. Zhao, L. Jiang, *ChemNanoMat*, **5**, 593 (2019).

31. C. Lin, Z. Gao, J. Yang, B. Liu, J. Jin, *J. Mater. Chem. A*, **6**, 6387 (2018).

32. X. Zhu, M. Liu, Y. Liu, R. Chen, Z. Nie, J. Li, S.Yao, *J. Mater. Chem. A*, **4**, 8974 (2016).

33. L. Tian, X. Yan, X. Chen, *ACS Catal.*, **6**, 5441 (2016).

34. Y. Xu, R. Wu, J. Zhang, Y. Shi, B. Zhang, *Chem. Commun.*, **49**, 6656 (2013).

35. S. Emin, C. Altinkaya, A. Semerci, H. Okuyucu, A. Yildiz, P. Stefanov, *Appl. Catal. B Environ.*, **236**, 147 (2018).

36. T. Shinagawa, A. T. Garcia-Esparza, K. Takanabe, *Sci. Rep.*, **5**, 13801 (2015).

Bio-oil and char production from *Jatropha Curcus* seed cake *via* slow pyrolysis: a comparative study of thermochemical and fuzzy modeling

V. K. Sohpal

Department of Chemical Engineering & Bio Technology, BCET, Gurdaspur, Punjab, India

Jatropha seed cake (JSC) biomass is one of the prominent feedstocks for renewable energy production through thermochemical conversion. In this work firstly slow pyrolysis was conducted to find the product yield of charcoal and bio-fuel in a fixed-bed reactor. Secondly, a fuzzy model of the operating variable was developed using ANFIS through mamdani MIMO system for thermochemical kinetic data. The proposed modeling was verified by comparing with the observed practical results obtained by thermochemical conversion under specific conditions. Results showed that the maximum oil yield was 18.42 wt.% obtained at 530ºC for the mesh size of -6+8 at a sweep gas velocity of 150 ml/min, due to the elimination of the mass and heat transfer limitations by high heating rates. At the lowest pyrolysis temperature of 500ºC high amounts of char products were obtained. Mamdani MIMO system provides a representation of the process parameters and its output is close to the experimental result.

Keywords: Biomass, thermochemical conversion, ANFIS, charcoal, bio-fuel.

INTRODUCTION

Agriculture-based residual and its availability as a waste product is a leading source of renewable energy. Amongst the many varied ways to utilise biomass as a source of energy is pyrolysis, a thermochemical decomposition process that occurs at elevated temperatures in the absence of oxygen gas. Biomass pyrolysis produces gas and liquid products and leaves a solid residue known as char [1]. The liquid product is a fuel termed as bio-oil, pyrolysis oil or bio-crude [2]. Presently, bio-oil produced from the pyrolysis of biomass can be used directly or after further physicochemical processes to heat boilers, or even drive diesel engines or turbines [3–5]. It can be stored and transported more efficiently compared to the original biomass because of its liquid state. During the combustion of bio-oil, its net-zero carbon dioxide (CO_2), as well as lesser nitrogen oxides (NOx) and/or sulfur oxides (SOx) emissions compared to fossil fuels make it a potential liquid fuel replacement [6]. The feedstock of interest is *Jatropha curcas (J. curcas)*, a drought-free inedible crop, which can be planted economically in tropical and sub-tropical regions [7]. Its seed is a source of oil that is currently used for commercial biodiesel production. Nevertheless, the extraction of oil for biodiesel production only takes up to 18 wt% of the dry fruit, but it has been reported that the remaining J. curcas fruit after biodiesel production has the potential of fuel production with twice the energy content compared to biodiesel [8]. Different parts of the J.

curcas shrub can be utilised in several thermochemical processes. J. curcas seed husk could successfully be used as feedstock for open core downdraft gasifier to generate producer gas. For pyrolysis, approximately 50 wt.% of its nutshell can be transformed into bio-oil and even its wood and leaves can be valorised for fuel extraction [9, 10]. The pressed cake remaining after oil extraction can also be used as a source of bio-oil production and it was found that the main thermal decomposition occurred over the temperature range of 523.15 – 723.15 K and could be described by the three-parallel reactions model [11]. Parametric study of flash pyrolysis was conducted for Jatropha oil cake in an electrically heated fluidised-bed reactor using nitrogen. The maximum oil yield of 64.25 wt.% was obtained at a particle size of 1.0 mm, and extract source of low-grade fuel directly [12]. Comparative analysis has been performed for different mesh sizes for product composition and result shows that slow pyrolysis experiments of Jatropha curcus seed cake in a fixed-bed reactor yield 18.42 wt. % of bio-oil at a pyrolysis temperature of 500°C, particle size of -6+8 mesh number and nitrogen gas flow rate of 150 ml/min. Heterogeneous catalysts and catalytic pyrolysis pretreatment can improve bio-oil quality and yield [13-15]. Palm oil-empty fruit bunches and rice husk were pyrolyzed to produce gas and liquid fuel in a semi-batch pyrolysis reactor [16]. Mathematical model and kinetic parameters were used to describe the pyrolysis of a single solid particle of biomass [17].

De-oiled seed cakes of African star apple and Silk cotton as a source of bio-oil were investigated using slow pyrolysis at temperatures of 300–450 °C for 60 min residence period in a nitrogen atmosphere. Maximum conversion of 72% takes place at 400 °C [18]. Pyrolysis of JC by-products adds to sustainable technology for energy production, heterogeneous catalyst and precursor of activated carbons/chemicals [19]. Response surface methodology was employed to optimum operating conditions for pyrolysis of Neem PSC. The highest liquid yield of 52.1 wt. % was achieved at 512.5 °C, 60 min and 0.5 L/min [20]. Fast pyrolysis of Jatropha was carried out in a fixed-bed batch reactor with temperature zone of 400°C to 550°C to produce liquid biofuel at an interval of 50°C. The higher temperature in the fast pyrolysis of the bio material produces maximum liquid yield [21]. Wheat straw was used as biomass material to produce bio-oil in a fluidized-bed fast reactor. The result shows that the highest bio-oil yield of 42 wt.% is obtained at a temperature of 500°C, feed particle size of 1 mm, and gas flow rate of 4 m^3h^{-1} [22]. Lignocellulosic and macro algae biomasses were used for bio char production using co-pyrolysis. It assists to change the morphological and surface composition of bio char [23]. Slow pyrolysis experiments of Jatropha curcus seed cake in a fixed-bed reactor yielded 18.42 wt % of bio-oil at a pyrolysis temperature of 500°C, particle size of -6+8 mesh number and nitrogen gas flow rate of 150 $ml.min^{-1}$ [24]. To date, while several research studies have indicated the potential of J. curcas

wastes as pyrolysis feedstock, this paper is an attempt to produce quality product using slow pyrolysis and optimize the process using adaptive neuro fuzzy system.

Experimental & Fuzzy Methodology

Analysis of Jatropha seed cake after the extraction of oil indicates that seed cake has a wide potential as feed stock for anaerobic slow pyrolysis. The seed cake has high protein content of 31.5% and significant percentages of cellulose and hemi-cellulose - 15.9% and 11.4%, respectively. In our experimental setup, a fixed-bed reactor was used for slow pyrolysis of JSC. Pretreatment of biomass was performed to reduce the size and remove the moisture content. After the biomass sample reached a constant weight (250 g), it was loaded into the fixed-bed reactor, and N_2 sweeping gas developed an inert atmosphere in the reactor. After constant heating, the reactions in the reactor began to take place at 450-500^{0}C through electrical heating. On further increasing the temperature (3^{0}K/min) products were formed which passed through the condenser for the desired liquid phase. Products were obtained using different techniques of the separation process for particle size -6+8 mesh number. Fuzzy model described in this thermochemical reactor system, shown in Fig. 2, is a MIMO system with two input parameters – nitrogen flow rate, and temperature of reactor and outputs as Biofuel and Biocahr. Possible universe of discourse for the input parameters is given in Fig. 1 for mamdani fuzzy system.
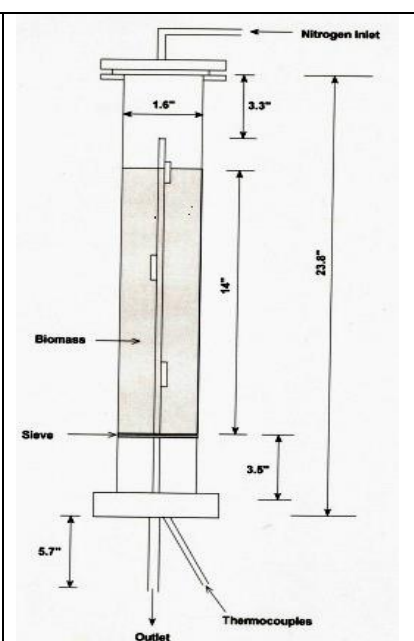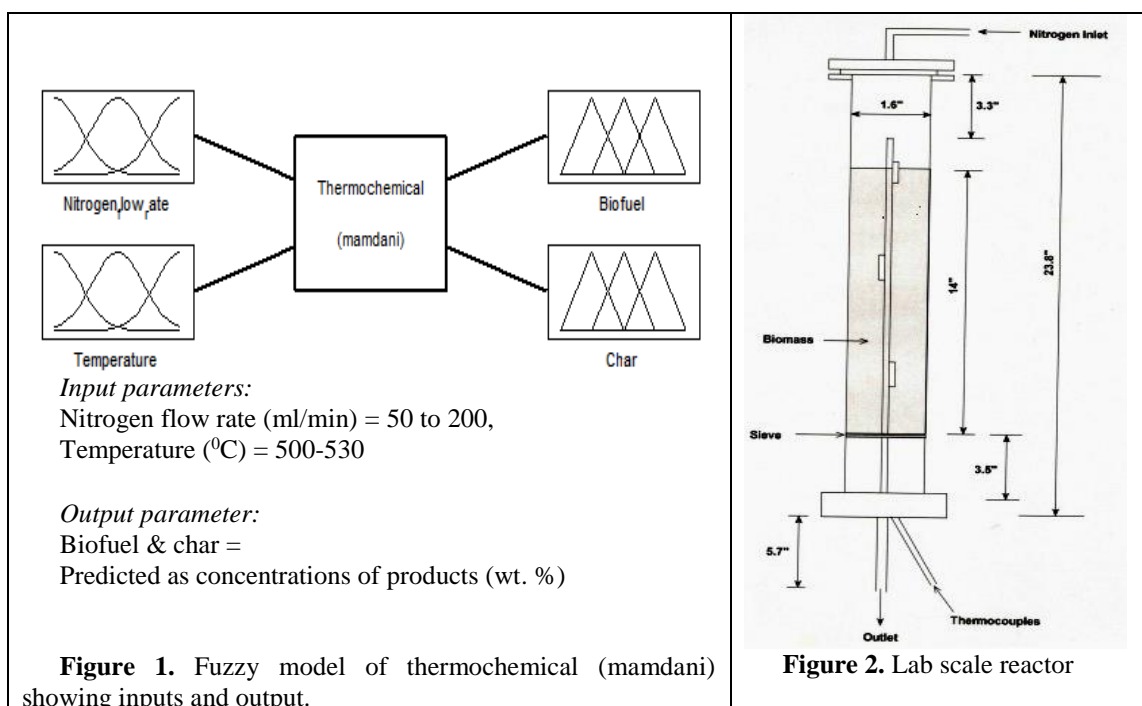

Input parameters:
Nitrogen flow rate (ml/min) = 50 to 200,
Temperature (^{0}C) = 500-530

Output parameter:
Biofuel & char =
Predicted as concentrations of products (wt. %)

Figure 1. Fuzzy model of thermochemical (mamdani) showing inputs and output.

Figure 2. Lab scale reactor

Table 1. Product yields (wt. %) of slow pyrolysis of JSC *vs.* temperature

Temperature (^{0}C)	500	505	510	515	520	525	530
Bio-Oil Yield (wt. %)	17.07	16.10	16.00	15.75	16.89	18.40	18.42
Char Yield (wt. %)	43.08	43.00	42.95	42.86	41.30	40.40	39.54

RESULTS AND DISCUSSION

Table 1 shows the product yields of JSC for pyrolysis temperatures of 500-530^{0}C for the particle size of -6+8 mesh number under sweep gas velocity of 50-150 ml/min. The maximum oil yield of 18.42 wt.% was obtained at 530ºC. The yield of oil increased from 17.07 wt. % to 18.42 wt. % when the pyrolysis temperature was increased from 500ºC to 530ºC. The oil yield increased due to the elimination of the mass and heat transfer limitations by high heating rates. The lowest pyrolysis temperature of 500ºC causes a relatively slow thermochemical conversion, and char products values are high. On further increasing the temperature the char wt % decreased due to the increase in the volatile matter.

Moreover, Table 1 clearly indicates that the bio-oil yield obtained by fixed-bed pyrolysis increases with the increase of N_2 flow rate causing cooling effect. As the pyrolysis reaction proceeds the N_2 flow rate reaches an equilibrium, this delay in cracking and bonding prolonging the duration of

the pyrolysis process in agreement with literature [25]. The above value of the temperature (^{0}C) used in the present investigation agrees well with the literature value of 636-800 ^{0}K for Jatropha pressed cake pyrolysis [26]. From the temperature range of 505-515^{0}C, the cellulose first breaks down, and then the lignin starts to crack down into char, water and heavy oil. This justifies the decrease in char production in favour of higher bio-oil product and these results also agree with previous work [27].

Fuzzy Modeling for Membership Functions for the Input and Output Variables: In this process, linguistic values were assigned to the variables and that was performed using fuzzy subsets and their associated membership functions. Modeling with grid partition involves three membership functions that were produced for each input variable of substitution matrices, and sequences based on ANFIS. The in1mf1, in1mf2, in1mf3 are three linguistic levels for nitrogen flow rate and in2mf1, in2mf2, and in2mf3 are for temperature as shown in Figures 3 and 4.
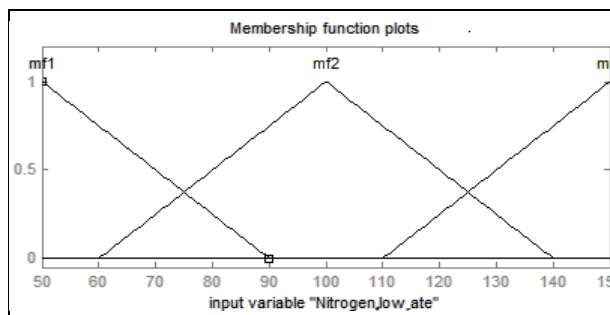

Figure 3 (a). Fuzzy model of thermochemical namdani) showing input variable nitrogen flow rate.
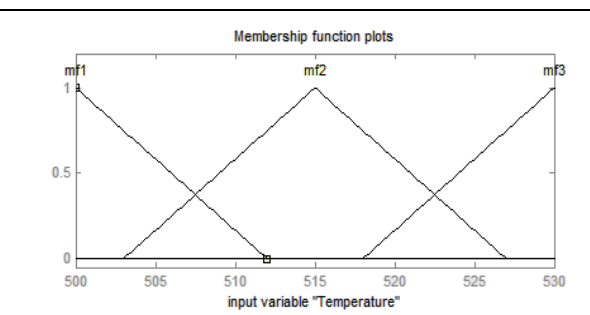

Figure 3 (b). Fuzzy model of thermochemical (mamdani) showing input variable temperature.
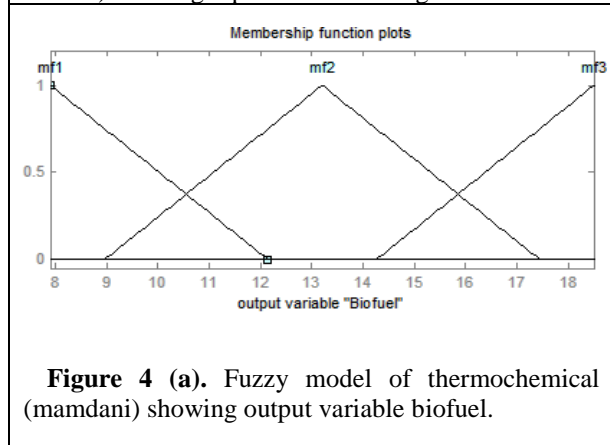

Figure 4 (a). Fuzzy model of thermochemical (mamdani) showing output variable biofuel.
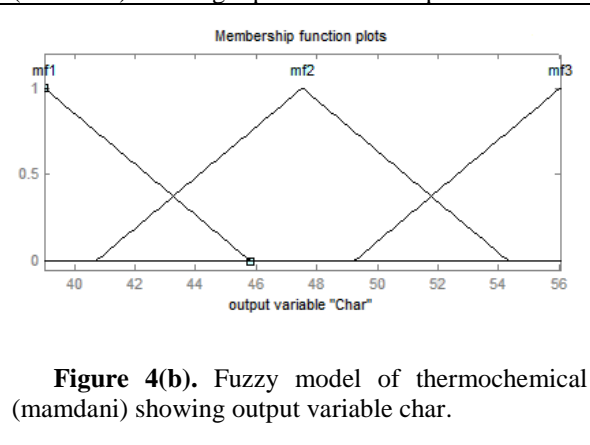

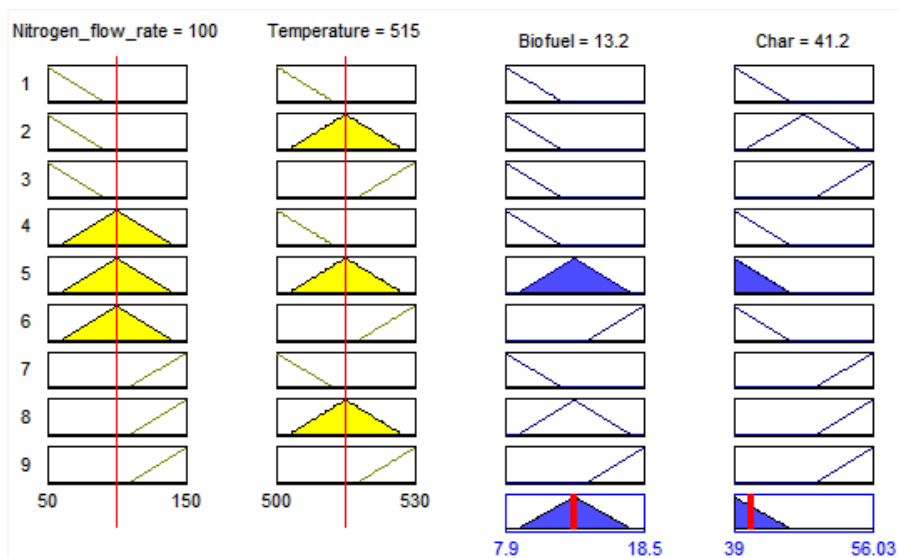**Figure 4(b).** Fuzzy model of thermochemical (mamdani) showing output variable char.

Figure 5. Ruler view of input variables (nitrogen flow rate and temperature) with output variables (biofuel and char)

Modeling for thermochemical (mamdani) involves nine membership functions that were produced for each output variable shown below:

1. If nitrogen_flow_rate is mf1 and (temperature is mf1, then biofuel is mf1 (char is mf1) (1).

2. If nitrogen_flow_rate is mf1 and temperature is mf2, then (biofuel is mf1 (char is mf2) (1).

3. If nitrogen_flow_rate is mf1 and temperature is mf3, then biofuel is mf1 (char is mf3) (1).

4. If nitrogen_flow_rate is mf2 and temperature is mf1), then biofuel is mf1 (char is mf1) (1).

5. If nitrogen_flow_rate is mf2 and temperature is mf2, then biofuel is mf2 (char is mf1) (1).

6. If nitrogen_flow_rate is mf2 and temperature is mf3, then biofuel is mf3 (char is mf1) (1).

7. If nitrogen_flow_rate is mf3 and temperature is mf1), then biofuel is mf1 (char is mf3) (1).

8. If nitrogen_flow_rate is mf3 and temperature is mf2, then biofuel is mf2 (char is mf3) (1).

9. If nitrogen_flow_rate is mf3 and temperature is mf3, then biofuel is mf3 (char is mf3) (1).

Figure 5 presents the rule viewer that shows the values of the various inputs to the model and computed outputs. Here, the biofuel and char concentration (output) can be predicted by varying the input parameters nitrogen flow rate and temperature. It shows a particular instance having input values given to the system for nitrogen gas flow rate of 100 ml/min, and temperature of 515^0C for analysis. The output generated by the system for biofuel concentration and char with experimental data shows similarity as 83% and 96%, respectively. This fuzzy model has generated other values of the output variable for a different set of data points in the specified range of input variables.

Figures 6 (a) and (b) show two different views of control surfaces, which are indicating the results predicted by the fuzzy model for different sets of data points. These control surfaces as shown give the interdependency of input and output parameters guided by the various rules in the given universe of discourse. It has already been finalized that there are nine rules predicting the concentration of products for MIMO fuzzy model. These rules were implemented in MATLAB environment using the sugeno type FIS of fuzzy logic toolbox. Results predicted from this fuzzy model were compared with the 70% experimental results data for its validation.

CONCLUSIONS

The experimental and ANFIS results allow to conclude that the increase in nitrogen gas flow rate from 50 to 200 ml/min increased the oil yield from 17.07 wt. % to 18.42. wt. %. The char yield decreased as the nitrogen gas flow rate was increased from 50 to 200 ml/min. Moreover, the char yield can rise as particle size increases from -6+8 onwards. The yield of bio-oil increased by approximately 8% when the pyrolysis temperature increased from 500ºC to 530ºC. The char yield decreased with increasing pyrolysis temperature and the same result was depicted by the mamdani ANFIS system. This study supports that the fuzzy logic technique can be introduced as a viable alternative to analyze complex thermo-kinetic variables. Moreover, fuzzy logic allowed modeling and optimization to be treated simultaneously.
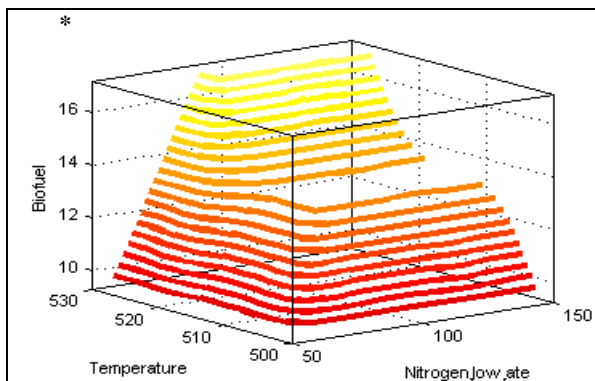
Figure 6 (a). Control surface view of the fuzzy model with nitrogen flow rate, temperature *vs.* biofuel
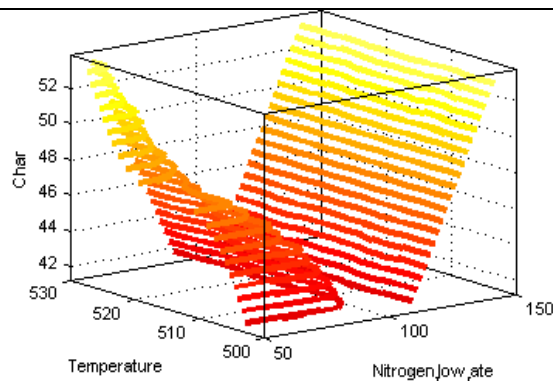

Figure 6 (b). Control surface view of the fuzzy model with nitrogen flow rate, temperature *vs.* char

REFERENCES

1. S. Yaman, *Energy Conversion and Management*, **45(5)**, 651 (2004).
2. Q. Zhang, J. Chang, T. Wang, Y. Xu, *Energy Conversion and Management*, **48(1)**, 87 (2007).
3. M. Balat, M. F. Demirbas, *Energy Sources, Part A,* **31(19)**, 1719 (2009).
4. D. Mohan, C. U. Pittman Jr, P. H. Steele, *Energy & Fuels*, **20(3)**, 848 (2006).
5. S. Kumar, R. Prakash, S. Murugan, R. K. Singh, *Energy Conversion and Management*, **74**, 323 (2013).
6. A. E. Pütün, B. B. Uzun, E. Apaydin, E. Pütün, *Fuel Processing Technology*, **87(1)**, 25 (2005).
7. J. S. de Oliveira, P. M. Leite, L. B. de Souza, V. M. Mello, E. C. Silva, J. C. Rubim, P. A. Suarez, *Biomass and Bioenergy*, **33(3)**, 449 (2009).
8. R. N. Singh, D. K. Vyas, N. S. L. Srivastava, M. Narra, *Renewable Energy,* **33(8)**, 1868 (2008).
9. D. K. Vyas, R. N. Singh, *Renewable Energy*, **32(3)**, 512 (2007).
10. R. Manurung, D. A. Z. Wever, J. Wildschut, R. H. Venderbosch, H. Hidayat, J. E. G. Van Dam, H. J. Heeres, *Food and Bioproducts Processing*, **87(3)**, 187 (2009).
11. V. Sricharoenchaikul, D. Atong, *Journal of Analytical and Applied Pyrolysis*, **85(1-2)**, 155 (2009).
12. S. A. Raja, Z. R. Kennedy, B. C. Pillai, C. L. R. Lee, *Energy*, **35(7)**, 2819 (2010).
13. N. Schmitt, A. Apfelbacher, N. Jäger, R. Daschner, F. Stenzel, A. Hornung, *Biofuels, Bioproducts and Biorefining*, **13(3)**, 822 (2019).
14. H. C. Ong, W. H. Chen, A. Farooq, Y. Y. Gan, K. T. Lee, V. Ashok Kumar, *Renewable and Sustainable Energy Reviews*, **113**, 109266 (2019).
15. S. Pang, *Biotechnology Advances*, **37(4)**, 589 (2019).
16. T. D. Kusworo, W. Widayat, A. F. Mahadita, D. Firizqina, D. P. Utomo, *Periodica Polytechnica Chemical Engineering*, **64**(2), 179 (2020).
17. B. Miljkovic, B. Nikolovski, D. Mitrović, J. Janevski, *Periodica Polytechnica Chemical Engineering*, **64(2)**, 192 (2020).
18. M. A. Sokoto, B. Biswas, J. Kumar, T. Bhaskar, *Renewable Energy*, **146**, 1710 (2020).
19. R. Piloto-Rodríguez, I. Tobío, M. Ortiz-Alvarez, Y. Diaz, S. Konradi, S, Pohl, *Energy Sources, Part A: Recovery, Utilization, and Environmental Effects*, **1**, (2020).
20. K. N. Dhanavath, S. Bankupalli, C. S. Sugali, V. Perupogu, S. V. Nandury, S. Bhargava, R. Parthasarathy, *Journal of Environmental Chemical Engineering*, **7(1),** 102905 (2019).
21. S. Saeed, I. Ashour, M. R. Ali, *Petroleum & Coal*, **61(6),** (2019).
22. A. S. Paul, N. L. Panwar, B. L. Salvi, S. Jain, D. Sharma, *Energy Sources, Part A: Recovery, Utilization, and Environmental Effects*, **1**, (2020).
23. O. A. Fakayode, E. A. A. Aboagarib, C. Zhou, H. Ma, *Bioresource Technology*, **297**, 122408 (2020).
24. V. K. Sohpal, R. K. Sharma, *International Journal of Energy and Power Engineering,* **7(12),** 1023 (2013).
25. S. A. Jourabchi, S. Gan, H. K. Ng, *Energy Conversion and Management*, **78***,* 518 (2014).
26. J. Kongkasawan, H. Nam, S. C. Capareda, *Energy*, **113,** 631, (2016).
27. A. E. Pütün, B. B. Uzun, E. Apaydın, E. Pütün, *Fuel Process Technol*., **87**, 25 (2005)

Photocatalytic degradation of xylene cyanol FF dye using synthesized bismuth-doped zinc oxide nanocatalyst

F. Akbar Jan[1]*, U. Shah[1], M. Saleem[1], R. Ullah[1], N. Ullah[2], M. Usman[3], Sh. Hameed[1]

[1]*Department of Chemistry, Bacha Khan University Chrasadda, Khyber-Pakhtunkhwa,24420 Pakistan*
[2]*Department of Chemistry, Qauid-i-Azam University Islamabad, 45320 Pakistan*
[3]*Center for Research Excellence in Nanotechnology, King Fahd University of Petroleum and Minerals, Dhahran 31261, Saudi Arabia*

Bismuth-doped zinc oxide nanoparticles were prepared through precipitation method. The synthesized nanoparticles were characterized by UV-Vis spectroscopy, Fourier transform infrared spectroscopy (FTIR), energy dispersive X-ray analysis (EDX) and high resolution-scanning electron microscopy (HR-SEM). The photo catalytic activity of the synthesized Bi-doped ZnO nanoparticles was evaluated in the photo degradation of xylene cyanol FF dye under UV-light. The effect of various reaction parameters like time, concentration, catalyst dosage, pH and temperature was also evaluated. Successful doping with bismuth reduced the band gap of zinc oxide from 3.25 eV to 2.9 eV. SEM study revealed that the synthesized nanoparticles have elongated morphology. From XRD the average crystallite size of Bi-doped ZnO was calculated to be 37 nm. At a duration of 120 min and low dye concentration (10 ppm) 67% degradation of the dye was achieved. Using an optimum catalyst dose (0.05 g) the degradation increased to 94% at pH 4. An increase in temperature decreased the rate of degradation and low temperature (15°C) is considered to be favorable for the best degradation of xylene cyanol FF dye.

Keywords: Bi-doped zinc oxide nanoparticles, xylene cyanol FF dye, photocatalytic degradation, characterization

INTRODUCTION

Water pollution caused by industrialization, growing population, and consumerism has become severe in recent years [1-3]. Textile and dyeing industries are the major sources of pollution of surface and underground water [4-6]. Presence of a number of organic compounds including dyes in the drainage effluents from various industries creates environmental problems. These organic compounds are not easily decolorized by the conventional water treatment methods such as adsorption, biological treatment and coagulation [7]. The dyes are the most important constituent of emulsifiers, cosmetics, stabilizers, viscosity enhancing agents, antioxidants, lubricating substances and moisturizing agents [8, 9].

According to literature about 10,000 tons of dyes are produced *per annum*. Approximately 12 % of the total amount of dyes produced is lost during manufacturing and processing operations [10]. Dye exposure or inhalation can cause problems of respiratory and immune system, itching, watery eyes, sneezing, asthma, coughing and wheezing [11]. Free aromatic amines have been found to be formed during metabolism at the intestinal wall and in the liver, that are potentially carcinogenic and mutagenic [12, 13]. Exposure to azo group containing dyes can cause bladder cancer in humans (hepatocarcinomas) and nuclear anomalies in experimental animals and chromosomal aberration in mammalian cells [14]. Some dyes are causing phototoxic or photo allergic reactions. Contact dermatitis may result when substances on the skin are exposed to ultraviolet light [15]. One of the most commonly used dye is xylene cyanol FF which is used in textile industry and as a laboratory substance for the spectrophotometric determination of amines, trace nitrite and aniline. The leuco xylene cyanol FF form (LXCFF) is used for the determination of trace quantities of gold, Cr (VI), iron and aluminum in ores and rocks [16]. It is an anionic compound which mediates the electron/proton transfer reaction easily on the carbon paste electrode. It also has an electron-rich oxygen group $(-SO^{3-})$ in its structure. These negatively charged $-SO^{3-}$ groups on the electrode surface have high affinity towards the positively charged analyte in the solution and produce high current signals with L-dopa [17]. Conventional waste water treatment methods such as coagulation, reverse osmosis, ion exchange, ozonation, flocculation, activated carbon adsorption are ineffective due to high operating cost and production of a large volume of sludge.

Owing to its economy and abundance of the materials photo catalysis using semiconductors has been recommended as a potential method for environmental clean-up. These methods degrade pollutants by using artificial or natural photons. No formation of sludge and catalyst regeneration are among the advantages of using photo catalysis [18]. Due to the wide band gap energy of 3.37 eV (bulk), harmless nature and high photosensitivity ZnO is generally considered as a good photo catalyst for the degradation of organic dyes. Electron-hole recombination rate is the only drawback of ZnO which reduces the degradation efficiency. For enhancing its activity many researchers reported doping of ZnO with impurity atoms [19]. The photo catalytic properties of ZnO could be enhanced by many transition metals such as Mn, Cu and Co or rare earth elements (La, Ce and Er) [20].

Keeping in view the benefits of photo catalysis it offers over other conventional treatment methods a study was designed to synthesize and characterize bismuth=doped zinc oxide nanoparticles and to apply them as a catalyst for the photo catalysis of xylene cyanol FF in aqueous medium.

EXPERIMENTAL

Instruments

UV-Vis spectrophotometer model Shimadzu UV-1800, Japan was used for all absorbance measurements. Perkin Elmer FTIR spectrometer version 10.4.00 was used for identification of functional groups. Elico (model IL-610) digital pH meter was used for pH measurements. Morphology and elemental composition of the doped nanoparticles was investigated using a SEM-EDX JEOL 5600LV microscope at an accelerating voltage up to 30 kV at the Center for Research Excellence in Nanotechnology, King Fahd University of Petroleum and Minerals, Dhahran, Saudi Arabia.

Reagents

Analytical grade reagents such as bismuth nitrate pentahydrate, zinc acetate, xylene cyanol FF dye, oxalic acid and nitric acid were purchased from Sigma Aldrich. For ensuring freedom of contamination all glass ware was rinsed with double distilled water.

Preparation of Bi-doped ZnO nanoparticles

Precipitation method was used for the preparation of Bi-doped ZnO nanoparticles. A calculated amount of $Bi(NO_3)_2.5H_2O$ was dissolved in 0.2M HNO_3 solution. Constant amounts of oxalic acid and zinc acetate dihydrate were also dissolved in distilled water. Oxalic acid-to-zinc acetate dihydrate atomic ratio was 0.8 at the doping ratio Bi/ZnO of 5.0. At room temperature and under vigorous stirring bismuth nitrate pentahydrate solution was added dropwise into the zinc acetate dihydrate solution until the formation of precipitate. The resulting precipitate was then thoroughly washed with double distilled water to remove the anions. The resulted precipitate was dried in an oven at 100°C for 12 hours followed by calcination in a furnace at 600°C for 3 hours.

Preparation of dye solution

Stock solution (500 ppm) of xylene cyanol FF dye was prepared by dissolving 0.125 g of dye in distilled water. Then working solutions of different concentrations were prepared using the following dilution formula (Eq. 1):

$$C_1V_1=C_2V_2 \qquad (1)$$

Procedure for photo catalytic degradation

First of all the absorbance of the original xylene cyanol FF solution was recorded and maximum absorption was found at 614 nm. This was recorded as a monitor wavelength for all the measurements. Appropriate amounts of photo catalyst, i.e bismuth-doped ZnO were separately added to working solutions. The mixed solution was stirred for 30 min in dark to establish adsorption/desorption equilibrium before the photo degradation reaction. The dispersions were kept in light source. During experiments a UV lamp with the power of 1500 watts was placed 15 cm away from the surface of the solution in a locally designed equipment. The dye degradation was checked at various intervals of time and the catalyst was removed by centrifugation. The absorbance of the centrifuged solution was measured on a UV-Vis spectrometer. The percent photo degradation of xylene cyanol FF was calculated by using the following relation (Eq. 2):

$$D\% = \frac{C_o - C_1}{C_o} x100 \qquad (2)$$

where C_0 and C denote the concentrations of xylene cyanol FF at time 0 min and t (s), respectively, and t is the irradiation time.

RESULTS AND DISCUSSION

Characterization of the catalyst (Bi-doped ZnO nanoparticles)

UV–Vis studies. The UV-Vis spectra of undoped ZnO and Bi-doped ZnO nanoparticles are shown in Fig. 1.
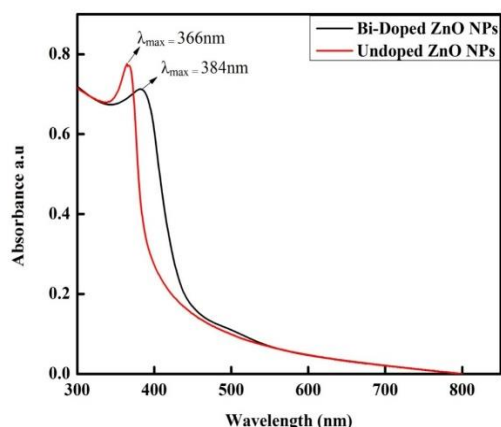
Fig. 1. UV-Vis spectra of undoped and Bi-doped ZnO NPs.

The characteristic absorption peak of undoped ZnO occurs at 366 nm and that of Bi-doped ZnO nanoparticles appears at 384 nm. From the spectra it can be seen that the maximum absorption of doped-ZnO nanoparticles is shifted towards the higher wavelengths, i.e. demonstrated a bathochromic shift as compared with undoped ZnO NPs and also band edge was red shifted [21].

The band gap was calculated using the following relation (Eq. 3):

$$\alpha h\upsilon = A(h\upsilon - E_g)^n \qquad (3)$$

where α is the absorption coefficient, $h\upsilon$ represents the energy of photon, A is proportionality constant, it is different for different materials while n represents the index. From the graph the optical band gaps of undoped ZnO and Bi- doped ZnO were calculated which came out to be 3.25 eV and 2.9 eV, respectively, as shown in Fig. 2. They are closely related to the literature value [22].
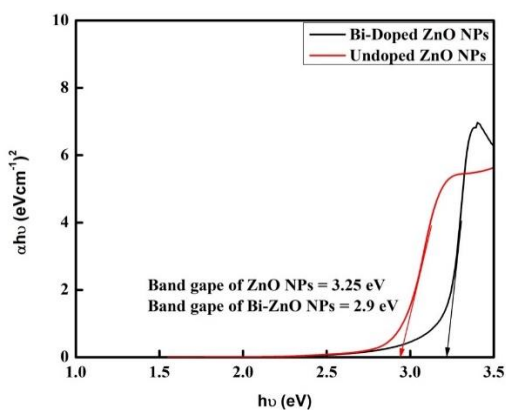
Fig. 2. Energy gap of undoped and Bi-doped ZnO NPs

XRD studies. XRD patterns of undoped ZnO and Bi-doped ZnO NPs are shown in Fig. 3. According to JCPDS card number 36-1451 all the diffraction peaks were related to the hexagonal wurtzite structure of undoped ZnO. In case of Bi-doped ZnO NPs additional small peaks star-marked at 2 theta of 27.89, 32.69, 56.22 and 55.47 were ascribed to the Bi_2O_3 peaks according to JCPDS card No. 712274 and 501088.This shows the minor phase of Bi_2O_3 as compared to ZnO major phase. From the pattern it can also be seen that due to Bi doping the intensity of the major peaks decreases. Debye-Scherrer equation was used to calculate the average crystallite size of undoped ZnO and Bi-doped ZnO nanoparticles:

$$L = K\lambda/\beta\cos\theta \qquad (4)$$

where L is an average crystalline site, K represents a dimensionless factor relating to shape having a value of 0.9, λ shows the wavelength of the X-rays, β is the Full width half maximum (FWHM) in radians and θ represents Bragg angle. The average crystalline size of undoped and Bi-doped ZnO NPs comes out to be 23 and 37 nm, respectively.
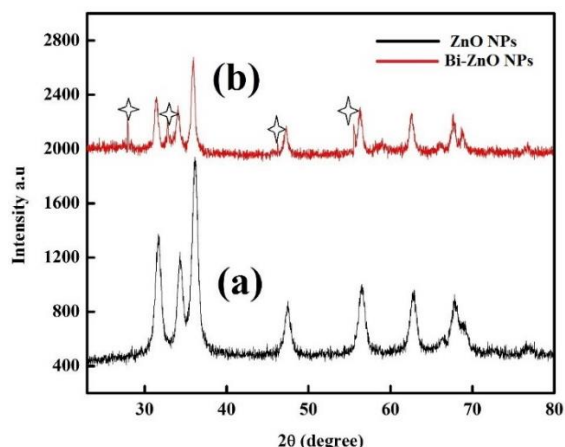

Fig. 3. X-ray diffraction patterns of **(a)** undoped ZnO and **(b)** Bi-doped ZnO.

SEM with EDX analysis. The SEM image given in Fig. 4 shows a collection of elongated particles of various plate-like shapes [23]. The average size of the particles is 2 μm. Energy dispersive X-ray spectroscopy was used for determining the elemental composition of Bi-doped ZnO nanoparticles as shown in Fig. 5. The EDX spectrum indicates the presence of Zn, O and Bi as major elements and gives the quantitative measurement of weight percentage of compositional elements. The elemental composition and weight percentage of the elements are summarized in Table 1 [24].
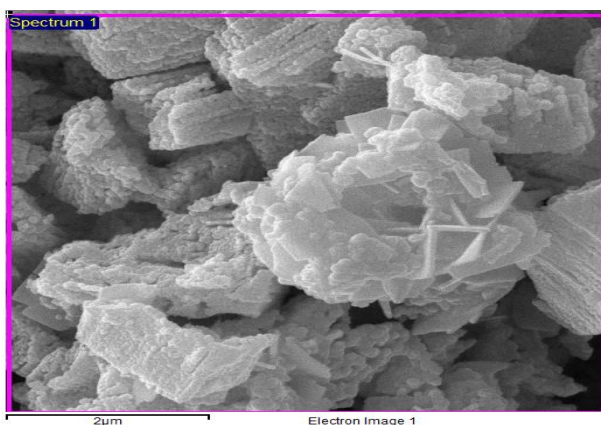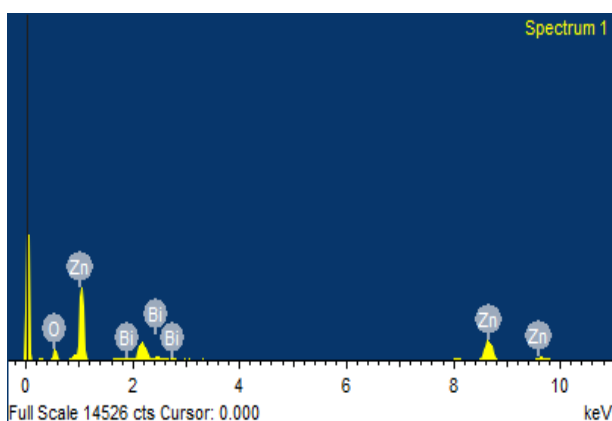
Fig. 4. SEM image of Bi doped-ZnO nanoparticles

Fig. 5. EDX spectrum of Bi-doped ZnO nanoparticles

Table 1. Elemental composition of Bi-doped ZnO nanoparticles

Element	Weight %	Atomic %
O K	18.47	50.64
Zn K	69.91	46.92
Bi M	11.62	2.44
Totals	100.00	
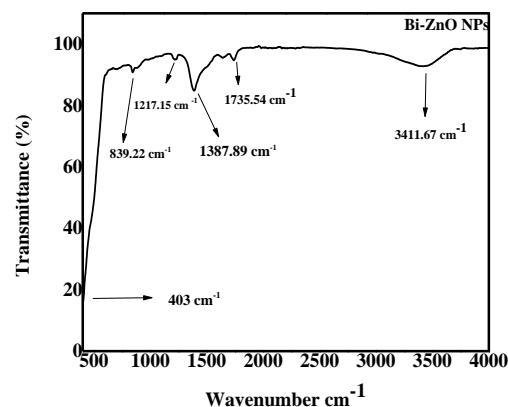
Fig. 6. FTIR spectrum of Bi-doped ZnO nanoparticles

Photo catalytic degradation of xylene cyanol FF dye

Effect of contact time on dye degradation. In order to study the effect of contact time on the degradation of xylene cyanol FF dye, 30 mL of the dye solution was taken in a beaker and 0.02 g of Bi doped-ZnO catalyst was added and kept in dark for 20 min. Then the mixture was irradiated by UV light for the time intervals of 20, 40, 60, 75, 90, 105, 115 and 125 min. Fig. 7 shows the changes recorded in the UV spectrum at various intervals of time during the experiment. Initially, at 20 min time duration the degradation was very low (6%) with an increase in time duration the degradation also increased as shown in Table 2. Increasing the time duration up to 120 min the degradation exponentially increased and about 67% of the dye was degraded. Time interval of 125 min was recorded as the optimum time for the degradation of the dye. This can be attributed to the fact that initially the photo catalyst surface is exposed to the light photons and with the passage of time the catalyst surface gets saturated by the adsorption of dye molecules, as a result the relative number of OH• needed for the dye molecules decreases, which eventually claims the photo catalyst activity [29].

Table 2. Effect of time on the dye degradation

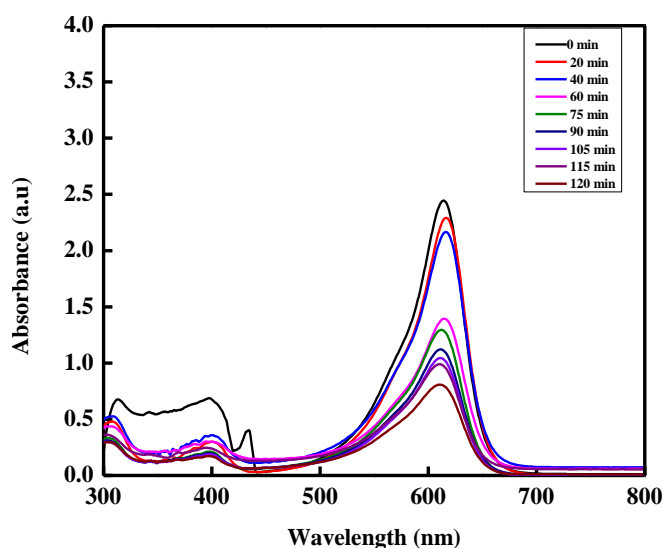| Time (min)	20	40	60	75	90	105	115	120
Degradation (%)	6	12.5	45	49	54	61	65	67

Fig. 7. Effect of time on dye degradation using Bi-doped zinc oxide NPs.

Table 3. Effect of dye concentration on the degradation

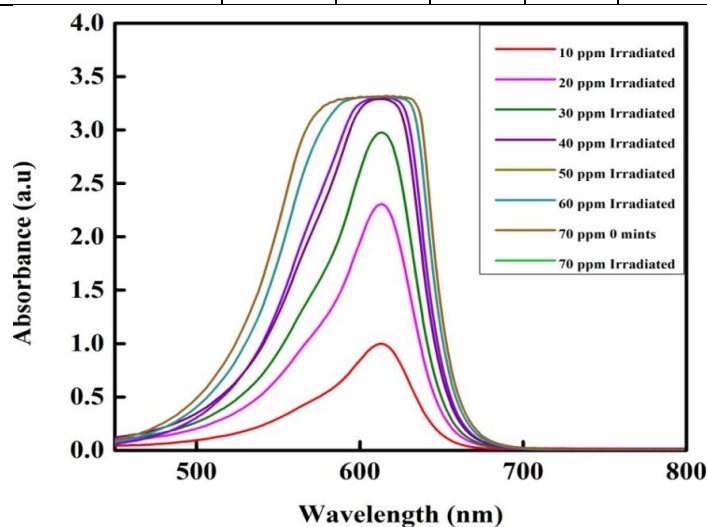| Initial concentration of the dye (ppm)	10	20	30	40	50	60	70
Degradation (%)	66	56	37	29	20	16	9.3

Fig. 8. Effect of concentration on dye degradation using Bi-doped zinc oxide NPs

Effect of initial concentration on the dye degradation. The concentration has an immense effect on the degradation of dye. Solutions of different concentrations ranging from 10 ppm to 90 ppm were prepared in 30 mL of distilled water. Then 0.02 g of the catalyst was added to each solution and placed under UV light for time duration of 120 min. Initially, at 10 ppm high percentage of degradation of xylene cyanol FF was recorded (Table 3) which eventually decreased with an increase in the concentration of dye solution.

Fig. 8 depicts the changes in the rate of degradation of xylene cyanol FF dye with increase in dye concentration. It is because as the dye concentration increases, more dye molecules get adsorbed on the photo catalyst surface and shield the catalyst surface from light photons which in turn reduces the path length of the photons entering the dye solution [30, 31]. This is also a reason that can explain that increased dye concentration saturates the photo catalyst surface and the requirement of catalyst for the process also

87

increases. Keeping the irradiation time and catalyst loading constant, the OH⁻ radical formation on the surface of the semiconductor also becomes constant. That is why on increasing dye concentration the relative number of OH• needed for the dye molecules decreases [32].

Effect of dosage rate on dye degradation.

Dosage of the catalyst may also affect the rate of degradation. For studying the effect of dosage rate on dye degradation, a working solution of 10 ppm was prepared in 250 mL of distilled water. Then 5 mL was taken from the original solution. Dosage of catalyst ranging from 0.01 to 0.07 g was used during experiments. The degradation at different dosage rates was recorded. Table 4 shows that initially, at a low dose of the catalyst (0.01 g) the degradation was 5.8% only which hiked to 37%, 40%, 52% and 86% upon increasing the dose rate from 0.01 to 0.05 g. On further increasing of the amount of catalyst beyond 0.05 g the degradation declined to 53% at 0.06 g and to 15% at 0.07 g. The rate of degradation increased with catalyst loading till certain weight and above this the rate of degradation of the dye decreased with increase in weight as reported by many researchers. This is not unusual because in solution phase reactions the exposed surface area of the catalyst will not be directly proportional to the amount of catalyst loaded. Since the amount that is adsorbed on the surface of the solid dye degradation is proportional to that and there can be a saturation point beyond which the solid amount may not have a direct relationship to the degradation extent. Maximum amount of the solid loaded for maximum activity is 3-4 g per liter of the dye solution as reported by studies [33]. The change in the degradation rate with increase in dosage rate is shown in Fig. 9.

Effect of pH on the dye degradation. The pH also has a strong effect on the dye degradation. The pH of the original solution of xylene cyanol FF dye was checked by the pH meter. The pH of xylene cyanol FF solution was 6.39, near to neutral. Then 20 ppm of the dye solution were added to 250 mL of distilled water. Then solutions of different pH were prepared by using 0.1 N NaOH and 0.1 N HCl. The pH was adjusted in the range from 4 to 10. An optimum weight of the catalyst (0.05 g) was added to each solution. Table 5 shows that at pH 4 high degradation (94%) was found while at pH 5 the degradation was 4.9% only. The effect of pH on

dye degradation is shown in Fig. 10. For the photo catalytic degradation process adsorption of dye is an essential step. Faster will degrade the dye which has a high adsorption capacity. The concentration of hydroxyl radicals and adsorption on photo catalyst will determine the extent of degradation. Activity of ions (e.g. H+ or pH) determines the potential of the surface charge in photo catalyst/aqueous systems. The property of a surface to become either positively or negatively charged is a function of pH. Maximum degradation of xylene cyanol FF was observed in acidic medium in our study [34].
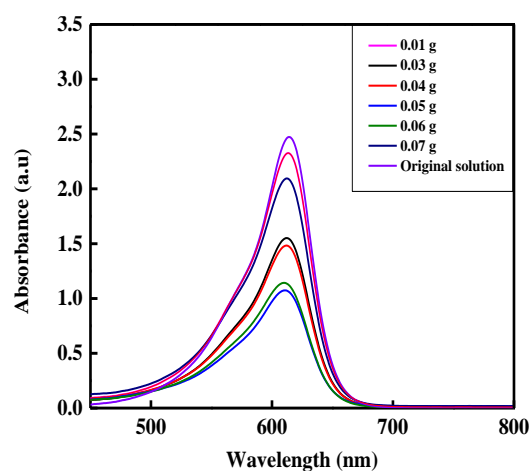

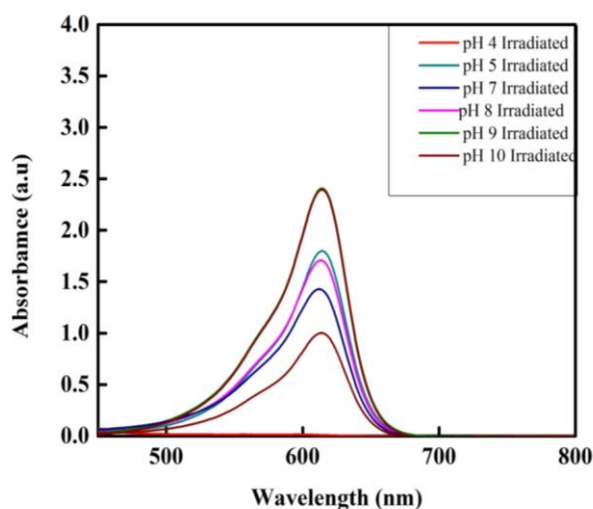**Fig. 9.** Effect of dosage rate on dye degradation using Bi-doped zinc oxide NPs

Fig. 10. Effect of pH on dye degradation using Bi-doped zinc oxide NPs.

Table 4. Effect of catalyst dosage on dye degradation

Catalyst mass (g)	0.01	0.02	0.03	0.04	0.05	0.06	0.07
Degradation (%)	5.8	37	40	52	86	53	15

Table 5. Effect of pH on dye degradation

pH value	4	5	7	8	9	10
Degradation (%)	94	4.9	6	5.2	6.4	5.6

Table 6. Effect of temperature on dye degradation

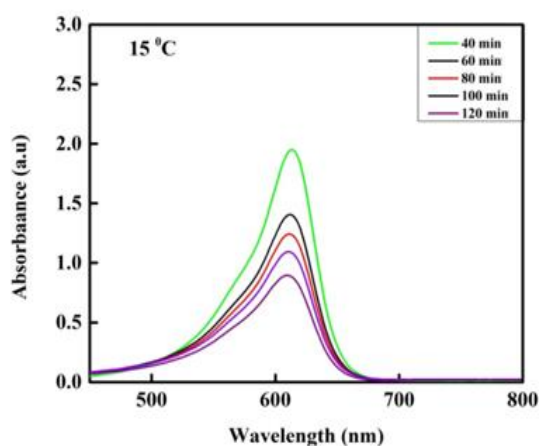| Temperature (ºC)	15	25	35	45	55
Degradation (%)	82	62	37	22	15

Fig. 11. Effect of temperature on dye degradation using Bi-doped zinc oxide NPs

Effect of temperature on dye degradation. Temperature also affects the degradation of dye. In order to establish the effect of the temperature on the dye degradation a solution of 20 ppm was prepared. Exactly 30 mL from the stock solution was taken in a beaker to which 0.05 g of Bi-doped ZnO nanoparticles were added. The temperature was kept at 15°C, 25°C, 35°C, 45°C, and 55°C, respectively. Maximum degradation (82%) was recorded at a temperature of 15ºC at 120 min time interval while the degradation at 25°C, 35°C, 45°C and 55°C was not appreciable. The effect of temperature on the degradation is shown in Fig 11 and Table 6. It can be seen that at 15ºC best percent degradation was observed. It can be attributed to the fact that an increase in temperature leads to the evaporation of the solvent, as a result percent degradation in open environment decreases.

CONCLUSIONS

It can be concluded from the present study that doping of zinc oxide with bismuth effectively decreases the band gap of the nanoparticles. Synthesized bismuth doped-ZnO nanoparticles have elongated shapes and are shown as a collection of particles. The degradation of xylene cyanol FF increases with an increase in time duration. Low concentration (100 ppm) of the dye and an optimum weight of the catalyst (0.05 g) was found best for the photo catalytic degradation of xylene cyanol FF dye. The pH study revealed that at pH 4 maximum degradation (94%) of xylene cyanol FF was noticed. Increase in temperature leads to evaporation of the dye solution and best degradation was noticed at 15°C temperature. Bismuth-doped zinc oxide catalyst can be effectively used for the degradation of xylene cyanol FF dye in waste water supplies.

Conflict of interest: The authors declare no conflict of interest for this publication.

REFERENCES

1. A. Minelgite, G. Liobikiene, *Sci. Tot. Environ.,* **672**, 174 (2019).
2. R. T. Kant, *Nat. Sci.*, **4**, 22 (2012).
3. G. J. Nohynek, R. Fautz, F. Benech-Kieffr, H. Toutain, *Food and Chem. Toxicol.,* **42**, 517 (2014).
4. S. Gita, A. Hussan, T. G. Choudry, *Environ. Ecol.,* **35**, 2349 (2017).
5. F. I. Vacchi, A. F. Albuquerque, J. A. D. A. Vendemiatti, Morales, A. B. Ormond, H. S. Freeman, G. Umbuzeiro, *Sci. Tot. Environ.,* **2**, 302 (2013).
6. D. Oliveira, A. R. Gisele, D. L. Joaquin, T. C. P. Elisabet, B. Miquel, D. Danielle, O. Palma, *Environ. Toxicol. Chem.,* **35**, 429 (2016).
7. W. A. Żukiewicz-Sobczak, P. Adamczuk, P. Wroblewska, J. Zwolinski, J. Chmielewska-Badora, E. Krasowska, J. Kozlik, *Adv. Dermatol. Allerg.,* **30**, 307 (2013).
8. A. R. Ribeiro, G. Arangaoumbuzeiro, *Environ. Sci. Eur.,* **26**, 22 (2014).
9. J. Sima, P. Hasal, *Chem. Eng.*, **32**, 79 (2013).
10. M. A. Hassan, A. El Nemr, F. F. Madkour, *Amer. J. Wat. Sci. Eng.,* **2**, 14 (2016).
11. E. A. Meulenkamp, *The J. Phys. Chem. B.,* **102**, 5566 (1998).
12. F. Akarsalan, H. Demiralay, *Acta. Physica Pol. A.,* **128**, 407 (2015).

13. T. Y. Lin, Y. T. Hsu, W. H. Lan, C. J. Huang, L. C. Chen, Y. H. Huang, K. F. Huang, *Adv. Nano. Res.,* **3**, 123 (2015).
14. B. S. Padhi, *Int. J. Environ. Sci.,* **3**, 940 (2012).
15. M. Pandurangachar, B. K. Swamy, U. Chandra, O. Gilbert, B. S. Sherigara, *Int. J. Electrochem. Sci.,* **4,** 672 (2009).
16. L. Cai, C. Xu, *J Braz. Chem. Soc.*, **22***(10), 1823 (2011).
17. L. A. Chanu, W. J. Singh, K. J. Singh, K. N. Devi, *Results in Phys.,* **12**, 1230 (2019).
18. V. L. Chandraboss, L. Natanapatham, B. Karthikevan, J. Kamalakkanan, S. Prabha, S. Senthilvelan, *Mat. Res. Bull.,* **48**, 3707 (2013).
19. E. F. Keskenler, S. Aydin, G. Turgut, S. Dogan, *Acta Physica Polonica, A,* **126**, 3 (2014).
20. T. Prakash, G. Neri, A. Bonavita, E. R. Kumar, K. Gnanmoorthi, *J. Mat. Sci. Mater. Electron.,* **26**, 4913 (2015).
21. K. Handore, S. Bhavsar, A. Horne, P. Chhattise, K. Mohite, J. Ambekar, V. J. Chabukswar, *Macromolec. Sci.* A, **51**, 941 (2014).
22. H. Barrak, T. Saied, P. Chevallier, G. Laroche, A. Mnif, A. H. Hamzaoui, *Arab. J. Chem.,* DOI:http//dx.doi.org/10.1016/j.arabjc.2016.04.019
23. R. N. Moussawi, D. Patra, *RSC Adv.,* **6**, 17256 (2016).
24. M. K. Trivedi, R. M. Tallapragada, A. Branton, D. Trivedi, G. Nayak, O. Latiyal, S. Jana, *Am. J. Nan. Res. Appl.,* **3**, 94 (2015).
25. A. Kumar, G. Pandey, *Mater. Sci. Eng. Int. J.*, 106 (2017).
26. N. Daneshvar, D. Salari, A. R. Khataee, *J. Photochem. Photobiol.,* **162**, 317 (2004).
27. E. M. Saggioro, A. S. Oliveira, T. Pavesi, C. G. Maia, L. F. V. Ferreira, J. C. Moreira, *Molecules*, **16**, 10370 (2011) .
28. Z. Mengyue, C. Shifu, T. Yaowu, *J. Chem. Technol. Biot.,* **64,** 339 (1995).
29. B. Viswanathan, *Curr. Cat.,* **7**, 99 (2018).
30. V. L. Chandrabos, J. Kamalkkannan, S. Prabah, S. Senthilvelan, *RSC Adv.,* **5**, 25857 (2015).
31. M. A. Hassaan, A. El Nemr, *Am. J. Environ. Sci. Eng.,* **1**, 64 (2017).
32. X. Li, Y. Hou, Q. Zhao Wang, *J. Colloid Interf. Sci.* **358**, 102 (2011).
33. U. G. Akpan, B. H. Hameed, *J. Hazard. Mater.,* **170**, 520 (2009).
34. F. Zhang, J. Zhao, T. Shan, H. Hidaka, E. Pelizzetti, N. Serpone, *Appl. Catalysis B-Environ.,* **15**, 147 (1998).

Microbiological parameters during storage of minimally processed melons with and without edible coating

S. Zhelyazkov[*], P. Ivanova

Institute of Food Preservation and Quality - Plovdiv, Bulgaria

The aim of the study was to analyze the microbiological parameters of minimally processed melons with and without edible coating during storage in the refrigerated state and to determine their shelf life. The use of chitosan coating with solutions of diferent concentrations on peeled and sliced melons stored at 4±1 °C was studied. It was found that all edible chitosan coatings inhibit the growth of microorganisms. We used a variant of edible coating of 1% chitosan and 1% calcium lactate as an alternative to prolong the shelf life of minimally processed melons according to their quality characteristics. The storage period was determined according to the analyzed microbiological indicators - 7 days for minimally processed melons with the edible coating compared to 5 days for the control.

Keywords: melon*,* edible coatings, chitosan, microorganisms

INTRODUCTION

Minimally processed fruits

Fresh-cut fruits and vegetables are defined as fresh fruits or vegetables, or any combination thereof, which has undergone physical changes from their original form but without treatment with heat, negative temperatures or chemical preservatives and remain fresh [1, 2]. Freshly chopped plant products include peeled, cleaned, washed, core-cut, sliced but still raw fruits and vegetables [3, 4]. They are categorized as ready-to-use, partially processed or minimally processed products [5-7].

Changes in whole and minimally processed plant products

By minimal processing of fruits and vegetables are obtained products convenient to use, but their shelf life is reduced. A current challenge for the rapidly expanding sector of minimally processed foods is to ensure their safety and quality [8].

Minimally processed products are very perishable, the main reasons for this are the removal of the bark (the natural protective layer) and the physical stress they go through during the processes of peeling, slicing, etc. [7-9]. As a result of the mechanical effects described above, the synthesis of ethylene, the water activity of the surface, the weight loss and the rate of respiration are increased [7-10]. These changes also lead to cell wall damage (which leads to enzymatic side effects), loss of cellular components, loss of moisture [10], which is the reason for the reduction of their shelf life [3, 4, 7, 8, 10, 11]. If these changes are not controlled, they can lead to rapid deterioration and aging of the product

[10]. Therefore, minimally processed products should be stored at temperatures below those recommended for whole fruits and vegetables [7]. But even during refrigerated storage, fresh fruits and vegetables are characterized by active metabolism [12, 13] reports that some of the factors that affect the intensity of decay are the type of plant product, the variety, the degree of maturity, the temperature, the concentration of oxygen and carbon dioxide, and the water vapor pressure. Studies of all these parameters are necessary to ensure that healthy and high-quality products are offered to consumers [7].

The minimum processing of fresh fruit aims to preserve the freshness of the fruit, with minimal loss of nutritional quality and to ensure a shelf life sufficient to allow distribution in the region of consumption. The microbiological, sensory and nutritional shelf life of the minimally processed fruit should be at least 4-7 days, depending on the market. During peeling and other technological operations of minimal processing, many of the cells of the product are disrupted, resulting in oxidative processes. The quality of minimally processed products deteriorates due to physiological aging, biochemical changes, and microbial spoilage, which can lead to degradation of color, texture, and aroma [14, 15].

Microbiological changes

As minimally processed fruits are not subjected to heat treatment, regardless of the presence of preservatives or the type of packaging, they have to be processed and stored at temperatures of 5 °C or

---

* To whom all correspondence should be sent:
E-mail: stoil_z@abv.bg

lower in order to achieve an optimally long shelf life and microbiological safety. Some pathogenic microorganisms that can be transmitted by plant products, such as *Escherichia coli* O157: H7, *Listeria monocytogenes, Yersinia enterocolitica, Salmonella spp.* and *Aeromonas hydrophila* can survive and thrive at the said low temperatures [16, 17].

Most of the microorganisms that are in the soil and air get into the fruit by insects, animals and humans but are not able to grow at pH that is typical for fruits. These conditions are favorable only for the growth and development of molds, yeasts and some lactic acid bacteria. Therefore, with few exceptions, the representatives of these three groups of microorganisms are the dominant microflora, causing the spoilage of fresh fruit. It has been shown that spoilage may occur much faster in minimally processed fruits than in unprocessed ones, as mechanical disruption of fruit integrity provides access to microorganisms to an environment with optimal concentrations of sugars, salts and water activity (aw).

In the case of mechanically injured fruits, in which adequate sorting has not been carried out before storage, the mold species *Penicillium expansum* and *Botrytis cinerea* have been identified. They can cause a significant loss of raw material, destroying the places of injury, creating lesions, causing cross-contamination of neighboring fruits. *P. expansum* [18] and *B. cinerea* [19] are pathogenic to apples, pears and a number of other pectin-rich fruits. Temperatures below 5 °C slow the growth of molds and yeasts and lead to an extension of the shelf life of the product [20, 21].

Bacteria cause a decay of minimally processed fruits with a neutral pH [22]. The most commonly isolated bacteria are members of the genera: *Erwinia, Xanthomonas, Pseudomonas*, *and Cytophaga*. They cause the so-called soft rot. The species that causes the most damage to a large group of vegetables and some fruits is *Erwinia carotovora* [23]. Relatively rarely, soft fruit rot is due to fluorescent bacteria from the *Pseudomonas river*. Bacterial growth is inhibited by storing the fruit in a controlled atmosphere (3% O_2 and 15 or 20% CO_2) [24].

There is no evidence that low levels of microbial contamination immediately after processing will provide an extension of shelf life in freshly chopped vegetables. However, with minimally processed fruit, the low concentration of microorganisms, especially yeast and mold, results in a longer shelf life.

Edible chitosan films on sliced melons

There is very little information in the scientific literature about edible coatings of chitosan on sliced melons [25]. These authors obtain two-layer polyelectrolyte coatings of alginate and chitosan, combining the good adhesion properties of alginate on sliced fruit and the proven antibacterial activity of chitosan. The melon slices covered in this way were stored at 6 °C for 21 days. The authors report a negligible effect of the coating on weight loss, while the texture of the packaged melons is preserved to a greater extent than that of the control. The addition of chitosan significantly reduces the rate of development of microorganisms on the surface. The authors conclude that physiological processes and microbiological spoilage of the fetus are probably the main factors influencing the texture.

MATERIALS AND METHODS OF ANALYSIS

Melons selected according to specified and summarized requirements after preliminary studies of the raw materials, were used as starting material for the experimental work.

Raw materials

Cantaloupe melon variety (*Cucumis melo* var. Cantalupensis) – Cantaloupe are musk-type melons. The fruit is round to oval, juicy and sweet with orange-colored fruit flesh. The peel is thin, with dark gray - gray-brown color, the surface is rough with green stripes The variety is suitable for desserts, fruit salads, purees and drinks. Melons were purchased from a local producer in consumer maturity, without physical and microbiological damage.

Materials

For the preparation of solutions intended for application as edible coatings were used: high molecular weight chitosan soluble in organic acids (M_w= 600 kDa) with 95% degree of N-deacetylation (DD); water-soluble chitosan with low molecular weight (M_w= 600 Da – 1.5 kDa) with 75-85% degree of N-deacetylation (DD). They were purchased and accompanied by a quality certificate. Drinking water meeting the requirements of Ordinance № 9/2001 on the quality of water intended for drinking and household purposes; lactic acid ($C_3H_6O_3$); acetic acid ($C_2H_4O_2$); calcium lactate ($C_6H_{10}CaO_6$) - all ingredients in the coatings were obtained from commercial sources of analytical purity and their application complies with Ordinance №8 / 2002 on the requirements for the use of food additives. Samples of fruit with edible coatings were stored in polypropylene boxes, complying with Ordinance №

2/2008 for materials and articles of plastics intended for contact with food.

Experimental staging

Preliminary preparation of the solutions

Solutions of high molecular weight chitosan used for application as edible coatings. All studied combinations of high molecular weight chitosan solutions were prepared as follows: quantities of 0.1%, 0.25%, 0.5%, and 1% high molecular weight chitosan were weighed on a technical scale, then added under constant stirring to 100 ml of 2% acetic acid solution at 25 °C to obtain a homogeneous solution. High molecular weight chitosan (0.5%) and 0.5%, 1%, 1.5% calcium lactate, respectively, were weighed on a technical scale, then added under constant stirring to 100 ml of lactic acid solution with concentrations of 1%, 1%, 1%, 1%, 0,5%, respectively, at a temperature of 25 °C to obtain a homogeneous solution.

Low molecular weight chitosan solutions used for application as edible coatings. A 1% solution of low molecular weight water-soluble chitosan and a solution of 1% low molecular weight water-soluble chitosan and 1% calcium lactate were prepared as follows: the dry ingredients were weighed on a technical scale and then added under constant stirring to 100 ml of water with a temperature of 45 °C.

Technological processing

Preliminary preparation of raw materials. Harvesting, delivery and handling of melon fruits, before refrigerated storage, was performed in two consecutive days to ensure uniform starting conditions.

Melons. Pretreatment of melons included washing with running water and removal of all physical impurities and injuries. The dried fruits were peeled, cored and chopped in pieces of $10 \times 10 \times 20$ mm.

Application of edible coatings. After preliminary preparation of the fruit, the pieces of melon were immersed in the solutions for 1 min. After removal, they were drained and dried under natural air circulation for 30 min. Of all the fruits, one control sample remained for comparison.

Packing. The products - pieces of melon with edible coatings were placed in polypropylene packaging with perforated lids.

Sample storage. The storage of the finished products, the pieces of melon with edible coatings based on chitosan, was carried out in a refrigerated state in a controlled-storage chamber HotCold at a temperature $T = 4 \pm 0.5$ °C and relative humidity $\varphi = 60 \pm 5\%$.

Methods of analysis

Antimicrobial activity of chitosan and microbiological parameters of the products. Each of the series during storage was analyzed for the presence of:

- *Listeria monocytogenes* - EN ISO 11290-2: 2017 Microbiology of food and feed. Horizontal method for the detection and enumeration of *Listeria monocytogenes*. Part 2: Enumeration method (ISO 11290-2: 1998);

- *Salmonella* - EN ISO 6579:2017 Microbiology of food and feed. Horizontal method for the detection of *Salmonella spp.* (ISO 6579: 2002);

- Coagulase-positive staphylococci (*Staphylococcus aureus*) - EN ISO 6888-1: 2005 / A1: 2005 Microbiology of food and feed. Horizontal method for enumeration of coagulase-positive staphylococci (*Staphylococcus aureus* and other species). Part 1: Technique using Baird-Parker agar. Amendment 1: Includes precision data (ISO 6888-1: 1999 / Amd 1: 2003);

- Coliforms - according to ISO 4832: 2006 Microbiology. Basic guide to listing coliforms. Colony-counting technique;

- *E. coli* - ISO 16649: 2014 Microbiology of food and feed. Horizontal method for the enumeration of β-glucuronidase-positive *Escherichia coli*. Colony counting technique at 440C using 5-bromo-4-chloro-3-indolyl β-D-glucuronide;

- Total number of microorganisms - EN ISO 4833-1: 2013 Microbiology of the food chain. Horizontal method for enumeration of microorganisms. Part 1: Counting of colonies at 300C by crop flooding technique (ISO 4833-1: 2013)

- Molds and yeasts - according to BDS ISO 21527-1: 2011 Microbiology of food and feed. Horizontal method for counting yeasts and molds. Part 1: Colony - counting technique in products with a water activity greater than 0.95.

RESULTS AND DISCUSSION

Antimicrobial activity of chitosan and microbiological indicators of minimally processed fruits during storage

In-vitro determination of the minimum inhibitory concentration (MIC) of chitosan against indicator and pathogenic species of microorganisms by the method of serial dilutions in liquid medium. One of the main requirements of edible coatings is that they do not support the development of microorganisms

that cause spoilage of the product or are pathogenic to humans. Chitosan is a polymer that has antimicrobial activity, highly dependent on its molecular weight, degree of acetylation, strain of the respective test microorganism and others. MIC is defined as the lowest concentration of test substance that inhibits the growth of microorganisms after incubation. Many studies have been performed to determine the MIC of chitin, chitosan, their derivatives or a combination thereof against a wide range of microorganisms. Quantitatively significant differences in the results for different microorganisms were obtained. Due to the fact that there are a number of non-standardized procedures

for determining the MIC, it is difficult to compare the results of different teams.

The minimum inhibitory concentration (MIC) of low molecular weight chitosan used in the experiments was determined for the following reference strains by the National Bank for Industrial Microorganisms and Cell Cultures (NBMPMK) - *Aspergillus niger, Candida tropicalis, Escherichia coli, Bacilluscous cereus*. The results of MIC determination show that in Mueller - Hinton broth with a chitosan concentration higher than 50 ppm the species *Candida tropicalis, Escherichia coli, Entherococcus faecalis* stop their development (Table 1).

Table 1. Determination of the minimum inhibitory concentration of chitosan against some conditionally pathogenic and indicator microorganisms

Microorganism	Chitosan concentration (ppm)							
	230	200	150	100	50	10	5	2
Aspergillus niger NBIMCC 3564	R	R	R	R	R	R	R	R
Candida tropicalis NBIMCC 8614	S	S	S	S	**S**	BS	R	R
Escherichia coli NBIMCC	S	S	S	S	**S**	BS	R	R
Bacillus cereus NBIMCC 1085	BS	S	S	S	**S**	S	R	R
Entherococcus faecalis NBIMCC 3915	S	S	S	S	**S**	BS	R	R
Salmonella choleraesuis NBIMCC 251	**S**	BS	R	R	R	R	R	R

Our results regarding the low MIC of chitosan relative to *E. coli* confirm the studies of Liu [26].

When determining the MIC of chitosan against strain 251 of *Salmonella choleraesuis*, no growth was observed at chitosan concentrations in the culture medium above 230 ppm. The results of our MIC determination are comparable to the data presented by Rejane [27], which also indicate that regardless of the different types of *Salmonella* bacteria and the MIC determination methods, *Salmonella* spp strains are suppressed by higher concentrations of chitosan, compared to those observed in *Candida tropicalis*, *Escherichia coli* and *Entherococcus faecalis.*

In our study, none of the concentrations of chitosan used had an inhibitory effect on the fungus *Aspergillus niger* which is the cause of the spoilage of a number of fruits and vegetables. Studies by Tsai [28] also show that species of the genus Aspergillus have very high resistance to chitosan (>

2000 ppm) and its MIC is higher than that for other tested microorganisms (*Staphylococcus aureus, Bacillus cereus* and *Escherichia coli*).

Microbiological parameters of chilled minimally processed fruit without and with edible coatings of water-soluble chitosan

Microbiological analysis of the components used and the edible coatings. The safety, quality and shelf life of ready-to-eat foods are largely determined by the species composition and quantity of pathogenic microorganisms, as well as those that cause spoilage of the product [29]. Consumption of fruits, vegetables and minimally processed products is usually defined as a risk factor for possible infection with pathogenic and toxicogenic microorganisms. Strains of *Listeria monocytogenes, Salmonella spp*, *E. coli* O157: H1, coliforms, *Yersinia enterocolitica*, *Staphylococcus ssp*, strains of *Enterobacteriaceae* were isolated from foods of plant origin. The sources of contamination of plant products with the listed

bacteria are diverse and include organic fertilizer, contaminated irrigation water, direct contamination by animals and poor hygiene of post-harvest technological processes (transportation, packaging, storage, distribution).

To ensure the microbiological stability and safety of the products (chilled minimally processed melons without and with edible coatings of chitosan and chitosan with calcium lactate), microbiological control of the incoming raw materials was initially performed. The microbiological criteria specified in their certificates are completely adequate and allow the production of a safe product that preserves its microbiological quality and stability. The results of the performed microbiological analysis are presented in Table 2.

Table 2. Microbiological characteristics of components and edible coatings

Object of test Microbiological criterion	Chitosan	Chitosan coating	Calcium lactate	Chitosan and calcium lactate coating
Total number of microorganisms cfu/g (1000)	<100	< 10	<100	< 10
Molds cfu/g (1000 - 10 000)	<100	<10	<10	<10
Yeast cfu/g (1000- 10 000)	<100	<10	<100	<10
L. monocytogenes cfu/25g (it is not allowed)	not established	not established	not established	not established
Salmonella cfu/25g (it is not allowed)	not established	not established	not established	not established
Coagulase-positive *Staphylococci* cfu/g (it is not allowed)	not established	not established	not established	not established
Coliforms cfu/g (it is not allowed)	not established	not established	not established	not established
E. coli cfu/g (it is not allowed)	not established	not established	not established	not established
Enterococcus sp. cfu/g	< 1	< 1	< 1	< 1

No strains of the pathogenic microorganisms *L. monocytogenes, Salmonella spp., E. coli* and Coagulase-positive staphylococci were identified in the study of chitosan, calcium lactate and edible coating solutions prepared therefrom. As a result of the conducted microbiological monitoring, compliance of the results obtained by us with those declared by the manufacturer was established. The absence of the mentioned pathogenic microorganisms in the raw materials for edible coatings is a proof of compliance with the Good Hygiene and Manufacturing Practices (GHMP) by the manufacturer. Absence of pathogenic microorganisms above the permissible quantities in the used raw materials is a major factor - a prerequisite for subsequent production of a safe product. The absence of ecterococci (faecal forms) and the low level of microbial contamination with a total number of microorganisms, yeasts and molds below 100 and below 10 cfu/g, respectively, is an indicator of good hygiene of technological operations and the absence of secondary contamination from the environment. Said groups of microorganisms affect the quality of the product in which they will be ingredients, as they are the main causes of spoilage.

Microbiological analysis of chilled minimally processed fruit with edible coatings

To prove the microbiological safety of chilled minimally treated melons without and with edible coatings based on water-soluble chitosan, they were tested on basic microbiological safety indicators (Table 3). According to Regulation (EC) № 1441/2007, in ready-to-eat foods that do not promote the growth of *L. monocytogenes*, the bacterium must not be found in 25 g of the product. No strains of *L. monocytogenes* were found in any of the products tested during the shelf life. As a result of studies by Sivapalasingam [30], *Salmonella* bacteria (≈60%)

and *E. coli* were found to be the main etiological agents in foodborne diseases caused by the consumption of foods of plant origin. In the present test, in chilled minimally treated melons without and with edible coatings based on water-soluble chitosan strains of *Salmonella spp* in 25 g of the tested samples were not isolated. Based on an analysis of the microbiological risk of minimally processed fruits and vegetables by the Institute of Environmental Science and Research - New Zealand, the main raw materials of melons and products developed from them were tested for the presence of coliforms and coagulase-positive staphylococci. The results of the microbiological analysis (Table 3) show that the amount of strains of the respective species in all tested samples is within the permissible limits of the indicated indicators. Based on the obtained results, it can be assumed that the raw materials used are not a source of coliforms and coagulase-positive staphylococci and all hygienic norms are observed during the technological processing. According to the national microbiological criteria [31], ready-to-eat fruits are considered safe when the amount of *E. coli* in all samples is below 100 cfu/g and does not exceed 1000 cfu/g. Microbiological analysis of the raw material and finished products revealed an amount of *E. coli* below 10 cfu/g, which proves the safety of the used batches of melons and their products.

Table 3. Conditionally pathogenic and pathogenic microorganisms in chilled minimally processed melons without and with edible coating

Product / Indicator	Day	Melon (washed, sliced, chilled)	Chilled pieces of melon coated with chitosan	Chilled pieces of melon coated with chitosan and calcium lactate
L. monocytogenes cfu/25g (it is not allowed)	1	not established	not established	not established.
	3	not established	not established	not established
	5	not established	not established	not established
	7	not established	not established	not established
Salmonella cfu/25g (it is not allowed)	1	not established	not established	not established
	3	not established	not established	not established
	5	not established	not established	not established
	7	not established	not established	not established
Coagulase-positive *Staphylococci* cfu (10-100)	1	< 1	< 1	< 1
	3	< 1	< 1	< 1
	5	< 1	< 1	< 1
	7	-	< 1	< 1
Coliforms cfu/g (100 - 1000)	1	< 10	< 10	< 10
	3	< 10	< 10	< 10
	5	< 10	< 10	< 10
	7	-	< 10	< 10
E. coli cfu/g (100 - 1000)	1	< 10	< 1	< 1
	3	< 10	< 1	< 1
	5	< 10	< 1	< 1

The fruits are characterized by a high content of carbohydrates and low values of active acidity (pH), which favors the growth of specific types of bacteria (lactic acid, *Pseudomonas spp.*, *Erwinia spp.* *Xanthomonas spp. Acidovorax spp.*), yeast (*Candida spp.*, *Torulopsis spp.*, *Rhodotorula spp.*) and molds (*Penicillium, Fusarium, Botrytis, Mucor, Rhizopus, Phthyophthora*). In general, the amount

of microbial associations on the fruit varies from 103 to 106 cfu/g. Molds, yeasts and bacteria cause various types of decay. The natural microflora, especially yeast, causes fermentation of the plant mass [32]. Based on the literature data for the purposes of the present study, all chilled fruits without and with edible coatings of chitosan and chitosan and calcium lactate were tested on the following indicators: total number of microorganisms, molds and yeasts.

In the present study, a microbiological test was performed on minimally treated melons without and with edible coatings of chitosan and chitosan with calcium lactate according to indicators determining the microbiological quality of the product. The data from the analysis are presented in Table 4. The results of the testing of the two products on the indicator total number of microorganisms show an increase in the number of mesophilic microorganisms during the storage period. The higher level of microbial contamination of melon products compared to those of cherries is due to the fact that microorganisms have direct contact with carbohydrates and other biologically valuable substances of the cell due to the cutting of the product This provides a larger contact surface and access to oxygen for microorganisms. At the beginning of storage in the minimally processed melons the amount of microorganisms reaches 450 cfu/g, and on the fifth day of their refrigerated storage they reach a quantity of 32.106 cfu/g. Due to the created conditions for decay (fermentation) and change in the organoleptic, physicochemical and rheological parameters, their storage has been suspended. When using edible coatings of chitosan and chitosan with calcium lactate, a slower increase in the amount of mesophilic microorganisms is observed.

Table 4. Indicator microorganisms in chilled minimally processed melons without and with edible chitosan coating

Product Indicator	Day	Melon (washed, sliced, chilled)	Chilled pieces of melon coated with chitosan	Chilled pieces of melon coated with chitosan and calcium lactate
Total number of microorganisms cfu/g	1	450	7	12
	3	95.10^3	32.10^3	13.10^2
	5	32.10^6	90.10^3	2.10^3
	7	-	76.10^5	58.10^5
Molds cfu/g	1	<10	<10	<10
	3	15	10	10
	5	26	15	10
	7	-	-	-
Yeast cfu/g	1	130	< 10	<10
	3	12.10^2	15.10^1	17
	5	65.10^3	58.10^2	25.10^2
	7	-	35.10^3	11.10^3

On the seventh day of storage of the samples of melons with edible coatings of chitosan and chitosan with calcium lactate, a total number of microorganisms over 105 cfu/g was reported, which is already an indication of deteriorating microbiological quality and creating conditions for microbial spoilage. From the conducted microbiological testing of the products (pieces of melon without and with edible coatings of chitosan) it was established that the main group of microorganisms causing spoilage in the product are yeasts. In the tested samples, a concentration of yeast cells in the range of 11.10^3 in pieces of melon with an edible film of chitosan and lactate to 65.10^3 cfu/g in untreated pieces of melon was registered. The microbiological analysis for the detection of molds did not show a high concentration of molds, which would cause the spoilage of the products.

CONCLUSION

The conducted microbiological testing of the minimally processed melons proves that the applied chitosan coatings have a strong effect against the microbial population (mesophilic microorganisms), the cause of the spoilage of the products. During the

technological stages used to obtain minimally processed fruits with edible coatings, no contamination of the product with the studied pathogenic and opportunistic microorganisms was found.

An edible coating of 1% chitosan and 1% calcium lactate is an alternative for storing minimally processed melons, with quality characteristics for a longer period and the requirement to extend the shelf life for consumption is met. The storage period was determined according to the analyzed microbiological indicators - 7 days for minimally processed melons with the edible coating compared to 5 days for the control.

REFERENCES

1. E. Garrett, *Journal of the Association of Food and Drug Officials,* **61**(1), 26 (1997).
2. A. D. King Jr, H. R. Bolin, *Food Technology*, **43**, 132, 139 (1989).
3. E. A. Baldwin, M. O. Nisperos, X. Chen, R. D. Hagenmaier, *Postharvest Biology and Technology,* **9**(2), 151 (1996).
4. J. A. Lindsay, K. C. Gross, D. W. Thayer, K. B. Hicks, *ARS News and Information*, http://www.ars.usda.gov/is/AR/archive/jun99/food0699.htm 10/8/2002 (1999).
5. M. Cantwell, Postharvest handling systems: minimally processed fruits and vegetables. Vegetable Research & Information Center. University of California Cooperative Extension, http://vric.ucdavis.edu/selectnewtopic.minproc.htm 10/8/2002 (2002).
6. F. Carlin, C. Nguyen-The, G Hilbert, Y. Chambroy, *Journal of Food Science*, **55**(4), 1033 (1990).
7. A. E. Watada, N. P. Ko, D. A. Minott, *Postharvest Biology and Technology,* **9**,115- (1996).
8. Y. Jiang, D. C. Joyce, *Journal of Horticultural Science and Biotechnology*, **77**(1), 19 (2002).
9. S. R. Rolle, G. W. Chism, *Journal of Food Quality,* **10,** 157 (1987).
10. E. A Baldwin, M. O. Nisperos-Carriedo, R. A. Baker, *Critical Reviews in Food Science and Nutrition*, **35**(6), 509 (1995).
11. R. J. Avena-Bustillos, J. M. Krochta, M. E. Saltveit, R. J. Rojas-Villegas, J. A. Sauceda-Perez, *Journal of Food Engineering,* **21**(2), 197 (1994).
12. S. Guilbert, N. Gontard, L. G. M. Gorris, *Lebensmittel-Wissenschaft und -Technologie*, **29**(1), 10 (1996):
13. J. K. Brecht, *Horticultural Science,* **30**(1), 18 (1995).
14. H. Kabir, Fresh-cut vegetables, in: A. L. Brody (ed.) Modified Atmosphere Food Packaging, Institute of Packaging Professionals, Herndon, VA, 1994, p. 155.
15. P. Varoquaux, R. Wiley, Biological and biochemical changes in minimally processed refrigerated fruits and vegetables, in: R. C. Wiley (ed.), Minimally Processed Refrigerated Fruits & Vegetables, Chapman & Hall, New York, 1994, p. 226.
16. R. E. Brackett, Microbiological spoilage and pathogens in minimally processed refrigerated fruits and vegetables, in: R. C. Wiley (ed.), Minimally Processed Refrigerated Fruits & Vegetables, Chapman & Hall, New York, 1994, p. 269.
17. F. Riquelme, M. T. Pretel, G. Martinez, M. Serrano, A. Amoros, F. Romojaro, Packaging of fruits and vegetables: recent results, in: M. Mathlouthi (ed.), Food Packaging and Preservation, Blackie Academic & Professional, Glasgow, 1994, p. 141.
18. E. Miedes & E. P. Lorences, *Journal of Agricultural and Food Chemistry,* **52**, 7957 (2004).
19. J. A. L. Van Kan, *Trends in Plant Science*, **11**, 247 (2006).
20. R. E. O'Connor-Shaw, R. Roberts, A. L. Ford, S. M. Nottingham, *J. Food Sci.,* **59**, 1202 (1994).
21. H. Qi, W. Hu, A. Jiang, M. Tian, Y. Li, *Innovative Food Science and Emerging Technologies*, 12, 62 (2011).
22. O. Lamikanra, J. C. Chen, D. Banks, P. A. Hunter, *J. Agric. Food Chem.,* **48**, 5955 (2000).
23. B. M. Lund, *Food Technology International Europe,* 196 (1993).
24. C. B. C. Cartaxo, S. A. Sargent, D. J. Huber, *Proc. Fla. Sta. Hort. Soc*., **110**, 252 (1997).
25. E. Poverenov, S. Danino, B. Horev, R. Granit, Y. Vinokur, V. Rodov, *Food Bioprocess Technol.* Available from: http://dx.doi.org/10.1007/s11947-013-1134-4, (2013).
26. H. Liu, Y. Du, X. Wang & L. Sun, *International Journal of Food Microbiology*, **95**(2), 147 (2004).
27. C. Rejane Goy, D. de Britto; O. B. G. Assis, *Polímeros*, **19**(3), São Carlos, Print version ISSN 0104-1428, On-line version ISSN 1678-5169, (2009).
28. G. J. Tsai, W. H. Su, *Journal of Food Protection,* **62**, 239 (1999).
29. C. Arzu, Z. Ustunol, E. T. Ryser, *Jurnal of Food Protection,* **67**(4), 833 (2004).
30. S. Sivapalasingam, C. R Friedman, L. Cohen, R. V Tauxe, *Journal of Food Protection,* **67**(10), 2342 (2004).
31. R. Enikova, Methodological guide for national microbiological criteria for food products that are not subject to EU Regulation 2073/2005 and EU Regulation 1441/2007, (2008).
32. R. Bibek, Fundamental Food Microbiology. Third edition, London, CRC Press, 2003.

Facile synthesis and electrochemical properties of Prussian Blue/MWCNT and PB/WO$_3$ films

E. Yakar

Department of Materials Science and Engineering, Faculty of Engineering, Çanakkale Onsekiz Mart University, Çanakkale, Turkey

In this study, Prussian Blue (PB)/MWCNTs and PB/WO$_3$ nanocomposite films were deposited onto In-SnO$_2$ (ITO) substrates by a simple chemical bath deposition method. The structural, morphological, and electrochemical properties of PB/MWCNTs films were systematically investigated in detail. Removing influence of ITO, it was evident that both of the patterns could be indexed in the cubic PB phase, from X-ray diffraction analysis. While intense tubular carbon and agglomerative formations were detected in PB/MWCNTs films, cubic PB and spherical WO$_3$ forms were depicted in PB/WO$_3$ films. Average particle sizes (D) of MWCNTs (5.8 nm) were smaller than WO$_3$ (10.5 nm) due to improved particle growth process as shown in this work. Raman analysis proved the production of PB structures. Typical Prussian Blue ν(CN) and stretching vibration of Fe-C at 2159 cm^{-1} and 507 cm^{-1} were observed, respectively. Improved electrochemical performance of PB/MWCNTs electrodes was indicated compared to PB/WO$_3$ electrodes.

INTRODUCTION

As a primary synthetic coordination compound, Prussian Blue (Fe$_4$[Fe(CN)$_6$]$_3$, PB) has been realized as an essential class of transition metal hexacyanides with its unique structure. With the increasing research interest and industrial need for electrochemical mediators, PB has found wide use in biosensors [1], electrochemical sensors [2], rechargeable batteries [3], electro-catalysts [4], and electrochromic devices [5]. In particular, researchers have explicated an intensified interest in the electrochemical activity of PB films due to the increasing demand for the integration of smart devices in our daily life. Although Prussian Blue has good oxidation/reduction properties with high electrochemical activity, the main challenge is the rapid degradation of electrochemical properties [6]. Because the PB layer has low stability where there is too much accumulation, chemical reaction kinetics can decrease between ferric chloride and ferricyanide ions [7]. To solve this problem, polymer matrix formation with PB analogues [8, 9], PB/C-based material nanocomposites [10, 11] and doping [12] processes have been preferred, using the advantage of structural designability and tunable redox potential of Prussian Blue.

On the other hand, unique physical and chemical properties of multi-walled carbon nanotubes (MWCNTs) have afforded developing new promising functional nanocomposites by exposing numerous functional groups at the end of tubes [13, 14]. Several studies have reported enhanced electrochemical performance of PB after modification with MWCNTs. Li *et al.* showed that the introduction of MWNTs resulted in improved electrochemical stability and enhanced response current to reducing hydrogen peroxide (H$_2$O$_2$) of the PG/PB electrode [15]. According to our previous study, the MWCNTs coating on PB/ZnO film yielded an enormous impact on its electrochemical properties by increasing defect sites [16]. Vieira *et al.* explained that the heterogeneous reaction between the electrolyte and iron species led to the formation of PB particles, and their decreasing sizes resulted in better interactions with MWCNTs depending on the scan rate. (10 and 100 mV s^{-1}) [17]. Boron [18], lanthanide [19], and zinc [20] ions were doped on PB films, which were utilized as H$_2$O$_2$ electrochemical sensors and in photothermal applications. Due to its structural transformations, substoichiometric phase transitions and good electrochemical properties, tungsten oxide was selected in this study [21].

Although some researches have been carried out on the modification of PB films with nanoparticles, there is very little scientific understanding of the impact of MWCNTs and WO$_3$ with various physical properties and morphologies on the electrochemical performance of PB films. The aim of this paper is to critically analyze the impact of the PB films of MWCNTs and WO$_3$ on their electrochemical performance and to address possible nano- and microscale mechanisms

* To whom all correspondence should be sent:
E-mail: eyakar@comu.edu.tr

contributing to their electrochemical properties. A facile chemical bath deposition method was used to the preparation of films. Different characterization techniques were utilized to reveal their structural, morphological and electrochemical properties.

EXPERIMENTAL

PB/MWCNT and PB/WO$_3$ films were prepared by a simple chemical bath deposition method onto In-doped SnO$_2$ (ITO) substrates. First, ITO substrates were cleaned by an aqueous solution mixed with ethanol and acetone in ultrasonic bath. Fe$_2$(SO$_4$)$_3$ (Sigma Aldrich, 97%), K$_4$[Fe(CN)$_6$]$_3$ H$_2$O (Sigma Aldrich) and HCl (30 %) were used for the preparation of PB films employing a modified synthesis reported in [22]. MWCNTs (0.02 g) purchased from Nanografi, Turkey (diameters about 20–30 nm and average length of 1.5 μm) was mixed with Fe$_2$(SO$_4$)$_3$ solution on a magnetic stirrer for 30 min to obtain PB/MWCNT films. In addition, 0.1 M Na$_2$WO$_4$.2H$_2$O was added to K$_4$[Fe(CN)$_6$] aqueous solution to obtain PB/WO$_3$ films. Both films were annealed at 150 ºC for 2 h to remove surface contaminations.

Characterization

All characterizations were realized at room temperature. The structural composition and structural parameters were investigated by X-ray diffraction (XRD) analysis by Rigaku SmartLab X-ray diffractometer with CuK$_\alpha$ (1.5406) which was operated at 45 KV and 40 mA. Average particle size (D), dislocation density (δ) and microstrain (ε) were measured by the equations given below:

$$D= 1.5406/\ \beta\ \cos\theta \qquad \text{(Equation 1)}$$

$$\delta= 1/D^2 \qquad \text{(Equation 2)}$$

$$\varepsilon= \beta/\ 4\ \tan\ \theta \qquad \text{(Equation 3)}$$

Surface morphology of the PB/MWCNT and PB/WO$_3$ films was depicted by JEOL JSM-7100 F SEM scanning electron microscope. To characterize the electrochemical properties of these films, cyclic voltammetry (CV) and electrochemical impedance spectroscopy (EIS) measurements were carried out. Electro-activity of the samples was determined by a standard three-electrode configuration (Electrochemical Compactstat Interface/ Ivium Page Technologies) with reference electrolyte type and the scan rate was chosen as 5 mM (Fe(CN)$_6$)$^{3-/4-}$/KCl and 50 mV/s. For the three-electrode configuration,

working electrode, counter electrode and reference electrode were ITO, BASI Pt wire and BASI Ag/AgCl, respectively. Impedance curves were obtained using a Compactstat Interface (Ivium Technologies-Eindhoven/ The Netherlands) and Autolab PGSTAT 128N potentiostat/galvanostat equipped with a FRA2 frequency response analyzer. Raman spectra of the films were recorded by Thermo DXR Raman spectrophotometer, exciting 780 nm laser line in the wavenumber range between 100-3000 cm^{-1}.

RESULTS AND DISCUSSION

Structural analysis

XRD patterns of the films in the range of 2θ = 20-80º are shown in Fig. 1. Both films displayed a polycrystalline structure. Three weak ITO-based peaks were identified in the range of 2θ = 50-70º, indicating that both films adhered well to the substrate. Both samples exhibited different PB corresponding peaks in the range of 2θ = 15-40º, which could be assigned to JCPDS Card No:73-0687 [23]. PB/MWCNTs samples showed characteristic carbon peaks as C(002) and C(100) at 2θ = 25.6º and 2θ = 43.2º, respectively [24]. Beside, PB/WO$_3$ samples had preferential orientation at 2θ = 31.8º, corresponding to the orthorhombic WO$_3$ (220) phase [25]. These results suggested that complex polycrystal forms were obtained [26]. Average particle sizes (D) of MWCNTs were smaller than those of WO$_3$ due to improved particle growth process as shown in Table 1 [27].

Surface Morphology

Surface morphology of the PB nanocomposite films is represented in Fig. 2. In general, crack-free film formations were observed for both films and relatively homogeneous film surface was confirmed. PB/MWCNTs sample surface was covered by tubular structures with different lengths and similar diameters. Partial cluster formations were also obtained due to PB particle growth process. Tubular forms provide a 3D-network that aids to decrease electrical resistance in in-plane and thorough thickness directions, therefore the electrode efficiency of the resulting structure could be increased [28]. On the other hand, it has been observed that PB nanocubes with side length between 50 to 100 nm and WO$_3$ nanospheres as a heterostructure form were obtained in PB/WO$_3$ films [26].
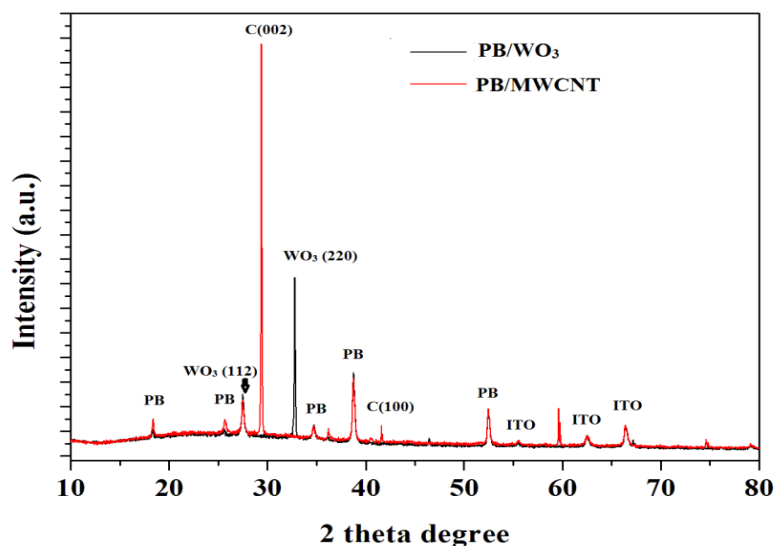
Fig. 1. XRD patterns of PB/MWCNT and PB/WO₃ films

Table 1. Structural parameters of PB/MWCNT and PB/WO₃ films

	2θ (º)	FWHM (rad)	d (Å)	D (nm)	Dislocation density (δ)	Microstrain (ε)
PB/MWCNT	32.7	0.0016	2.730	5.8	0.029	0.000110
PB/WO₃	29.3	0.0010	3.036	10.5	0.009	0.000089
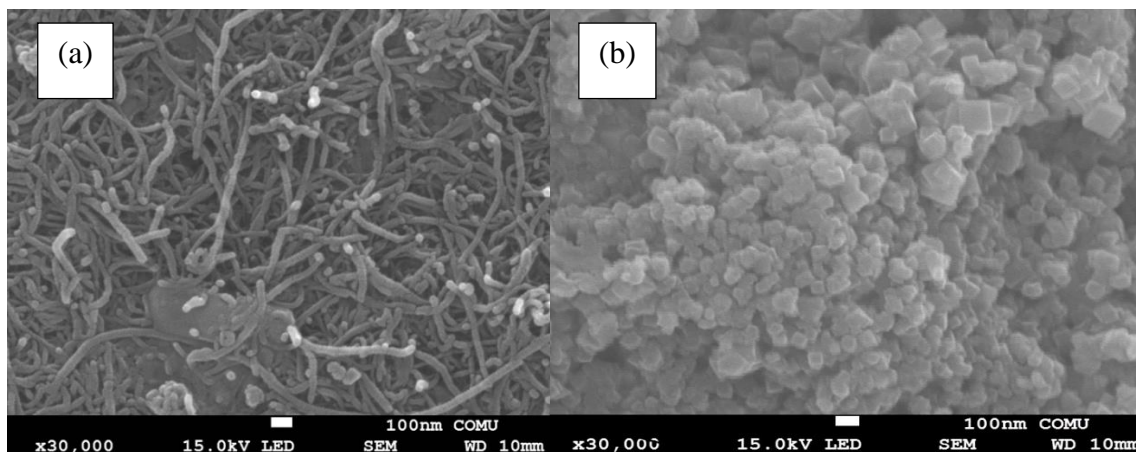
Fig. 2. SEM images of a) PB/MWCNT and b) PB/WO₃ thin films

Electrochemical Characterization

The electrochemical performance of PB/MWCNTs and PB/WO₃ electrodes was investigated by cyclic voltammetry in 5 mM $K_3[Fe(CN)_6]$, $K_4[Fe(CN)_6].3H_2O$ in KCl including redox couple solution at a scan rate of 50 mV/s as represented in Fig. 3. Higher anodic and cathodic response was observed in PB/MWCNT electrode compared to PB/WO₃ electrode. The cathodic response was higher than the anodic response for both samples, as shown in Table 2 due to the lack of proper lattice coordination of iron ions. The reversible conversion cycle was determined between -1 V (-0.9 V) and 1 V (0.8 V) for PB/MWCNTs nanocomposite PB/WO₃ electrode that indicated an increased electrochemical stability effect on PB [29]. These results showed that along with the large surface area provided by MWCNTs, it provides enhanced Fe-carboxyl-CN interactions compared to Fe^{3+}-W^{6+} ions interactions on the

101

electrode surface [30]. To investigate the charge-transfer process at the electrode/solution interface, electrochemical impedance spectroscopy (EIS) is a powerful tool.
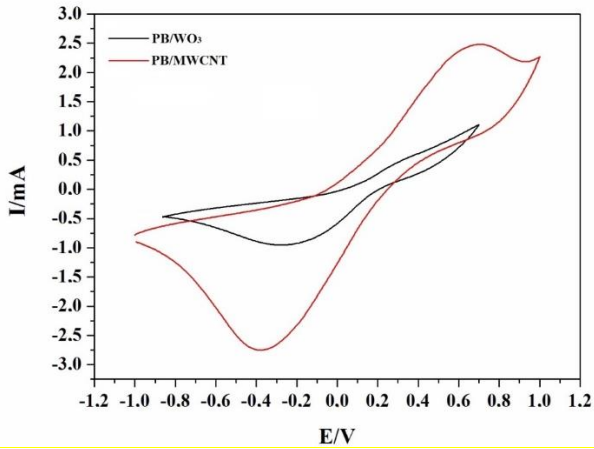
Fig. 3. Cyclic voltammogram of PB/MWCNT and PB/WO$_3$ electrodes in background solution (5 mM K$_3$[Fe(CN)$_6$], K$_4$[Fe(CN)$_6$].3H$_2$O in KCl) at an optimum scan rate of 50 mV/s

In the range between 0.10 Hz and 10^5 Hz, Nyquist plots of PB/MWCNTs and PB/WO$_3$ nanocomposite electrodes are shown in Figs. 4(a) and 4(b), respectively; fitting the electric model presented in Fig. 4(c). The impedance behavior of the electrodes was different and showed a high semicircle diameter for both electrodes with 5 mM KCl supporting electrolyte solution. The R$_{ct}$ (Ω) values indicated an improvement in the conductivity by WO$_3$ implementation of PB when compared to MWCNTs coating in PB [31]. Warburg line extrapolation in the low frequency's limit is the double layer capacitance at the ITO/sample interface and no serious differences were seen for both electrodes, indicating that the diffusion process was relatively improved by W^{6+} ions and conductive MWCNTs coating [32].

Raman spectra of PB/MWCNTs and PB/WO$_3$ nanocomposite films are shown in Fig. 5. Typical Prussian Blue ν(CN) and stretching vibration of Fe-C at 2159 cm^{-1} and 507 cm^{-1} are observed, respectively. ν(CN) band of PB/WO$_3$ appears sharper and with higher intensity compared to the PB/MWCNTs nanocomposite films, indicating improved crystallization [33]. The agglomerated ferricyanide ion bands appeared at 1200 cm^{-1} [34]. Both MWCNT- and WO$_3$- related bands are not observed due to their low concentration for interacting Prussian Blue particles.

Table 2. CV and EIS measurement results (R_{ct}: Charge transfer resistance; E^o: Formal potential)

Electrode	EIS Analysis	CV Response in 5.0 mM Fe(CN)$_6^{3-/4-}$				
	R_{ct} (Ω)	E_a (V)	E_c (V)	E^o (V)	I_a (µA)	I_c (µA)
PB/WO$_3$	888	0.315	-0.275	0.295	2.5	745
PB/MWCNT	1956	0.685	-0.380	0.533	850	2413
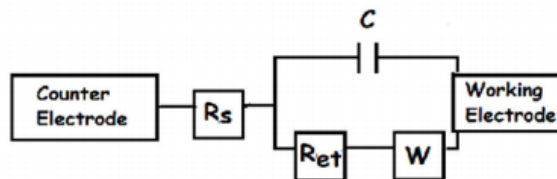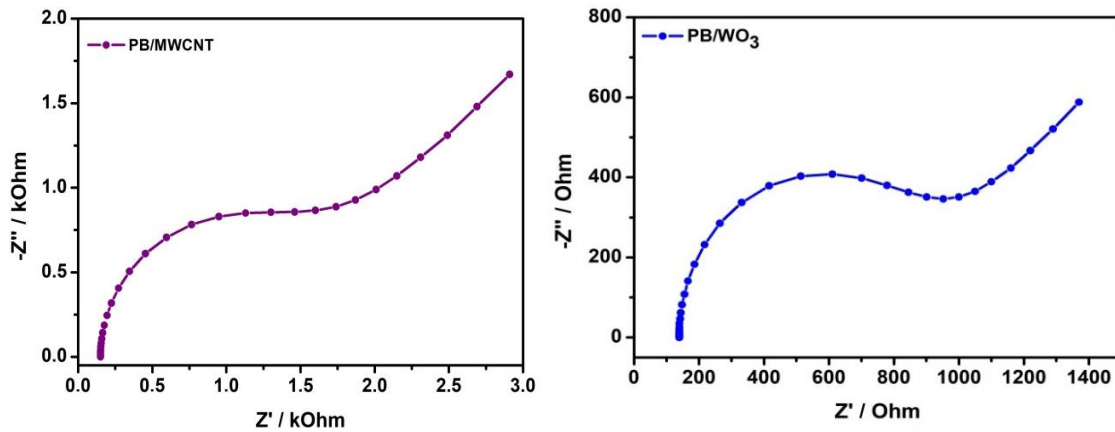
Fig. 4. Nyquist plots a) PB/MWCNT; b) PB/WO$_3$ with redox couple; c) electric model
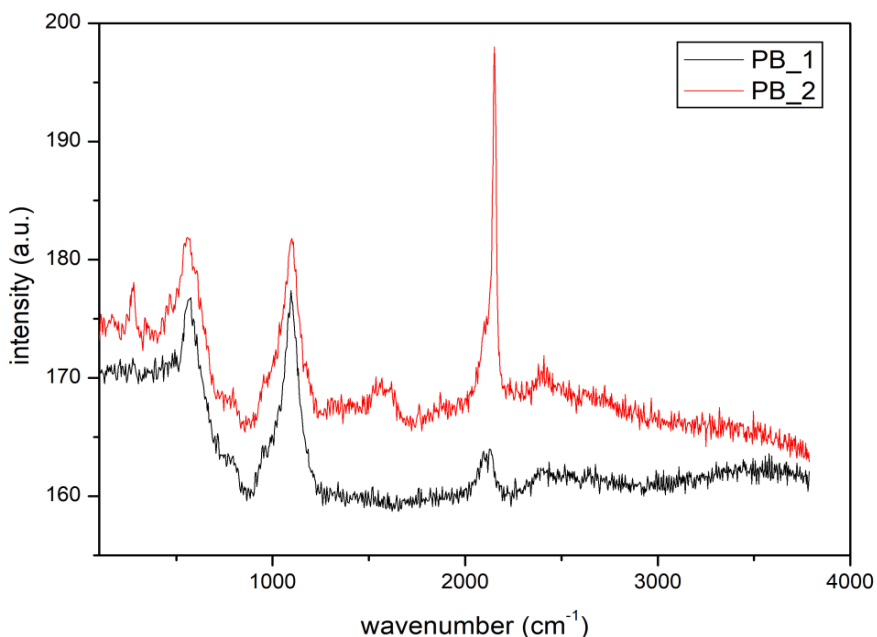
Fig. 5. Raman spectrum of PB/MWCNT (PB_1) and PB/WO₃ (PB_2) films

CONCLUSION

In this study, PB/MWCNTs and PB/WO₃ structures were successfully synthesized by the chemical bath deposition method on electrically conductive In-doped SnO_2 substrates. The intense X-ray patterns were narrow and sharp indicating that Prussian Blue was well crystallized. SEM images showed various types of PB morphologies with different sizes (tubes, cubes and clusters) in both films. Upon redox cycling, PB/MWCNTs nanocomposite electrodes in a wider potential range were electrochemically more stable than PB/WO₃ electrodes. From these results it may be concluded that MWCNTs would be an appropriate nanocomposite part for PB-based electrochemical devices.

REFERENCES

1. N. Ç. Kurt, M. S. Çelebi, *Ordu Univ. J. Sci. Tech.*, **1**, 31 (2018).
2. M. D. J. Masaquiza, L. Fernández , G. González, *Nanomaterials*, **10**, 1328, (2020).
3. B. Huang, Y. Shao, Y. Liu, Z. Lu, X. Lu, S. Liao, *CS Appl. Energy Mater.*, **2**(9), 6528 (2019).
4. Y. Feng, X. Wang, P. Dong, J. Li, L. Feng, J. Huang, L. Cao, L. Feng, K. Kajiyoshi, C. Wang, *Scientific Reports*, **9**, 15965 (2019).
5. A. Takahashi, K. Noda, H. Watanabe, T. Kawamoto, *RCS Advances*, **9**, 40183 (2019).
6. K. Hurlbutt, S. Wheeler, I. Capone, M. Pasta, *Joule,* **2**, 1 (2018).
7. F. Doroftei, T. Pinteala, A. Arvinte, *Microchim. Acta,* **181,** 111 (2014).
8. L. Wu, T. Pang, Y. Guan, Y. Li, *Polymers,* **11**, 266 (2019).
9. L. V. Lukachova, E. A. Kotelnikova, D. D'Ottavi, E. A. Shkerin, E. E. Karyakina, D. Moscone, G. Palleschi, A. Curulli, A. A. Karyakin, *IEEE Sensors Journal*, **3**, 3 (2003).
10. M. Chen, Z. Zhang, X. Liu, Y. Li, Y. Wang, H. Fan, X. Liang, Q. Chen, *RSC Advances*, **10**, 31773 (2020).
11. S. Husmann, S. G. Booth, A. G. J. Zarbin, R. A. W. Dryfe, *J. Braz. Chem. Soc.,* **29**(5), 1130 (2018).
12. Y. Zhu, Z. Zhang, J. Bao, S. Zeng, W. Nie, P. Chen, Y. Zhou, Y. Xu, *Int. J. Energy Res.,* **44**, 9205 (2020).
13. K. K. Gangu, S. Maddila, S. B. Jonnalagadda, *Science of the Total Environment*, **646**, 1398 (2019).
14. E. Moaseri, M. Karimi, M. Maghrebi, M. Baniadam, *Science of the Total Environment*, **51** 774 (2014).
15. Z. Li, J. Chen, W. Li, K. Chen, L. Nie, S. Yao, *Journal of Electroanalytical Chemistry,* **603**, 59 (2007).
16. F. Ozutok, E. Yakar, *Journal of New Materials for Electrochemical Systems,* **21**, 119 (2018).
17. T. A. Vieira, J. R. Souza, D. T. Gimenes, R. A. A. Munoz, E. Nossol, *Solid State Ionics*, **338** 5 (2019).
18. M. A. Komkova, A. Pasquarelli, E. A. Andreev , A. A. Galushin, A. A. Karyakin, *Electrochimica Acta*, **339**, 135924 (2020).
19. X. Chena, G. Wua, J. Tanga, L. Zhou, S. Weia, *Inorganic Chemistry Communications*, **114**, 107821 (2020).
20. J. Li, X. Liu, L. Tan, Z. Cui, X. Yang, Y. Liang, Z. Li, S. Zhu, Y. Zheng , K. W. K. Yeung, X. Wang, S. Wu, *Nature Comminications,* **10**, 4490 (2019).
21. K. Rong, H. Zhang, H. Zhang, Y. Hu, Y. Fang, S. Dong, *ACS Appl. Electron. Mater.*, **1**, 1038 (2019).

22. J. Velevska, M. Pecovska-Gjorgjevich, N. Stojanov, M. Najdoski, *IJSBAR*, **25**(3), 380 (2016).
23. N. Ghasdian, Y. Liu, R. McHale, J. He, Y. Miao, X. Wang, *J. Inorg. Organomet. Polym.*, **23**, 111 (2013).
24. T. Arunkumar, R. Karthikeyan, R. Ram Subramani, K. Viswanathan, M. Anish, *International Journal of Ambient Energy,* **41**(4), 452 (2020).
25. S. Zhuiykov, E. Kats, *Nanoscale Research Letters*, 9, 401 (2014).
26. S. Tadano, B. Giri, *Science and Technology of Advanced Materials,* 12, 064708, (2011).
27. K. H. Bhuiyan, M. Rahman, F. Mina, M.R. Islam, A. Gafur, A. Begum, *Composites: Part A,* **52,** 70 (2013).
28. Y. Yao, X. Bai, K. K. Shiu, *Nanomaterials*, **2**, 428 (2012).
29. N. S. Pham, Y. H. Seo, E. Park, T. D. D. Nguyen, I. S. Shin, *Electrochimica Acta*, **353**, 136446 (2020).
30. L. M. N. Assis, R. C. Sabadini, L. P. Santos, J. Kanicki, M. Łapkowski, A. Pawlicka, *Electrochimica Acta*, **182**, 878 (2015).
31. M. Saravanan, M. Ganesan, S. Ambalavanan, *RSC Advances*, **5**, 26081 (2015).
32. H. Fu, C. Liu, C. Zhang, W. Ma, K. Wang, Z. Li, X. Lu, G. Cao, *J. Mater. Chem. A*, **5**, 9604 (2017).
33. G. Moretti, C. Gervais, *J. Raman Spectrosc.*, **49**, 1198 (2018).
34. F. Grandjean, L. Samain, G. J. Long, *Dalton Trans.*, **45**, 18018 (2016).

A new Bulgarian strain of *Scenedesmus* sp.– identification, growth, biochemical composition, and oil recovery

I. Vasileva[1*], S. Boyadzhieva[2], G. Kalotova[2], J. Ivanova[1], L. Kabaivanova[3], G. Naydenova[2],
M. Jordanova[2], D. Yankov[2], R. P. Stateva[2]

[1]Institute of Plant Physiology and Genetics, Bulgarian Academy of Sciences, Acad. G. Bonchev str. 21, 1113 Sofia, Bulgaria

[2]Institute of Chemical Engineering, Bulgarian Academy of Sciences, Acad. G. Bonchev str. 103, 1113 Sofia, Bulgaria

[3]The Stephan Angeloff Institute of Microbiology, Bulgarian Academy of Sciences, Acad. G. Bonchev str. 26, 1113 Sofia, Bulgaria

In the present study a new Bulgarian strain of *Scenedesmus* sp. was taxonomically and molecularly identified as *Scenedesmus obliquus*. The most favorable cultivation conditions in terms of temperature, light intensity and growth phase were determined. The biochemical composition analyses showed that the strain is among the best producers of proteins, carbohydrates and lipids from the genus. The algal oil was recovered from the biomass applying conventional extraction methods and solvents with varying polarity. The highest cumulative yield of 28 % of dry weight was achieved by a two-step Soxhlet with *n*-hexane and ethanol, on a biomass pretreated by sonication. GC-MS analyses of the oils showed that saturated and polyunsaturated fatty acids content changed within (19.5-27.3) % and (15.7-23.8) %, respectively, and GC-FID analyses of fatty acids demonstrated the dominance of oleic and palmitic esters. The results obtained reveal the feasibility of the newly isolated strain as a renewable resource for the biofuel industry.

Keywords: *Scenedemus* sp., growth, lipid extraction methods, fatty acid composition, biofuels

INTRODUCTION

Algae, as a biological resource, have been the focus of prolific research in the last years and are advertised as the most suitable and sustainable feedstock for producing green energy (as the whole process is carbon-neutral in nature) and value-added compounds.

More than one million algae species exist and the diversity of compounds produced by them is estimated to be over 10 times greater than those produced by land plants [1] and despite their potential to help changing the economy and society in general from oil-based to bio-based systems they are still a highly unused resource. Microalgae are regarded as a revolutionary raw material and an alternative, the so-called third generation feedstock. That is because they possess essential advantages over conventional land plants, e.g. about 10–50 times higher biomass productivities and higher CO_2 fixation rate, but also because arid or low-quality agricultural land is used for their cultivation.

In recent years, the biorefinery (BioRef) concept is believed to be one of the most important tools towards the development of a sustainable circular economy. The diversity in composition of biomass/biowaste offers huge perspectives to industry as their BioRef processing can deliver a spectrum of marketable products and energy.

It is well known that algae biomass composition is influenced by the cultivation parameters and varies greatly in different algae representatives. Hence, the composition of the specific algae biomass could be used as an indicator of the spectrum of potential products that can be recovered, e.g. either energy and/or non-energy related and bioactives, and, subsequently, the multitude of possible techniques that can be applied to realize the particular valorization desired. Therefore, the application of algae biomass in a one feedstock-multiproduct BioRef platform fits perfectly within the circular economy concept.

Among the over 150 000 algal species identified in the world [2], green unicellular eukaryotic algae (*Chlorophyceae*) and in particular *Scenedemus* sp., are subjected to various studies due to their effective nutrient uptake, high photosynthetic efficiency, rapid reproduction and relatively simple culture maintenance, as well as commercial and pharmaceutical value [3, 4]. In the past decade, a number of species – *S. obliquus, S. dimorphus, S. quadricauda, S. protuberans* – to name just a few, have been a subject of extensive research from the viewpoint of their application as excellent renewable, sustainable, and economical sources in

* To whom all correspondence should be sent:
E-mail: ivanina_vasileva1@abv.bg

the food, pharmaceutical and biofuels industries [5-7].

One of the strains among the *Scenedemus* species, *S. obliquus,* has been a target of considerable research owing to its rich biochemical composition that opens a number of different avenues for application of its biomass. *S. obliquus* was firstly reported to evolve hydrogen in dark or light under anaerobic conditions [8] that triggered scientific interest to the strain. Since then, it was demonstrated that this organism accumulates up to 45 % w/w triacylglycerol (TAG) under nitrogen (N) starvation and hence can be considered to be among the most promising microalgae species for sustainable biofuel applications [9]. Moreover, taking into consideration that for example at present, over 95 % of the biodiesel produced globally is from edible vegetable oils, recovered from plants grown on agricultural land, while *S. obliquus* oil is not used in food industry, and hence the species biomass can be used as a feedstock to produce biofuels without any threat to food production. It has also been shown that *S. obliquus* possesses antioxidant and antitumor activity since it produces the bioactives astaxanthin and lutein [10, 11].

Recently, a new previously unidentified strain of the genus *Scenedesmus* was isolated from a rainwater puddle in Sofia, Bulgaria at an average temperature of 20 °C, and named *Scenedesmus* sp. BGP. Preliminary studies revealed that it possesses metabolic plasticity towards the application of different N sources in the nutrient medium while preserving the growth rate [12]. However, the potential of the *Scenedesmus* sp. BGP as a renewable bioresource is still far from being examined. Consequently, additional research and analyses are required to gather quality new information that could serve as a basis for assessing and outlining the capabilities of this totally unused at present biomass as a potential viable feedstock in a future BioRef targeted at products with multiple and diversified applications.

The main objectives of our work were to: 1. Conduct taxonomic identification of the new Bulgarian strain; 2. Examine the influence of cultivation conditions and factors like temperature and light intensity on its growth and biochemical composition; 3. Study the influence of solvents on the yield and composition of the algae oil extracts recovered from the strain biomass by conventional extraction methods; 4. Perform a preliminary assessment of the potential of the above extracts as a source of biofuel related compounds.

MATERIALS AND METHODS

Algal strain collection and taxonomic identification

A rain water sample from Sofia, Bulgaria was collected and provided in July 2013. Among the microalgae (*Haematococcus pluvialis*) present, an unidentified strain, of genus *Scenedesmus,* was found, and was taxonomically and molecularly analyzed. The taxonomic identification was performed following the classification system adopted by Komárek and Fott [13]. Microphotography and light microscopy were done using an Olympus BX50 microscope equipped with HI 100x/1.35 corr. objective (Picture 1).

Picture 1. Image of monoalgal culture of *Scenedesmus* sp. BGP containing single cells and four-cell cenobia

To perform DNA isolation and PCR analysis the following procedures were adopted. Monoalgal, non-axenic culture of *Scenedesmus* sp. BGP was cultivated at 25°C and 8000 Lux light illumination for 96 h. Pellets of microalgae samples were collected following centrifugation and stored at -80 ºC. By applying a Tissue Lyser II (Qiagen) the samples were disintegrated, the DNA was isolated by GeneJT Plant Genomic Purification Kit (Thermo Scientific) and used as a template for PCR amplification of the internal transcribed spacer (ITS) region using universal primers [14] ITS1 (5'AGCGGAGGAAAAGAAACTA) and ITS4 (5'TACTAGAAGGTTCGATTAGTC). In the PCR reaction the Phusion High-Fidelity DNA Polymerase master mix (Thermo Scientific) was used and the experimental setting included 30 s denaturation at 98 ºC. After that 35 cycles at 98 ºC for 10 s, 57 ºC for 30 s and 72 ºC for 15 s and final extension at 72 ºC for 3 min (Quanta Biotech QB-96) were performed. The PCR fragment was purified using a GeneJET Gel Extraction Kit (Thermo Scientific). After that it was sequenced using Macrogen Europe B.V. services. The sequences obtained were constructed and manually edited using Vector NTI v. 10 (Life Technologies). The

proximity of the Internal Transcribed Spacers (ITS) sequences with other sequences deposited at the GenBank was assessed by Basic Local Alignment Search Tool (BLAST). The ITS sequence plus the selected pools of the GenBank retrieved sequences were utilized for the construction of phylogenetic tree using MEGA 4.1 [15].

Cultivation conditions

Monoalgal, non-axenic cultures of *Scenedesmus* sp. BGP were grown autotrophically on a temperature block [16]. The block uses a constant water flow to maintain gradually increasing temperatures in its different parts. On the top of the block cool-white fluorescent lamps were attached and provided the continuous light for the cultivation. This equipment enables to set and maintain the desired temperatures (15, 20, 25, 30, 35 °C) simultaneously at two different light intensities – 132 μmol photons m^{-2} s^{-1} unilateral (conditionally marked as LLI – low light intensity) and 2×132 μmol photons m^{-2} s^{-1} bilateral (HLI – high light intensity). Individual flasks of 100 ml with the culture were grown for each temperature and light intensity. The algae were cultured in the modified nutritive medium of Setlik [17, 18], diluted to ¼ of its original concentration, routinely used in the lab for green algae cultivation, but only with one *N* source – urea with preserved equimolar quantity. All cultures were continuously bubbled with air enriched with 2 % CO_2. The experimental cultures were harvested after 144 hours. Cells were collected by centrifugation (5000 × g, 20 min), rinsed three times with distilled water, frozen, and stored at -70 °C until analyzed.

Growth and specific growth rate

The growth of *Scenedesmus* sp. BGP was assessed by the increment in the dry weight (DW) of the algal biomass in g L^{-1} which was determined gravimetrically. For this purpose, algae suspensions (3 × 5 ml each) were filtered through Whatman GF/C glass filters (Whatman International Ltd, Maidstone, UK), rinsed with tap water to eliminate salts and oven dried at 80 °C to a constant weight.

The specific growth rate (μ) was calculated as follows [19]:

$$\mu = \ln(mt_2/mt_1)/t_2–t_1 \qquad (1)$$

where mt_1 and mt_2 represent the *Scenedesmus* cells DW at the starting day of the experiment (t_1) ($t_1=0$) and at the final day of the experiment (t_2) ($t_2=4$).

Biochemical composition
Protein content

Total protein content (g L^{-1}) was measured following the method of Lowry [20], with Bovine serum albumin (BSA, Sigma-Aldrich) as a standard. The algal suspension was flooded with hot methanol (1:1, Merck), then the mixture was centrifuged. To the residue 4 ml of 1N NaOH (Honeywell Fluka) were added. The reaction was conducted on a water bath for 20 min, followed by centrifugation. The supernatant, ($NaCO_3$ + (Na-K tartrate+$CuSO_4$) and Folin-Chiocalteu reagent (Sigma-Aldrich) formed the final mixture, followed by absorption measurement.

Carbohydrate content

Total carbohydrates (g L^{-1}) were estimated by the phenol-sulfuric acid method using glucose (99.5%, Sigma-Aldrich) as a standard [21]. To 0.5 ml of algal suspension 0.5 mL of 5% phenol solution and 2.5 mL of concentrated H_2SO_4 (95-97%, Merck) were added After 30 min incubation, the absorption was measured.

Lipid content

Two methods were employed to determine the lipid content. The method described by Petkov [22] is suitable for extraction of lipids for all classes of microalgae. However, in a parallel study co-authored by the same author [23], it was ascertained that on green microalgae another safer and quicker method can be used. In Petkov's method [22], the centrifuged algae biomass was extracted *via* a boiling solution of chloroform+methanol (2:1) on a reverse condenser. The extract was filtered in order to remove the cell fragments. Next, chloroform (> 99 %, Merck) and methanol were separated by a solution of 11.5 % NaCl (to 1/5 of the volume of the extract, > 99 %, Sigma-Aldrich). On a rotary vacuum evaporator, back-extraction with chloroform was performed at (40–45) °C and the extract was dried by applying Na_2SO_4 (> 99 %, Sigma-Aldrich). The lipid quantity (g L^{-1}) was determined gravimetrically.

Following the second method advocated by Petkov and Dilov [23], the algae suspension was centrifuged, then algae biomass was extracted twice with hot ethanol (1:20, 96%, Chimspectar) under reflux. The ethanol extract was evaporated and back-extracted with chloroform. The latter was removed by evaporation at (40–45) °C on a rotary vacuum evaporator. Lipids were gravimetrically quantified (g L^{-1}) following Petkov and Dilov [23].

Extraction techniques

Conventional extraction techniques, characterized by low equipment cost and easy operation, were applied to recover the algal oil from the biomass. Solvents with different polarity were used. Also, in certain cases, mild pretreatment methods – flooding with boiling ethanol and ultrasonication – were applied.

The procedure adopted for the sample preparation was the following: The harvested biomass was centrifuged at 5500 × g for 15 min and then frozen at -22 °C until lyophilization. In our case, lyophilization was conducted on a LGA 05 lyophilizer (Janetzki, Leipzig, Germany) at +20 °C for 24-30 h until the sample was completely dry. The lyophilized biomass was conserved at 4 °C in dark.

Petkov and Dilov and Petkov extraction methods

The extraction techniques are described in the sections *Lipid content, Two-step atmospheric extraction with stirring*.

The experiments were carried out on a temperature-controlled magnetic stirrer. Two solvents were tested: *n*-hexane (99 % Honeywell/Riedel-de Haen), and ethanol (96 %, Chimspectar). For step 1 the procedure was the following: 1 g of pre-ground lyophilized algae was mixed with 30 ml of *n*-hexane in a flask. The extract was recovered and dried. In step 2, the residual biomass was dried, weighed and ethanol quantity was calculated to satisfy 1:30 (biomass:ethanol) ratio. The contact time for both steps was 60 min.

Soxhlet extractions

Soxhlet extraction is an effective method that guarantees high yield and continuous contact with fresh solvent, which is easily recovered afterwards by evaporation, etc. Still, the use of an organic solvent (e.g. *n*-hexane), the relatively high temperatures and long extraction times which might increase the possibilities of thermal degradation of heat sensitive compounds, are some of its drawbacks. In our Soxhlet experiments the influence of biomass pretreatment and solvents on the oil yield and composition were studied.

With regard to the biomass pretreatment, it was noted that the selection of a disruption technique is exceedingly specific and depends on the strain and structural morphology of each microalgal cell wall, and on the nature of the products expected to be recovered and/or their application [24]. In this study, two pretreatment methods were used: Flooding twice with boiling ethanol and ultrasonication. The latter is favored by some authors, who have pointed out its effectiveness in enhancing the extraction yield

of various intracellular compounds including lipids [24]. Still, on the other end are authors (see for example [25]) who state that the microwave oven method is more effective for lipid extraction than sonication.

One-step Soxhlet with ethanol

In this case, the biomass pretreatment was as follows: two grams of algae biomass were placed in the extractor thimble and flooded twice with 40 ml of boiling ethanol. The solution gradually turned green and after cooling for about 15 min was transferred to a round-bottom flask and another 70 ml of ethanol were added, hence the total volume was 150 ml (solvent/solid ratio 75 ml/1 g). The working volume of the Soxhlet extractor was 70 ml. The process time was 8 hours. The criterion for stopping the Soxhlet extraction was a change in the color of the solution – it slowly faded from green to light yellow. The biomass and the extract were separated by filtration with Millipore (0.22 μm). The extract obtained was separated from the solvent by a rotary vacuum evaporator (Heidolph/ Germany) at $T = 40\ ^0C$ and $p = 175$ mbar. Picture 2 shows an image of a disrupted *Scenedesmus* sp. BGP single cell after flooding the biomass with boiling ethanol.
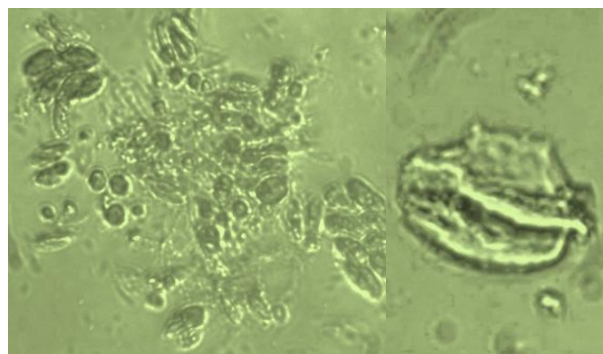
Picture 2. Image of *Scenedesmus* sp. BGP cells after sonification

Two-step Soxhlet extraction

In step 1 the solvent used was *n*-hexane. Firstly, the biomass mixed with *n*-hexane was sonicated in an ultrasonic disintegrator UD 20 (Techpan, Warsaw) with ultrasonic field of 8-24 kHz. The optimum operating parameters were determined in a series of preliminary sonications at different resonance, cycles and time. After each sonication, the sample treated was examined by a microscope to establish the level of cell disintegration. As a result, the procedure adopted was the following: in a volumetric flask two grams of algae biomass were mixed with 30 ml of *n*-hexane, and subjected to five consecutive ultrasonications at the maximum ultrasonic field level, followed by a cool-down

period in ice water for 1 min. Total time of pretreatment was 10 min.

After the sonication pretreatment, the whole quantity was transferred to the extractor thimble and additional 120 ml of *n*-hexane were added in the round-bottom flask to achieve a solvent volume of 150 ml (solvent/solid ratio 75 ml/1 g). After 4 hours, the process was stopped and the extract was filtered through Millipore (0.22 μm). After drying, the residual biomass from step 1 was extracted with 150 ml of 96 % ethanol. The second step was stopped after 8 hours and the liquid extract obtained was filtered and dried.

GC analyses of the extracts obtained

Fatty acids (FAs) composition of selected extracts was determined by gas chromatography (GC) of methyl esters (FAME). The methodology is discussed in details by Taneva *et al.* [26] and is briefly summarized here. Each sample was transmethylated with 1% sulfuric acid in methanol. The FAME were purified by preparative silica gel thin-layer chromatography (TLC) using hexane-acetone (100:6, v/v) as a mobile phase. The gas chromatograph was Shimadzu 17A (Shimadzu, Japan) equipped with a flame ionization detector and Supelcowax-10 column (100 m × 0.25 mm × 0.25 μm, SUPELCO). The temperature gradient of the column was 4 K min^{-1} in the range $T = (433 – 543)$ K. Upon reaching the maximum temperature desired, it was sustained for 20 min. The temperature of the injector was 533 K and that of the detector– 553 K. Split injection mode (1:50) was used, each sample was 15 μg and helium was used as a carrier gas at a 1.1 ml min^{-1} flow rate. The peaks identification was according to retention times of the reference FAME. The qualitative analysis of selected extracts was carried out by GC-MS. The gas chromatograph was Agilent 7890B equipped with Agilent 5977A mass selective detector, the column - DB-5 MS ((5%-phenyl)-methylpolysiloxane, 30 m × 0.25 mm × 0.25 μm I.D.) and helium was used as a carrier gas. The temperature of the injector and detector was 533 K. The temperature of the column – 333 K, held for 4 min, the temperature gradient was 3 K, held for 1 min up to reaching 573 K. The FAs were identified by interpreting and comparing their mass spectra to existing databases. The relative content of FAs was expressed as percentage (%) of individual fatty acid to total fatty acids.

Statistical analysis

All experiments were conducted in three independent biological replicates and each measurement had three replicates. The data were presented as the means ± standard deviation. The significance of differences between the treatments was evaluated by ONE WAY analysis of variance (ANOVA) and Bonferroni's post hoc test using GraphPAD InStat software (San Diego, CA, USA). Values of $P < 0.05$ were considered significant.

RESULTS AND DISCUSSION

Taxonomic identification

Monoalgal culture of *Scenedesmus* sp. BGP contained single cells and four-cell cenobias. In the lag phase, more single cells were observed, while in the exponential phase the culture was dominated by cenobias. The morphological analysis showed that the investigated cells were non-motile and zoospores were not observed. The cells had elongated shape with approximate length of 12 × width of 5 μm. After performing the morphological analysis, the newly isolated strain was identified as *Scenedesmus obliquus* (Turpin) Kutzing [2].

The sequence comparison results are presented on Fig. 1. From the BLAST search performed and from the phylogenetic tree it can be deduced that the strain has the closest proximity in terms of likelihood to the *Tetradesmus obliquus* strain *Scenedesmus obliquus*. From the algae data base [2] it can be confirmed that right now *S. obliquus* (Turpin) Kützing 1833 is considered a synonym of *Tetradesmus obliquus* (Turpin) [27], which substantiates our taxonomic and molecular analyses. Hence, to be consistent with the initially given name in what follows the Bulgarian strain is referred to as *S. obliquus* BGP.

Effect of temperature and light intensity on the growth and specific growth rate of Scenedesmus obliquus BGP

Temperature and light are the basic parameters that affect the photosynthesis and respiration, therefore, the biomass productivity. Although it is known that the influence of light on the growth and productivity depends on temperature and *vice versa* [28], still, the combined effect of these factors has been less studied than their individual impact [29, 30].
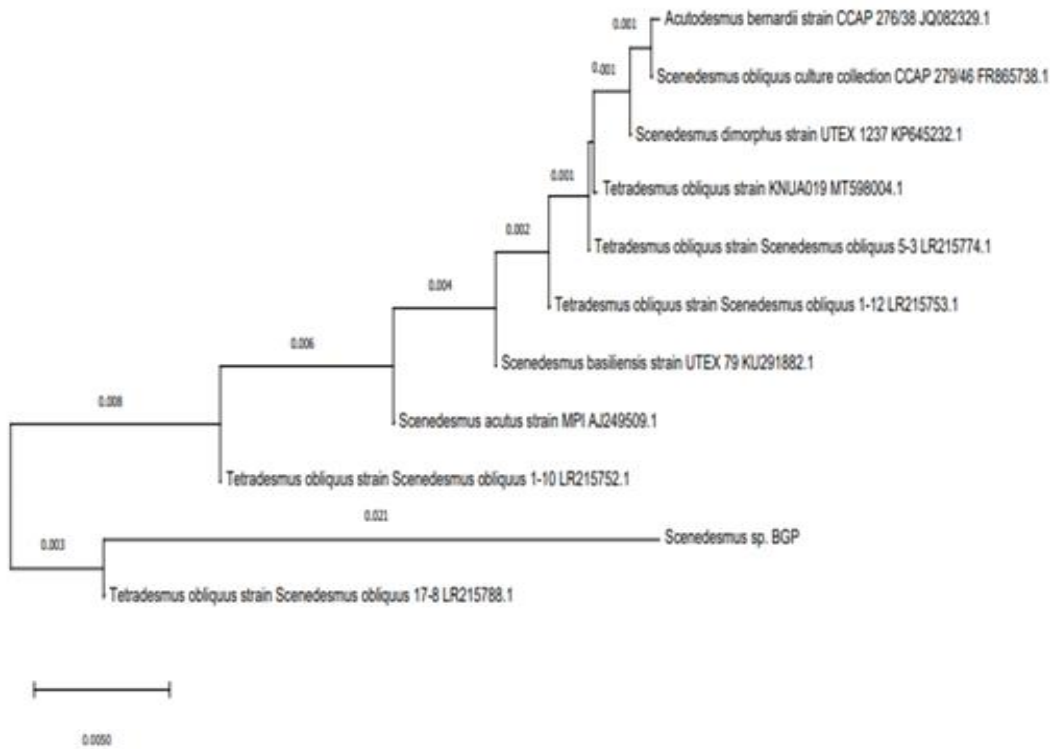
Fig. 1. Maximum likelihood tree. Numbers at the nodes indicate bootstrap probabilities (> 50 %) of maximum likelihood analyses (1000 replicates). The scale bar represents 0.02 % difference in nucleotide sequences.
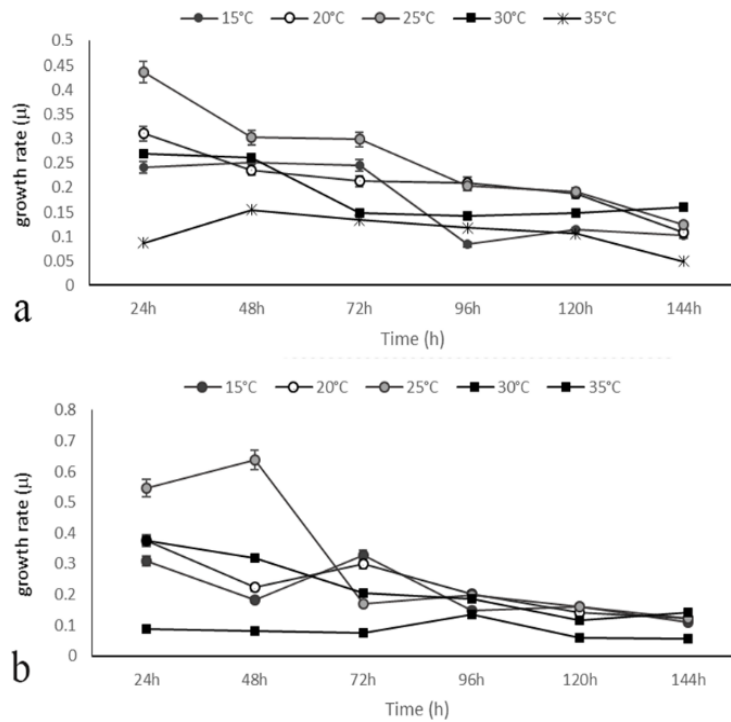

Fig. 2. Dependence of the accumulated biomass on the cultivation temperature and time of *Scenedesmus obliquus* BGP at LLI (a) and HLI (b).
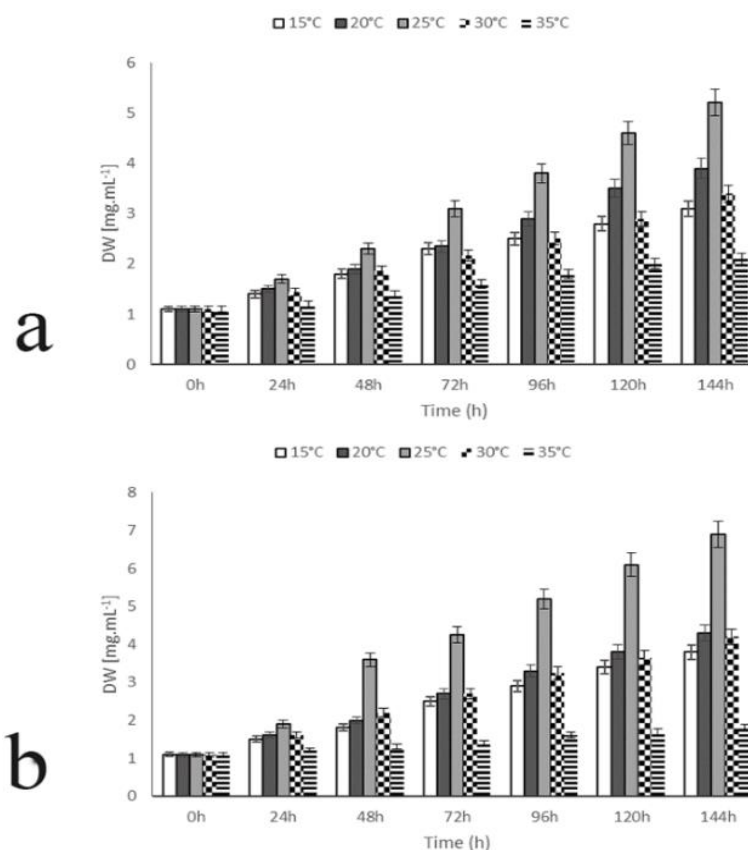
Fig. 3. Dependence of the specific growth rate on the cultivation temperature and time of *Scenedesmus obliquus* BGP at LLI (a) and HLI (b).

It was demonstrated for the first time in the present work that *S. obliquus* BGP grew well within the temperature range of (15–30) ° C at both light intensities on modified Setlik medium (Figure 2). The highest biomass yield and the maximal growth rate were observed at 25 °C at both LLI and HLI (optimal temperature) – 5.2 and 6.9; $\mu = 0.26$ and 0.31, respectively (Figure 2 and Figure 3). As briefly discussed previously, *S. obliquus* BGP has a natural habitat of lower temperatures than many other representatives from the same species. For example, *S. dimorphus* responded to changes in the cultivation temperature in a different way. Just like the Bulgarian strain, the lowest and the highest growth rate and dry biomass weight were observed at (15 and 25) °C, respectively (the results for 35 °C are not taken into consideration, Figure 2). However, in the case of *S. obliquus* BGP, the highest temperature (35 °C) along with the high light intensity were particularly unfavorable growth conditions as was observed with some other microalgae. A similar conclusion can be made when it comes to the specific growth rate. In the work of Duan *et al*. [31], during the cultivation of *S. obliquus*, $\mu = 0.26$ was reached just at the 48th hour of cultivation, and then the values of μ rapidly decreased.

Effect of temperature and light intensity on the biochemical composition of Scenedesmus obliquus BGP

The optimal temperature promotes best the protein synthesis, although protein production was higher at HLI than at LLI at all temperatures tested - 2.4 g L^{-1} and 1.9 g L^{-1}, respectively (Figure 4).
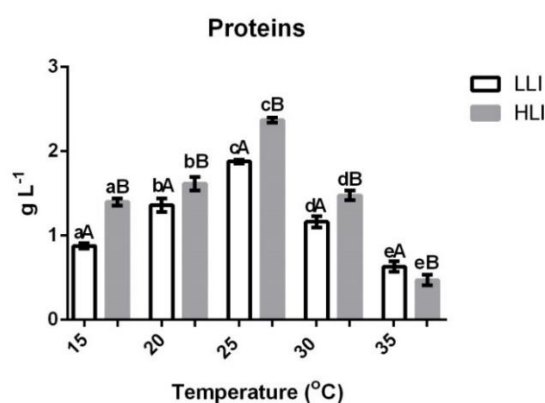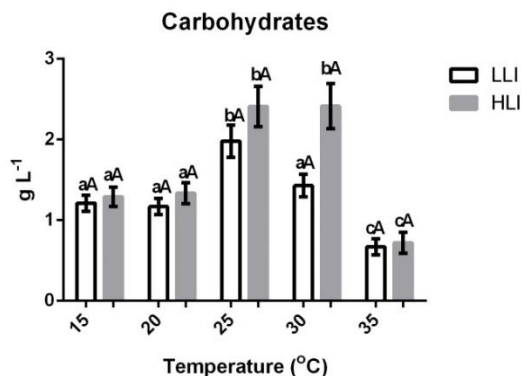

Fig. 4. The joint effect of temperature and light intensity on the protein content of *Scenedesmus obliquus* BGP. Means with different lowercase letters are significantly different (P < 0.05) between temperatures for a specific light intensity. Different capital letters indicate significant difference for a specific temperature between LLI and HLI.

The quantity of carbohydrates at the suboptimal temperatures was almost the same regardless of the light intensity. The highest yield was achieved when conditions of 25 °C (both light intensities - 2 g L^{-1} and 2.4 g L^{-1}, respectively) and 30 °C (HLI; 2.4 g L^{-1}) were applied. (Figure 5).

Fig. 5. The joint effect of temperature and light intensity on the carbohydrate content of *Scenedesmus obliquus* BGP. Means with different lowercase letters are significantly different (P < 0.05) between temperatures for a specific light intensity. Different capital letters indicate significant difference for a specific temperature between LLI and HLI.
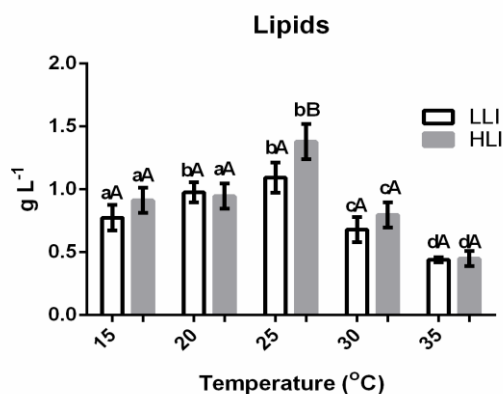
Fig. 6. The joint effect of temperature and light intensity on the lipid content of *Scenedesmus obliquus* BGP. Means with different lowercase letters are significantly different (P < 0.05) between temperatures for a specific light intensity. Different capital letters indicate significant difference for a specific temperature between LLI and HLI.

All suboptimal and the optimal temperature stimulated the lipid synthesis compared to 30 and 35°C. 25 °C was the only temperature investigated where the light intensity significantly stimulated the accumulation of lipids – from (1.1 to 1.4) g L^{-1} (Figure 6). Turns out that the strain is among the best producers of lipids from *Scenedesmus* sp. reported in the literature, being inferior only to *S. protuberans* (up to 29 % according to [5]), *S. dimorphus* (up to 40 %, [32]) and few others. However, if most of the

representatives are considered for their actual yield, the picture changes. For example, in the research of Gris *et al.* [33] it is reported that the lipid content is 40 % of DW, which is about 1.3 g L^{-1}, compared to 1.4 g L^{-1} and 20 % of DW in our study. The purpose of the study of Gris *et al.* [33] was to increase the lipid accumulation by applying stress (high light intensity). Another approach to this can be the one of Mandal and Mallick [34] who applied N-deficiency in order to increase the lipid content of *S. obliquus* (Trup.) Kütz, although at the expense of the growth. In contrast, *S. obliquus* BGP has a higher actual yield compared to the other representatives. Another advantage of our strain is the fact that unlike *S. obliquus* CNWN, for example, the increase of the light intensity positively affects the accumulation of lipids by 30 % [35], while the algal growth is preserved. The above considerations served as an impetus to study further the Bulgarian strain advantages and potential as a viable BioRef feedstock targeted at biofuel production.

Influence of extraction techniques and solvents on the lipid yield

Commonly, based on the polarity of a lipid head-group, it can be classified as either neutral/non-polar (e.g. TAGs) or as polar/complex (e.g. phospholipids). Microalgae lipids normally comprise neutral and polar lipids, and other complex lipophilic materials. The yield and composition of total lipids are influenced by a number of factors, e.g. biological nature of the algal biomass, its pretreatment, particular technique and nature of the solvents employed in their recovery, etc. Pertaining to the latter, as demonstrated by authors who studied solvents' efficiency concerning recovery of the different lipid classes (see for example [36]), low-polarity solvents are best for the extraction of neutral lipids, while polar solvents should be the choice when lipids from chloroplasts and membranes, which contain polar lipids like glycolipids and phospholipids, are to be recovered. Still, it is pointed out that in a direct extraction of the algal biomass by polar solvents a joint recovery of polar and certain neutral lipids could be realized. The latter are lipids that might form complexes with polar lipids, which also form hydrogen bonds with proteins in the cell membrane. Nonpolar solvents cannot extract such complexed neutral lipids since they cannot break those hydrogen bonds. Polar organic solvents, on the other hand, are capable of breaking the lipid-protein complexes and consequently polar and complexed neutral lipids are recovered from the cells [36].

The lipid yields shown in Table 1 were calculated according to:

$$Yield\ (\%) = \frac{mass\ of\ extract\ (g)}{mass\ of\ sample\ (g)} * 100 \qquad (2)$$

Petkov and Dilov and Petkov method

The yield according to Petkov and Dilov [23] method was (25 ± 4.2) %, while that of Petkov - (27±1.4) %. The higher yield achieved by the latter method can be explained within the light of the above discussion. On the one hand, methanol, the solvent with the highest polarity $E_T^N = 0.762$ [37] among all solvents used in our study, is supposed to be more effective in the recovery of polar and complexed neutral lipids than ethanol ($E_T^N = 0.654$). On the other - chloroform ($E_T^N = 0.259$) promotes the extraction of non-polar lipids which might not be extracted by the polar ethanol used in Petkov and Dilov method. Notwithstanding, the advantages of

Petkov and Dilov method, which is suitable for green algae only, are not just its price and speed, but the most important is the fact that it is GRAS.

Two-step atmospheric extraction with stirring

In step 1 *n*-hexane ($E_T^N = 0.09$) was chosen because of its proven selectivity to non-polar lipids. The yield achieved, as shown in Table 1, was quite low - on average 2.4 %. That came as no surprise as firstly no pretreatment of the algal biomass was performed. Hence, the lipids remained entrapped within the cell walls which hindered the contact with the solvent. Secondly, *n*-hexane, because of its very low polarity, is totally incapable of recovering complexed neutral lipids. In contrast, the yield of step 2 was 15.2 %, which can be explained taking

Table 1. Experimental conditions and yields for the extraction techniques employed.

Extraction method	Solvent	Temperature (°C)	Extraction yield (wt %)
Petkov and Dilov, 1987	Ethanol	70	25±4.2
Petkov, 1990	Methanol:chloroform (2:1)	61	27±1.4
Two-step atmospheric with stirring	*n*-Hexane (step 1) Ethanol (step 2)	60 70	2.4 ± 0.34 15.2±0.31 Cumulative yield: 17.6
Soxhlet	Ethanol	78	23.6±2.8
Two-step Soxhlet	*n*-Hexane (step 1) Ethanol (step 2)	68 78	11.1±0.5 16.9±1.6 Cumulative yield: 28

Table 2. Fatty acid composition from FAME GC-FID analysis of selected extracts expressed as relative percent of total fatty acids identified.

Fatty acid identified		Extract recovered			
		1	2	3	4
12:0	Lauric	traces	traces	1.0	traces
14:0	Myristic	0.2	0.2	0.5	0.2
15:0	Pentadecylic	0.1	0.1	0.1	0.1
16:0	Palmitic	17.5	22.3	18.8	24.1
16:1	Palmitoleic	3.9	5.0	3.8	5.7
16:2	Hexadecadienoic	6.9	3.1	2.6	3.6
16:3	Palmitolinolenic	6.1	3.0	2.4	3.5
16:4	Palmitidonic	traces	2.4	1.7	3.0
17:0	Margaric	0.1	0.2	0.2	0.3
18:0	Stearic	1.6	2.7	3.2	2.2
18:1 (n-9)	Oleic	28.6	32.8	38.7	27.6
18:1 (n-7)	Vaccenic	1.0	0.7	0.6	0.8
18:2 (n-6)	Linoleic	16.3	14.3	13.5	14.8
18:3 (n-6)	Gamma-Linolenic	-	0.8	0.6	1.0
18:3 (n-3)	Alfa-Linolenic	17.7	9.5	9.1	9.9
18:4	Stearidonic	-	1.9	1.9	2.0
20:0	Arachidic	traces	0.1	0.1	0.1
20:1	Gondoic	-	0.3	0.4	0.4
22:0	Behenic	-	0.2	0.6	0.3
22:1	Erucic	-	0.4	0.2	0.4
SFA		19.5	25.8	24.5	27.3
MUFA		33.5	39.2	43.7	34.9
DUFA		23.2	17.4	16.1	18.4
PUFA		23.8	17.6	15.7	19.4

into consideration that polar ethanol is the solvent for the recovery of polar and complexed lipids from the biomass residue already depleted to a certain extent from non-polar lipids.

Soxhlet extractions

The yield achieved by the one-step Soxhlet with ethanol is commensurable with the yield of Petkov and Dilov (1987) method but lower than that of Petkov's method (Table 1). The reasons for that were briefly discussed previously.

The yield of step 1 of the two-step Soxhlet was 11.1 %, which is over 4 times higher than that of the atmospheric extraction with stirring applying the same solvent *n*-hexane. Apparently, the increase in the yield is a result of the biomass pretreatment, which caused thinning and disruption of the cell walls. Hence, the mass transfer and diffusion of lipids into the solvent was accelerated. The yield of the second step Soxhlet was 16.9 %, just slightly higher than that of the analogous atmospheric with stirring step, regardless of the fact that no pretreatment of the biomass was performed in the latter case. The cumulative yield of the two-step Soxhlet was about 28 %, which is 1.5 times higher than the cumulative yield of atmospheric with stirring, at the expense of the very low yield of its step 1, and commensurable with Petkov's method. However, it is greener than the latter, as the use of methanol is avoided [38]. Yet, it should be taken into consideration that the Soxhlet process time and volume of the solvents required are considerably higher than those of the other methods examined.

Composition of the extracts recovered depending on the techniques and solvents employed

Microalgae, in general, produce predominantly FAs with chain lengths of 16 and 18 carbon atoms (though there are species that can make FAs of up to 24 carbon atoms in length), both saturated and highly unsaturated. *S. obliquus* BGP is not an exception – about 90 % of its total lipid fraction is formed by C_{16} and C_{18} acids as can be deduced from the FA profile of the extracts recovered, applying different techniques and solvents, and shown in Table 2. Table 2 also displays the relative percentage of saturated (SFA), mono- (MUFA), di- (DUFA) and poly-unsaturated (PUFA) fatty acids in all four extracts, respectively.

Oleic acid, a MUFA, is the dominant FA. The highest (38.7 %) percentage was registered in the *n*-hexane extract (extract 3); the lowest - 27.6 % - in extract 4 recovered by ethanol from the already partially depleted biomass matrix, respectively. The latter is commensurable with the oleic acid

percentage in extract 1. The FA with the second-highest relative percent is the saturated palmitic acid. Extract 4 stands out with 24.1 % of palmitic acid, while extract 1 registers just 17.5 %. In the latter, alpha-linolenic, a PUFA, is not only the second dominant FA, but has the highest percentage among all four extracts analyzed. Although an analogous trend is observed for linoleic acid, a DUFA, for which the highest percentage (16.3 %) is registered in extract 1, still it should be noted that the percentage is commensurable with those of the other three extracts.

Further examination of the FA profiles displayed in Table 2 can help assessing, on the basis of some general considerations, the potential of the *S. obliquus* BGP extracts recovered, as a viable biosource of biofuel-related compounds. Firstly, because oxidation has a detrimental effect on some fuel properties including cetane number (CN), therefore, the higher the content of esters of unsaturated, and particularly PUFAs, in a fuel, the higher is its proneness to oxidation. So, on the one hand, the presence of PUFAs lowers the CN and oxidation stability and is, therefore, undesirable for any fuel. On the other hand, however, it is useful since PUFAs are characterized with lower melting points which improve the cold-flow [39-41]. Also, if the relative rate of oxidation as a function of the degree of unsaturation for methyl esters of the respective FAs is examined it increases as follows: oleic < linoleic < linolenic < stearidonic (Table 2). Taking into consideration the relative percent of each of the above FAs in the extracts recovered, then the extract least prone to oxidation is extract 3, while the most susceptible – extract 1, in which the highest percentages of PUFAs and unsaturated FAs are registered even though it doesn't contain stearidonic acid. Secondly, the lower the PUFA:SFA ratio is in an extract, the more suitable it is as a source for biofuels production. If the corresponding PUFA:SFA ratios for the extracts are calculated, it appears that extract 1 is the only one with PUFA:SFA > 1, while extract 3 has the lowest PUFA:SFA = 0.64. Therefore, based on the above general considerations, extract 3 stands out among the rest with its capacity, either as a stand-alone or mixed with other carefully chosen extracts, as a source for biofuel production.

The experiments performed in our study revealed that *S. obliquus* BGP has a potential as a viable biosource of energy-related compounds. Consequently, that first initial study should be further expanded and intensified in order to outline the possible new horizons to the future applications and uses of this totally unutilized algal strain.

Also, the results of the above analysis can serve as a starting point towards the development of a future strategy targeted at designing a BioRef for algal biomass processing that can deliver a broad spectrum of products by performing a careful selection and sequencing of techniques, operating conditions and solvents. Products with compositions that could either be used directly for biofuels production or mixed with other to realize the delicate desired balance of FAs, will guarantee oxidative stability and CN without compromising the flow, lubricity and viscosity of a high-quality biofuel [39, 42].

CONCLUSIONS

The study presents the biotechnological advantages of the new strain *Scenedesmus obliquus* BGP. The ability to maintain substantial growth and balanced biochemical composition in a broad temperature range and under high light intensity indicates that it can be cultivated on a large scale with substantial reduction of cultivation costs. Moreover, its valuable components accumulate under conditions favorable to growth rather than in response to stress. Finally, because of the richness of BGP biochemical composition in lipids it can be exploited as an excellent, totally unused at present bioresource of compounds suitable for biofuels production.

REFERENCES

1. O. M. Adeniyi, U. Azimov, A. Burluka, *Renew. Sust. Energ. Rev.,* **90,** 316 (2018).
2. https://www.algaebase.org
3. K. Skjanes, C. Rebours, P. Lindblad, *Crit. Rev. Biotechnol.,* **33**(2), 172 (2013).
4. A. Ishaq, H. Matias-Peralta, H. Basri, *Pertanika J. Trop. Agric. Sci.,* **39**(1), 1 (2016).
5. El A. Idrissi Abdelkhalek, B. Mohamed, A.M. Mohammed, A. Lotfi, *Mediterr. Mar. Sci.,* **17**(1), 323 (2016).
6. C. G. Khoo, Y. K. Dasan, M. K. Lam, K. T. Lee, *Bioresour. Technol.,* **292,** 121964 (2019).
7. R. Ganesan, S. Manigandan, M.S. Samuel, R. Shanmuganathan, K. Brindhadevi, N. T. L. Chi, P. A. Duc, A. Pugazhendh, *Biotechnol. Rep.,* **27** (2020).
8. H. Gaffron, J. Rubin, *J. Gen. Physiol.,* **26**, 219 (1942).
9. L. de Jaeger, R. Verbeek, J. Springer, G. Eggink, R.H. Wijffels, *Biotechnol. Biofuels*, **7**(69), 69 (2014).
10. S. Qin, G.X. Liu, Z.Y. Hu, *Process Biochem.,* **43**(8), 795 (2008).
11. M. Zuluaga, V. Gueguen, G. Pavon-Djavid, D. Letourneur, D., *Bioimpacts,* **7**(1), 1 (2017).
12. I. Vasileva, PhD Thesis, IPPG-BAS, Sofia, 2019.
13. J. Komárek, B. Fott, in: Die Binnengewässer, Band 16, Schweizerbartsche Verlagsbuchhandlung (Nägele u. Obermiller), G. Huber-Pestalozzi (ed.), Stuttgart, 1983.
14. T. J. White, T. D. Bruns, S. B. Lee, J. W. Taylor, in: PCR Protocols: A Guide to Methods and Applications, M. A. Innis, D. H. Gelfand, J. J. Sninsky, T. J. White (eds.), Academic Press, New York, 1990, p. 315.
15. K. Tamura, J. Dudley, M. Nei, S. Kumar, *Mol. Biol. Evol.,* **24,** 1596 (2007).
16. C. Dilov, D. Georgiev, M. Bozhkova, *Arch. Hydrobiol.*, **20,** 35 (1985).
17. I. Šetlik, *Ann. Rep. Algol. for the Year 1966*, 89 (1967).
18. D. Georgiev, H. Dilov, S. Avramova, *Hydrobiol.,* **7,** 14 (1978).
19. M. Levasseur, P. Thompson, P. Harrison, *J. Phycol.*, **29**(5), 587 (1993).
20. O. Lowry, N. Rosenbrough, A. Z. Farr, R. J. Randball, *J. Biol. Chem.,* **193,** 265 (1951).
21. M. DuBois, K. A. Gilles, J. K. Hamilton, P. A. Rebers, F. Smith, *Anal. Chem.*, **28**(3), 350 (1956).
22. G. Petkov, PhD Thesis, IPP-BAS, Sofia, 1990.
23. G. Petkov, H. Dilov, *Hydrobiol.*, **29**, 41 (1987).
24. W. N. Phong, P. L. Show, T. Ch. Ling, J. Ch. Juan, E.-P. Nge, J-Sh. Chang, *Algal Res.,* **31**, 506 (2018).
25. J.-Y. Lee, Ch. Yoo, So-Y. Jun, C.-Y. Ahn, H.-M. Oh, *Bioresour. Technol.,* **101**, 75 (2010).
26. S. Taneva, A. Konakchiev, I. Totzeva, M. Kamenova-Nacheva, Y. Nikolova, S. Momchilova, V. Dimitrov, *Bulg. Chem. Commun.,* **49 B**, 126 (2017).
27. M. J. Wynne, J. K. Hallan, *Feddes Repert.*, **126**, 83 (2016).
28. O. Bernard, B. Remond, *Bioresour. Technol.*, **123**, 520 (2012).
29. L. Gigova, N. Ivanova, G. Gacheva, R. Andreeva, S. Furnadzhieva, *J. Phycol.*, **48**, 85 (2012).
30. G. Gacheva, L. Gigova, N. Ivanova, P. Pilarski, J. Lukavsky, *Phycol. Res.*, **61**, 217 (2013).
31. Y. Duan, X. Guo, J. Yang, M. Zhang, Y. Li, *R. Soc. Open Sci.,* **7**, 191214 (2020).
32. B. H. Um, Y. S. Kim, *J. Ind. Eng. Chem.*, **15**(1), 1 (2009).
33. B. Gris, T. Morosinotto, G.M. Giacometti, A. Bertucco, E. Sforza, *Appl. Biochem. Biotech.,* **172**, 2377 (2014).
34. S. Mandal, N. Mallick, *Appl. Microbiol. Biotechnol.,* **84,** 281 (2009).
35. S. H. Ho, C. Y. Chen, J. S. Chang, *Bioresour. Technol.*, **113,** 244 (2012).

36. E. Ryckebosch, C. Bruneel, R. Termote-Verhalle, K. Muylaert, I. Foubert, *Algal Res.,* **3**, 36 (2014).
37. Ch. Reichardt, in: Solvents and Solvent Effects in Organic Chemistry, Third Edition, 2003, p. 472.
38. F. P. Byrne, S. Jin, G. Paggiola, T. H. M. Petchey, J. H. Clark, T. J. Farmer, A. J. Hunt, C. R. McElroy, J. Sherwood, *Sustain. Chem. Process.,* **4**(7) (2016).
39. G. Knothe, *Energy Fuels,* **22**(2), 1358 (2008).
40. J. Pullen, K. Saeed, *Ren. Sust. Energ. Rev.,* **16** (8), 5924 (2012).
41. T. Ismagulova, K. Chekanov, O. Gorelova, O. Baulina, I. Semenova, I. Selyakh, O. Chivkunova, E. Lobakova, O. Karpova, A. Solovchenko, *J. Appl. Phycol.,* **30**(5), 2737 (2017).
42. G. Hu, J. A. Heitmann, O. J. Rojas, *BioResour.,* **3**, 270 (2008).

Acknowledgement to Reviewers for vol. 52 (2020)

The Editors of Bulgarian Chemical Communications would like to take this opportunity to thank you for the effort and expertise that you contributed to reviewing, without which it would be impossible to maintain the high standards of our journal:

A

A. Ahmedova
A. Ivanova
A. Popova
A. Prabhu
A. Subramania
A. Trendafilova
A. Vassilev

B

B. Galabov
B. Nikolova
B. Saha
B. Shivachev
B. Stambolijska

D

D. Antonova
D. Bruno
D. Cheshmedjieva
D. Djonova
D. Kovacheva
D. Ottor
D. Pantaleeva
D. Selloum

E

E. Nesterov
E. Razkazova-Velkova
E. Vassileva
E. Velcheva

F

F. Mahjoubi

G

G. Angelov
G. Antova
G. Gencheva
G. Kadinov
G. Stavrakov

I

I. Angelov
I. Avramova
I. Awan
I. Bangov
I. Doytchinova
I. Georgieva
I. Grabchev
I. Havezov
I. Ivanov
I. Karadunan
I. Pajeva
I. Slavchev
I. Svinyarov
I. Trendafilova

J

J. Kaneti

K

K. Alipieva
K. Kostova
K. Semkov

L

L. Antonov
L. Fachikov
L. Tancheva

M

M. Bogdanov
M. Dangalov
M. Georgieva
M. Kamenova
M. Khajenoori
M. Marudova
M. Ognyanov
Marg. Popova
Mil. Popova
M. Radojkovic
M. Rogozherov
M. Tsvetkov

N

N. Anastasova
N. Boshkov
N. Burdjiev
N. Dimcheva
N. Dishovski
N. Koseva
N. Petkova
N. Tahsin
N. Toshkov

P

P. Denev
P. Nedyalkov
P. Shestakova

R

R. Dhar
R. Kalfin
R. Kaur
R. Lyapchev

R. Maksimovic
R. Mammadov
R. Manonmani
R. Raichev
R. Rashkov
R. Stoyanova

S

S. Angelova
S. Bakalova
S. Belaidi
S. Boyadjiev
S. Chtita
S. Georgieva
S. Ilieva
S. J. Chung
S. Keyf
S. Kukuc
S. Minkovska
S. Momchilova
S. Sahreen
S. Simeonov
S. Simova
S. Statkova
S. Stoykova

T

T. Tsoncheva
T. Yanardag

V

V. Delchev
V. Ilcheva
V. Jayaraman
V. Kurteva

V. Pavlovic

Y

Y. Acikbas
Y. Georgiev
Y. Kalvachev
Y. Mitrev
Y. Nikolova
Y. Zagranyarski

Instructions about Preparation of Manuscripts

General remarks: Manuscripts are submitted in English by e-mail The text must be typed on A4 format paper using Times New Roman font size 11, normal character spacing. The manuscript should not exceed 15 pages (about 3500 words), including photographs, tables, drawings, formulae, etc. Authors are requested to use margins of 2 cm on all sides

Manuscripts should be subdivided into labelled sections, e.g. **Introduction, Experimental, Results and Discussion**, *etc*. **The title page** comprises headline, author's names and affiliations, abstract and key words. Attention is drawn to the following:

a) **The title** of the manuscript should reflect concisely the purpose and findings of the work. Abbreviations, symbols, chemical formulas, references and footnotes should be avoided. If indispensable, abbreviations and formulas should be givenin parentheses immediately after the respective full form.

b) **The author**'s first and middle name initials and family name in full should be given, followedby the address (or addresses) of the contributing laboratory (laboratories). **The affiliation** of the author(s) should be listed in detail by numers (no abbreviations!). The author to whom correspondence and/or inquiries should be sent should be indicated by asterisk (*) with e-mail address.

The abstract should be self-explanatory and intelligible without any references to the text andcontaining not more than 250 words. It should be followed by key words (not more than six).

References should be numbered sequentially in the order, in which they are cited in the text. The numbers in the text should be enclosed in brackets [2], [5, 6], [9−12], etc., set on the text line. References are to be listed in numerical order on a separate sheet. All references are to be given in Latin letters. The names of the authors are given without inversion. Titles of journals must be abbreviated according to Chemical Abstracts and given in italics, the volume is typed in bold, the initial page is given and the year in parentheses. Attention is drawn to the following conventions:a) The names of all authors of a certainpublications should be given. The use of "*et al*." inthe list of references is not acceptable.b) Only the initials of the first and middle names should be given. In the manuscripts, the reference to author(s) of cited works should be made without giving initials, e.g. "Bush and Smith [7] pioneered...". If the reference carries the names of three or more authors it should be quoted as "Bush *et al*. [7]", if Bush is the first author, or as "Bush and co-workers [7]", if Bush is the senior author.

Footnotes should be reduced to a minimum. Each footnote should be typed double-spaced at thebottom of the page, on which its subject is first mentioned.**Tables** are numbered with Arabic numerals on the left-hand top. Each table should be referred to inthe text. Column headings should be as short as possible but they must define units unambiguously.The units are to be separated from the preceding symbols by a comma or brackets. Note: The following format should be used when figures, equations, *etc*. are referred to the text (followed by the respective numbers): Fig., Eqns., Table, Scheme.

Schemes and figures. Each manuscript should contain or be accompanied by the respective illustrative material as well as by the respective figure captions in a separate file (sheet).As far as presentation of units is concerned, SI units are to be used. However, some non-SI units are also acceptable, such as °C, ml, l, etc.The author(s) name(s), the title of the manuscript, the number of drawings, photographs, diagrams, etc., should be written in black pencil on the back of the illustrative material (hard copies) inaccordance with the list enclosed. Avoid using more than 6 (12 for reviews, respectively) figures in the manuscript. Since most of the illustrative materials are to be presented as 8-cm wide pictures, attention should be paid that all axis titles, numerals, legend(s) and texts are legible.

The authors are required to submit the text with a list of three individuals and their e-mail addresses that can be considered by the Editors as potential reviewers. Please, note that the reviewers should be outside the authors' own institution or organization. The Editorial Board of the journal is not obliged to accept these proposals.

The authors are asked to submit **the final text** (after the manuscript has been accepted for publication) in electronic form by e-mail. The main text, list of references, tables and figure captions should be saved in separate files (as *.rtf or *.doc) with clearly identifiable file names. It is essential that the name and version of the word-processing program and the format of the text files is clearly indicated. It is recommended that the pictures are presented in *.tif, *.jpg, *.cdr or *.bmp format.

The equations are written using "Equation Editor" and chemical reaction schemes are written using ISIS Draw or ChemDraw programme.

EXAMPLES FOR PRESENTATION OF REFERENCES

REFERENCES
1. D. S. Newsome, *Catal. Rev.–Sci. Eng*., **21**, 275 (1980).
2. C.-H. Lin, C.-Y. Hsu, *J. Chem. Soc. Chem. Commun*., 1479 (1992).
3. R. G. Parr, W. Yang, Density Functional Theory of Atoms and Molecules, Oxford Univ. Press, New York, 1989.
4. V. Ponec, G. C. Bond, Catalysis by Metals and Alloys (Stud. Surf. Sci. Catal., vol. 95), Elsevier, Amsterdam, 1995.
5. G. Kadinov, S. Todorova, A. Palazov, in: New Frontiers in Catalysis (Proc. 10th Int. Congr. Catal., Budapest,(1992), L. Guczi, F. Solymosi, P. Tetenyi (eds.), Akademiai Kiado, Budapest, 1993, Part C, p. 2817.
6. G. L. C. Maire, F. Garin, in: Catalysis. Science and Technology, J. R. Anderson, M. Boudart (eds), vol. 6, SpringerVerlag, Berlin, 1984, p. 161.
7. D. Pocknell, *GB Patent* 2 207 355 (1949).
8. G. Angelov, PhD Thesis, UCTM, Sofia, 2001, pp. 121-126.
9 JCPDS International Center for Diffraction Data, Power Diffraction File, Swarthmore, PA, 1991.
10. CA **127**, 184 762q (1998).
11. P. Hou, H. Wise, *J. Catal.*, in press.
12. M. Sinev, private communication.
13. http://www.chemweb.com/alchem/articles/1051611477211.html.

Texts with references which do not match these requirements will not be considered for publication!!!

CONTENTS